Pore-Scale Network Modelling of Residual Oil Saturation in Mixed-Wet Systems

Andrey Ryazanov

Submitted for the degree of Doctor of Philosophy

Heriot-Watt University

Institute of Petroleum Engineering

February 2012

ABSTRACT

The prediction of residual oil saturation (S_{or}) and relative permeabilities after waterflooding in mixed-wet systems is a very challenging task. These are important parameters which must be estimated for a full field simulation of waterflooding. The S_{or} also defines the target oil for any proposed EOR process after an initial waterflood. Pore-scale network modelling can be used to estimate relative permeabilities, and the amount and nature of the trapped residual oil if the correct physics of oil displacement are properly included.

During the waterflooding of mixed-wet systems, oil may drain down to relatively low residual saturations. Such S_{or} levels can only be calculated correctly when oil layers in pore corners are included in the pore-scale modelling. van Dijke and Sorbie (J. Coll. Int. Sci. **293** (2006) 455) obtained an accurate thermodynamically derived criterion for oil layers' existence in pores with non-uniform wettability caused by ageing, which is more restrictive than the previously used geometrical layer existence criterion. This thermodynamic criterion has been included in a newly developed two-phase pore network model to calculate realistic S_{or} values for mixed-wet sandstones. A new *n*-cornered star pore shape characterization technique has also been implemented in this model since the precise description of the pore shape was found to be important.

Two unstructured networks, derived from Berea sandstone have been used for a number of sensitivities of the S_{or} and relative permeabilities with respect to wettability conditions. It is shown that S_{or} is lower for the more strongly oil-wet cases, while the water relative permeability curves increase gradually with oil-wetness at the higher water saturations. It has also been shown that pore shape approximations and oil layers collapse criterion have a significant impact on the S_{or} and the relative permeabilities. In particular, the thermodynamic oil layer existence criterion gives higher and more realistic S_{or} compared to previously used geometrical criterion. The network modelling has been used to match experimental data for water-wet and mixed-wet systems. In particular, the good agreement with mixed-wet systems strongly indicates that using the correct oil layer existence criteria is a significant step forward in the reliable prediction of S_{or}.

ACKNOWLEDGMENTS

I would like to thank my supervisors Doctor Rink van Dijke and Professor Ken Sorbie for their constant support, guidance and encouragement during this study. Without their assistance, this work would have not been completed.

DECLARATION STATEMENT

TABLE OF CONTENTS

LIST OF TABLES

LIST OF FIGURES

LIST OF PUBLICATIONS BY THE CANDIDATE

Helland J.O., A.V. Ryazanov and M.I.J. Van Dijke, 2008, *Characterization of pore shapes for pore network models*, In Proceedings of the 11th European Conference on the Mathematics of Oil Recovery (ECMOR XI), September (2008), Bergen, Norway.

Ryazanov A.V., M.I.J. Van Dijke and K.S. Sorbie, 2008, *Two-phase pore-network modelling with non-uniform wettability: existence of oil layers*, In Proceedings of 10th International Symposium on Evaluation of Reservoir Wettability and Its Effect on Oil Recovery, Abu Dhabi, United Arab Emirates.

Ryazanov A.V., M.I.J. Van Dijke and K.S. Sorbie, 2009, *Two-phase pore-network modelling: existence of oil layers during water invasion*, Transport in Porous Media, **80**(1), 79-99.

Ryazanov A.V., M.I.J. Van Dijke and K.S. Sorbie, 2010, *Pore-network Prediction of Residual Oil Saturation Based on Oil Layer Drainage in Mixed-wet Systems*, In Proceedings of SPE Improved Oil Recovery Symposium, Tulsa, Oklahoma, USA: Society of Petroleum Engineers.

Ryazanov A.V., M.I.J. Van Dijke and K.S. Sorbie, 2010, *Prediction of residual oil saturation in mixed-wet networks using accurate pore shape descriptors*, In Proceedings - Computational Methods in Water Resources XVIII International Conference (CMWR XVIII), Barcelona, Spain.

CHAPTER 1 - INTRODUCTION

Large scale numerical simulation of multi-phase flow in porous media is of great importance in prediction of various phenomena in hydrology, environmental engineering and petroleum engineering. For example, these phenomena could be transportation of non-aqueous phase liquid (NAPL) through unsaturated soils in hydrology or the enhanced oil recovery scenario in petroleum engineering. This numerical reservoir simulation of multi-phase flow requires an accurate description of macroscopic properties such as capillary pressures and relative permeabilities as functions of the phase saturations, including waterflooding residual oil.

These macroscopic properties can be measured by laboratory experiments which are quite expensive, time consuming and therefore can be conducted only for a limited set of conditions. Alternatively, a reliable physically-based model can be developed to predict multiphase flow at the pore-scale and consequently to estimate relative permeabilities and capillary pressures at the macro-scale (**Figure 1.1**).

The physically-based models are usually based on pore level physics of displacement mechanisms and require a proper representation of the pore space structure. The pore space structure is obtained as a 3D image either by computer tomography (CT) imaging

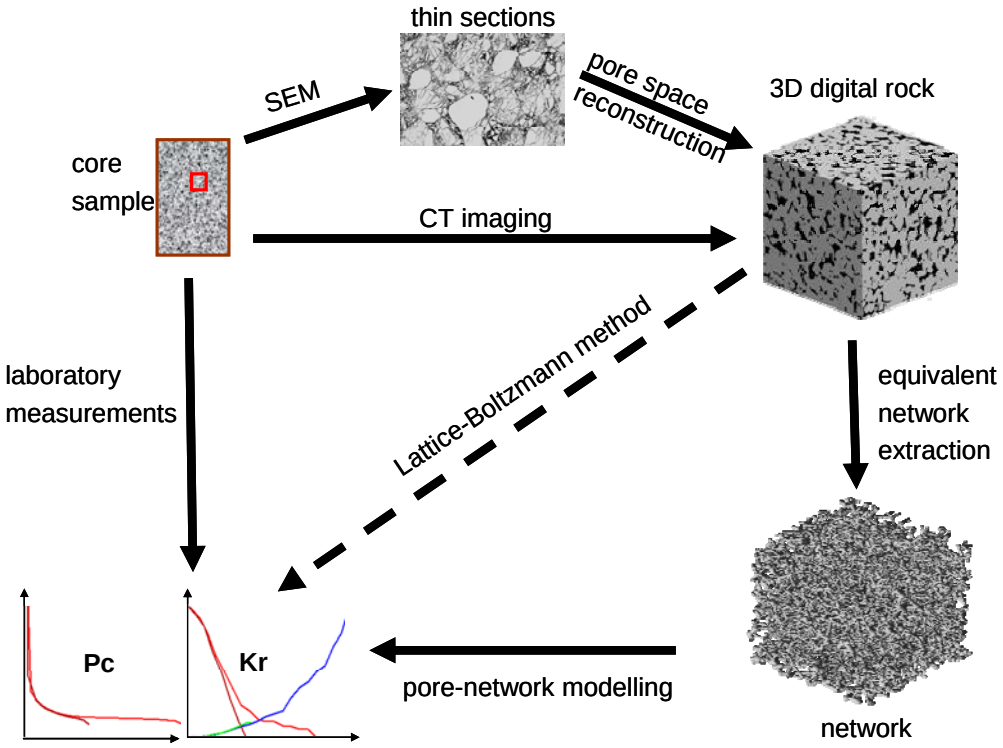

Figure 1.1 Alternative workflows from core sample to relative permeabilities and capillary pressures.

(Dunsmuir et al. 1991, Spanne et al. 1994, Coles et al. 1996) of core samples or by numerical 3D reconstructions from 2D thin sections: process-based algorithms (Bakke and Øren 1997, Øren and Bakke 2003) and statistical methods (Wu et al. 2006, Okabe and Blunt 2007). Once the 3D image is available, it is possible to simulate fluid flow directly using e.g. the Lattice-Boltzmann method (Grunau et al. 1993, Ferreol and Rothman 1995, Chen and Doolen 1998). However, for multi-phase flow that method is computationally ineffective and pore-scale network modelling (Øren et al. 1998, Patzek 2001, Valvatne and Blunt 2004) can be used instead.

The network modelling approach requires as input a topologically and geometrically equivalent network of pore bodies interconnected by pore throats, which can be extracted from 3D images of the pore space (Øren and Bakke 2003, Al-Kharusi and Blunt 2007, Dong et al. 2007, Jiang et al. 2007). Additionally, to predict multiphase flow an accurate description of the pore level flow physics is needed. Thus, if a pore space network is supplied, pore-network modelling is a very attractive tool for estimating macroscopic transport properties with arbitrary wetting conditions.

Capillary pressure and relative permeability functions predicted by pore-network modelling strongly depend on the pore shapes and presence of fluid films and layers in pore corners. During water flooding of mixed-wet systems, oil may drain down to relatively low residual saturations. A number of studies have indicated that such low saturations can only be reached when oil layers in pore corners are included in the pore-scale modelling. van Dijke and Sorbie (2006) obtained accurate thermodynamically derived criteria for oil layers' existence in pores with non-uniform wettability caused by ageing, which is more restrictive than the previously used geometrical layer existence criteria. In addition, because real pore shapes are generally highly irregular and often non-convex it is important to use an appropriate shape characterization. Therefore, in addition to the commonly used Circle-arbitrary Triangle-Square (CTS) shape representation we developed a new *n*-cornered star (Star) shape characterization technique, which takes shape factor and dimensionless hydraulic radius as input parameters.

In this work, we present a newly developed state-of-the-art pore scale network modelling tool which incorporates the correct intra-pore physics, in particular,

thermodynamical oil layer existence criteria and the new pore shape characterization technique Star.

In Chapter 2, we review the literature on different aspects of pore network modeling and its related areas: pore space reconstruction, pore-scale network extraction, pore shape characterization, contact angle hysteresis and wettability alteration, pore-scale displacement mechanisms and entry pressures, network modelling of experimental data, effect of wettability on residual oil saturation and relative permeabilities.

In Chapter 3 we describe the newly developed pore-scale network modelling tool, which takes as input the geometrically and topologically equivalent network (extracted) from a real pore space. In particular, besides the commonly used CTS pore characterization, we also present a new pore shape characterization technique to identify the equivalent regular n-cornered star shape (Star). Then, we describe the expressions for the single-phase and two-phase conductances for different shape characterizations.

In Chapter 4 we describe possible fluid configurations and displacements which can occur during primary drainage, water invasion (after ageing) and secondary drainage. We present corresponding entry pressures for displacements in Star and CTS pores, in particular, the thermodynamic oil layers collapse criterion and the geometrical collapse criterion. We also describe three possible scenarios for the formation of oil layers, involving these criteria.

In Chapter 5, to test the accuracy of the pore shape characterization (Star and CTS), we consider 70 pore shapes, which were extracted from high-resolution 2D images of a Bentheimer rock sample. For each real shape, we derive the corresponding CTS and Star approximations. Then, for the real shapes we calculate drainage entry pressures using the newly developed method (Helland et al. 2008) and calculate single phase conductance using a finite element approach, and compare these properties with those for the equivalent shapes. Finally, we construct a capillary bundle model from the 70 pores and test the predictive capabilities of the characterization approaches in terms of relative permeabilities and capillary pressures.

In Chapter 6 we perform a wide range of network model sensitivity calculations of water flood residual oil saturation (S_{or}) to various wettability conditions and we also

analyze the effect of pore shape characterization on S_{or} behaviour. We compare residual oil saturations from simulations for two Berea networks with different wettability conditions for the thermodynamic oil layer existence scenario with the two other scenarios resulting. Sensitivity results of oil residual and number of displacements are analysed with respect to various water flood end-point capillary pressures. Additionally, we examine the sensitivity of relative permeability to average contact angle and to the fraction of oil-wet pores. We also investigate the effect of oil layer existence criteria and pore shape characterization on the relative permeability curves.

In Chapter 7, to validate the pore-scale network model, we compare relative permeabilities for two Berea networks with water-wet and oil-wet experiments. We also show the matching results of comparison with mixed-wet waterflooding recovery experimental data by Jadhunandan and Morrow (1995).

Finally, in Chapter 8 we will summarize the important findings of this work, give suggestions for future research and recommend possible applications of the newly developed state-of-the-art pore network modelling tool.

CHAPTER 2 - LITERATURE REVIEW

In this chapter we review the literature on different aspects of pore network modelling of water flood residual oil and related areas: pore space reconstruction, pore-scale network extraction, pore shape characterization, contact angle hysteresis and wettability alteration, pore-scale displacement mechanisms and entry pressures, network modelling of experimental data, effect of wettability on residual oil saturation and relative permeabilities. Based on the presented literature review we summarize which methods we employ in this work and what new features we have implemented to improve previous results.

2.1 Pore Space Reconstruction

The network modelling approach requires as input a topologically and geometrically equivalent network of pore bodies connected by pore throats, which can be extracted from 3D images of the pore space. This 3D image pore space structure is obtained either by computer tomography (CT) imaging of core samples or by numerical 3D reconstructions from 2D thin sections: process-based algorithms and statistical methods.

2.1.1 3D CT Scanning

Direct imaging of the porous media can be obtained by means of X-ray computed micro-tomography (micro-CT) which can have a resolution down to few microns (Dunsmuir et al. 1991, Arns et al. 2004, Arns et al. 2005). A Synchrotron micro-CT provides even better resolution, possible to sub-microns 0.3-0.7μm (Coenen et al. 2004). This is a non-destructive approach and provides an image very close to reality. However, there is a "trade off" between the size of the image and its resolution and, for relatively large sample sizes, the resolution of CT scanning may not be high enough to resolve micro porosity, as found in many carbonate reservoirs. In this case, 2D thin section scanning electronic microscope (SEM) images can be used to reconstruct the 3D pore space with reasonable resolution by means of approaches such as process-based modelling (Bryant and Raikes 1995, Øren and Bakke 2003) or stochastic reconstruction (Wu et al. 2006, Okabe and Blunt 2007).

2.1.2 Process-Based Algorithm

Process-based reconstruction algorithms model sedimentation, compaction and diagenesis of granular material explicitly. Bryant et al. (1992, 1993a, 1993b, 1995)

were the first to propose process-based pore reconstruction methods. They modelled the sandstone rock-forming process using a random close packing of equal spheres. Compaction and diagenesis were also included in the process. This approach was extended later by packing spheres of different size (Bakke and Øren 1997, Øren et al. 1998, Øren and Bakke 2002, 2003). The grain size distribution and other petrographical information were derived from 2D thin section images. Then similar approaches were used to model sandstone formation including sedimentation, compaction and diagenesis. For diagenesis, besides a quartz cementation they also introduced clay content. These reconstructions showed very good rock connectivity representation and have been successfully used for prediction of multi-phase transport properties (Øren et al. 1998, Patzek 2001, Øren and Bakke 2003, Valvatne and Blunt 2004, Piri and Blunt 2005b). However, where complex diagenetic processes are important, for example in many carbonates where multi-scale pore systems can evolve (Lucia 2007), these methods do not produce reasonable results.

2.1.3 Statistical Methods

Various statistical methods have been developed to reconstruct the 3D rock from 2D thin sections (Quiblier 1984, Adler et al. 1990, Roberts 1997). These methods recreate the 3D pore space by matching single- and two-point statistics derived from the input 2D images. However, these methods fail to reproduce the long-range connectivity of the original pore space, for example in rocks with low porosity. To overcome this problem, multi-point statistical methods were developed (Okabe and Blunt 2004, 2005, 2007). The latter use 2D thin sections as input training images to derive multi-point statistical information. The subsequent 3D rock representation reproduces typical patterns of the pore space. However these iterative multi-point methods are computationally very demanding. Instead, Wu et al. (2004, 2006) developed a much more efficient single scan stochastical reconstruction algorithm based on Markov Chain Monte Carlo (MCMC) simulation. Wu et al's approach is a Markov Random Mesh method, for which thin sections in three orthogonal directions are used as training images. The transition probabilities between the void and solid (pore and rock) are calculated from the input images for all the local predefined patterns which may occur in a "stencil" of a certain size. The MCMC reconstruction differs from the other methods in that it uses a multiple-voxel interaction scheme to obtain the realisations that match structural characteristics and patterns from the input data.

2.2 Pore Scale Network Extraction

The topologically and geometrically equivalent pore networks can be extracted from 3D images of the pore space. There are several types of algorithms for network extraction, e.g.: medial-axis based, maximum ball based, Voronoi diagram. We will review these algorithms here.

2.2.1 Medial Axis Based Algorithm

The medial axis based algorithm reduces the digital pore space to the topological skeleton of the pore network. Then the pore bodies and pore throats are identified by pore space partitioning. One of the first implementations of this algorithm was developed by Lindquist et al. (1996) and Lindquist and Venkatarangan (1999). The medial axis based methods preserve topological information very well, but have some problems with partitioning the pore bodies. Sheppard et al. (2005, 2006) developed some "cleaning" procedure to overcome these problems. They suggested removing spurious pore throats and merging connected individual pore bodies to reduce the high local coordination number. Jiang et al. (2007) made the medial axis extraction algorithm more computationally efficient and improved the pore body identification procedure by using a "junctions" concept for nodes (pore bodies) and "not junctions" for bonds (pore throats).

2.2.2 Maximum Ball Based Algorithm

The maximum ball algorithm (Silin et al. 2003, Silin and Patzek 2006) was developed to derive the topology of the rock pore space based on 3D images. The idea was to define the maximum ball for each void voxel, which fits in the surrounding pore space. The largest maximum balls defined the pore bodies and the smallest balls residing between them were assigned to pore throats. Others later extended the algorithm for network extraction and improved the method for distinguishing between pore throats and pore bodies (Al-Kharusi and Blunt 2007, Dong et al. 2007, Dong and Blunt 2009a).

2.2.3 Voronoi Diagram

For the pore space models reconstructed by the process-based algorithm (see Section 2.1.2), the coordinates of all the grain centres are known and this information is used to extract the pore space skeleton using Voronoi tessellation (Bryant and Blunt 1992, Bryant et al. 1993a, Bryant et al. 1993b, Øren and Bakke 2003).

2.3 Types of Network Flow Models

There are two main types of network modelling tools which are defined by the flow regime: capillary dominated and viscous dominated. In the case of low capillary number, N_c, which is defined as:

$$N_c = \frac{\mu u}{\sigma} \leq 10^{-5}, \tag{2.1}$$

where μ is viscosity, u is fluid velocity and σ is interfacial tension, the viscous forces are insignificant and the flow is governed by capillary forces. In this case quasi-static network modelling can be applied. Otherwise, dynamic network modelling should be used where both viscous and capillary forces are accounted for.

2.3.1 Quasi-Static Models

In a quasi-static network model the capillary pressure is the "driving" force that determines the saturation evolution in the model. This quantity is changed gradually and, for each capillary pressure value, the equilibrium position of the fluid-fluid interfaces is determined, based on distinct pore fluid displacements (see Section 2.5). The displacements or fluid configurations changes occur sequentially, according to distinct capillary pressure criteria (McDougall and Sorbie 1995, Blunt 1998, Øren et al. 1998, Dixit et al. 1999, Man and Jing 2000, Patzek 2001, van Dijke and Sorbie 2002, Valvatne and Blunt 2004, Piri and Blunt 2005a). In this thesis a quasi-static network model is employed, the description of which can be found in Chapter 3.

2.3.2 Dynamic Models

In dynamic pore scale models, pressure gradients form the "driving" force. At each time step, the pressure distribution in the network is calculated, then the fluid-fluid interfaces are updated and the displacements occur based on pressure difference criteria. There are two families of dynamic pore-scale models. The first family of models does not include the flow through wetting films (Mohanty 1982, Salter and Mohanty 1982, Mohanty and Salter 1983, Koplik and Lasseter 1985, Dias and Payatakes 1986a, b, Koplik et al. 1988, Blunt and King 1991, Vizika et al. 1994, Aker et al. 1998). Most of these models were used to investigate the effect of capillary number (flow rate, interfacial tension) and viscosity ratio on the relative permeability, residual oil saturation and microdisplacement mechanisms.

A second family of dynamic models includes flow through wetting films (Blunt and Scher 1995, Mogensen and Stenby 1998, Constantinides and Payatakes 2000, Hughes

and Blunt 2000, Singh and Mohanty 2003, Al-Gharbi and Blunt 2004, 2005, Joekar-Niasar et al. 2010a). Using such models it is possible to analyse the balance between piston-like and snap-off displacements (see Section 2.5) and its effect on residual oil for a wide range of capillary numbers and viscosity ratios.

2.4 Pore Shape Characterization

2.4.1 Type of Shapes

The main network model characteristics, such as conductances (see Section 2.4.2) and capillary entry pressures (see definition in Section 2.7), depend on the shapes of the pore bodies and the pore throats cross-sections. Most of the earliest network models assumed circular cross-sections for simplicity (Fatt 1956a, b, c, McDougall and Sorbie 1995, Dixit et al. 1998, Dixit et al. 1999, Dixit et al. 2000). One major disadvantage of a circular shape is that it cannot accommodate more than one fluid in a stable configuration in a single pore and it therefore does not allow any films or layers of additional phases to be formed during the displacement processes. In contrast, it can be clearly seen from thin section images of any rock that real pore shapes are very irregular and have many corners. It has been shown experimentally that in pores with angular cross-section the wetting phase can occupy the corners with the non-wetting phase in the centre (Lenormand et al. 1983). These corner wetting films provide additional phase connectivity and they may reduce the trapping level of the defending phase. Thus, networks that have pore elements with circular cross sections will not be able to predict experiments where the film flow is crucially important (Or and Tuller 1999, Tuller et al. 1999).

A number of network models have been used where the pore space is idealised as a regular cubic lattice with square cross-sections for both pore bodies and pore throats (Blunt 1997a, b, 1998, Fenwick and Blunt 1998b, Larsen et al. 2000). Equilateral triangular shapes have also been used in capillary bundle models (Hui and Blunt 2000a, b, Helland and Skjaeveland 2006a, Helland and Skjaeveland 2006b) and in cubic networks (Fenwick and Blunt 1998a).

Mason and Morrow (1991) introduced the concept of the shape factor $G=A/P^2$, with cross sectional area A and perimeter P. They derived the capillary entry pressure expression for a pore with a cross-section shaped as an arbitrary triangle in terms of its

shape factor G. Thus Mason and Morrow (1991) demonstrated the importance of the shape factor for capillary entry pressure calculation and others have used this approach to characterize complex shapes by regular shapes with the same G. Later, an algorithm for arbitrary triangular shape identification based on shape factor was presented by Øren et al. (1998) and Patzek and Silin (2001). Øren et al. (1998) used this technique for the unstructured network extracted from the process-based reconstruction of the pore space. They characterized pore shapes exclusively as arbitrary triangles. The shape factor value for an arbitrary shape lies between 0 and 0.0785 but the maximum possible shape factor for an arbitrary triangle is limited by that for the equilateral triangle, which is 0.048. Therefore, additional shapes should be used for a more accurate pore shape representation. Most modern network pore-scale simulators approximate the real pore shapes by Circle, arbitrary Triangle and Square shaped pores (denoted CTS), for which the shape factor is matched (Patzek 2001, Valvatne and Blunt 2004, Piri and Blunt 2005a, Valvatne et al. 2005). Patzek (2001) actually used the CTS approach only for pore throat characterization and he then used square shapes for pore body representation.

Kovscek et al. (1993) noticed that many realistic pore shapes are non-convex and proposed the use of a 4-cornered curved star shape formed by 4 touching spheres (see **Figure 2.7**). This so-called grain boundary pore (GBP) shape was then used in a capillary bundle model (Kovscek et al. 1993) as well as in network models (Goode and Ramakrishnan 1993, Man and Jing 1999, 2000, 2001).

Joekar-Niasar et al. (2010b) proposed a procedure for pore shape characterization based on shape factors or a shape factor distribution extracted from input rock images, which allowed them to reproduce a continuous ranges of shape factors between 0 and the maximum for a circle 0.785. They used regular n-hyperbolic polygons, which are GBPs, (and irregular polygons for n=3) for pore throat description and prolate spheroids for pore body representation. The main idea was to identify the type of cross-section based on the shape factor and its overall distribution.

In this thesis, we apply the CTS approach and additionally suggest the use of a new n-cornered star shape characterization technique (Star) (for details see Chapter 3).

2.4.2 Conductance (single-phase and two-phase)

When calculating absolute and relative permeabilities from network models, single phase and two-phase hydraulic conductances g have to be specified (or calculated) for each pore element (body or throat). The hydraulic fluid conductance g is the coefficient of proportionality between the fluid flowrate q and the pressure gradient ∇P:

$$q = g\nabla P \tag{2.2}$$

Patzek and Silin (2001) obtained single phase conductances for equilateral triangular, rectangular, and elliptic shapes analytically and for arbitrary triangular shapes semi-analytically (using conformal mapping). They also demonstrated that dimensionless conductances g/A^2 for arbitrary triangular, rectangular and elliptic shapes are approximately proportional to the shape factor G. Helland et al. (2006) calculated single phase conductances for regular star shapes with different numbers of corners (n), using a finite element method. They also showed that the commonly assumed proportionality between g/A^2 and G breaks down for increasing n.

Two-phase conductances are usually defined as flow conductances of corner wetting films. Zhou et al. (1997) derived approximate analytical solutions for the corner flow resistance (reciprocal of conductance). They suggested that the boundary condition should be perfect-slip for any oil-gas interface and no-slip for the oil-water interface. Later, Hui and Blunt (2000a) slightly modified the analytical expressions and extended them to non-zero contact angles (see Section 2.6.1). Patzek and Kristensen (2001) published correlations between corner film conductance and corner film shape factor, corner half-angle, and contact angle based on finite element calculations. They showed that their correlation performed better than the previous one (Zhou et al. 1997, Hui and Blunt 2000a). However, Valvatne and Blunt (2004) showed that a correlation proposed by Øren et al. (1998) was superior to the other published expressions (Zhou et al. 1997, Patzek and Kristensen 2001), which was also confirmed later by Helland et al. (2006).

In the ***three***-phase case, an oil layer may be sandwiched between the water filled corner films and bulk gas. Similarly, in the case of two-phase water invasion with non-uniform wettabiliy an oil layer may be sanwiched between the water in the corners and the water in the center of the pore. Initially, Zhou et al. (1997) obtained analytical solutions for the oil layer flow resistance in the three-phase case (perfect-slip for the oil-gas interface and no-slip for the oil-water interface). Hui and Blunt (2000a) then

slightly modified this previously derived solution (Zhou et al. 1997) and generalized it for a non-zero contact angle. Al-Futaisi and Patzek (2003c) used the finite element method to obtain the conductance of a sandwiched oil layer between the water film and gas in the pore centre. They considered four different boundary conditions at the fluid-fluid interface (all possible combinations of no-slip and perfect-slip for oil-water/gas-oil boundaries) and derived related correlations. By comparison with numerical results, they also showed that their correlation performed much better than previously proposed solutions (Zhou et al. 1997, Hui and Blunt 2000a). Valvatne and Blunt (2004) derived their own correlation for oil layers sandwiched between water films and bulk water by using a no-slip boundary condition at the oil-water interface. They made comparison only with the solutions previously derived by Hui and Blunt (2000a) and showed that their correlation gave more accurate predictions.

2.5 Displacements

Invasion percolation is a dynamic process of one fluid (invading phase) displacing another (defending phase), during which the invading phase cluster (see Section 4.1) has to be connected to the inlet face of the network (Wilkinson and Willemsen 1983, Dias and Wilkinson 1986).

There are two types of invasion percolation (IP): with and without trapping (Knackstedt et al. 2000). In the second case, the defending fluid is thought of as infinitely compressible and the invading phase can displace the defending phase from any accessible pore element. A pore element is accessible if it has a neighbouring pore element that is occupied by the invading phase and the latter is connected to the inlet face by means of the corresponding invading cluster. The first type, invasion percolation with trapping, is most commonly used: the defending phase is considered incompressible and defending phase occupying an accessible pore element needs to be connected to the outlet face to be displaced. If a defending phase cluster becomes disconnected from the outlet, this cluster is said to be trapped.

Al-Futaisi and Patzek (2003a) noticed that the drainage process in a strongly water-wet systems (with water wetting films) is effectively bond invasion percolation without trapping (Stauffer and Aharony 1992). As the capillary pressure increases, the accessible bonds (and the adjoining nodes) are invaded in order of increasing capillary entry pressure by piston-like displacements and water is always connected to the outlet through wetting films in the pore corners. For a less strongly water-wet case (without water wetting films) drainage becomes invasion percolation *with* trapping, since there is no escape for water through films.

Lenormand et al. (1983) observed three main types of displacements during imbibition based on water-wet micro-model experiments (**Figure 2.1**): piston-like displacement, snap-off (Section 2.5.1) and pore-body filling (Section 2.5.2). During water imbibition, the oil-water capillary pressure drops and the bonds and nodes are filled in order of decreasing capillary entry pressure of the relevant displacements. Al-Futaisi and Patzek (2003a) described imbibition as a combination of bonds and nodes invasion percolation and bond ordinary invasion percolation with trapping.

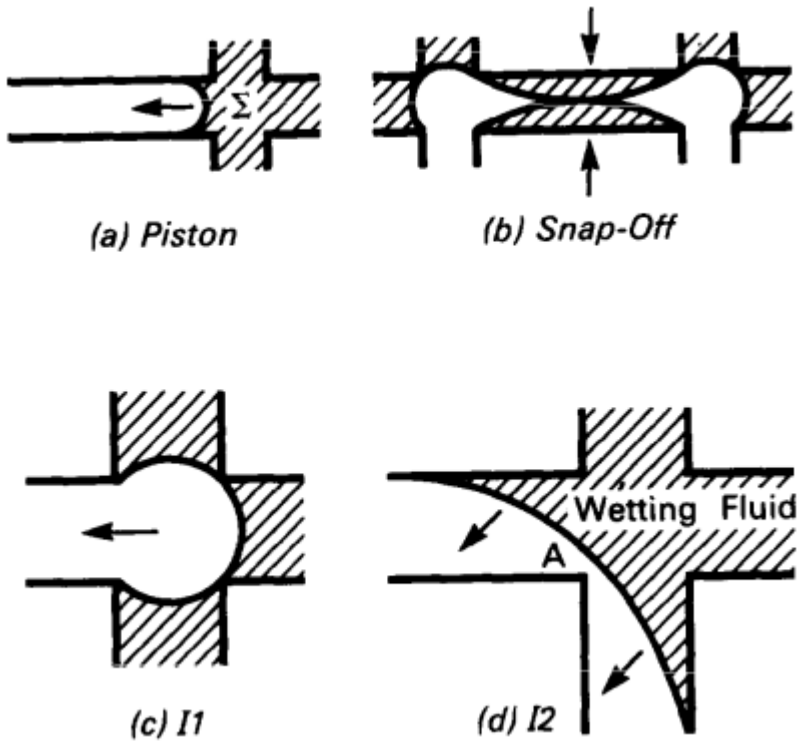

Figure 2.1 Different types of displacement: (a) piston-like; (b) snap-off (choke-off); (c),(d) - I1 and I2 PBF events with 1 and 2 throats occupied by non-wetting fluid (oil) correspondingly (Lenormand and Zarcone 1984)

2.5.1 Snap-off

Mohanty et al. (1980) modelled snap-off and described this mechanism as "choke-off". During snap-off, water films start swelling until the oil-water interface becomes unstable, at which point the node or bond becomes entirely filled with water (see Figure 2.2). If during water imbibition a pore element is occupied by bulk oil and water films, but does not have any neighbouring bulk water filled pore elements, it can be filled with water by means of snap-off.

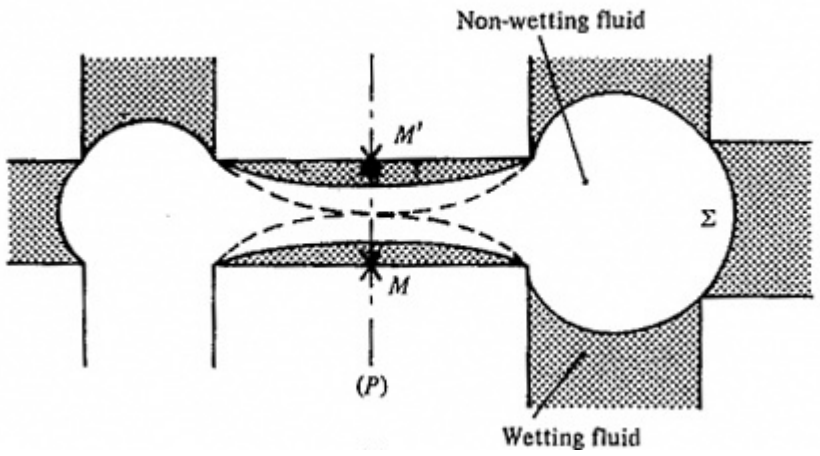

Figure 2.2 Snap-off (choke-off) displacement mechanism. The (water) wetting films are swelling to form a "collar" and then cause the non-wetting fluid (oil) to snap-off (Lenormand et al. 1983)

Valvatne and Blunt (2004) noticed that piston-like displacement is always favoured over snap-off in terms of capillary entry pressure, but only if the pore element is accessible. Thus, snap-off can still be an important mechanism since it does not require any neighbouring pore elements to be filled with bulk water connected to the inlet. In the case of wettability alteration and contact angle hysteresis, the snap-off mechanism becomes more complicated and will be considered later.

2.5.2 Pore Body Filling (PBF) Events

Pore body filling (PBF) is defined as the displacement of non-wetting fluid (oil) from the centre of a pore body by the collective movement of interfaces from connecting pore throats filled with wetting fluid (see **Figure 2.1c,d**). The capillary entry pressure for PBF is restricted by the largest radius of curvature that is required to fill the pore body (Lenormand et al. 1983). This radius depends on the size of the pore body and on the number of oil-filled pore throats connected to it. Thus, if the pore body has coordination number Z, then it can be invaded by means of Z-1 displacement events (denoted as I_1.. I_{Z-1}) each with different capillary entry thresholds (e.g. I_1 and I_2 in

Figure 2.1c,d). If only one of the connected pore throats is oil-filled, then the corresponding PBF event (an I_1 event) will be similar to piston-like displacement with a similar entry pressure (Blunt 1997a, 1998, Øren et al. 1998, Patzek 2001, Valvatne and Blunt 2004). The I_n PBF events, n=1,...,Z-1, take place only if the water imbibition is spontaneous (with positive capillary entry pressures, as explained in Section 4.2.3). Otherwise, the PBF events will again be similar to piston-like displacement with the same entry pressure as for the I_1 displacement (Øren et al. 1998, Valvatne and Blunt 2004).

The I_n entry pressures have been described by a number of parametric models (Blunt 1997a, 1998, Øren et al. 1998, Patzek 2001, Valvatne and Blunt 2004). Most of them depend on the inscribed radius of the pore body, the number of oil-filled connecting pore throats, random weighting coefficients and aspect ratios between pore bodies and pore throats. Valvatne (2004) noted that the selection of weighting coefficients for PBF events or aspect ratios between pore bodies and pore throats will affect what kind of displacement is more likely to occur. For example, larger aspect ratios between pore bodies and pore throats make snap-off more favourable compared to PBF.

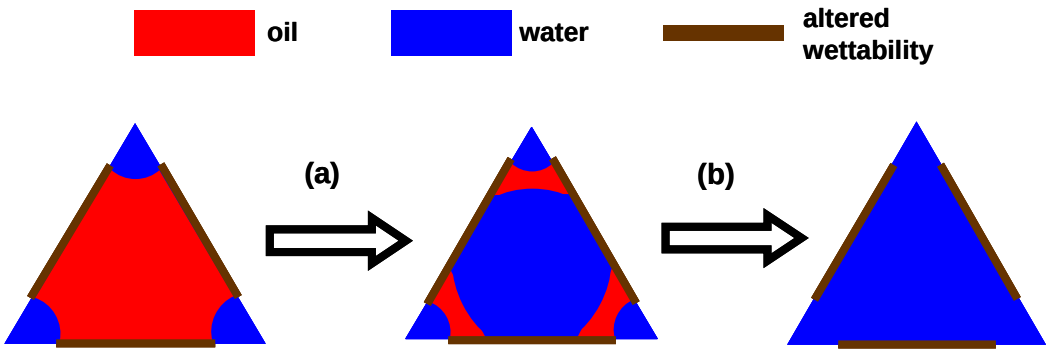

Figure 2.3 Displacements with oil layers in triangular pore with non-uniform wettability: (a) piston-like displacement with oil layers formation; (b) oil layers collapse.

2.5.3 Layer Formation and Collapse

An additional type of displacement, oil layer formation and collapse, can occur in pores of non-uniform wettability for large advancing contact angles (Kovscek et al. 1993, Blunt 1997b, 1998). Non-uniform wettability is caused by wettability alteration of part of the pore space due to ageing or hysteresis of contact angles (see Sections 2.6 and 2.6.4 for details). As a result, the centre and corners of the invaded pore element are occupied by water and the oil is left sandwiched between them as layers (**Figure 2.3a**). The oil phase connectivity and oil recovery can be improved significantly by means of

these oil layers as long as they are stable. However, oil layers may become unstable and collapse, as shown in **Figure 2.3b,** at some critical capillary pressure (Blunt 1998, Hui and Blunt 2000a, Piri and Blunt 2004, van Dijke and Sorbie 2006). The oil layers stability will be discussed later in Sections 2.6.5 and 2.7.

2.6 Wettability Alteration

2.6.1 Wettability Classification

The multi-phase properties of porous rocks depend on the wettability of the surfaces of the medium. Wettability is, by definition, the degree of molecular affinity of the rock surface for either water or oil. The oil-water contact angle (θ_{ow}) measured through the water phase is normally used as a measure of wettability. When the contact angle $\theta_{ow}<90^{o}$, then the rock surface has a wetting preference for water, similarly, if the contact angle $\theta_{ow}>90^{o}$, then the rock surface has a wetting preference for oil. If the contact angle $\theta_{ow}=90^{o}$, the rock surface has neither a strong preference for oil nor for water (Craig 1971). There are three broad wettability classes: water-wet, oil-wet and intermediate-wet or neutrally-wet. There are a lot of cut-off contact angle values for this classification in the literature. For example, $\theta_{ow}<75^{o}$ and $\theta_{ow}>105^{o}$ correspond to water-wet and oil-wet respectively, while the remaining range $75^{o}<\theta_{ow}<105^{o}$ defines the intermediate-wet class (Anderson 1986). There is also a definition for the limiting wettability cases: strongly water-wet for θ_{ow} close to 0^{o} and strongly oil-wet for θ_{ow} close to 180^{o}.

There is a more complex wettability classification for the porous rock, which operates in addition to the previous class definitions (water-wet, oil-wet and intermediate-wet). McDougall and Sorbie (1995) defined two types of wettability: uniform and non-uniform. Uniform wettability corresponds to a porous rock, which has the same class of wettability (water-wet, oil-wet or intermediate-wet) for the entire rock surface, with roughly the same contact angle throughout the porous medium. The other type of wetting is non-uniform or heterogeneous wettability. In this case the contact angle and, as a consequence, the wettability class can vary from pore to pore throughout the rock. This type consists of two subdivisions: mixed-wet large (MWL) and mixed-wet small (MWS), where the fraction of the largest and smallest pores respectively are oil-wet, as well as fractionally-wet (FW), where the fraction of oil-wet pores does not depend on

the pore size. McDougall and Sorbie also mentioned possible variations in wettability within a single pore element, but did not consider this in their wettability classification. In Section 2.6.5, we present physical explanations for the development of mixed wettability (MWL or MWS) in reservoir rocks based on depositional arguments.

The terminology of wettability classification in the literature is ambiguous. For example, Cuiec (1991) defined two main types of wettability: homogeneous (or uniform) and heterogeneous. The first type of wettability is the same as the uniform wettability defined by McDougall and Sorbie (1995). The second type defined by Cuiec, heterogeneous wettability, is similar to that defined by McDougall and Sorbie (1995). They also defined two subdivisions of the second type, but slightly different from McDougall and Sorbie (1995). The first subdivision introduces the mixed-wet type: different parts of the rock surface have different wettability (e.g. water-wet or oil-wet), while surfaces of each wettability are continuous throughout the rock. The second subdivision relates to the case where continuous water-wet surfaces enclose discontinuous oil-wet surfaces. This wettability type is referred to as spotted, Dalmatian or speckled wettability (Cuiec 1991). In the second case, a single pore may have different wettability on different parts of the pore walls. We refer to this case as non-uniform wettability within the single pore.

2.6.2 Wettability Measurement and Indices

Anderson (1986) made a thorough review of experimental wettability measurements and considered three main quantitative methods: contact angle measurement, Amott test and USBM method.

Contact angle measurements on surfaces work well for pure fluids and artificial cores, in particular the sessile drop method (McCaffery and Mungan 1970, Hjelmeland and Larrondo 1986) and its modified version (Leach et al. 1962, Treiber et al. 1972), which is widely used in petroleum industry. However, contact angle measurement is restricted to a single mineral crystal and can not capture heterogeneous wettability of the real rock surface. The other two methods (Amott and USBM) can overcome that problem.

Amott (1959) proposed a wettability test that evaluates the ratio of spontaneously imbibed fluid volume to the total invaded fluid volume, due to both spontaneous imbibition and forced drive (under centrifugation). For example, for water invasion,

spontaneous imbibition corresponds to positive capillary pressures and forced drive to negative capillary pressures (see **Figure 2.4**). This ratio is calculated for both water invasion, the "displacement by water-ratio" or Amott index to water I_w, and for oil invasion, the "displacement by oil-ratio" or Amott index to oil, I_o (**Figure 2.4** and **Table 2.1**). The indices are usually combined in a single Amott-Harvey index $I_{AH}=I_w-I_o$ (Boneau and Clampitt 1977, Trantham and Clampitt 1977). I_o and I_w vary from 0 to 1, giving $I_o=0$ and $I_w>0$ for preferentially water-wet cores and $I_o>0$ and $I_w=0$ for oil-wet cores (**Table 2.1**). The Amott-Harvey index ranges from -1 (strongly oil-wet) to 1 (strongly water-wet) (**Table 2.1**). Unlike the contact angle method, the Amott test is a measure of the average core wettability. However, (Anderson 1986) mentions several shortcomings: the test is time consuming and it is insensitive near neutral wettability, since for the corresponding contact angles between 60° and 120° none of the fluids will spontaneously displace the other one.

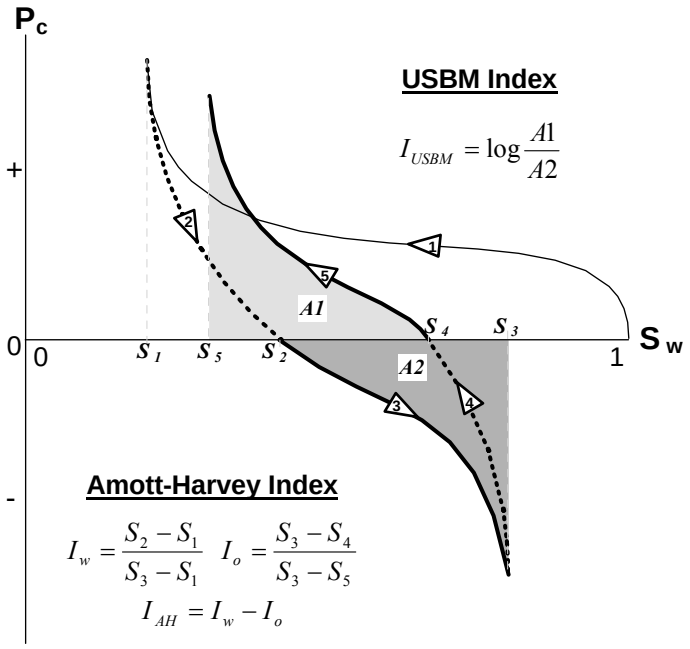

Figure 2.4 Calculation of the Amott indices I_w, I_o, Amott-Harvey index I_{AH} (I_{wo}) and USBM index. Numbers on arrows indicate 1 – primary drainage, 2 - spontaneous imbibition, 3 – forced imbibition, 4 – spontaneous drainage, 5 - forced drainage. S_i denotes endpoint water saturation at the end of the i th flood (i=1..5)(Dixit et al. 2000)

The USBM method (Donaldson et al. 1969) calculates the index I_{USBM} as the logarithm of the ratio between the work required for oil to displace water and the work required for water to displace oil, where work is proportional to the area under the P_c curves:

$$I_{USBM} = log_{10}\left(A_1 / A_2\right), \tag{2.3}$$

where A_1 and A_2 are the areas under the P_c curves for the forced oil drive and forced water drive respectively (**Figure 2.4**). The USBM index I_{USBM} can vary from -∞

(strongly oil-wet) to +∞ (strongly water-wet), but is usually reported as $-1<I_{USBM}<1$. The USBM index is positive for more water-wet cores and negative for more oil-wet cores (**Table 2.1**). The near zero values of I_{USBM} mean neutral wettability. Similar to the Amott test, this method also gives us an average wettability of the core. One of the advantages of the USBM index over the Amott index is the more accurate estimation of neutral wettability (Anderson 1986). However, unlike the USBM index, the individual Amott indices can indicate that the system is not uniformly wetted when both are positive ($I_w>0$, $I_o>0$).

The wettability distribution has a significant effect on simulation results (relative permeabilities, capillary pressures and recovery efficiency) and therefore has to be specified accurately, preferably from pore to pore. At the moment, there is no universal procedure, neither experimental nor numerical, that can uniquely identify the wettability state: the wettability class and related parameters, e.g., oil-wet fraction, water-wet and oil-wet contact angle intervals.

There are two experimental measurements of oil-wet fraction for the FW model: nuclear magnetic relaxation (Brown and Fatt 1956, Devereux 1967, Kumar et al. 1969) and dye adsorption (Holbrook and Bernard 1958). However, they work well only for sandpacks and they do not perform well enough for reservoir cores. Moreover, they only provide just a bulk wettability measure (oil-wet fraction), without contact angle intervals for oil-wet and water-wet pores. Notice, that none of these methods is extensively applied nowadays.

McDougall and Sorbie (1995) performed network simulations of spontaneous water imbibition for FW and MWL cases and demonstrated significant qualitative differences in patterns of K_{ro} vs. $1/P_c$ between these two wettability classes. They suggested design of an experiment measuring oil relative permeability as a function of reciprocal P_c to distinguish between FW and MWL.

Both Amott and USBM indices can be measured from the same combined experiment (Sharma and Wunderlich 1985, 1987). Dixit et al.(2000) calculated Amott and USBM indices from network simulations for the different wettability classes (FW, MWL, MWS). Under some simplifying assumptions they derived analytical relationships between Amott and USBM for each class, which provides a way of distinguishing

between the classes based on the indices values (Amott and USBM) from the combined experiment.

Assuming that the wettability class (FW, MWL) is known, Øren and Bakke (2003) derived an approach for pore-to-pore wettability characterization from measured Amott indices. They validated the approach by reproducing Amott indices using network modelling. They noted that for the matching of Amott indices the spatial distribution of oil-wet pores is less important than the oil-wet fraction and therefore the pore-to-pore wettability distribution cannot be uniquely identified based on these indices.

Valvatne and Blunt (2004) in turn proposed an iterative method for pore-to-pore scale wettability characterization, based on matching of measured Amott indices. Again, the wettability class must be determined beforehand: MWL, MWS, FW. The oil-wet fraction is adjusted to match the Amott water index I_w, whereas the contact angle distribution in the oil-wet pores is determined by matching the Amott oil index I_o.

Table 2.1 Relationship between different measures of wettability (Anderson 1986)

	Water-Wet	Neutrally Wet	Oil-Wet
Contact angle			
Minimum	0°	60 to 75°	105 to 120°
Maximum	60 to 75°	105 to 120°	180°
USBM wettability index	*W* near 1	*W* near 0	*W* near −1
Amott wettability index			
Displacement-by-water ratio	Positive	Zero	Zero
Displacement-by-oil ratio	Zero	Zero	Positive
Amott-Harvey wettability index	$0.3 \le I \le 1.0$	$-0.3 < I < 0.3$	$-1.0 \le I \le -0.3$

2.6.3 Experimental evidence of ageing and oil layers

Even if the clean rock samples for most oil reservoirs are water-wet, in the presence of refined oil, the wettability in real reservoir conditions is usually far from strongly water-wet. This is due to direct contact of crude oil with the rock surface, mediated by the formation brine, which leads to more oil-wet conditions on the rock mineral surface. The evidence of wettability alteration from water-wet to oil-wet (ageing) has been observed in many experiments (Morrow et al. 1986, Buckley et al. 1989, Buckley et al. 1996). Fassi-Fihri et al. (1995) obtained visual proof of non-uniform wettability in a single pore, using cryo-scanning electron microscopes.

Salathiel (1973) treated rock cores with different oils including refined oil and crude oil, which contained asphaltenes. Following saturation by refined oil (in primary drainage), the imbibition behaviour showed that the rock was still water-wet. In contrast, after primary drainage using crude oil followed by ageing, the rock was inferred to be oil-wet. The reason given for the latter behaviour was the wettability alteration of only the oil-contacted pore walls due to adsorption of surface-active components (asphaltenes) from the crude oil. Therefore, Salathiel referred to this case as mixed-wet. He noticed that, for the waterflood in the mixed-wet case, water breakthrough happened earlier than for the water-wet case. But the mixed-wet case showed the slow recovery of additional oil, which continued over a large number of injected PV (1000 PV or more). The ultimate or residual oil saturation for the mixed-wet case was significantly lower than for the water-wet case. To explain these results, Salathiel suggested the existence of oil films on the pore walls, which had formed due to the altered wettability. Thus, the oil phase could remain connected and the oil could drain by means of these oil films resulting in low residual saturations. The detailed physical description and quantitative study of this mechanism of oil drainage at the pore level in mixed-wet systems is the central theme of this thesis.

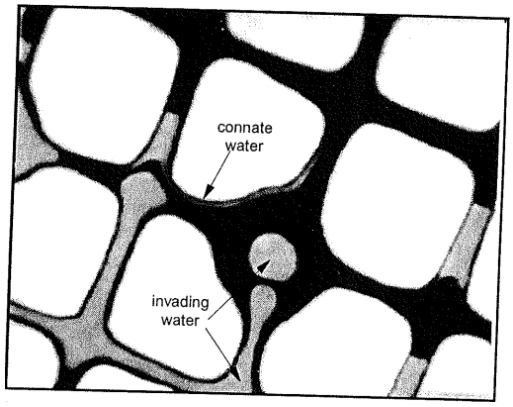

Figure 2.5 Evidence of oil films and layers formation during oil-wet micro-model displacement experiments (Buckley 1995, Buckley 1996).

Buckley (1995, 1996) conducted several experiments on an etched-glass micro-model: crude oil drainage, wettability alteration by ageing and then water injection. In some experiments, when crude oil with asphaltenes was used for drainage, she observed the so-called pseudo oil-wet displacement during the water invasion: water remaining in the corner films (called connate water) was isolated from the invading water in the centre by stable and persistent oil layers (**Figure 2.5**). When these oil layers collapsed, the water corner films reconnected with the water in the centre.

2.6.4 Contact Angle Hysteresis and Wettability Alteration

There are ***two*** physical reasons for a contact angle change between different flooding cycles. Firstly, the wettability alteration due to ageing leads to non-uniform wettability

(see Subsection 2.6.3). Secondly, the contact angle may show some degree of hysteresis since it depends on the displacement direction (drainage or imbibition). Very smooth pore surfaces give almost identical contact angle values for opposite displacement directions (Zisman 1964) and this contact angle is usually denoted as an equilibrium or intrinsic contact angle θ_i. However, many real pore surfaces show contact angle hysteresis due to surface roughness, which leads to different contact angles for different displacement directions: an advancing contact angle θ_a during water displacing oil and a receding contact angle θ_r during oil displacing the water. Morrow (1975) showed that in the case of hysteresis, the receding contact angle is lower than the advancing contact angle, and the difference between the angles increases with surface roughness (Morrow 1975). He experimentally derived three models for prediction of advancing and receding contact angles from the intrinsic angle (Morrow 1975):

- Class I: all angles are equal, no hysteresis, smooth surface
- Class II: moderate hysteresis due to slight roughness
- Class III: substantial hysteresis due to significant roughness

Morrow (1975) also noted that smooth surfaces could show contact angle hysteresis only, due to adsorption or ageing. Thus, for real reservoirs, only superposition of hysteresis due to roughness onto the wettability alteration due to adsorption can provide a proper reservoir wettability description (Morrow 1975).

Following the above discussion, we have three scenarios for contact angle alteration:

1) smooth surface with wettability alteration or ageing (Kovscek et al. 1993, Ma et al. 1996, Blunt 1998, Øren et al. 1998, Piri and Blunt 2002)
2) contact angle hysteresis due to pore surface roughness only (Patzek 2001)
3) wettability alteration ***and*** contact angle hysteresis (Øren and Bakke 2003, Al-Futaisi and Patzek 2004, Piri and Blunt 2004, Valvatne and Blunt 2004, Piri and Blunt 2005a, Helland and Skjaeveland 2006a)

We discuss only the third scenario here since the first two are special cases of the third. In the third scenario, initially, the contact angles will be different due to hysteresis: $\theta_r<\theta_i<\theta_a$. Then, after primary drainage on the pore surface of altered wettability due to ageing the associated contact angles will change as follows: $\theta_r^{alt}<\theta_i^{alt}<\theta_a^{alt}$, where $\theta_i^{alt}>\theta_{i,}$ $\theta_a^{alt}>\theta_a$, $\theta_r^{alt}>\theta_r$. The remainder of the surface will have the original contact angle values ($\theta_r<\theta_i<\theta_a$). During water invasion only θ_a^{alt} will be relevant. During secondary drainage, the receding contact angle will be different for the different pore surface parts: θ_r for an unaltered part in the corners and θ_r^{alt} for the altered pore surface.

An important consequence of all three contact angle models is that, due to the difference between the drainage receding θ_r contact angle and the advancing contact angle θ_a^{alt}, the three-phase point (oil-water-solid) and corresponding arc meniscus may be pinned or fixed during water invasion, while the associated contact angle θ_h (hinging angle) increases from θ_r to θ_a^{alt} (**Figure 2.6**) (Ma et al. 1996). The arc meniscus will be hinging until a displacement takes place or until θ_h reaches θ_a^{alt}, as explained in Section 4.3. In the latter case the fluid-fluid interface starts advancing onto the surface of altered wettability with the θ_a^{alt} angle.

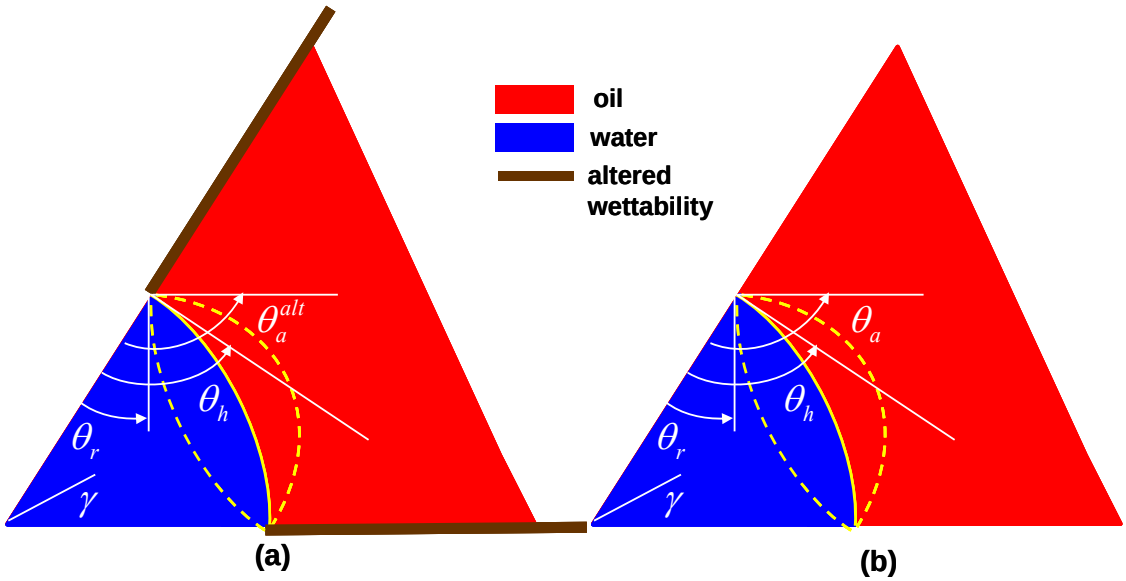

Figure 2.6 Corner of angular shape with pinned arc meniscus during water invasion: (a) wettability alteration(1st and 3rd scenarios), (b) contact angle hysteresis without wettability alteration (2nd scenario).

From now on, we will rarely refer to the 2nd scenario described above. We will refer to the "no contact angle change" case (no hysteresis and no alteration) as uniform wettability within a single pore. And we will refer to the 1st or 3rd scenarios as non-uniform wettability within a single pore.

2.6.5 Wettability Alteration and Oil Layers in the Network Models

Many network models specify only uniform wettability for a single pore and ignore the complex pattern of wettability alteration within a single pore (Kovscek et al. 1993). For example, McDougall and Sorbie (1995) created network models with only pore throats of circular cross-sections and uniform wettability within the same pore, but allowed these to have mixed-wettability distributions at the pore-to-pore scale, thus generating fractionally wet (FW) and mixed-wet large (MWL) systems.

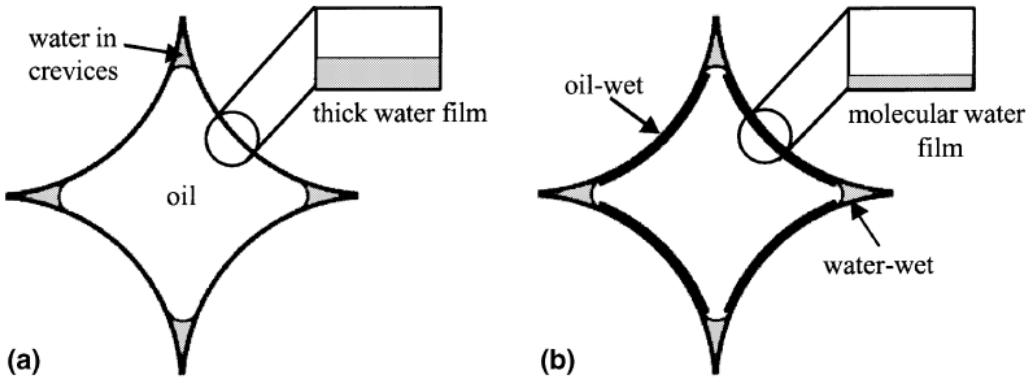

Figure 2.7 Wettability scenarios in a GBP pore cross-section after primary oil drainage: **(a)** Pore elements with a thick water film coating the pore rock surface. The rock surface remains water-wet. **(b)** Pore elements where the thick water films have collapsed into molecular absorbed ones. The bold line indicates the rock surface regions of altered wettability, which become oil-wet, while the rock surfaces in the corners occupied by water remain water-wet (Man and Jing 2001)

Kovscek et al. (1993) proposed a pore-level scenario for the wettability alteration in a pore with a grain boundary pore shape (GBP) cross-section. In a strongly water-wet system, immediately after the oil drainage displacement of water, water remains in the corners and rather thick water films form coating the remaining pore rock surface (**Figure 2.7a**). When some critical capillary pressure is exceeded, the latter films become unstable and collapse into molecularly adsorbed thin film. Then, the asphaltenes from the oil are adsorbed along the pore wall where the thick films were broken, making those parts of the pore wall oil-wet (**Figure 2.7b**). Kovscek et al. (1993) defined this type of pore as mixed-oil-wet which implies that there is a non-uniform wettability distribution within the same pore (strongly water-wet in the corners and oil-wet away from corners). If the critical capillary pressure has not been exceeded for some pores at the end of the drainage process, then these pores do not change their wettability state, since the protective water films are still stable. Kovscek et al. (1993) defined that type of pore as water-wet (**Figure 2.7a**). Kovscek et al. (1993) also suggested an expression for the critical capillary pressure that depends on the curvature of the pore wall. For the GBP shapes (concave) the curvature is negative and therefore the critical capillary pressure value increases with pore size. Hence, at the end of the oil drainage, water films tend to collapse in the smaller pores making them mixed-oil-wet, while the larger pores remain water-wet due to thick protective water films. Note, that this scenario is also the basis for the mixed-wet small (MWS) model. Conversely, for the curved pore shapes with a positive curvature (convex, e.g. eye-shaped) the larger pores become mixed-wet and smaller remain water-wet making this as a basis for the mixed-wet large (MWL) model.

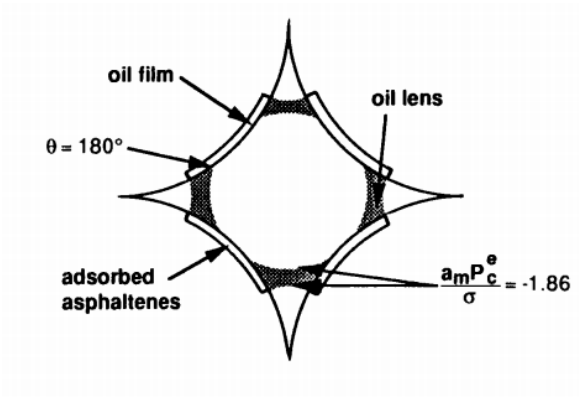

Figure 2.8 Fluid configuration with oil layers formed during water invasion in the pore with non-uniform wettability (Radke et al. 1992)

Kovscek et al. (1993) implemented their pore-level scenario of wettability alteration in a capillary bundle model. They managed to qualitatively reproduce experimental capillary pressure curves. The residual oil saturation for the mixed-wet case turned out to be significantly lower compared to the water-wet case, in agreement with experiment (Salathiel 1973). As mentioned before, Salathiel (1973) originally explained higher oil recovery from the mixed-wet system by oil flow through the thin oil films along the rock surface of altered wettability. Kovscek et al. (1993) suggested that, in pores with non-uniform wettability (mixed-oil-wet pores), also stable oil lenses or layers, which bridge the corner walls, can be formed during the water invasion (**Figure 2.8**). Although Salathiel (1973) used drainage through oil thin films to explain extended oil recovery, the contribution to volume and flow of these films was actually much smaller than the contribution of oil lenses or layers envisaged by Kovscek et al. (1993). Thus, only using oil lenses or layers in their model, Kovscek et al. were able to predict the waterflooding experiments with reasonable accuracy.

McDougall et al. (1996) developed a 3D cubic network with cylindrical pore throats only. After drainage, ageing was simulated by changing the contact angles of oil-filled pores to obtain a fractionally-wet system. After ageing the contact angles were specified according to a random uniform distribution between 0^o and 89^o for the water-wet pores and between 91^o and 179^o for the oil-wet pores. They included oil and water films notionally, since the circular pore cross-section strictly does not allow corner films, by using cut-off contact angle values to decide the presence of oil or water films in a pore: 35^o maximum contact angle for water films and 145^o minimum contact angle for oil films. They considered a strongly water-wet case (no ageing) and a number of fractionally-wet distributions after ageing with the fraction of oil-wet pores α being varied from 0 to 1. The calculated oil recovery for the FW with α=0 and α=0.25 were higher than that for the strongly water-wet case, which was in agreement with experimental observations (Jadhunandan and Morrow 1991). The effect of end-point

capillary pressure on the qualitative behaviour of oil recovery was investigated for the larger oil-wet fractions. If a relatively small and negative end-point capillary pressure is assumed, oil recovery reaches its local maximum for oil-wet fractions around 0.5. However, if a large negative capillary pressure is reached, the recovery will be optimum for the oil-wet case with $\alpha=1$. This was explained by the presence of a spanning cluster of strongly oil-wet pores with oil wetting films, which allowed oil to escape.

Blunt (1997b, 1998) used an approach similar to Kovscek et al. (1993) for the pore-level scenario of wettability alteration. He represented the critical capillary pressure for water film stability in parametric form, which included as input two parameters and random numbers between 0 and 1. The oil-filled pore body or pore throat, which has collapsed water films, changes its contact angle and becomes oil-wet. Thus, the fraction of oil-wet pores is determined by adjusting the input parameters for the critical disjoining pressure for water film collapse. Blunt (1997b, 1998) extended the work (Kovscek et al. 1993) by allowing any contact angle values for oil-wet and water-wet rock surfaces.

Blunt implemented this model for wetting alteration into a 3D regular cubic network model with square pore cross-sections, including oil layers formation in the non-uniformly wetted pores and throats during water invasion. He thus confirmed that these oil layers, sandwiched between water in the corners and water in the centre of oil-wet pores, allowed the oil phase to be drained to a very low residual saturation during the water invasion.

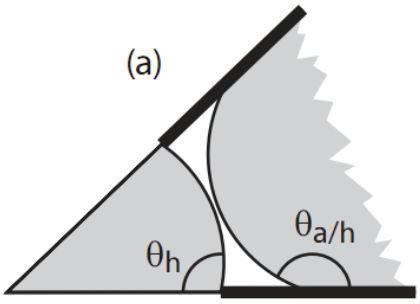

Figure 2.9 Fluid configuration in the pore corner with oil layers which corresponds to geometric collapse criterion (Valvatne and Blunt 2004)

Blunt (1997b) also analysed the stability of these layers. He assumed that the layers would collapse when the surrounding oil–water interfaces met (**Figure 2.9**) and derived the corresponding geometrical collapse criterion. Many authors have used these criteria for formation and collapse of oil layers in capillary bundles (Hui and Blunt 2000a, Helland and Skjaeveland 2006a) and network models (Blunt 1997b, Øren et al. 1998, Piri and Blunt 2004, Valvatne and Blunt 2004, Piri and Blunt 2005a). However, the

collapse criterion proposed by Blunt is purely geometrical and is not based on a firm thermodynamic argument.

In contrast, van Dijke and Sorbie (2006) developed a thermodynamically based criterion for the existence of oil layers. This criterion is consistent with the MS-P capillary entry pressures for other water invasion displacements and it is more restrictive than the geometrical collapse criterion. So far, this criterion for layer collapse was implemented only into a capillary bundle model (Helland and Skjaeveland 2006a). In this thesis we implement it in a full two-phase network model (Chapter 4).

2.7 Capillary Entry Pressure

The capillary pressure P_c is defined at the pore level as the pressure difference across the interface between two immiscible fluids, in particular oil and water. The capillary entry pressure P_{entry} is defined as the phase pressure difference that is required for one phase to displace another from a pore or throat. For a circular pore cross-section, in which films and layer cannot be present, the Young-Laplace equation is used as an expression for the capillary entry pressure

$$P_{entry} = \frac{2\sigma_{ow}\cos\theta}{R}, \tag{2.4}$$

where σ_{ow} is oil-water interfacial tension, θ oil-water contact angle and R radius of the circular capillary. This formula cannot be applied to irregular cross-sections with corners and cavities.

For uniform wettability within a pore (no ageing) and identical contact angles for the different floods (no contact angle hysteresis), the capillary entry pressures for all floods are identical, except for some special cases, for example for snap-off displacement. In contrast, for non-uniform wettability there may be different contact angle values for primary drainage, water invasion and secondary drainage and for different parts of the pore wall. Thus, for non-uniform wettability, as well as contact angle hysteresis, separate entry conditions for water invasion and secondary drainage must be derived.

As mentioned above, for each pore-level displacement during a two- or three-phase flooding cycle, a capillary entry pressure is required. The so-called MS-P method (Mayer and Stowe 1965, Princen 1969a, b, 1970) is normally used for calculating the

entry pressures in non-circular capillaries. This method is based on free energy minimization, which is explained in detail in Section 4.2.

2.7.1 Uniform wettability

Two-phase case. Princen (1970) derived the entry pressures for the equilateral triangular and square cross-sections for zero contact angles. Legait (1983) used this methodology to derive the entry curvature for any rectangular shape and any contact angle. Mason and Morrow (1984) first obtained capillary entry pressure conditions for the regular n-polygon with any contact angle value. Later, they also extended and applied MS-P theory for the perfectly wetted (zero contact angle) pore with arbitrary triangular shape (Mason and Morrow 1991). Lago and Araujo (2001) extended MS-P theory to irregular polygons and presented analytical formulas for the regular polygons, arbitrary triangular and rectangular shapes with arbitrary contact angle. The same authors (Lago and Araujo 2003) derived the entry pressure expressions for the regular hyperbolic polygons (3 and 4 corners) and some other cross-sections with curved boundaries.

Three-phase case. Øren and Pinczewski (1995) as well as Fenwick and Blunt (1998b, a) assumed that every three-phase piston-like displacement can be represented as a combination of two-phase events, i.e. they used two-phase MS-P derived entry pressures for three-phase displacements in both equilateral triangles and in square cross-sections. The necessary geometrical conditions for the existence of intermediate-wetting phase layers were also obtained by these workers, which are similar to the geometrical layer collapse criteria for two-phase oil layers (Blunt 1997b, 1998). Similar to previous studies (Øren and Pinczewski 1995, Fenwick and Blunt 1998b, a), Lerdahl et al. (2000) derived the three-phase entry pressures in the case of a CTS pore shape characterization and combined contact angle hysteresis with uniform wettability (2nd scenario, see **Figure 2.6b**). van Dijke and Sorbie (2003) considered for the first time true three-phase capillary entry conditions. They extended two-phase MS-P theory by considering piston-like displacements of two phases in the presence of the third phase in pore corners. General expressions for the entry pressures in non-circular shapes were derived and formulas for the specific cases of equilateral triangular and rhombus cross-sections were provided. van Dijke et al. (2004) extended their three-phase results by deriving the new existence criterion (in terms of capillary pressures) for the intermediate-wetting phase layers from the free energy balance equation. This new

criterion, in combination with the previously derived geometrical criterion, uniquely defined the presence of intermediate-wetting phase layers. The results were derived in general form for arbitrary polygons, as well as for the special case of isosceles triangles.

2.7.2 Non-uniform wettability

Two-phase case. If ageing takes place after primary drainage, then the part of the pore surface, that is in contact with oil may change its wettability (see Section 2.6). Ma et al. (1996) derived the entry pressure conditions for drainage and imbibition with non-uniform wettability. They considered the n-sided regular polygon case and presented expressions for the equilateral triangular and square shapes, but the oil layers described by Kovscek et al. (1993) were not mentioned at all. Blunt (1997b, 1998) actually considered the formation and collapse of oil layers in a pore with a square cross-section and derived the corresponding geometrical collapse criterion (capillary pressure). Over several publications, MS-P theory was used to derive the entry pressures for the CTS pore shape characterization with non-uniform wettability (Øren et al. 1998, Patzek 2001, Valvatne and Blunt 2004). Helland and Skjaeveland (2004) considered drainage, imbibition and secondary drainage in equilateral triangular pores with non-uniform wettability. They presented appropriate MS-P derived entry pressures for all displacements, except for oil layers collapse, for which the geometrical criterion was used. van Dijke and Sorbie (2006) developed a thermodynamically based criterion for the existence of oil layers. Helland and Skjaeveland (2006a) improved their previous results (Helland and Skjaeveland 2004) by using the new thermodynamical criterion instead of the geometrical assumption.

Three-phase case. Hui and Blunt (2000a, b) described the three-phase entry pressures based on two-phase MS-P theory and used geometrical criteria for the stability of the intermediate-wetting phase layers. For the first time, Piri and Blunt (2004) presented entry pressures results derived from three-phase MS-P theory (van Dijke and Sorbie 2003) for the arbitrary triangular pore with non-uniform wettability. Later they extended it to the CTS pore characterization (Piri and Blunt 2005a). The layer stability was described by the geometrical criterion as before. Helland and Skjaeveland published similar results, but only for the case of equilateral triangular pores (Helland and Skjaeveland 2006b). Eventually, van Dijke et al. (2007) derived from three phase MS-P theory the entry conditions for all possible three-phase displacements for angular pores

with non-uniform wettability, including the complete thermodynamical layers existence criterion.

2.8 Prediction of Water-Wet and Oil-Wet Experimental Relative Permeabilities

A number of studies have appeared in the literature, which present simulations of drainage and imbibition with altered wettability for Berea Sandstone (Øren and Bakke 2003, Valvatne and Blunt 2004, Piri and Blunt 2005b, Høiland et al. 2007) and for Bentheimer Sandstone (Øren et al. 1998, Patzek 2001, Al-Futaisi and Patzek 2004). All these studies use the geometrical oil layer collapse criteria for oil-wet pores.

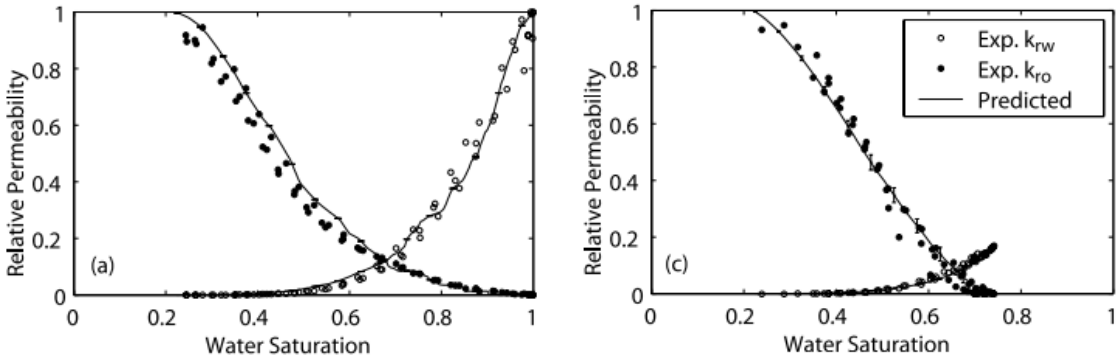

(a) **(b)**

Figure 2.10 Comparison between predicted and experimental relative permeabilities: (a) primary oil drainage, (b) water imbibition (Valvatne and Blunt 2004)

There have been a number of studies in which two-phase water-wet experimental relative-permeabilities have been modelled. Water-wet experiments for Berea sandstone (Oak 1990) (primary drainage and water imbibition relative permeabilities) have been matched (**Figure 2.10**) with reasonable accuracy (Øren and Bakke 2003, Valvatne and Blunt 2004, Piri and Blunt 2005b) by using Berea network extracted from the process-based reconstructed digital pore space (Øren and Bakke 2003). The calculated residual oil saturation S_{or} was very close to the experimental value of 25%. The good agreement between experimental and predicted relative permeabilities (drainage and imbibition) was also obtained for water-wet Bentheimer sandstone (Øren et al. 1998, Patzek 2001). Again, the experimental residual oil saturation S_{or} of 35% was very well predicted.

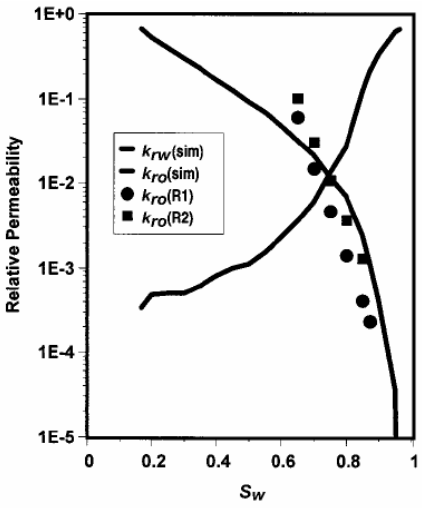

Figure 2.11 Comparison between simulated and measured waterflood relative permeabilities for mixed-wet reservoir rock (FW with α=0.85) (Øren et al. 1998).

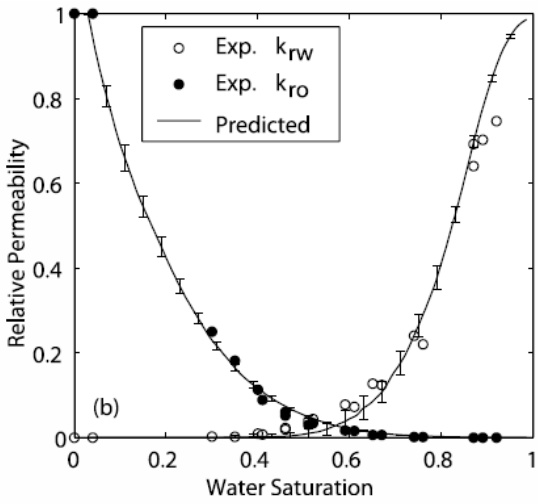

Figure 2.12 Comparison between predicted and experimental water flooding relative permeabilities for oil-wet reservoir sandstone (Valvatne and Blunt 2004).

There are fewer studies where the experimental relative permeabilities for oil-wet and mixed-wet systems are modelled (Øren et al. 1998, Valvatne and Blunt 2004). Firstly, Øren et al. (1998) considered a network extracted from a mixed-wet reservoir rock sample. The experimental water flood residual oil saturation for this sample was 5% and they used this to infer the mixed-wet wettability conditions (oil-wet fraction α =0.85, receding contact angle during the primary drainage θ_{pd}=20°, advancing contact angles for the altered surface in water-wet pore elements θ^{ww}_a=40° and in oil-wet elements θ^{ow}_a=180°). Although they obtained good results for the water flood capillary pressure, they overestimated the experimental oil relative permeability for oil saturations close to S_{or} (**Figure 2.11**). Additionally, they indicated that such small oil saturations could only be reached when oil layers were included. Valvatne and Blunt (2004) in turn used the modified Berea network (Øren and Bakke 2003) to match experimental data for some oil-wet sandstones. The experimental oil residuals were from 8 to 13%, but the predicted S_{or} value turned out to be much lower, i.e. ~1% (**Figure 2.12**).

2.9 Wettability Effect on Residual and Remaining Oil Saturation

2.9.1 Experimental Studies

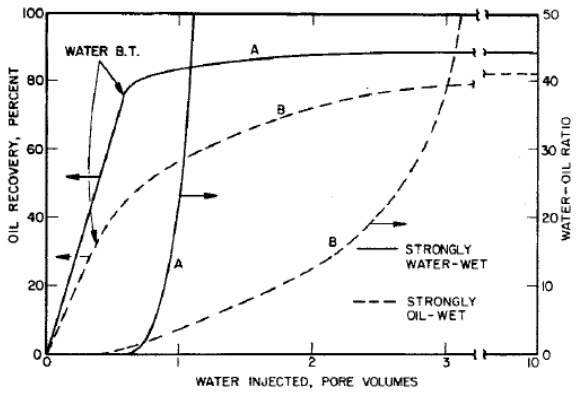

Figure 2.13 Typical waterflood recovery curves for strongly water-wet and strongly oil-wet sandstone samples (Raza et al. 1968)

The effect of wettability on residual oil saturation during water flooding has been investigated in many experimental studies (Kennedy et al. 1955, Raza et al. 1968, Owens and Archer 1971, Lorenz et al. 1974, Jadhunandan and Morrow 1995, Skauge and Ottesen 2002). Anderson (1987b) presented an extensive review of the effects of wettability on various measured quantities. In all reviewed studies the residual oil saturations were obtained under a capillary dominated flow regime, i.e. viscous and buoyancy forces were negligible compared to capillary forces.

One study was conducted by Raza et al. (1968), who analysed waterflooding performance for strongly water-wet and strongly oil-wet conditions (**Figure 2.13**). For strongly water-wet conditions, water breakthrough occurred relatively late and most oil had already been displaced by that time. For strongly oil-wet conditions, the breakthrough occurred much earlier, at a fairly low oil recovery, and most oil was produced after the subsequent injection of many pore volumes. Therefore, based on the criterion of oil recovery at breakthrough and beyond, waterflooding of oil-wet cores is less efficient than for water-wet cores, as more water has to be injected to displace the same amount of oil (Anderson 1987b).

Anderson (1987b) introduced three definitions for (residual) oil saturations: breakthrough saturation, practical (economical) saturation and true residual saturation. The corresponding oil recoveries can be defined as breakthrough recovery, practical recovery and ultimate recovery. The breakthrough oil saturation corresponds to the moment of first water production at the core outlet. The core is at a practical final oil saturation (practical oil recovery) when the water-oil production ratio is so high that the waterflooding is no longer economically feasible; e.g. we might define this as a watercut of 99%. Generally, the practical final oil saturation for uniformly water-wet conditions is lower than for uniformly oil-wet conditions. In the case of oil-wet

systems, even if the economical recovery is reached, small amounts of oil can still be produced at very low oil flow rates. Finally, after injection of many pore volumes, when it is not possible to displace any more oil, the true oil residual (ultimate oil recovery) has been achieved. "True" residual oil also corresponds to the lowest achievable capillary pressure during centrifuge experiments.

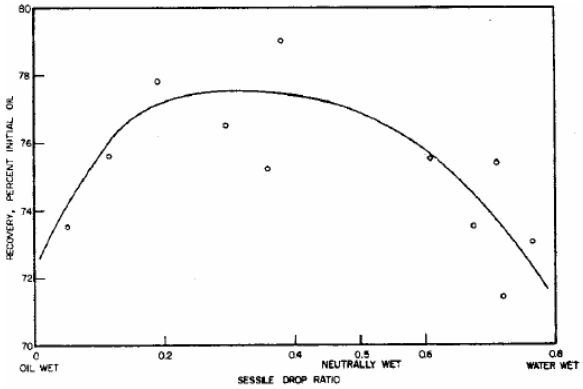

Figure 2.14 Effect of wettability (measured by sessile drop) on ultimate oil recovery for a synthetic silica core (Kennedy et al. 1955)

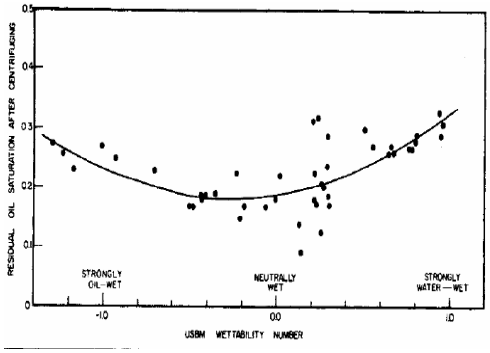

Figure 2.15 Core averaged centrifuge residual oil saturation vs. USBM wettability index for Torpedo sandstone (Lorenz et al. 1974).

Based on several studies, Anderson (1987b) arrived at a number of conclusions. All three final oil saturations (oil recoveries) are almost identical for water-wet conditions, since there is little oil production after breakthrough. The breakthrough and practical final oil saturations increase as the wettability conditions become more oil-wet. However, since the practical saturation increases at a slower rate than the breakthrough saturation, the difference between them also increases gradually. Thus, for oil-wet conditions small oil volumes can still be produced for a considerable time after breakthrough. The "true" residual oil saturation varies much less than the others. Minimum breakthrough and practical oil saturations (maximum breakthrough and practical oil recoveries) occur at strongly water-wet conditions, while the minimum true oil residual (maximum ultimate oil recovery) corresponds to neutrally wet or slightly oil-wet conditions.

Besides the above mentioned three final oil saturations, there is also the quantity of "remaining oil saturation", which is the oil saturation at some prescribed conditions. Such conditions may be a predetermined end-point capillary pressure during centrifuge experiments or a given number of pore volumes injected during core waterflooding, as discussed by Skauge and co-workers (Skauge and Ottesen 2002, Høiland et al. 2007).

Thus, the breakthrough and practical oil saturations are essentially cases of remaining oil saturations.

Anderson (1987b) also described core waterflooding experiments conducted by Kennedy et al. (1955). They analysed the effect of wettability on ultimate oil recovery and used the sessile-drop ratio as a measure of wettability. The results demonstrated that the maximum ultimate oil recovery (or minimum true residual oil saturation) corresponds to slightly oil-wet conditions (**Figure 2.14**). The variation of the true residual oil saturation due to wettability was relatively small ≈5%.

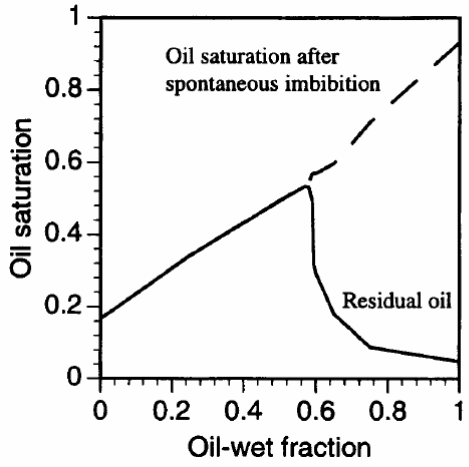

Figure 2.16 Residual oil saturation as a function of the oil-wet fraction of pore elements filled with oil, α (θ_{pd}=22.5°, $\theta^{ow}{}_a$=34°, $\theta^{ow}{}_a$=180°) (Blunt 1997b)

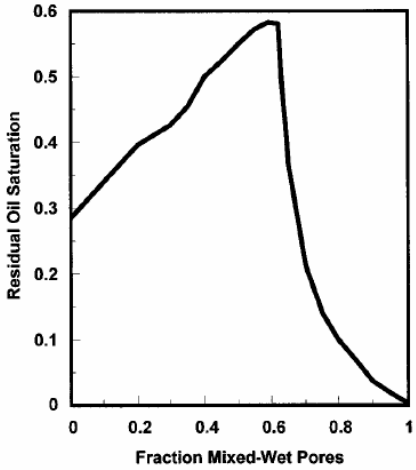

Figure 2.17 Residual oil saturation as a function of the oil-wet fraction of pore elements filled with oil, α (θ_{pd}=20°, $\theta^{ow}{}_a$=40°, $\theta^{ow}{}_a$=180°) (Øren et al. 1998)

Anderson (1987b) also mentioned one study of centrifuge measurements of capillary pressure, carried out by Lorenz et al. (1974), who investigated the wettability effect (measured by the USBM Index) on the true residual oil saturation. The final results showed that the optimum (minimum) true residual also occurred at slightly oil-wet conditions (**Figure 2.15**), which is in good agreement with core waterflooding results (**Figure 2.14**).

The experimental results discussed here (Kennedy et al. 1955, Lorenz et al. 1974) correspond to uniformly wetted systems. However, for mixed-wet large (MWL) systems, a continuous oil-wet cluster (of large pores) can be formed and the oil can be drained through oil layers to a very low true residual saturation (Salathiel 1973) (see Section 2.6.3). This, in turn, will require many pore volumes to be injected. Therefore, for mixed wettability cases, the true oil residual for more oil-wet conditions will be lower than that for water-wet conditions (Salathiel 1973). This would also be true in the

uniformly oil-wet cases, however the contact angles should be large enough to allow oil layers formation (Anderson 1987b). Notice, that the uniformly oil-wet system is a limiting case of MWL, hence in the MWL case the oil-wet contact angles should also be large enough to allow displacement through oil layers.

2.9.2 Network Modelling

The effect of wettability on residual or remaining oil saturation has also been investigated in many numerical studies by means of network modelling (McDougall and Sorbie 1995, Blunt 1997b, 1998, Øren et al. 1998, Dixit et al. 1999, Høiland et al. 2007).

Blunt (1997b, 1998) considered cubic regular networks with square pore cross-sections. He applied a wettability alteration scenario based on Kovscek et al. (1993) with oil layers and included pore bodies in the displacement process. Initially, the receding contact angle during the primary drainage θ_{pd} was 22.5°. Then, after the ageing, he considered a fractionally-wet wettability distribution for the oil-filled pore elements with oil-wet fraction α. The advancing contact angle for the altered surface in water-wet pore elements $\theta^{ww}{}_a$ was 34° and $\theta^{ow}{}_a$ was 180° in oil-wet pore elements. Eventually, residual oil saturation S_{or} was calculated for a range of oil-wet fractions (from 0 to 1) (**Figure 2.16**). Moreover, the remaining oil saturation at 0 capillary pressure (after spontaneous imbibition) was also calculated for each case. Initially, residual oil increases with fraction α until some critical value (0.59) and then it starts decreasing. The smallest residual corresponds to the strongly oil-wet case (α=1) and the minimum recovery (maximum oil residual saturation) occurs at α=0.59. For the oil-wet fractions below the critical value α^*=0.59, the oil-wet pore elements, which may contain oil layers, form isolated clusters and cannot contribute significantly to the forced imbibition. This is why there is no noticeable difference between residual oil and remaining oil (at P_c=0). However, at an oil-wet fraction above the critical value, oil-wet pore elements form a spanning cluster and oil can now be displaced from these pore elements by forced water imbibition through oil layers. This explains the difference between residual and remaining oil results. The bigger the oil-wet fraction, the smaller is the number of pore elements involved in spontaneous imbibition. Hence the remaining oil saturation at P_c=0 and the amount of oil displaced by the forced imbibition will be larger.

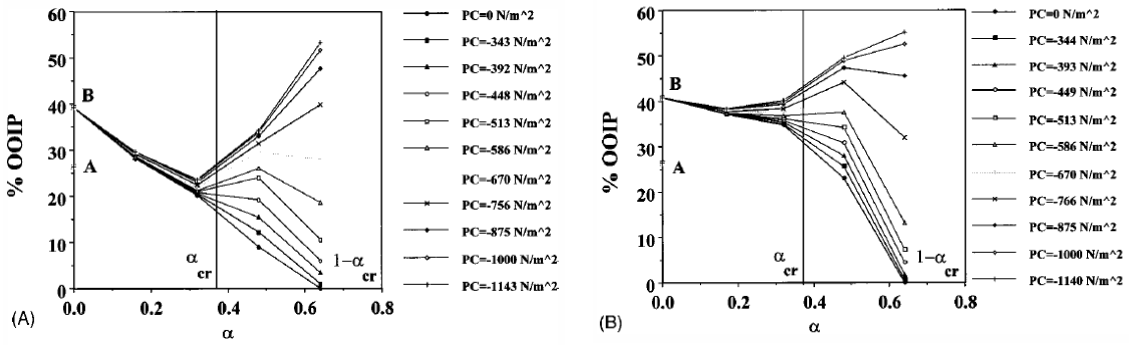

Figure 2.18 Waterflood recovery vs oil-wet fraction of oil-filled pore elements α terminated at various end-point capillary pressures for (A) mixed-wet large system and (B) fractionally wet system. (θ_{pd}=0°, $\theta^{ww}{}_a \in [0°,89°]$, $\theta^{ow}{}_a \in [91°,180°]$). Data point A corresponds to strongly water-wet case without wettability alteration and B- UWW after ageing (FW with α=0). %OOIP – recovery efficiency as a percentage of oil originally in place (OOIP) (Dixit et al. 1999)

Øren et al. (1998) used networks extracted from some mixed-wet reservoir rock. They included wettability alteration and pore bodies in their model and used the following contact angles for the fractionally wet wettability: θ_{pd}=20°, $\theta^{ww}{}_a$=40°, $\theta^{ow}{}_a$=180°. Sensitivity of residual oil saturation to oil-wet fraction showed behaviour similar to Blunt's results (**Figure 2.17**).

Dixit et al. (1999) conducted network modelling of oil recovery efficiency on regular lattices with cylindrical pore throats of identical length and without pore bodies. A simplified version of wettability alteration was implemented, since circular cross-sections could not retain water in the corners explicitly and as a consequence the non-uniform wettability within the single pore throat could not be assigned. Thus, they simply specified the advancing contact angle for the entire pore throat. Nevertheless, oil (water) films were assigned implicitly, if the corresponding contact angle was larger (smaller) than some predefined threshold values. As in many similar studies, two wettability classes were considered for the advancing contact angle distributions of the oil-filled pore throats: MWL and FW. For drainage, they used the following contact angles: θ_{pd}=0°, and for imbibition $\theta^{ww}{}_a \in [0°,89°]$, $\theta^{ow}{}_a \in [91°,180°]$. The ultimate oil recovery efficiency was calculated for FW and MWL cases for the range of oil-wet fractions α from 0 to 0.65. Moreover, before reaching the ultimate recovery (at the minimum end-point P_c values) the network forced water invasion was terminated at some predefined end-point P_c values and the corresponding recovery efficiency was calculated as well (**Figure 2.18**). Since the remaining oil saturation is inversely proportional to oil recovery efficiency, the behaviour of this quantity is opposite to the recovery efficiency. The ultimate oil recovery decreases with α until some critical value and increases above that critical value. The effect of forced imbibition on oil

recovery is minor for oil-wet fractions below the critical value, but above the critical value the recovery trend changes from increasing (ultimate recovery or large absolute P_c value) to decreasing (small absolute P_c value). Hence, the optimum oil-wet fraction with maximum oil recovery depends on end-point P_c. Despite the fact that oil layers are not modelled explicitly, the obtained results are in very good qualitative agreement with Blunt's studies **(Figure 2.16)**. Note that the obtained critical α value is very different from Blunt's studies.

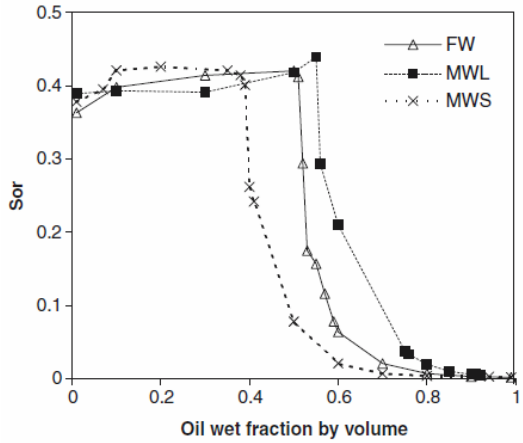

Figure 2.19 Residual oil saturation versus oil-wet volume fraction for MWS, MWL and FW with wettability alteration and no contact angle hysteresis (θ_{pd}=0°, $\theta^{ww}{}_a$=0°, $\theta^{ow}{}_a$=180°) (Høiland et al. 2007).

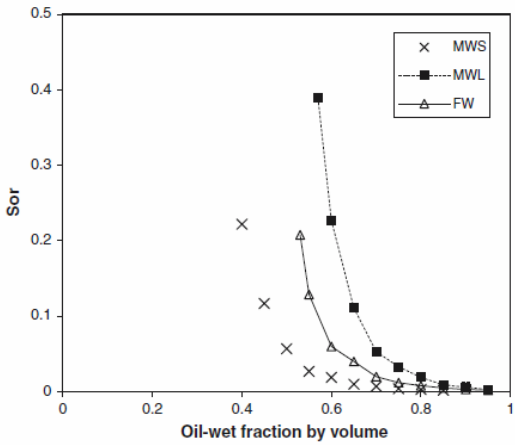

Figure 2.20 Residual oil saturation versus oil-wet volume fraction for MWS, MWL and FW with wettability alteration and contact angle hysteresis (θ_{pd}=0°, $\theta^{ww}{}_a\in[0°,85°]$, $\theta^{ow}{}_a\in[170°,180°]$) (Høiland et al. 2007)

Høiland et al. (2007) used an extracted Berea network (Øren and Bakke 2003) and Valvatne and Blunt's network modelling tool (Valvatne and Blunt 2004) to analyse the effect of wettability on residual oil saturation. They considered all three mixed wettability classes: FW, MWS and MWL. In addition, contact angle hysteresis was included, although this will only be relevant for secondary drainage (see Section 2.7.1). The residual oil saturation S_{or} was calculated as a function of the volume fraction of oil-wet pores for all wettability classes. For the cases with constant contact angle (and no hysteresis) (θ_{pd}=0°, $\theta^{ww}{}_a$=0°, $\theta^{ow}{}_a$=180°), the resulting S_{or} behaviour against the oil-wet fraction (**Figure 2.19**) seems to be consistent with previous studies (Blunt 1997b, 1998, Øren et al. 1998). That is, the S_{or} slightly increases with oil-wet fraction α_V until some critical value α_V^* and then, as α_V increases above α_V^* the residual oil drops dramatically due to the formation of the oil-wet spanning cluster. For the case with a random uniform contact angle distribution (and hysteresis) (θ_{pd}=0°, $\theta^{ww}{}_a\in[0°,85°]$, $\theta^{ow}{}_a\in[170°,180°]$), residual oil results were presented only beyond the critical oil-wet volume fraction (**Figure 2.20**), which are again in qualitative agreement with the results

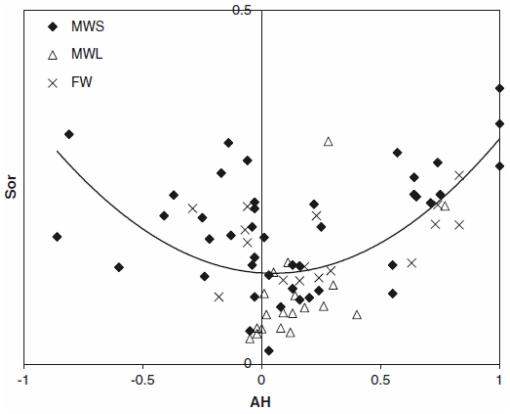

Figure 2.21 Experimental remaining oil saturation versus I_{wo} from different oil-fields classified as MWL, FW or MWS based on I_{wo} and USBM, where line is the trend for all data points (Skauge and Ottesen 2002, Høiland et al. 2007)

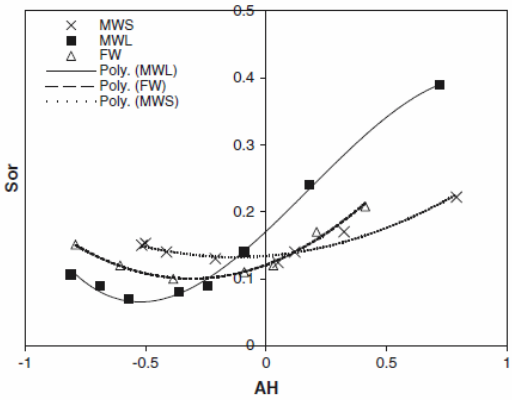

Figure 2.22 Remaining oil saturation vs Amott-Harvey index terminated at some end-point capillary pressure (with polynomial fit) for MWS, MWL and FW with wettability alteration and contact angle hysteresis (Høiland et al. 2007)

shown above. Høiland et al. compared their results with an experimental remaining oil saturations data set (**Figure 2.21**). The experimental qualitative behaviour is different from the network results (**Figure 2.20**), since, as we have discussed already, the remaining oil saturation can be higher than the true residual S_{or}, especially for the oil-wet cases. Moreover, they noticed that during the waterflooding experiments, through capillary end effects some oil accumulates at the core outlet, which may result in overestimation of the remaining oil saturation. On the other hand, they also suggested that such low simulated residual oil saturations may be the result of flow through the very stable oil layers, which are described by the geometric existence criteria. Thus, to suppress the oil layers flow they stopped simulation at some predefined end-point capillary pressure and calculated the corresponding remaining oil saturation. Finally, they managed to reproduce the experimental qualitative behaviour for remaining oil

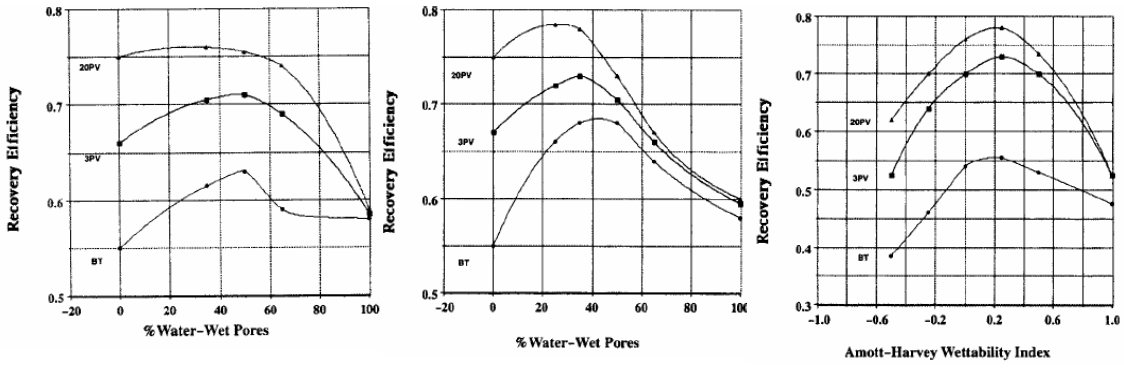

Figure 2.23 (a), (b) Recovery efficiency vs water-wet pore fraction for FW and MWL cases correspondingly (McDougall and Sorbie 1995); (c) Experimental recovery efficiency as a function of Amott-Harvey Index Iwo (Jadhunandan and Morrow 1995)

saturation versus Amott-Harvey Index I_{wo} (with the minimum at intermediate wettability) (**Figure 2.22**).

2.9.3 Comparison with Mixed-Wet Experiments

As an alternative to stopping the network water flooding at some arbitrary end-point capillary pressures, the experimental remaining oil saturation after a given number of pore volumes of injected water can also be predicted from a 1-D Buckley-Leveret model (Dullien 1992), in which the network derived relative permeabilities (and capillary pressures) are used.

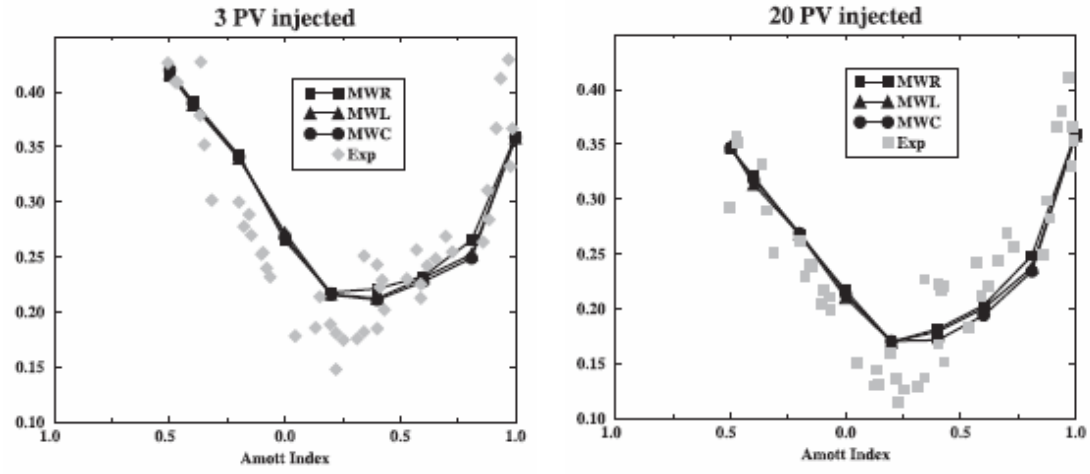

Figure 2.24 Simulated and experimentally measured remaining oil saturations versus Iwo: (a) after 3PV injected, (b) after 20PV injected (Øren and Bakke 2003)

Using a cubic network model with pore elements of circular cross-section, McDougall and Sorbie (1995) conducted sensitivity studies of recovery efficiency vs. water-wet fraction (α) for two different types of wettability: mixed-wet large (MWL) and fractionally-wet (FW). They only simulated the case of direct water invasion in a pore network fully saturated with oil. Thus, wettability alteration was not simulated explicitly, and different wettability distributions were specified only for the water flood. McDougall and Sorbie (1995) generated relative permeabilities for the FW and MWL with different oil-wet fractions (from 0 to 1) and used these to generate the oil recovery curves vs. number of pore volumes injected, by applying Buckley-Leverett analysis (**Figure 2.23a,b**). The results showed that the optimum recovery corresponds to case with approximately equal fractions of oil-wet and water-wet pores, which is in a good qualitative agreement with laboratory experiments (**Figure 2.23c**) conducted on Berea sandstone samples (Jadhunandan and Morrow 1995). However, in the experimental

study (Jadhunandan and Morrow 1995), the residual saturation and recovery efficiency were plotted against the Amott-Harvey index I_{wo} and the optimum was found to be the weakly water-wet case (i.e. I_{wo} is a small positive value).

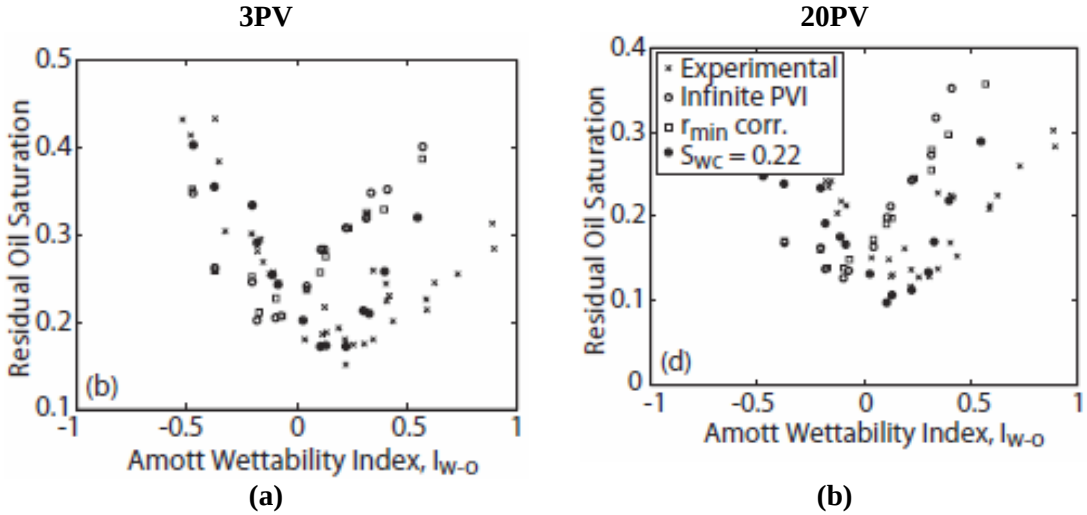

Figure 2.25 Waterflood remaining oil saturation as a function of Amott-Harvey index Iwo (calculated and experimental data) (a) after 3 PV injected, (b) after 20 PV injected (Valvatne 2004)

Unlike McDougall and Sorbie (1995), Øren and Bakke (2003) considered the network extracted from Berea sandstone and attempted to reproduce the corresponding range of mixed-wet experiments for remaining oil saturation vs. Amott-Harvey index (Jadhunandan and Morrow 1995). Following McDougall and Sorbie, they applied Buckley-Leveret analysis to generate recovery curves and they compared the corresponding remaining oil saturations with experiments for the different water pore volumes injected (**Figure 2.24**). The qualitative behaviour was very well matched. The experimental remaining oil after 20 pore volumes of injected water varied from 12% to 35%, while predicted values varied from 17% to 37%. However, the remaining oil saturation was significantly overpredicted for weakly water-wet cases.

Valvatne and Blunt (2004) also used the Berea network (Øren and Bakke 2003) to predict the mixed-wet experiments by Jadhunandan and Morrow (1995). The qualitative trends were matched reasonably well (**Figure 2.25**), but a quantitatively good match was obtained only for the case of 3 pore volumes injected (**Figure 2.25a**).

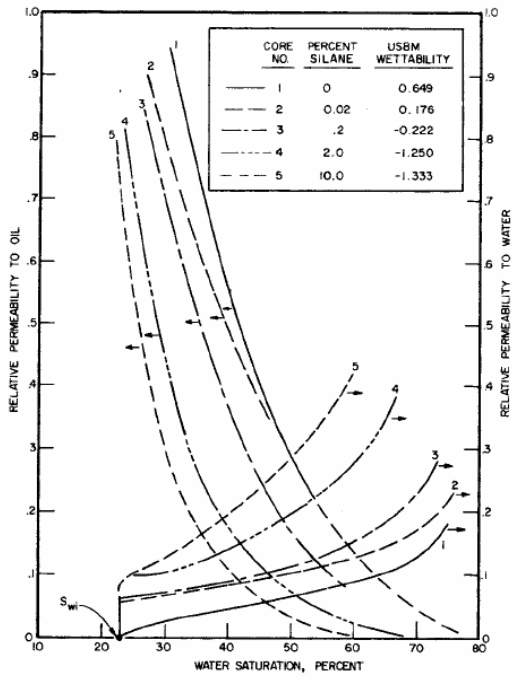

Figure 2.26 Effect of wettability (USBM index) on relative permeability for outcrop Torpedo sandstone. Relative permeabilities are normalized by absolute water permeability (Donaldson and Thomas 1971).

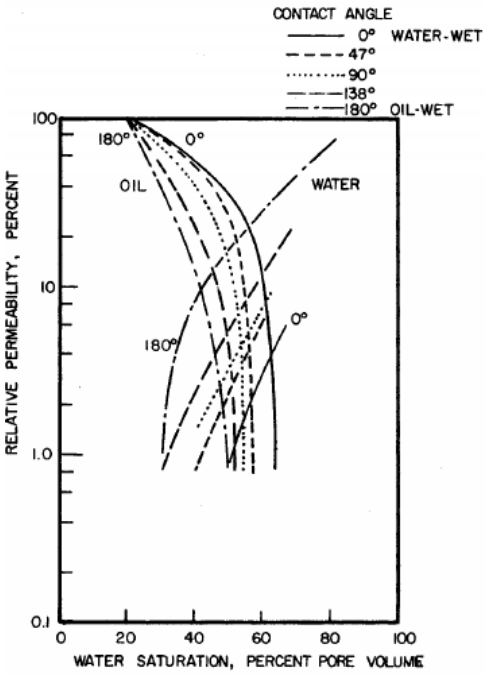

Figure 2.27 Relative permeabilities for a range of contact angles (from 0o to 180o) for outcrop Torpedo sandstone. Permeabilities are normalized by effective oil permeability at Swi (Owens and Archer 1971).

2.10 Wettability Effect on Relative Permeabilities

2.10.1 Experimental Studies

The effects of wettability on relative permeability curves during water flooding have been analysed in several experimental studies (Donaldson and Thomas 1971, Owens and Archer 1971, Morrow et al. 1973). Anderson (1987a) presented a good overview of different experimental results including the studies just mentioned. Anderson (1987a) made the general conclusion that the oil relative permeability decreases and the water relative permeability increases as the wettability distribution becomes more oil-wet.

In particular, Anderson (1987a) described the experiments conducted by Donaldson and Thomas (1971). They analysed the wettability effect (USBM Index) on relative permeabilities calculated by the JBN method (Johnson et al. 1959) from unsteady-state core flooding experiments. The obtained relative permeabilities showed typical trends: K_{ro} decreases and K_{rw} increases as USBM decreases or system becomes more oil-wet (**Figure 2.26**). The relative permeabilities were normalized with absolute permeability which does not depend on wettability. Therefore since the effective oil permeability at initial water saturation decreases as oil-wetness increases (Owens and Archer 1971), K_{ro} also decreases.

Anderson (1987a) also mentioned the steady-state measurements by Owens and Archer (1971). They investigated the effect of contact angle on relative permeability curves which were measured by the Penn State steady-state relative permeability measurement technique (Morse et al. 1947). Again, the results demonstrated similar behaviour to the above study: i.e. K_{ro} decreases and K_{rw} increases as contact angle increases (**Figure 2.27**). However, in this study the relative permeability curves were normalized with the effective oil permeability and as a consequence the K_{ro} values all started at the same point.

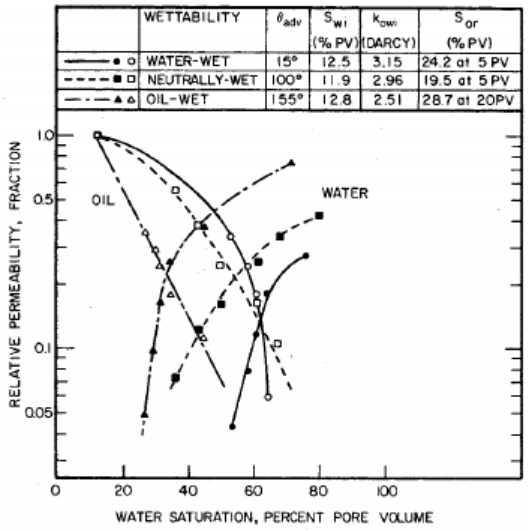

Figure 2.28 Relative permeabilities for 3 wettability systems (water-wet θ_{adv}=15°, neutrally-wet θ_{adv}=100° and oil-wet θ_{adv}=155°) for dolomite pack. Permeabilities are normalized by effective oil permeability at S_{wi} (Morrow et al. 1973)

Another study which Anderson (1987a) also referred to was the steady-state measurements of relative permeabilities reported by Morrow et al. (1973). To observe the wettability effects, they measured relative permeabilities for the three different wettability conditions: water-wet (θ_{adv}=15°), neutrally-wet (θ_{adv}=100°) and oil-wet (θ_{adv}=155°). As expected, their results showed typical trends with contact angle (**Figure 2.28**). They also noticed that the water saturation that corresponds to the crossover point tends to be lower for more oil-wet cases.

2.10.2 Network Modelling

To analyse the effect of wettability on relative permeability, several sensitivity studies have been conducted using network modelling tools (McDougall and Sorbie 1995, Al-Futaisi and Patzek 2004, Zhao et al. 2010).

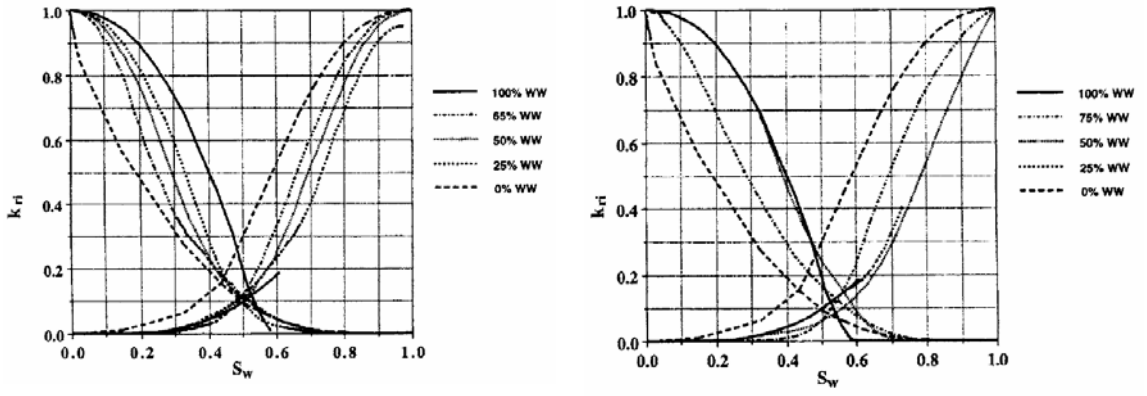

(a) **(b)**

Figure 2.29 Relative permeability curves for a range of water-wet fractions (from 0 to 100%): (a) fractionally wet system (b) mixed-wet large system (McDougall and Sorbie 1995)

In the same study as described in Section 2.9.3, McDougall and Sorbie (1995) generated relative permeabilities for the FW and MWL with different oil-wet fractions α (from 0 to 1). For the FW case (**Figure 2.29a**), they found that oil relative permeabilities K_{ro} tend to be inside the limiting cases with 0 and 1 oil-wet fractions and decrease with increasing α at low water saturations S_w. The water relative permeability K_{rw} increases with α at high S_w and, as a consequence, the critical endpoint K^*_{rw} also increases with α. In the case of MWL wettability (**Figure 2.29b**), they could not see such clear trends as in FW case, however they noticed that the K_{ro} curves also change curvature from convex to concave as the oil-wet fraction α increases, while the K_{rw} curves show the opposite, which is in agreement with general conclusion by Anderson (1987b).

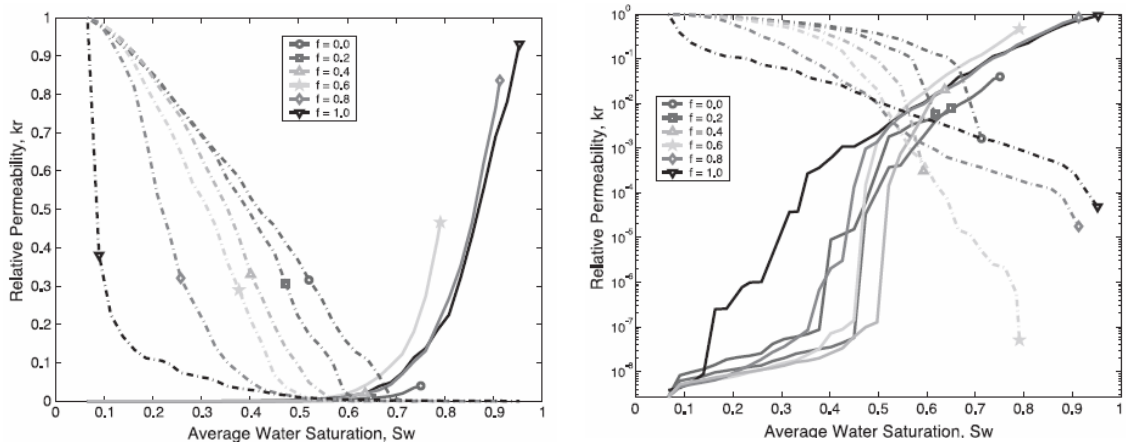

(a) **(b)**

Figure 2.30 Relative permeability curves for a range of NAPL-wet fractions (from 0.0 to 1.0): (a) linear scale (b) semi-log scale (Al-Futaisi and Patzek 2004)

Al-Futaisi and Patzek (2004) used a network extracted from Bentheimer sandstone to investigate the effect of wettability alteration on water imbibition in a NAPL-invaded mixed-wet soil, where NAPL is non-aqueous phase liquid. Their sensitivity study was conducted with respect to wettability parameters, such as advancing contact angle, fraction of NAPL-wet pores in the NAPL-invaded zone and initial water saturation at the end of the primary drainage. They showed that the different ranges of advancing contact angle and the fraction of hydrophobic (i.e. oil-wet) pores both have a significant effect on the relative permeabilities and capillary pressures during waterflooding. Sensitivity of relative permeabilities with respect to fraction of NAPL-wet pores (**Figure 2.30**) demonstrated that the water relative permeability generally decreases as α increases, but increases for α above 0.4 and water saturation S_w less than 0.5. The permeability of the hydrophobic phase usually decreases as α increases, but it has the opposite behaviour for α above 0.6 at high S_w greater than 0.5.

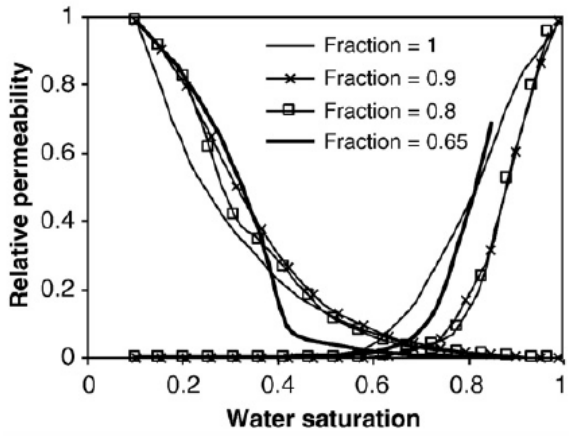

Figure 2.31 Relative permeability curves for a range of oil-wet fractions (from 0.65 to 1.0) fractionally wet system (Zhao et al. 2010)

Zhao et al. (2010) investigated the effect of wettability on relative permeabilities during water invasion. They used a two-phase network modelling tool developed by Valvatne and Blunt (2004) and an extracted Berea network (Øren and Bakke 2003) to simulate primary drainage and water invasion. The water invasion relative permeabilities were calculated for fractionally-wet conditions (including wettability alteration) for a number of oil-wet fractions (from 0.65 to 1.0). The results are shown in **Figure 2.31** and can be interpreted as follows. For low water saturations S_w, K_{ro} decreases as the oil-wet fraction α increases, although after reaching some critical S^*_w (≈0.4) the trend changes to the opposite where K_{ro} starts increasing with α. However, there is no clear evidence of any trends in the water relative permeability K_{rw}; at high S_w, K_{rw} increases with α. They also confirmed that the residual oil saturation decreases as the oil-wet fraction increases.

2.11 Discussion and Closing Remarks

In this thesis we describe the newly developed state-of-the-art pore-network modelling tool for two-phase flow in mixed-wet systems and results of its applications. Based on the presented literature review we will summarize which methods we employ in this work and discuss the improvements that have been additionally implemented.

2.11.1 Pore Space Reconstruction & Network Extraction

In this work, two networks have been used as input for our pore-scale network model. The first network has been extracted from a CT image using the medial-axis type method (Jiang et al. 2007). The second network has been extracted from the 3D digital pore space using the Voronoi diagram approach (Øren and Bakke 2003), where the digital rock was reconstructed by applying the process-based algorithm (Bakke and Øren 1997, Øren and Bakke 2003).

2.11.2 Type of model

We assume that capillary number N_c (see Eq. (2.1)) is relatively low, hence the viscous forces are insignificant and the flow is governed by capillary forces. In our case the quasi-static network modelling is applied similar to previously developed models (Øren et al. 1998, Man and Jing 2000, Patzek 2001, Valvatne and Blunt 2004, Piri and Blunt 2005a).

2.11.3 Pore Shape Characterization

Because the shapes of the real pore cross-sections are generally highly irregular, it is important to use idealized shapes that lead to accurate approximations of pore conductances and capillary entry pressures. The most common approach in the literature has been to choose a circle/ (arbitrary) triangle / square (CTS) pore geometry with a shape factor that matches that of the real pore shape (Patzek 2001, Valvatne and Blunt 2004, Piri and Blunt 2005a, Valvatne et al. 2005). For these shapes, simple correlations between the flow parameters and the shape factor are available. However, the parameters for these very regular convex shapes are often inaccurate compared to those for the real pore shapes. We suggest the use of a new n-cornered star shape characterization technique (Star) in addition to the CTS approach. Apart from the shape factor, we also consider dimensionless hydraulic radius as a second input parameter in the procedure, which allows us to reproduce the initial shape factor distribution and reduce ambiguity in shape type selection. This new pore shape characterization technique (Star) will be described in Chapter 3. We describe implementation of this

technique in a capillary bundle model in Chapter 5 (Helland et al. 2008) and in the unstructured pore-network model in Chapters 6 and 7 (Ryazanov et al. 2009, 2010a, b).

2.11.4 Conductance (single phase and two-phase)

In this thesis, we assume no-slip boundary conditions along the fluid-solid and fluid-fluid interfaces since we simulate only two-phase oil water processes to calculate fluid conductance. In addition to existing expressions for the correlation between single-phase conductances and the CTS pore shapes parameters (Patzek and Silin 2001), we present new correlations for n-cornered star shapes in Chapter 3 (Ryazanov et al. 2009) based on previously published numerical results (Helland et al. 2006).

In Chapter 3 we also present the two phase conductances. For the corner film flow we use correlations previously proposed by Øren et al. (1998, Valvatne and Blunt 2004). Correlations derived by Valvatne and Blunt (2004) are applied for the oil layer conductances.

2.11.5 Wettability Classification

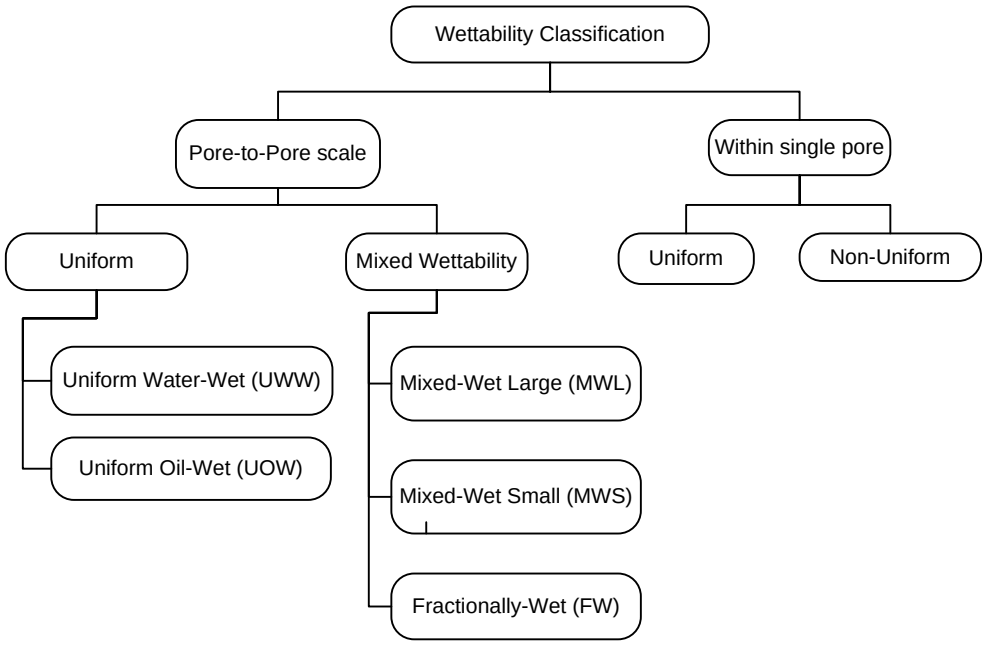

Figure 2.32 Wettability classification employed in this thesis.

Due to the numerous contradictory wettability classifications in the literature, we propose the wettability classification of Figure 2.32, which is employed consistently

throughout this thesis. Firstly, we consider wettability on two different scales: pore-to-pore scale (entire network) and single pore scale. The latter can be divided into uniform (same contact angle for the entire pore wall) and non-uniform (different contact angles for different parts of the pore wall). The non-uniform wettability within a single pore may be the result of wettability alteration with or without contact angle hysteresis. In the case of pore-to-pore scale wettability variation, we have two subdivision: uniform and mixed wettability cases. In this case, uniform wettability consists of two classes: uniform water-wet (UWW) and uniform oil-wet (UOW). For both classes, the contact angle is distributed across the pores within some interval $[\theta_{min,}\ \theta_{max}]$ according to a random uniform distribution. The intervals must be included in the water-wet range ($\theta_{max}<90^o$) for the UWW class and in the oil-wet range ($\theta_{min}>90^o$) for the UOW class. The mixed wettability case is subdivided into three classes: mixed-wet large (MWL), mixed-wet small (MWS) and fractionally wet (FW). In all these classes, some fraction of pores is oil-wet and the remaining pores are water-wet. The only difference is how these oil-wet and water-wet pores are correlated with pore size. As in the uniform cases (UWW, UOW), the contact angles are distributed within some interval $[\theta^{ww}{}_{min}, \theta^{ww}{}_{max}]$ for the water-wet pores and within $[\theta^{ow}{}_{min}, \theta^{ow}{}_{max}]$ for the oil wet-pores, where $\theta^{ww}{}_{max}<90^o$ and $\theta^{ow}{}_{min}>90^o$. The oil-wet pores are chosen based on thresholds R^{ow} for the inscribed radius: for MWL pores larger than $R^{ow}{}_{min}$ and for MWS pores smaller than $R^{ow}{}_{max}$ are oil-wet. For the FW class a fraction α of pores of every size is oil-wet. Note, that UWW and UOW are limiting cases of FW class with oil-wet fraction 0 and 1 respectively.

2.11.6 Wettability Alteration & Contact Angle Hysteresis

There are ***two*** reasons for contact angle change in different flooding cycles. Firstly, wettability alteration (ageing) occurring after primary drainage, in which the oil-contacted part of the pore surface changes its wettability (contact angle) due to adsorption of some hydrophobic components (Kovscek et al. 1993). Secondly, the contact angle may show hysteresis depending on the displacement direction (drainage or imbibition) due to surface roughness (Morrow 1975). We will use the pore-level scenario for wettability alteration (Kovscek et al. 1993) along with contact angle hysteresis and we refer to this combined scenario as non-uniform wettability within a single pore (Figure 2.32)

In general, our network model is used to simulate three consecutive floods: primary oil drainage, water invasion and secondary oil drainage. We apply various wettability distributions after the primary drainage due to ageing for the oil-filled pores, based on the presented classification (including non-uniform wettability within a single pore) (Figure 2.32) during these floods (see Chapter 3).

2.11.7 Intra-Pore Physics

For every displacement during a given flood, a capillary entry pressure is required. The so-called MS-P method (Mayer and Stowe 1965, Princen 1969a, b, 1970) is used for calculating the entry pressures in non-circular capillaries. We assume the wettability alteration along with contact angle hysteresis (non-uniform wettability within a single pore) (Øren and Bakke 2003, Al-Futaisi and Patzek 2004, Piri and Blunt 2004, Valvatne and Blunt 2004, Piri and Blunt 2005a, Helland and Skjaeveland 2006a).

For CTS shapes we use entry pressure solutions for primary drainage and water invasion derived in the literature (Øren et al. 1998, Patzek 2001, Valvatne and Blunt 2004), except the layer formation and collapse criteria. For the Star pore shape characterization, the existing capillary entry pressure solutions for *n*-sided regular polygons (Ma et al. 1996, Lago and Araujo 2001, Piri and Blunt 2005a) and 3-cornered star shapes (van Dijke and Sorbie 2006) are generalized for *n*-cornered stars in Chapter 4.

During water invasion oil layers can be formed in pores of non-uniform wettability. The understanding of oil layer stability is of great importance for the prediction of residual oil in mixed-wet systems. Many authors have used inaccurate geometrical criteria for formation and collapse of layers in capillary bundles (Hui and Blunt 2000a, Helland and Skjaeveland 2006a) and network models (Blunt 1997b, Øren et al. 1998, Piri and Blunt 2004, Valvatne and Blunt 2004, Piri and Blunt 2005a). van Dijke and Sorbie (2006) developed a more physically correct thermodynamically based criterion for the existence of oil layers. This criterion is consistent with the MS-P capillary entry pressures for other water invasion displacements and is more restrictive than the geometrical collapse criterion. So far, this thermodynamical criterion for layer collapse was implemented only into a capillary bundle model (Helland and Skjaeveland 2006a),

but here we implement it in a full two-phase network model (Ryazanov et al. 2008, 2009, 2010a, b).

2.11.8 Prediction of experimental data

The comparisons between network modelling and experiments from the literature show that good predictions of S_{or} can be obtained for (strongly) water-wet systems (Øren et al. 1998, Patzek 2001, Øren and Bakke 2003, Valvatne and Blunt 2004, Piri and Blunt 2005b). However, for systems with altered wettability, the final predictions of S_{or} can be too low when oil layers are included (Øren et al. 1998, Valvatne and Blunt 2004) and the experimental S_{or} values can only be matched by assuming predefined endpoint capillary pressures (Høiland et al. 2007). On the other hand, matching S_{or} by varying the wettability state and then predicting the water flood relative permeability (Øren et al. 1998) may also lead to errors if incorrect criteria for oil layer existence are used. To remedy this, we have incorporated the correct thermodynamically based physics for layer existence and accurate pore shape descriptions, which governs what we believe the "true" S_{or} should be. In Chapter 7, we show improvements in the prediction of oil-wet relative permeabilities data (Valvatne and Blunt 2004) and mixed-wet experiments (remaining oil saturation vs Amott-Harvey index) conducted by Jadhunandan and Morrow (1995).

2.11.9 Wettability effect on Sor and Relative Permeabilities

The effect of wettability on S_{or} and relative permeabilities has been investigated before, both experimentally (Kennedy et al. 1955, Raza et al. 1968, Donaldson and Thomas 1971, Owens and Archer 1971, Morrow et al. 1973, Lorenz et al. 1974, Jadhunandan and Morrow 1995, Skauge and Ottesen 2002) and using network modelling (McDougall and Sorbie 1995, Blunt 1997b, 1998, Øren et al. 1998, Dixit et al. 1999, Al-Futaisi and Patzek 2004, Høiland et al. 2007, Zhao et al. 2010). It has been shown that this effect can be significant and, hence, wettability conditions should be determined accurately before making any network modelling predictions. In this thesis, we analyse the effect of different wettability distributions on S_{or} and relative permeabilities (see Chapter 6). In the same chapter we investigate the effect of pore-shape characterization (CTS and Star) and oil layers existence criteria (thermodynamical and geometrical) on S_{or} and relative permeabilities for the different wettability conditions.

2.11.10 Conclusions

To sum up, in this work, we present a newly developed state-of-the-art pore scale network modelling tool which takes as input the geometrically and topologically equivalent network (extracted) from a real pore space. This model incorporates accurate two-phase intra-pore physics, in particular the thermodynamical oil layer existence criterion, and the new pore shape characterization technique using n-cornered stars.

CHAPTER 3 - MODEL DESCRIPTION

3.1 Introduction

In this chapter, we describe the novel network modelling code that has been developed in the course of this research (see code's GUI description in Appendix A). We consider possible wettability scenarios that can be applied during simulation of three consecutive floods: primary drainage, water invasion (after ageing), secondary drainage. Furthermore, besides the commonly used Circle-arbitrary Triangle-Square (CTS) pore shape characterization, we also present a new pore shape characterization technique to identify the equivalent regular *n*-cornered star shape (Star). Then, we describe the expressions for the single-phase and two-phase conductances for different shape characterizations. Specifically, a new correlation for single-phase conductance for the *n*-cornered star shape is derived.

3.2 Network Model

This new pore-network modelling tool is similar in certain respects to models found in the literature (Øren et al. 1998, Patzek 2001, Valvatne and Blunt 2004) in that it takes as input the geometrically and topologically equivalent network extracted from a real pore space image. The interconnected network consists of pores bodies (nodes) and pore throats (bonds) for which the characteristic properties (volume, shape factor, inscribed and hydraulic radii, length for bonds) have been derived from the original sample. The data structure for these unstructured networks has been described by Bakke and Øren (1997) and Piri and Blunt (2005a) and their general input description and format has been adopted here for consistency.

Also in common with existing models, we represent the pore throats as straight tubes, but we have two options for pore bodies (*PB*) representation. The first option (*with PB*) is the same as in the existing models: pore bodies are included in the model explicitly and involved in displacement processes. For the second option (*without PB*), we distribute the pore body volume between the throats connected to that pore body and ignore any displacements related to it. However, even for the *with PB* case we only use an (effective) throat conductance, which is the harmonic mean of the throat and adjoining body conductances (Øren et al. 1998). Although the first option (*with PB*)

may be more realistic, the second option (*without PB*) is much faster due to a more efficient phase clustering algorithm.

Notice that in addition to previously used pore properties, we also use the hydraulic radius, when available, as an additional parameter to characterize pore shapes by *n*-cornered stars, as explained further in Section 3.4.2. Man and Jing (2000) used star-like grain boundary pore (GBP) shapes for pore throat cross-sections (piecewise-smooth representation), somewhat similar to our *n*-cornered stars with straight sides, but they assumed pores as constricted tubes with a smooth transition between pore body and pore throat shapes and sizes.

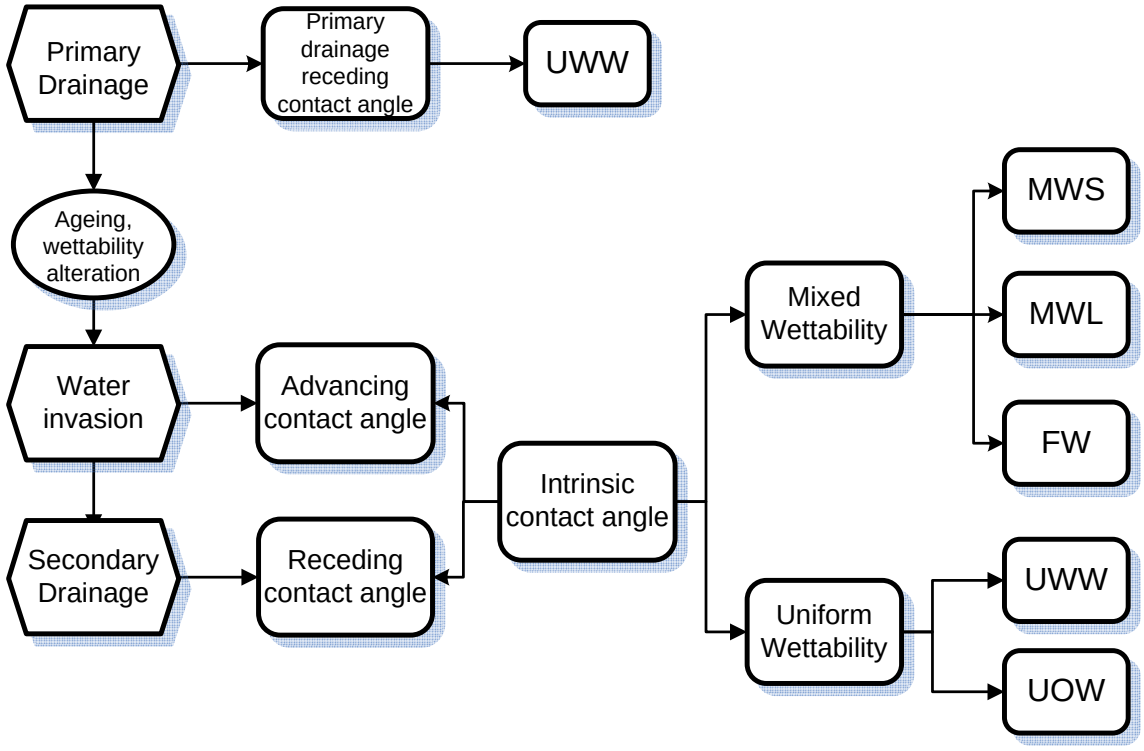

Figure 3.1 Possible pore-to-pore wettability scenarios (right) for the consecutive floods (left) and the assigned contact angles

For the model simulations in this thesis, we consider two pore networks derived from different Berea sandstone samples. The first network (*BereaPB*) has been extracted from the process-based pore space reconstruction of a Berea sandstone (Øren and Bakke 2003). The process-based reconstruction approach (Section 2.2) incorporates grain size distributions and some other petrographical data from 2D thin section images. This approach aims to simulate the three main sandstone-forming geological process steps: sand grain sedimentation, compaction and diagenesis (Bakke and Øren 1997, Øren and Bakke 2002). The second network (*BereaCT*) has been extracted from a 3D micro–

computerized tomography image of a different Berea sandstone sample, using the enhanced extraction technique of Jiang et al. (2007). The input data set for the *BereaCT* network includes the hydraulic radius. Therefore, *BereaCT*'s pore cross-sections can be characterized by *n*-cornered star shapes.

3.3 Wettability Distribution

In general, the presented network model is used to simulate three consecutive floods: primary oil drainage, water invasion and secondary oil drainage. We also include ageing (wettability alteration) after primary drainage and contact angle hysteresis. Various wettability scenarios (i.e. assignments of the oil-water contact angles) can be applied during this simulation. Universal wettability classifications on two scales (pore-to-pore and single pore) have been introduced in Section 2.11.5 (**Figure 2.32**) and will be used to describe the wettability scenarios used in the network simulations presented in this thesis (**Figure 3.1**).

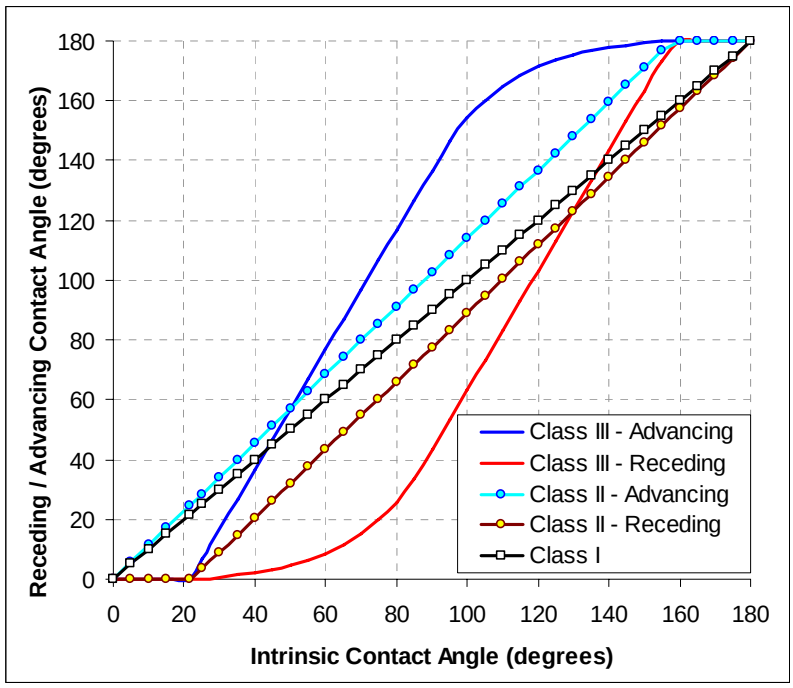

Figure 3.2 Receding and advancing contact angle versus intrinsic contact angle for three different classes I,II,III of contact angle hysteresis (Morrow 1975).

During primary drainage, pores are uniformly wetted (i.e. a single contact angle is assigned to each pore) and the primary drainage receding contact angle is distributed throughout the pore network as uniformly water-wet (UWW). After primary drainage, the oil-filled pores are aged. During ageing, the wettability may change only on the part

of the pore wall that was in contact with oil, thus creating non-uniform wettability within individual pores (Kovscek et al. 1993). For the oil-contacted surfaces of the oil-filled pores we specify a new wettability distribution of advancing and receding contact angles. The distribution can be from one of the uniform wettability classes (UWW, UOW) or mixed wettability classes (MWL, MWS, FW).

Usually, wettability distributions specify intrinsic contact angles, which are used to calculate advancing and receding contact angles from some empirical model for contact angle hysteresis. Morrow (1975) proposed three hysteresis models (**Figure 3.2**): no hysteresis (Class I), moderate hysteresis (Class II) and substantial hysteresis (Class III). During water invasion only receding contact angles from primary drainage, on the non-aged surfaces, and advancing contact angles derived from intrinsic angles after ageing are utilized. For secondary drainage, the receding angle derived from the aged intrinsic angle is used, as well as primary drainage receding contact angle on the non-aged surfaces.

Because we focus on water invasion after primary oil drainage followed by ageing, we specify advancing contact angles directly without reference to the intrinsic angles. However, when we need to simulate the subsequent secondary drainage process, the receding contact angles on the aged surfaces are back calculated (through the intrinsic angle, Class III) from the previously assigned advancing contact angles.

3.4 Real Shape Characterization

3.4.1 Circle-Triangle-Square (CTS) Shape Characterization

Most of the earliest network models assumed circular pore cross-sections for simplicity. However, to represent features such as corner wetting films and non-wetting phase layers explicitly, angular shapes (like triangle and square) are necessary. The most common approach to represent the real shape of a pore cross-section is to idealise it as a circle, an (arbitrary) triangle or a square (CTS) with a shape factor G that approximates that of the real pore shape (Øren et al. 1998, Patzek 2001, Valvatne and Blunt 2004). The shape factor is defined as $G= A/L^2$ (Mason and Morrow 1991), where A and L are the area and perimeter of the cross section, respectively.

The CTS shape characterisation uses the following rules:

$$\text{idealized shape is } \begin{cases} \text{arbitrary } \underline{\text{T}}\text{riangle with the same } G, \text{ if } G \le \sqrt{3}/36 \\ \underline{\text{S}}\text{quare with } G = 1/16, \text{if } \sqrt{3}/36 < G \le 1/16 \\ \underline{\text{C}}\text{ircle with } G = 1/4\pi, \text{if } G > 1/16 \end{cases} \tag{3.1}$$

Generally, the majority of pore shape factors falls into the arbitary triangle interval $(0, \sqrt{3}/36]$, in which case the shape factor can be kept the same as the real G value. The set of half angle values for arbitrary triangle is selected by special procedure proposed by Øren et al. (1998) and Patzek and Silin (2001). The disadvantage of the CTS characterisation is that these shapes are all convex, while a significant fraction of shapes in a realistic porous rock can be non-convex.

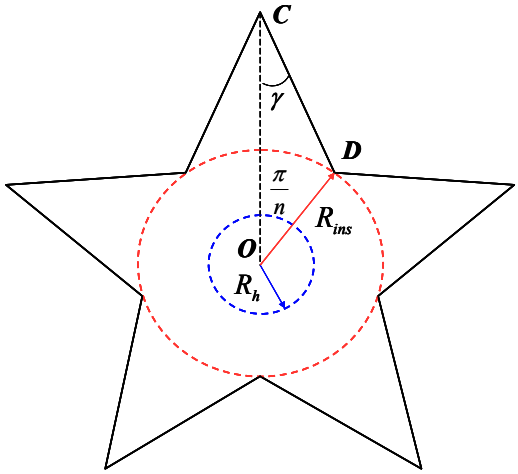

Figure 3.3 5-cornered star pore shape, with half-angle γ, hydraulic radius R_h, and inscribed radius R_{ins}, for which $H=R_h/R_{ins}$ is less than 0.5. The elementary triangle *COD* is used for conductance calculations

Convexity can be indicated by the ratio of the hydraulic radius R_h and the inscribed radius R_{ins} of the cross section, the dimensionless hydraulic radius $H=R_h/R_{ins}=(A/L)/R_{ins}$, where the hydraulic radius R_h is defined as $R_h=A/L$ (Hwang 1977, Patzek and Silin 2001, Lindquist 2006). H is always greater than *1/2* for convex shapes which follows from inequality $2A \ge LR_{ins}$ (Scott and Awyong 2000). Thus, if $H<0.5$ a shape is non-convex, while convex shapes have $H \ge 0.5$. It is easy to show that circle, square and arbitrary triangle all satisfy $H=0.5$.

3.4.2 n-cornered Star Shape Characterization

The regular *n*-cornered star shape (**Figure 3.3**), which is always non-convex, can be used to represent non-convex shapes, contrary to the arbitrary triangle. The regular star has two parameters, the number of corners n and the corner half-angle γ. The

corresponding expressions for the dimensionless hydraulic radius $H_{n,\gamma}$ and the shape factor $G_{n,\gamma}$ are

$$H_{n,y} = \frac{1}{2}\sin\left(\gamma + \frac{\pi}{n}\right),\ G_{n,\gamma} = \frac{1}{4}\frac{\sin(\gamma)\sin\left(\gamma + \frac{\pi}{n}\right)}{n\sin\left(\frac{\pi}{n}\right)} \text{ with } \gamma < \frac{\pi}{2} - \frac{\pi}{n}. \tag{3.2}$$

To derive Eq. (3.2) the following definitions for $H_{n,\gamma}$ and $G_{n,\gamma}$ should be used:

$$R_h = \frac{A_{n,\gamma}}{L_{n,\gamma}},\ H_{n,\gamma} = \frac{R_h}{R_{ins}} = \frac{A_{n,\gamma}}{R_{ins}L_{n,\gamma}}, G_{n,\gamma} = \frac{R_h}{L_{n,\gamma}} = \frac{A_{n,\gamma}}{\left(L_{n,\gamma}\right)^2}, \tag{3.3}$$

where $A_{n,\gamma}$ and $L_{n,\gamma}$ are the area and perimeter respectively of the n-cornered star shape with half-angle γ (Helland et al. 2006, Helland et al. 2008):

$$A_{n,\gamma} = \frac{nR_{ins}^2\sin\left(\frac{\pi}{n}\right)\sin\left(\gamma + \frac{\pi}{n}\right)}{\sin\gamma},\ L_{n,\gamma} = \frac{2nR_{ins}\sin\left(\frac{\pi}{n}\right)}{\sin\gamma}. \tag{3.4}$$

Eq. (3.2) can be obtained now after substituting Eq. (3.4) into Eq. (3.3)

Note, that the shape factor G for the n-cornered star can be expressed as a function of n and H by eliminating γ from both formulas in Eq. (3.2):

$$G = \frac{1}{2}\frac{\sin\left(\sin^{-1}(2H) - \frac{\pi}{n}\right)H}{n\sin\left(\frac{\pi}{n}\right)}. \tag{3.5}$$

For a given arbitrary shape factor G there is no unique pair (n, γ), but it can be shown that with one additional parameter, the dimensionless hydraulic radius H<0.5, a star can be uniquely identified (Helland et al. 2008). In **Figure 3.4** curves with H<0.5 represent stars with different numbers of corners and is described by Eq.(3.5). For a given arbitrary shape with shape factor and dimensionless hydraulic radius (G,H) Eq. (3.2) is used to find the pair (n,γ) on the nearest n-cornered star curve (**Figure 3.4**) by fixing G and approximating H. We explain this procedure in more details now. Firstly, by fixing G the n_1 and n_2 are identified as follows (**Figure 3.4**)

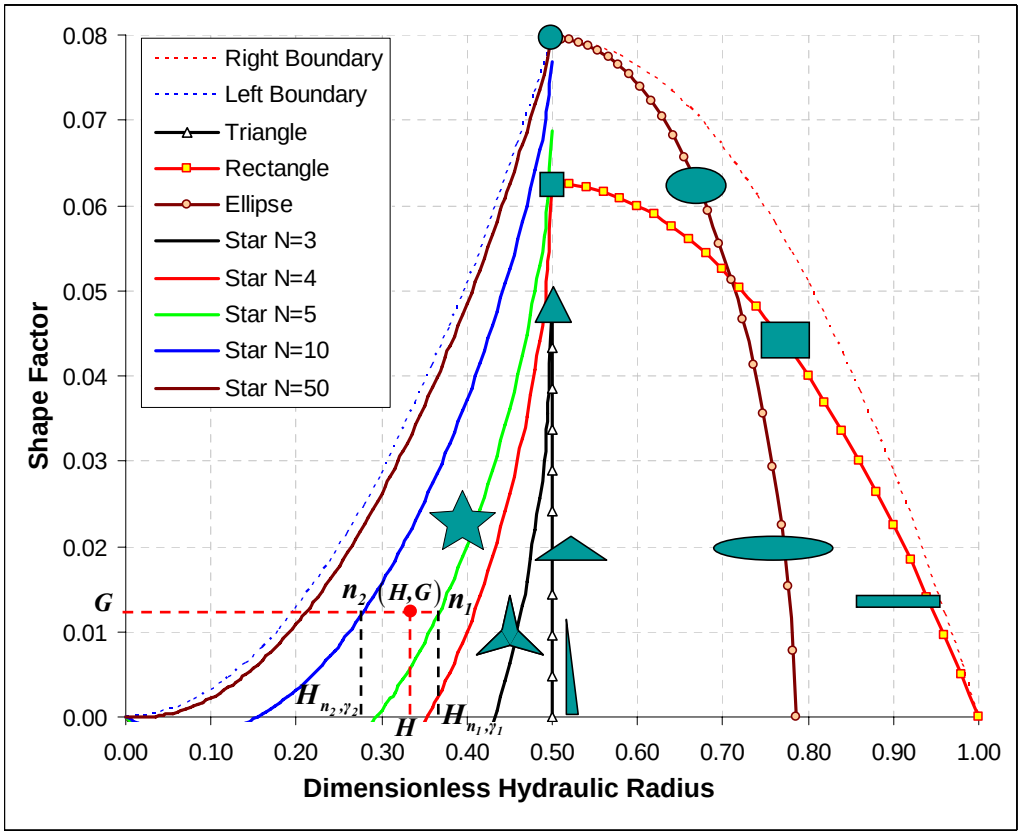

Figure 3.4 Shape factor G vs dimensionless hydraulic radius H for various shapes including n-cornered stars, arbitrary triangles, rectangles and ellipses. The left boundary $G=H^2/\pi$ and the right boundary $G=(H-H^2)/\pi$ (see Appendix B.1) are the theoretical limits for the (G,H) values of any shape

$$H_{n_2,\gamma_2} \le H \le H_{n_1,\gamma_1},\ n_2 = n_1 + 1. \tag{3.6}$$

where

$$\gamma_i = f(n_i, G) = -\frac{\pi}{2n_i} + \frac{1}{2}\cos^{-1}\left(\cos\left(\frac{\pi}{n_i}\right) - 8n_i G \cdot \sin\left(\frac{\pi}{n_i}\right)\right), \text{ (see Appendix B.2)} \tag{3.7}$$

and H_{n_i,γ_i} are estimated from the 1st formula of Eq (3.2). Then the number of corners n is selected as n_1 or n_2 depending on the following delta

$$\Delta H_i = \left|H - H_{n_i,\gamma_i}\right|,\ i = 1,2. \tag{3.8}$$

If $\Delta H_1 < \Delta H_2$ then $n=n_1$ otherwise $n=n_2$:

$$n = n_k,\ k = \arg\min_{i=1,2}\left|H - H_{n_i,\gamma_i}\right|. \tag{3.9}$$

Thus, the corresponding idealized shape will be identified as a regular star shape with n corners and half angle $\gamma = f(n,G)$.

On the line H=0.5 in **Figure 3.4** the arbitrary triangles are represented, as well as the regular n-cornered polygons P, including the square (n=4) and the circle (n=∞). Notice

that the polygons are the limiting shapes of the stars for $\gamma = \frac{\pi}{2} - \frac{\pi}{n}$. Curves for H>0.5 represent some convex shapes, although in general there are also non-convex shapes with H>0.5. For cross-sections with $H \geq 0.5$ the CTS-P approach (CTS and polygons P) is applied, in which the nearest point on the line H=0.5 is found and the corresponding shape is used.

Since for H<0.5 we match the real G and H quite closely with the n-cornered star, we also find a good approximation of the area and perimeter $A = R_{ins}^2 H^2 / G$ and $P = R_{ins} H / G$. However, for H>0.5 the area and perimeter approximation may not be very accurate.

3.5 Single-Phase Conductance

Calculation of relative permeability in a pore-scale model requires accurate expressions for the fluid conductances in the cross-sectional bulk, layer and corner areas that the fluids flow through. We assume steady state, laminar flow of incompressible fluids with constant viscosity. First, we consider single-phase conductance calculations, when the fluid occupies the entire cross section and then we look at conductances of films and layers in pore corners, as well as the conductance of the remaining bulk phase.

3.5.1 Conductance Prediction for the CTS Shapes

The single-phase conductance g for capillary tubes with CTS cross-sections can be approximated by the following expression (Øren et al. 1998, Valvatne and Blunt 2004, Piri and Blunt 2005a)

$$g = \frac{C_g A^2 G}{\mu} = \frac{C_g R_h^4}{\mu G} = \frac{C_g R_h^2 A}{\mu}, \tag{3.10}$$

where μ is viscosity, C_g is a constant, which is equal to 3/5 for arbitrary triangles, 0.5623 for squares and 1/2 for circles.

3.5.2 Conductance Prediction for n-cornered Stars

To derive the single-phase conductance for capillary tubes with n-cornered star cross-sections numerically, we solve the elliptic Poisson equation for the "reduced" velocity u in the tube cross-section Ω (see derivation in Appendix B.3),

$$\nabla^2 u = -1 \text{ on } \Omega \tag{3.11}$$

with no-slip conditions on the boundary, using the finite elements method (FEM) in the MATLAB PDE toolbox (Mathworks 1998) (**Figure 3.5**). Note, that u has dimension

length^2 and is equal to $vl\mu/\Delta P$, where v denotes real fluid velocity, ΔP pressure drop along the tube and l tube length. Then, the pore conductance follows as

$$g = \langle u \rangle \frac{A}{\mu} = \left(\frac{1}{A} \int_{\Omega} u \mathrm{d}A \right) \frac{A}{\mu} \tag{3.12}$$

Based on this approach n-cornered star conductances have previously been calculated numerically (Helland et al. 2006, Helland et al. 2008, Ryazanov et al. 2009) and these are presented in **Figure 3.6** as a function of the shape factor. This figure shows that for a given shape factor value G, dimensionless conductances strongly vary with the number of corners.

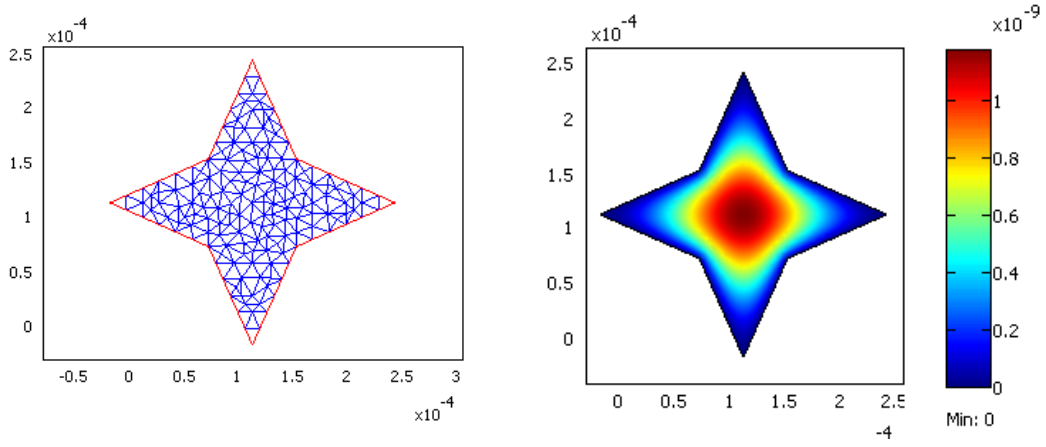

(a) **(b)**

Figure 3.5 Mesh (a) and corresponding "reduced" velocity field (b) calculated by FEM (MATLAB PDE toolbox) for a 4-cornered star shape.

We derived a new correlation (non-linear regression) (Ryazanov et al. 2009) based on the numerical results (**Figure 3.6**):

$$g = \frac{\tilde{g} A^2}{\mu} \text{ with } \tilde{g} = \min\left(C(n), 0.0398\right) \left(\frac{G_{n,\gamma}^t}{G_n^{t,\max}} \right)^{B(n)}, \tag{3.13}$$

where $\tilde{g}$ is the dimensionless n-cornered star single-phase conductance. The correlation is based on the shape factor $G_{n,\gamma}^t$ of the elementary triangle COD shown in **Figure 3.3**, which is derived based on the shape factor definition (see Appendix B.4):

$$G_{n,\gamma}^{t}=\frac{1}{2}\frac{\sin(\gamma)\sin\left(\frac{\pi}{n}\right)\sin\left(\gamma+\frac{\pi}{n}\right)}{\left(\sin(\gamma)+\sin\left(\frac{\pi}{n}\right)+\sin\left(\gamma+\frac{\pi}{n}\right)\right)^{2}},\ 0<\gamma\le\frac{\pi}{2}-\frac{\pi}{n}. \tag{3.14}$$

$G_n^{t,\max}$ is the shape factor of the elementary triangle for the limiting regular *n*-cornered polygon, i.e. $G_n^{t,\max}=G^{t}_{n,\frac{\pi}{2}-\frac{\pi}{n}}$. $B(n)$ and $C(n)$ are fifth order polynomials of n (see **Table 3.1**).

Table 3.1 Coefficients for fifth order polynomials of n used in Eq. (3.13)

	n^5	n^4	n^3	n^2	n	1
$B(n)$	4.479E-08	-7.135E-06	4.418E-04	-1.340E-02	2.041E-01	6.900E-01
$C(n)$	5.120E-06	-1.897E-04	2.787E-03	-2.039E-02	7.505E-02	-7.389E-02

The quality (robustness) of predictions based on the derived non-linear regression is very good and the regression correlation coefficient is large (**Figure 3.7**).

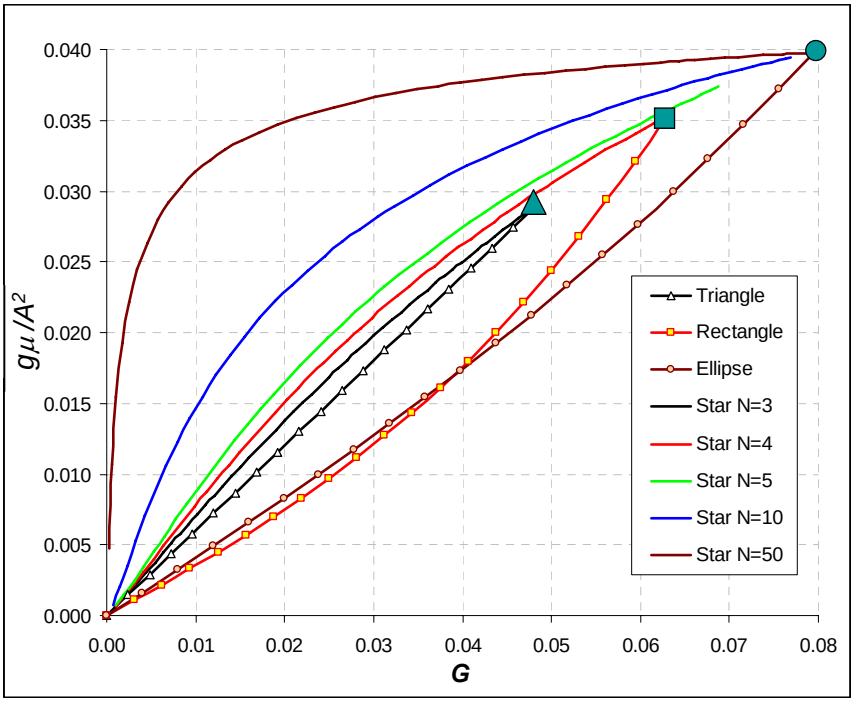

Figure 3.6 Dimensionless conductance $g\mu/A^2$ vs shape factor G for n-cornered stars, arbitrary triangle, rectangle and ellipse. g – single-phase conductance, A – cross-sectional area, μ - fluid viscosity

3.6 Two-Phase Areas and Conductances

If two phases co-exist in the same pore throat, we have to estimate volumes, areas and conductances for each phase separately. Therefore, we should estimate area and conductances for oil or water corner films, oil layers and bulk oil or water phases. In **Figure 3.8** the most complicated corner fluid configuration is sketched with a water corner film, an oil layer and bulk water, including two arc menisci AM1 and AM2, with their respective contact angles θ_h and θ_a. The dimensionless area of a corner film, for example for AM2, is given by Eq. (4.6), from which other areas are easily derived.

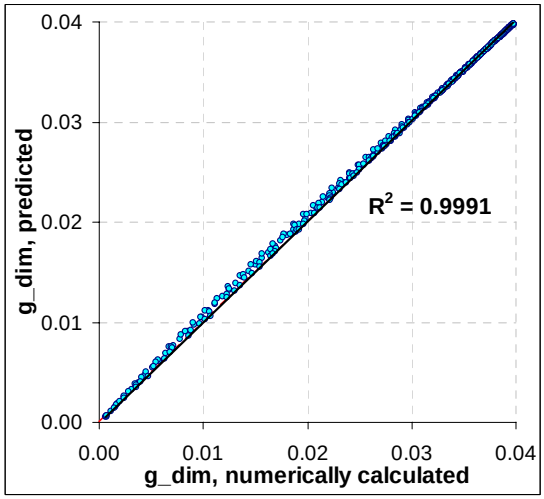

Figure 3.7 Cross-plot of predicted against numerically calculated dimensionless single-phase conductance (g_dim) for *n*-cornered star shapes (3≤n≤50). The coefficient of determination (R squared) is large.

3.6.1 Area and Conductance of Corner Films

For the flow conductance $g_{p,c}$ of films of phase p in corners, we use the correlation derived by Øren et al. (1998), which assumes no-slip boundary conditions at AM1, and is given by

$$g_{p,c} = C\frac{A_{c1}^2 G_c}{\mu_p}, C = 0.364 + 0.28\frac{G_c^*}{G_c}, \tag{3.15}$$

where A_{c1} is the area of the film in the corner bounded by AM1, G_c is the shape factor of the film area, G_c^* is the shape factor in case of zero curvature of the fluid-fluid interface and μ_p is the phase viscosity.

3.6.2 Area and Conductance of Oil Layers

The sandwiched oil layer is bounded by AM1 and AM2. The oil layer area A_l for a single corner can be estimated in terms of the corner areas A_{c1} and A_{c2}, which are bounded by the AM1 and AM2 respectively (**Figure 3.8**):

$$A_l = A_{c2} - A_{c1}. \tag{3.16}$$

A correlation suggested by Valvatne and Blunt (2004) has been used for the oil layer conductance:

$$g_{o,l} = \frac{L_o^4 \tilde{g}_l}{\mu_o}, \ \ln \tilde{g}_l = a_1 \ln^2\left(\tilde{A}_l^3 G_l\right) + a_2 \ln\left(\tilde{A}_l^3 G_l\right) + a_3, \tag{3.17}$$

where L_o is the apex distance for the AM2 position, $\tilde{A}_l$ is the dimensionless area of the oil layer (by division by L_o^2), G_l is the shape factor of the layer and $\tilde{g}_l$ is the dimensionless conductance of the layer, $a_i (i = 1..3)$ are the polynomial fitting parameters.

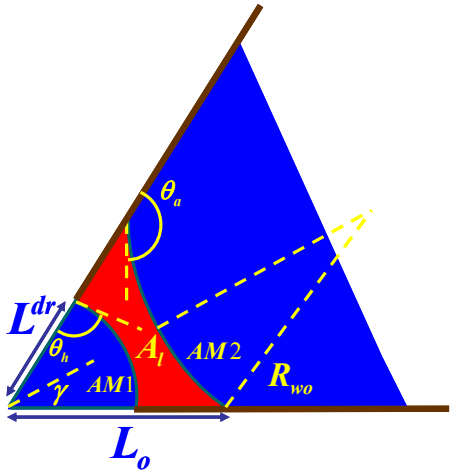

Figure 3.8: Corner fluid configuration with sandwiched oil layer bounded by arc menisci AM1 and AM2, with their respective contact angles θ_h and θ_a. L^{dr} and L_o – apex distance for AM1 and AM2 positions respectively, A_l – oil layer area, R_{wo} – radius of curvature for AM2, γ – corner half-angle. (Red – oil phase, blue – water phase, brown lines – surfaces of altered wettability)

3.6.3 Area and Conductance of Bulk Phase

The area of the bulk phase A_b is determined from the pore throat cross-sectional area A, the corner film area A_c and the area of the oil layer A_l if present. The bulk conductance $g_{p,b}$ is approximated as (Blunt 1998):

$$g_{p,b} = \frac{A_b}{A} g \,,\; A_b = A - n\left(A_l + A_c\right). \tag{3.18}$$

3.7 Porosity, Absolute Permeability and Relative Permeability

Porosity is estimated from the total pore volume of bonds and nodes relative to the cubic volume occupied by the network. For absolute permeability the pressure distribution is calculated from the set of equations based on mass conservation at each node in response to a pressure gradient between inlet and outlet (Øren et al. 1998):

$$\sum q_{ij} = 0 \text{ for each node } i\,, \tag{3.19}$$

where j goes through indices of the nodes connected to node i. The flow rate q_{ij} between nodes i and j is given by the following formula

$$q_{ij} = \frac{g_{ij}}{L_{ij}} \Delta P_{ij} \tag{3.20}$$

where g_{ij} denotes effective hydraulic conductance between node i and node j, L_{ij} distance between the centres of the nodes i and j and ΔP_{ij} pressure difference between the nodes. The effective bond conductance g_{ij} is defined as the harmonic mean of the conductances of the bond and the adjoining nodes (Øren et al. 1998):

$$\frac{L_{ij}}{g_{ij}} = \frac{L_i^n}{g_i^n} + \frac{L_{ij}^b}{g_{ij}^b} + \frac{L_j^n}{g_j^n}\,, \tag{3.21}$$

where g_i^n and g_j^n denote conductances through the nodes, g_{ij}^b bond conductance, L_i^n and L_j^n denote half lengths of the nodes and L_{ij}^b bond length. Then, using the total flow through the model Q, the applied pressure gradient $\Delta P/L_T$ and Darcy's law, the absolute permeability K_{abs} can be estimated from

$$K_{abs} = \frac{\mu Q L_T}{A_T \Delta P}\,, \tag{3.22}$$

where A_T denotes total cross-sectional area of the model perpendicular to flow direction and L_T length of the model from inlet to outlet.

The phase relative permeability is not zero if the network has at least one spanning cluster (connected to inlet and outlet) of network elements (bonds and nodes) occupied by the considered phase. Similar to the absolute permeability calculation, the pressure distribution for each phase is computed in response to a pressure gradient applied across the pore space occupied by the considered phase at a given saturation. During this

computation the effective phase conductances for each bond in a spanning cluster are estimated from Eq.(3.21), but with phase conductances g_p instead of g. Phase conductances g_p are calculated for each relevant network element by summation of the conductances for different occupancies of the considered phase: corner films Eq.(3.15), oil layers Eq.(3.17) or bulk phase Eq.(3.18). For example, for the cross-sectional fluid configuration in **Figure 3.8** the oil conductance g_o is equal to sum of the oil layer conductances $g_{o.l}$ for each corner and the water conductance g_w is the sum of the corner conductances $g_{w,c}$ and the bulk conductance $g_{w,b}$:

$$g_o = \sum_{k=1}^{n} g_{o,l}^k \,,\; g_w = \sum_{k=1}^{n} g_{w,c}^k + g_{w,b} \,. \tag{3.23}$$

Then, from the pressure distribution the effective permeability K_p is estimated by a formula similar to Eq.(3.22). The relative permeability K_{rp} is calculated as the ratio of K_p and absolute permeability K_{abs}:

$$K_{rp} = \frac{K_p}{K_{abs}} \,. \tag{3.24}$$

3.8 Summary and Closing Remarks

In this chapter we described a newly developed pore-scale network modelling tool, which takes as input the geometrically and topologically equivalent network (extracted) from a real pore space.

The wettability alteration, due to ageing after primary drainage, and contact angle hysteresis were included in the model. Based on the wettability alteration model and the universal wettability classification **(Figure 2.32**) we implemented various wettability scenarios (**Figure 3.1**). Each of these represent contact angle distributions for one of the 3 consecutive floods: primary drainage, water invasion (after ageing), secondary drainage. Besides the commonly used CTS pore characterization, we also presented a new n-cornered star shape characterization technique (Star), which takes one extra input parameter, the dimensionless hydraulic radius. Expressions for the single-phase and two-phase conductances for different shape characterizations (CTS, Star) have been presented. In particular, a newly derived relation for *n*-cornered star single-phase conductances and shape factor correlated well with numerically FEM calculations (see Eq.(3.13) and **Figure 3.7**).

The accuracy of the new pore shape characterization *Star* will be compared with *CTS* in Chapter 5 based on a set of 70 real pore shapes. We will compare real pore shape parameters (entry radius, area, conductance etc.) with the corresponding parameters for different approximations (CTS and Star). Then, a capillary bundle model involving the real and approximating pore shapes will be used to compare the predictive capabilities of the characterization approaches in terms of relative permeabilities and capillary pressures.

In Chapter 4 we will describe all possible fluid configurations and displacements that can occur during primary drainage, water invasion (after ageing) and secondary drainage. We will present the corresponding entry pressures for CTS shapes and derive generalized solutions for Star shapes. Furthermore, besides the commonly used geometrical collapse criterion for oil layers, we will also consider the new MS-P derived thermodynamic criterion (van Dijke and Sorbie 2006), which is more accurate and consistent with the entry pressures for other displacements. For the first time this criterion has been implemented in a two-phase pore network model.

CHAPTER 4 - DISPLACEMENT PROCESSES

4.1 Introduction

In the displacement processes considered in this work, initially every network element contains only water. Then, primary drainage is simulated by oil injection to initial oil saturation, S_{oi}. This is followed by ageing, which involves changing the wettability of the oil contacted part of the oil-filled pores, as described in Chapter 2. Then, water invasion into the system at $S_o = S_{oi}$ takes place. Additionally, secondary oil drainage may be simulated. In this chapter, we present all possible pore fluid configurations and pore level displacements, which may occur during all three floods (primary drainage, imbibition and secondary drainage). However, we focus mainly on water invasion, in particular the formation and collapse of oil layers during this process. Two criteria for this layer formation and collapse are studied in detail, the MS-P derived thermodynamic criteria and the geometrical criteria, which result in three scenarios for oil layers existence.

To model the various floods, we specify the pressure boundary conditions at the inlet and outlet faces. During primary and secondary oil drainage, the oil pressure P_o at the inlet is gradually increased while the water pressure P_w is kept constant at the outlet, which results in an increase of the overall capillary pressure, defined as $P_c = P_o - P_w$ (Patzek 2001, Valvatne and Blunt 2004). During water invasion, the water pressure P_w at the inlet is increased while the oil pressure P_o is kept constant at the outlet, thus decreasing the capillary pressure. Pore level displacements are carried out according to invasion-percolation with trapping (Valvatne and Blunt 2004, Piri and Blunt 2005a).

Every pore fluid configuration in the cross-section of a straight tube may contain several different fluid elements, e.g. water corner films, oil layers and bulk water, as discussed in Section 3.6 (see **Figure 4.1**). Additionally, a cluster is defined as an interconnected set of bonds (pore throats) and nodes (pore bodies) that contain at least one fluid element of the cluster phase. For example, a water cluster could contain bonds and nodes containing water corner films, bulk water or both. Therefore, a given bond or node can be part of both an oil and a water cluster (Piri and Blunt 2005a).

The fluid element volumes of every pore (corner film, oil layer, bulk element) are only recalculated at prescribed saturation steps, unless the cluster which contains the fluid elements becomes trapped (isolated from the outlet).

Pore (level) displacements are defined as events where the configuration of fluid elements changes, for example in a piston-like displacement the bulk fluid element is displaced. For each pore displacement a corresponding entry pressure needs to be overcome. We define an entry pressure P_{entry} in terms of an entry radius R_{entry}:

$$P_{entry} = \frac{\sigma_{ow}}{R_{entry}}, \tag{4.1}$$

where σ_{ow} is oil-water interfacial tension. Note, that the entry radius R_{entry} is an "effective" radius of curvature, which is related to two principal radii of curvatures (R_1,R_2) through the Laplace equation:

$$\frac{1}{R_{entry}} = \left(\frac{1}{R_1} + \frac{1}{R_2} \right). \tag{4.2}$$

The R_{entry} must be specified for specific shapes and displacements. The existing entry radius solutions for *n*-sided regular polygons (Ma et al. 1996, Lago and Araujo 2001, Piri and Blunt 2005) and 3-cornered stars (van Dijke and Sorbie 2006) will be generalized to *n*-cornered stars. In Subsections 4.2.2, 4.3.2 and 4.4 we present entry pressures for all possible pore level displacements occurring during primary drainage, water invasion and secondary drainage for the *n*-cornered star. For shapes in the CTS approximation, expressions have been derived in the literature and we only give an overview below.

For the circular pore cross-section the entry pressure for the piston-like displacement is given by the Young-Laplace equation:

$$P_{entry} = \frac{2\sigma_{ow}\cos\theta}{R_{ins}},\ R_{entry} = \frac{R_{ins}}{2\cos\theta}, \tag{4.3}$$

where θ is equal to θ_{pd} during primary drainage, θ_a during water invasion and θ_r during secondary drainage. For angular pore shapes the MS-P theory (Mayer and Stowe 1965, Princen 1969a, b, 1970) is used to obtain the entry pressures. The entry pressures for the arbitrary triangles have been derived by many authors (Valvatne and Blunt 2004, Patzek 2001, Øren et al. 1998, Mason and Morrow 1991, Piri and Blunt 2005) and will not be presented here. The square is the limiting case of the 4-cornered star when γ

=π/4, hence its entry pressure follows from the generalized MS-P entry pressure formula for the regular *n*-cornered star.

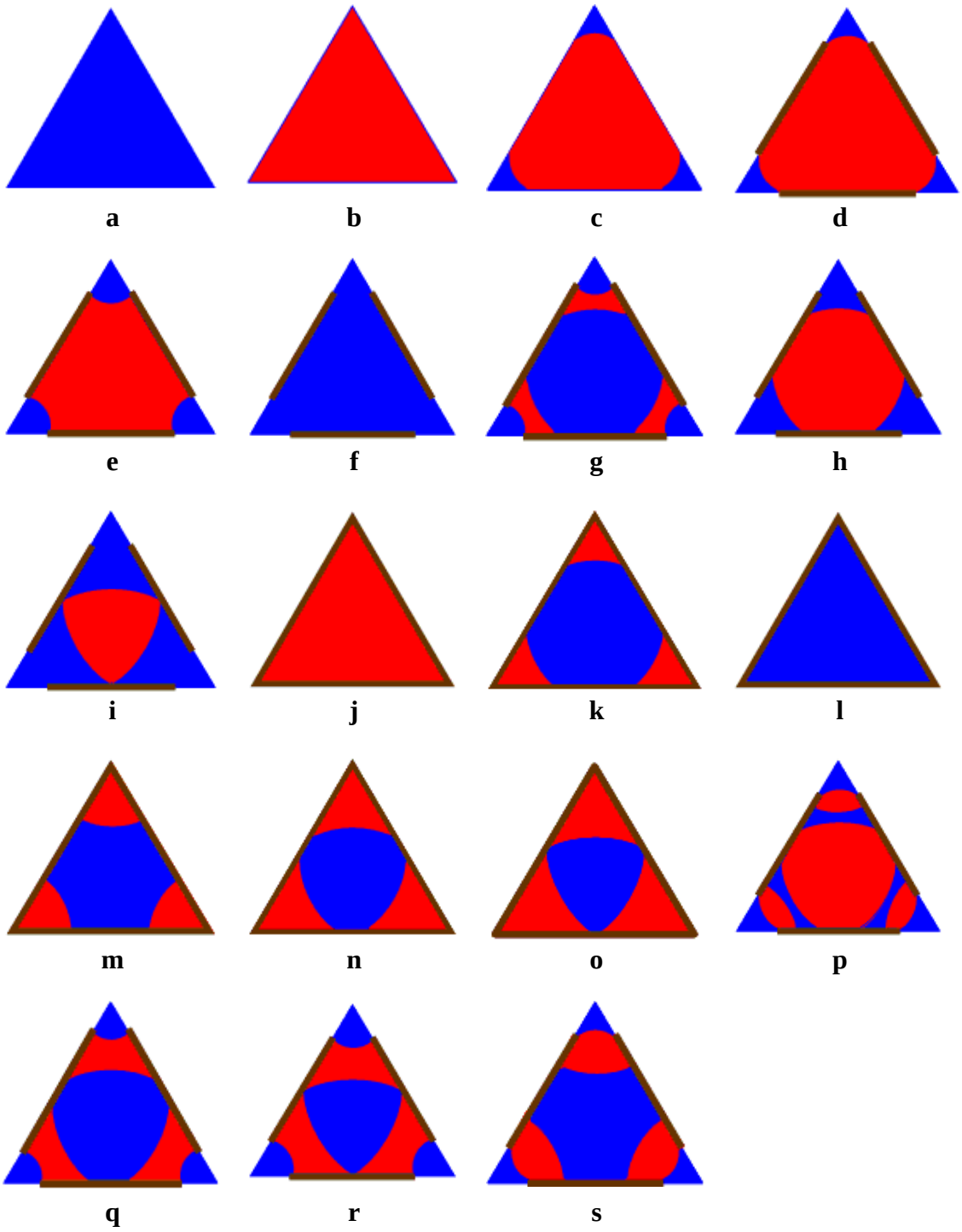

Figure 4.1 Fluid configurations which can exist in n-cornered star shaped pore cross-sections during primary oil drainage, water invasion and secondary oil drainage. Red indicates oil phase, blue water phase, brown lines surfaces of altered wettability. For simplicity, the equilateral triangle is used, which is the limiting shape of a 3-cornered star.

Table 4.1 Pore displacements which may occur during primary drainage and water invasion (after ageing). See Sections 4.2 and 4.3 for details.

	Displacement	Configuration before	Configuration after	Description	θ_{pd}			θ_a			θ_h		Entry radius iterative/ explicit
					$\theta_{pd} < \pi/2\text{-}\gamma$	$\pi/2\text{-}\gamma \leq \theta_{pd} \leq \pi/2+\gamma$	$\theta_{pd} > \pi/2+\gamma$	$\theta_a < \pi/2\text{-}\gamma$	$\pi/2\text{-}\gamma \leq \theta_a \leq \pi/2+\gamma$	$\theta_a > \pi/2+\gamma$	$\theta_h < \theta_a$	$\theta_h = \theta_a$	
Primary Drainage	A-Dr	**a**	**c**	piston-like with water corner films formation	✓								$F_{entry}^{A-Dr}\left(\theta_{pd},\gamma,n\right)$ explicit
	B-Dr	**a**	**b**	piston-like without water corner films		✓	✓						$F_{entry}^{B-Dr}\left(\theta_{pd},\gamma,n\right)$ explicit
Water Invasion	A-Imb	**e**	**g**	piston-like with sandwiched oil layers formation	✓					✓			$-F_{entry}^{A-Dr}\left(\pi-\theta_a,\gamma,n\right)$ explicit
	A1-Imb	**j**	**k**	piston-like with oil corner films formation		✓	✓			✓			$-F_{entry}^{A-Dr}\left(\pi-\theta_a,\gamma,n\right)$ explicit
	B-Imb	**e**	**f**	piston-like with water corner films before	✓			✓	✓	✓	✓		$F_{entry}^{B-\mathrm{Imb}}\left(L^{dr},\theta_a,\gamma,n\right)$ iterative
	B1-Imb	**h**	**f**	piston-like, while AM1 moving with θ_a	✓			✓				✓	$F_{entry}^{A-Dr}\left(\theta_a,\gamma,n\right)$, explicit
	B2-Imb	**j**	**l**	piston-like without water corner films		✓			✓				$-F_{entry}^{B-Dr}\left(\pi-\theta_a,\gamma,n\right)$ explicit
	C – T/G-Imb	**g**	**f**	oil layers collapse (thermodynamical/ geometrical criteria)	✓					✓	✓		$F_{entry}^{C-\mathrm{Imb\text{-}T/G}}\left(L^{dr},\theta_a,\gamma,n\right)$ iterative
	D-Imb	**e**	**f**	snap-off (forced)	✓				✓	✓		✓	$F_{entry}^{D-\mathrm{Im}b}\left(L^{dr},\theta_a,\gamma,n\right)$ explicit
	D1-Imb	**i**	**f**	snap-off (spontaneous)	✓			✓				✓	$F_{entry}^{D1-\mathrm{Im}b}\left(\theta_a,\gamma,n\right)$ explicit

The fluid configurations in each individual corner for equilateral triangular and *n*-cornered star shapes are the same. Therefore, for simplicity, the equilateral triangle is used for all possible configurations representation in this chapter (**Figure 4.1**). For illustration, 3 typical configurations that occur during the water invasion (bulk oil +

water corner films; bulk water, oil layers and water corner films; filled with water) for 3-cornered star are presented here (**Figure 4.2**).

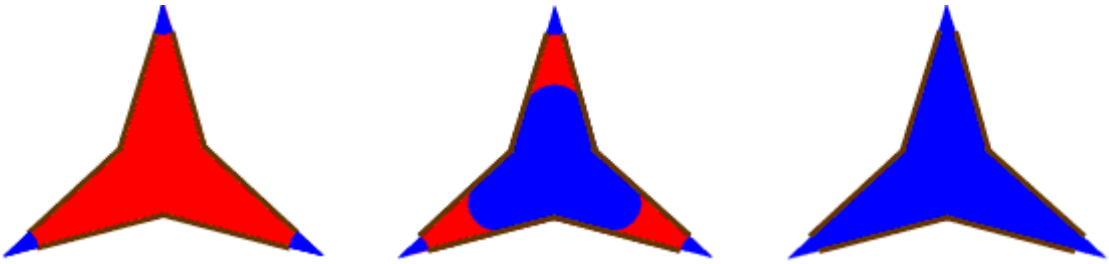

(a) (b) (c)

Figure 4.2 Typical fluid configurations which can exist in 3-cornered star shaped pore cross-sections during water invasion: (a) bulk oil with water corner films, (b) oil layers sandwiched between bulk water and water corner films, (c) fully filled with water. Red indicates oil phase, blue water phase, brown lines surfaces of altered wettability.

4.2 Primary Drainage

4.2.1 Fluid configurations and displacements

Primary drainage is the proccess of oil invasion into water. At the start of primary drainage all pores (bodies and throats) are assumed to be water-filled and water-wet with contact angle $\theta_{pd} < \pi/2$. For each pore there are only 3 possible fluid configurations during primary drainage: **a, b, c (Figure 4.1a,b,c)** and 2 corresponding displacements *A-Dr* and *B-Dr* (**Table 4.1**). If a pore is sufficiently strongly water-wet with

$$\theta_{pd} < \pi/2 - \gamma\,, \tag{4.4}$$

then a piston-like (PL) displacement (*A-Dr*, and the corresponding change in pore fluid configuration **a→c**) will lead to the formation of water corner films, creating arc menisci such as AM1 in **Figure 3.8**. On the contrary, if θ_{pd} does not satisfy Eq.(4.4), then a PL displacement will lead to a configuration without films (*B-Dr* and **a→b**).

4.2.2 Capillary Entry Pressures

According to MS-P theory, the entry radius for displacement *A-Dr* can be obtained from the following equation

$$-A_{n,\gamma} + R_{entry} L_{n,\gamma} \cos\theta_{pd} - nR_{entry}^2 A_\alpha = 0\,, \tag{4.5}$$

where

$$A_\alpha = \theta_{pd} + \gamma - \frac{\pi}{2} + \frac{\cos\theta_{pd}\cos\left(\theta_{pd}+\gamma\right)}{\sin\gamma} \tag{4.6}$$

is the dimensionless film area in a single corner α corresponding to AM1, $A_{n,\gamma}$ and $L_{n,\gamma}$ are the area and perimeter respectively of the *n*-cornered star shape with half-angle γ (Helland et al. 2006, Helland et al. 2008) (see Eq.(3.4)).

The entry radius

$$R_{entry} = F_{entry}^{A-Dr}\left(\theta_{pd},\gamma,n\right) = \frac{1}{2}\frac{\cos\theta_{pd}L_{n,\gamma} - \sqrt{\cos^2\theta_{pd}L_{n,\gamma}^2 - 4nA_\alpha A_{n,\gamma}}}{nA_\alpha} \tag{4.7}$$

is the solution of Eq.(4.5) that is smaller than the radius $R_{entry}^{\max}$ associated with snap-off of bulk oil by the water films

$$R_{entry} < R_{entry}^{\max} = \frac{R_{ins}\sin\left(\frac{\pi}{n}\right)}{\cos\left(\theta_{pd}+\gamma\right)}. \tag{4.8}$$

Because during displacement *B-Dr* (**a→b**) no water films form, the corresponding entry radius solution can be deduced from Eq.(4.5) by substituting 0 for A_α, i.e.

$$R_{entry} = F_{entry}^{B-Dr}\left(\theta_{pd},\gamma,n\right) = \frac{A_{n,\gamma}}{L_{n,\gamma}\cos\theta_{pd}} = \frac{R_{ins}}{2}\frac{\sin\left(\gamma+\frac{\pi}{n}\right)}{\cos\theta_{pd}}. \tag{4.9}$$

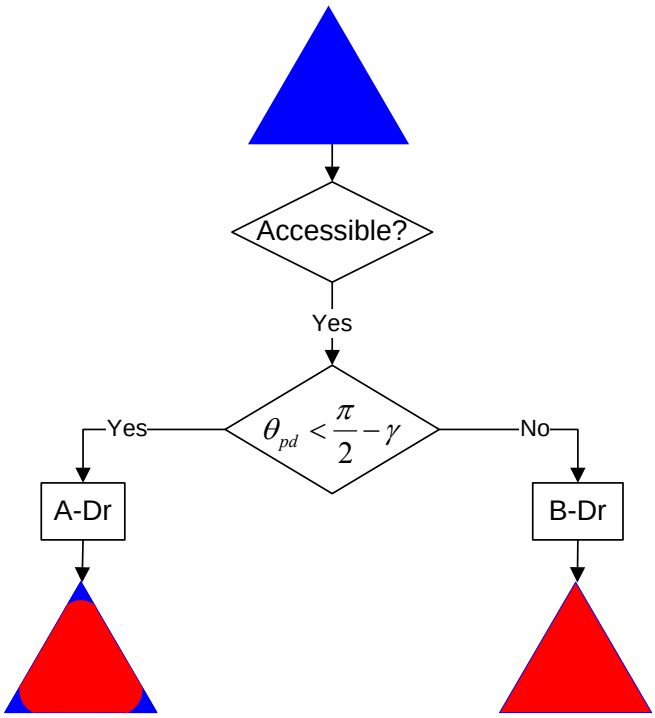

Figure 4.3 Flowchart of possible displacement scenarios during primary oil drainage for the *n*-cornered star. Note, that for each displacement to happen the defending phase should be connected to the outlet by means of a continuous cluster.

4.2.3 Primary Drainage Scenarios

During primary drainage the pressure in the oil phase P_o at the inlet is increased while the water phase pressure P_w at the outlet is kept constant, resulting in increased capillary pressure P_c throughout the network. To decide consecutive invasion events, all pores (bodies and throats) are sorted in order of increasing entry pressure. At every step the bulk water-filled pore with the lowest entry pressure is identified. If this pore has a neighbouring oil-filled pore, i.e. it is accessible, and it is part of a water cluster that is connected to the outlet, then it is invaded PL according to displacement A-Dr or B-Dr as described in Section 4.2.1 (see **Figure 4.3**). This process continues until all accessible bulk water-filled pores have been invaded by oil. When PL displacements without water films formation *B-Dr* take place, the invaded pores will not have water corner films. This may result in the formation of trapped water clusters. At the end of drainage the irreducible water consists of trapped bulk water and water corner films. Notice that corner films that are part of an outlet connected cluster may continue to shrink, as long as the network P_c increases. This shrinkage is not strictly a pore displacement, but it does lead to reduction of the irreducible water saturation.

4.3 Water Invasion

4.3.1 Fluid Configurations and Displacements

After primary drainage, ageing is introduced in the model by changing the wettability of the oil-contacted part of the oil-filled pores and a distribution of advancing contact angle θ_a values is assigned. Consequently, the wettability within a pore becomes non-uniform, which corresponds to fluid configuration **d** (**Figure 4.1d**).

At the start of water invasion the length of contact of the water corner film with the solid in a corner L^{dr} (shown in **Figure 3.8** for fluid configuration **d**) is fixed as

$$L^{dr} = R_{\min}^{dr} \frac{\cos\left(\theta_{pd} + \gamma\right)}{\sin\gamma} \quad , \tag{4.10}$$

where $R_{\min}^{dr}$ is the minimum radius of curvature reached during primary drainage, which corresponds to AM1 position at maximum drainage capillary pressure $P_{c,\max}^{dr}$. The jump in contact angle values at position L^{dr} results in pinning of AM1 with an associated hinging contact angle θ_h (see **Figure 3.8**). As the capillary pressure decreases, the hinging contact angle varies from θ_{pd} towards θ_a (fluid configuration **e** in **Figure 4.1**)

(Ma et al. 1996). A second AM, called AM2, may exist during imbibition, delineating an oil layer as sketched in fluid configuration **g** (**Figure 4.1g**), but only if, similar to Eq.(4.4),

$$\theta_a > \frac{\pi}{2} + \gamma \,. \tag{4.11}$$

Hence, three main fluid configurations are possible during water invasion (see **Figure 4.1e,f,g**) and there are four possible displacements between them as indicated in **Table 4.1** (*A-Imb*, *B-Imb*, *C-Imb*, *D-Imb*). The focus of this section is on the displacement of oil layers (*C-Imb*), for which two criteria exist, a geometrical (*C-G-Imb*) and a thermodynamical (*C-T-Imb*) criterion (van Dijke and Sorbie 2006). There are six other possible fluid configurations **d,h,i,j,k,l** (see **Figure 4.1**) and four corresponding displacements *A1-Imb, B1-Imb, B2-Imb, D1-Imb* (**Table 4.1**). These displacements (apart from *D1-Imb*) are beyond the scope of our study and criteria for these can be easily derived from the other displacements described here (see **Table 4.1**).

We calculate the capillary entry pressures below for the four typical displacements (*A-Imb*, *B-Imb*, *C-Imb*, *D-Imb*) during water invasion with non-uniform wettability. The equations for the corresponding entry radii are formulated for the *n*-cornered star, which is a relatively straightforward generalization from the 3-cornered star (van Dijke and Sorbie 2006).

4.3.2 Capillary Entry Pressures

Displacement *A-Imb* (**e→g**) is a piston-like displacement, during which oil layers are formed. The *A-Imb* event is similar to piston-like displacement with water corner films formation (*A-Dr)* which happens during the primary drainage. Hence, the *A-Imb* entry radius can be derived from the *A-Dr* solution (4.7) as

$$R_{entry} = -F_{entry}^{A-Dr}\left(\pi - \theta_a, \gamma, n\right) = \frac{1}{2}\frac{\cos\theta_a L_{n,\gamma} + \sqrt{\cos^2\theta_a L_{n,\gamma}^2 - 4nA_\alpha A_{n,\gamma}}}{nA_\alpha} \tag{4.12}$$

where

$$A_\alpha = \frac{\pi}{2} - \theta_a + \gamma + \frac{\cos\theta_a \cos\left(\theta_a - \gamma\right)}{\sin\gamma} \tag{4.13}$$

is the dimensionless film area in a single corner α corresponding to AM2 with a negative curvature (the radius of curvature is pointing into the water phase). Note that similar to Eq.(4.8) the physically correct entry radius solution (4.12) should be larger than the radius $R_{entry}^{\min}$ associated with snap-off of bulk water by the oil layers (van Dijke and Sorbie 2006):

$$R_{entry} > R_{entry}^{\min} = \frac{R_{ins}\sin\left(\frac{\pi}{n}\right)}{\cos\left(\theta_a - \gamma\right)}. \tag{4.14}$$

Displacement *B-Imb* (**e→f**) is a piston-like displacement that completely removes oil from the pore. From the MS-P theory we obtain the following system of two equations:

$$\begin{aligned} &-A_{n,\gamma} + R_{entry}L_{n,\gamma}\cos\theta_a + \\ &+nR_{entry}^2\left\{\frac{\pi}{2} - \theta_h - \gamma + \left(\cos\theta_h - 2\cos\theta_a\right)\frac{\cos\theta_h\cos\left(\theta_h+\gamma\right)}{\sin\gamma}\right\} = 0, \end{aligned} \tag{4.15}$$

$$R_{entry} = L^{dr}\frac{\sin\gamma}{\cos\left(\theta_h+\gamma\right)}, \tag{4.16}$$

which is solved iteratively for R_{entry} and θ_h with initial guess $\theta_h^0 = \theta_{pd}$. The final solution can be represented as a function $R_{entry} = F_{entry}^{B-\mathrm{Im}b}\left(L^{dr},\theta_a,\gamma,n\right)$. Note, that if θ_{pd} is close to θ_a then the resulted hinging angle solution may be such that $\theta_h \geq \theta_a$. In this case, once the hinging angle reached θ_a, AM1 starts moving towards to the centre on the surface of altered wettability until the PL displacement *B1-Imb*(**h→f**) takes place (see **Table 4.1** and **Figure 4.4**).

Displacement *C-Imb* (**g→f***)* represents oil layer collapse (or displacement of oil layers from corners) and occurs according to the thermodynamical criterion *C-T-Imb*(**g→f**). Previously, a less accurate criterion for this displacement was used, the geometrical criterion *C-G-Imb*(**g→f**). These displacements correspond to the same change in fluid configurations, but occurring at different entry pressures.

The thermodynamical layer collapse criterion *C-T-Imb* has been derived using MS-P theory in terms of an equation for θ_h (van Dijke and Sorbie 2006):

$$\pi-\theta_a-\theta_h+\cos\theta_a\frac{\cos(\theta_a-\gamma)}{\sin\gamma}+(\cos\theta_h-2\cos\theta_a)\frac{\cos(\theta_h+\gamma)}{\sin\gamma}=0. \qquad (4.17)$$

This equation is solved iteratively with initial guess $\theta_h^0=\theta_{pd}$, while the resulting θ_h is inserted in Eq.(4.16) to estimate the corresponding radius of curvature $R_{entry}=F_{entry}^{C-T-\mathrm{Im}b}\left(L^{dr},\theta_a,\gamma,n\right)$.

The geometrical layer collapse criterion *C-G-Imb* is based on the configuration in which AM1 and AM2 touch (Øren et al. 1998, Hui and Blunt 2000a, Piri and Blunt 2004):

$$\cos\theta_h-2\sin\gamma-\cos\theta_a=0. \qquad (4.18)$$

Combining Eq.(4.18) with Eq.(4.16) yields the explicit expression for the entry radius:

$$R_{entry}=F_{entry}^{C-G-\mathrm{Im}b}\left(L^{dr},\theta_a,\gamma,n\right)=\frac{L^{dr}\sin\gamma}{\cos\gamma\left(2\sin\gamma+\cos\theta_a\right)-\sin\gamma\sqrt{\sin^2\theta_a-4\sin^2\gamma-4\sin\gamma\cos\theta_a}}. \qquad (4.19)$$

The snap-off displacement *D-Imb* (**e→f**) (snap-off of bulk oil by water corner films) only occurs in pores which have no adjacent bulk water filled pores. Expressions for snap-off entry pressures can be found in Hui and Blunt (2000a), Valvatne and Blunt (2004), Ma et al. (1996).

There is a special snap-off case *D1-Imb* (**i→f**) (see in **Table 4.1**) for $\theta_a<\pi/2-\gamma$. Once the hinging angle reached θ_a, AM1 starts moving towards to the centre and when the AM1s meet, they will become unstable and snap-off *D1-Imb* occurs. The corresponding entry radius is calculated by

$$R_{entry}=F_{entry}^{D1-\mathrm{Im}b}\left(\theta_a,\gamma,n\right)=\frac{R_{ins}\sin\left(\frac{\pi}{n}\right)}{\cos(\theta_a+\gamma)},\ \theta_a<\pi/2-\gamma \qquad (4.20)$$

For $\pi-\gamma>\theta_a\geq\pi/2-\gamma$, once the hinging angle θ_h reaches the advancing angle θ_a, the AM1 becomes unstable and snap-off event *D-Imb*(**e→f**) occurs immediately. For $\theta_a\geq\pi-\gamma$ the AM becomes unstable when the hinging angles reach $\pi-\gamma$ according to the half-cylinder criterion (Ma et al. 1996). The entry radius of curvature for the *D-Imb* displacement is given by

$$R_{entry} = F_{entry}^{D-\mathrm{Im}b}\left(L^{dr}, \theta_a, \gamma, n\right) = \begin{cases} \dfrac{L^{dr}\sin\gamma}{\cos\left(\theta_a+\gamma\right)}, & \dfrac{\pi}{2}-\gamma \le \theta_a < \pi-\gamma \\ -L^{dr}\sin\gamma, & \theta_a \ge \pi-\gamma \end{cases} \tag{4.21}$$

4.3.3 Pore Body Filling

When pore bodies are explicitly included in the model pore body filling (PBF) events should be considered additionally. The capillary entry pressure during pore body filling depends on the number of connected oil-filled pore throats (Lenormand et al. 1983). Thus for the pore body with *Z* throats connected to it, there are *Z*-1 possible pore body entry events I_n (n=1..*Z*-1). The I_n entry pressures have been described by a number of parametric models (Blunt 1997a, 1998, Øren et al. 1998, Patzek 2001, Valvatne and Blunt 2004). They are all ad hoc models and are not rigorous. Please see the literature review (Section 2.5.2) for further details. In this work, the corresponding entry pressure is calculated from the following expression (Blunt 1998):

$$I_n : P_{entry}^n = \frac{2\sigma_{ow}\cos\theta_a}{R_{ins}} - \sigma_{ow}\sum_{i=1}^{n} a_i x_i,\ n = 1..Z-1, \tag{4.22}$$

where n denotes the number of oil-filled pore throats connected to the pore body and x_i are random numbers between 0 and 1, a_i are arbitrary weighting coefficients specified beforehand. Valvatne (2004) noted that the selection of weighting coefficients a_i will affect what kind of displacement is more likely to occur. We define a_i according to Valvatne and Blunt (2004) as

$$a_1 = 0,\ a_i = \frac{0.03}{\sqrt{K_{abs}}},\ i = 2..Z-1, \tag{4.23}$$

where K_{abs} denotes absolute permeability in m^2. Valvatne and Blunt (2004) used absolute permeability because of its connection to the pore throat distribution and since the corresponding weighting coefficients were close to those previously used by Blunt (1998). If there is only one connected oil-filled pore throat, the displacement (I_1) is similar to piston-like (Øren et al. 1998, Valvatne and Blunt 2004).

The I_n PBF event takes place only if the displacement is spontaneous, in other words, the corresponding piston-like entry pressure should be positive (Øren et al. 1998, Valvatne and Blunt 2004). On the contrary, if the entry pressure for piston-like is

negative (i.e. the displacement is forced), then the PBF event does not depend on the number of connected oil-filled pore throats and will be the same as the piston-like displacement (Øren et al. 1998, Valvatne and Blunt 2004).

4.3.4 Water Invasion Scenarios

All possible displacement scenarios during water invasion are presented in the flowchart shown in **Figure 4.4**. Since we are mainly interested in four displacements (*A-Imb, B-Imb, C-T/G-Imb, D-Imb*), we consider the corresponding scenarios in much more detail. From now on, we omit "-Imb" when we refer to these displacements. Starting from configuration **e**, formed after primary drainage and ageing, during water invasion the following three displacement scenarios can happen in a single pore:

1. *B* (**e→f**)
2. *A* (**e→g**) followed by *C* (**g→f**), for which different sub-scenarios are available when different collapse criteria are used (*C-T* or *C-G*), as described below
3. *D* (**e→f**)

Scenarios 1 and 2 are illustrated in **Figure 4.5**, for a realistic set of parameters with n=3, $\gamma=\pi/6$, $\theta_{pd}=0$ and the minimum radius of curvature reached during primary drainage $R_{\min}^{dr}$ (see Eq.(4.10)) ten times lower than the drainage entry radius R_{entry}^{dr}. Additional displacement example scenario calculations can be found in the paper by van Dijke and Sorbie (2006).

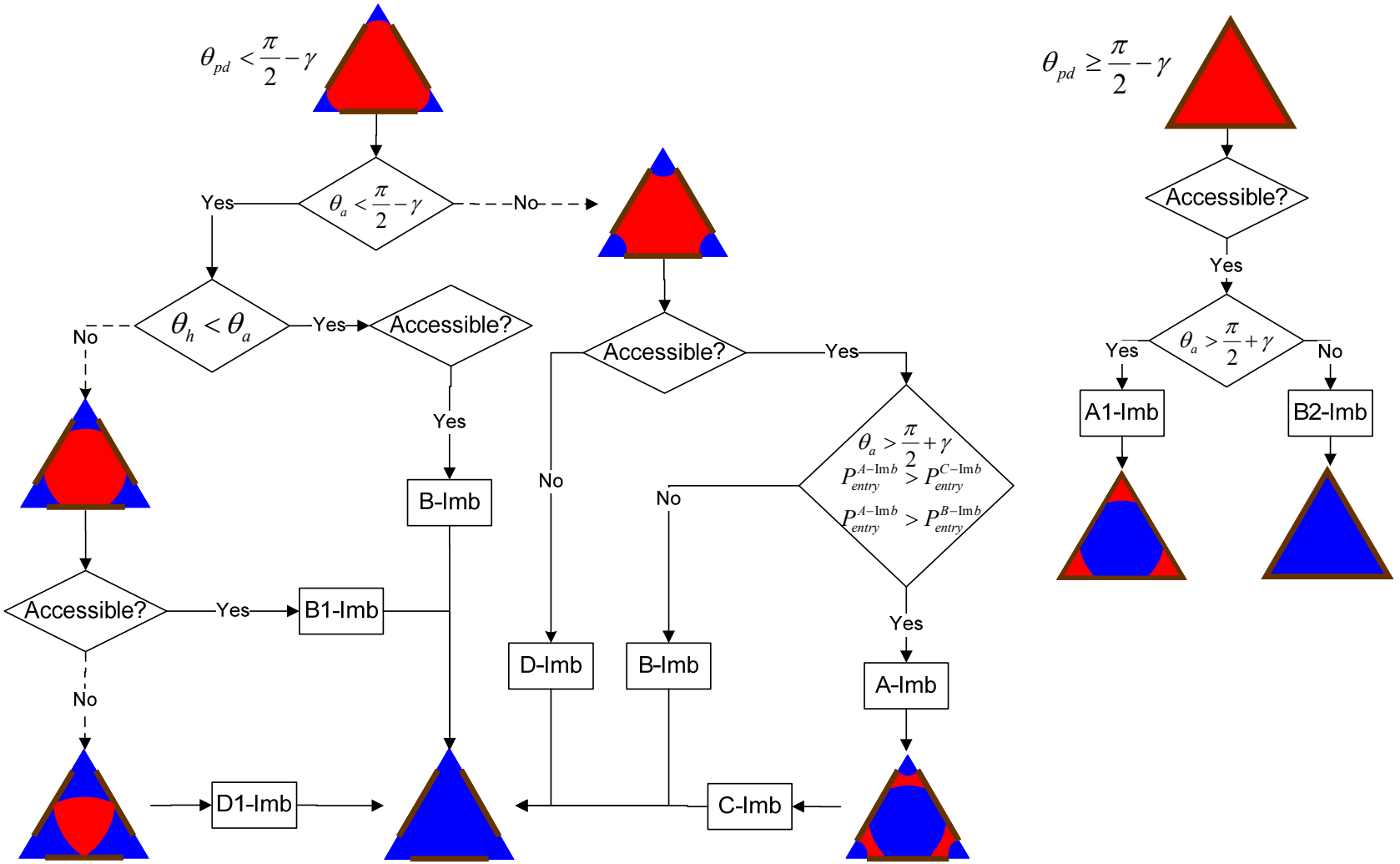

Figure 4.4 Flowchart of possible displacement scenarios during water invasion for the *n*-cornered star. Note, that for each displacement the defending phase should be connected to the outlet .

Below, we describe the sub-scenarios for scenario 2. The capillary pressure has been made dimensionless by division by σ_{ow} / R_{ins}.

Therm and *Geom* sub-scenarios **(Figure 4.5a,c):** We calculate entry pressures for the *A*, *C-T* and *C-G* displacements. If $P_{entry}^{A} > P_{entry}^{C-T/G}$ then displacements *A* and *C-T* and *C-G* both occur in this order (path 2), otherwise displacement *B* takes place and P_{entry}^{B} is calculated (path 1). The *Geom* sub-scenario has been described by Helland and Skjaeveland (2004). A description of the *Therm* sub-scenario can be found in van Dijke and Sorbie (2006).

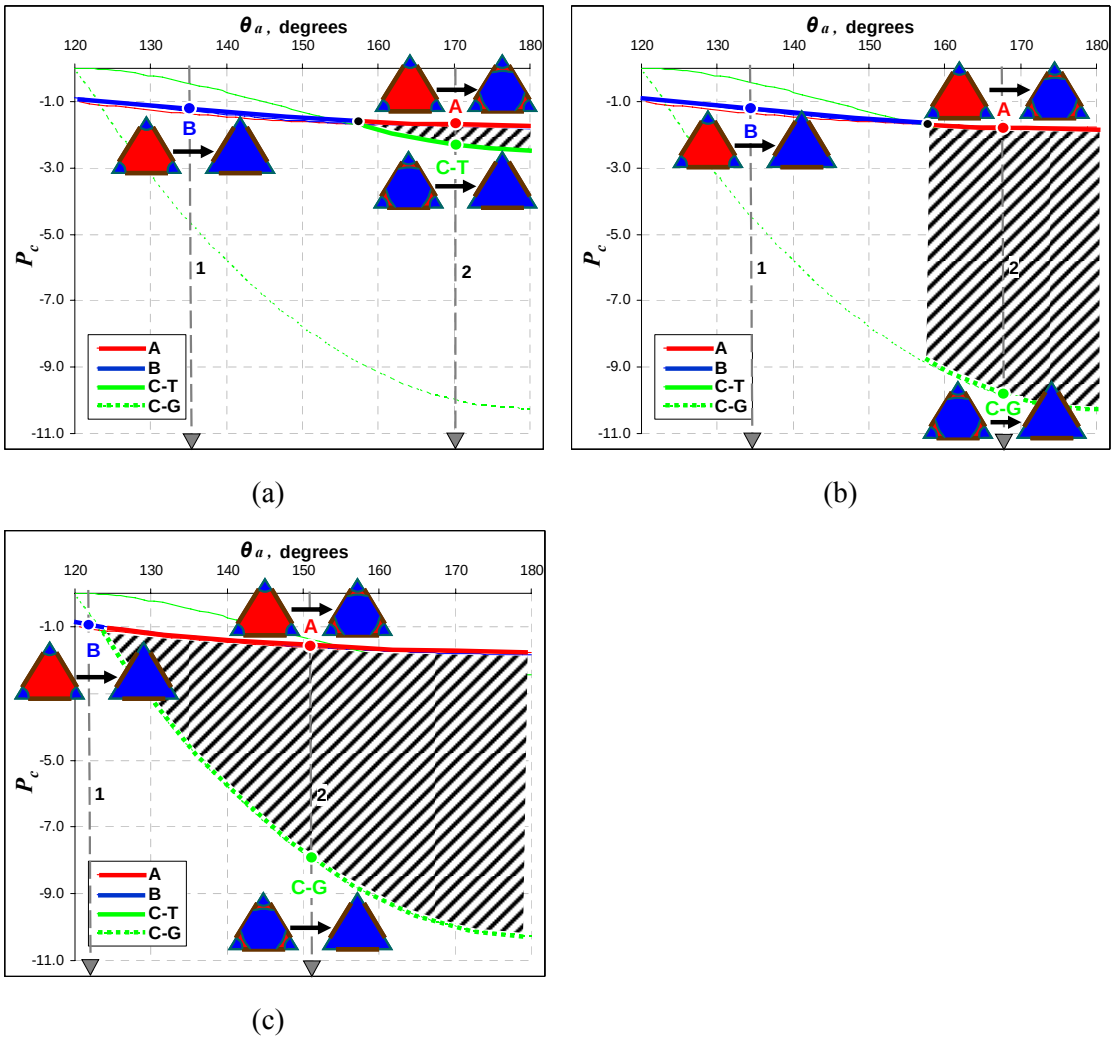

Figure 4.5 Dimensionless capillary entry pressures P_c versus advancing contact angle θ_a for the various displacements in an equilateral triangle, including layers formation and collapse scenarios: (a) *Therm*, (b) *Geom2*, (c) *Geom*. Shaded regions indicate curvatures for which layers exist. Vertical dashed grey lines indicate water invasion scenarios, i.e. decreasing P_c, for different advancing contact angles, as described in the text.

Geom2 sub-scenario (**Figure 4.5b**): We calculate entry pressures for displacements *A, C-G* and *B*. If $P^{A}_{entry} > P^{C-G}_{entry}$ and $P^{A}_{entry} > P^{B}_{entry}$ then, like in the previous cases, *A* and *C-G* occur one after another (path 2), otherwise displacement *B* takes place (path 1). The *Geom2* sub-scenario has been described by Piri and Blunt (2004).

It may be clear from **Figure 4.5** that the range of contact angles for which layers can exist is strongly reduced in sub-scenarios *Geom2* and *Therm*, and that the range of $\boldsymbol{P_c}$ values for which layers exist according to *Therm* is much smaller compared to the ranges for *Geom* and *Geom2* (van Dijke and Sorbie 2006).

4.4 Secondary Drainage

After water invasion secondary oil drainage can be simulated. At the start of secondary drainage the apex distance L^{imb} for the AM2 position (such as L^{o} in **Figure 3.8**) is fixed as

$$L^{imb} = \frac{\sigma_{ow}\cos(\theta_a - \gamma)}{P_c^{\min}\sin\gamma}\ , \tag{4.24}$$

where $P_c^{\min}$ is the minimum capillary pressure reached during water invasion. This results in pinning of AM2 at position L^{imb} with the associated hinging contact angle. As the capillary pressure increases, the hinging contact angle decreases from θ_a towards the receding contact angle θ_r. A third AM, called AM3 may exist during secondary drainage, forming a water layer, sandwiched between the bulk oil in the centre and oil layers in the corners (see **Figure 4.1p**), but this is possible only if:

$$\theta_r < \frac{\pi}{2} - \gamma\,. \tag{4.25}$$

Additionally, 7 new fluid configurations may exist during secondary drainage (see **Figure 4.1m,n,o,p,q,r,s**). There are 16 possible displacements which could happen during this flood, as indicated in **Table 4.2**, in particular, an oil layer reformation *C1-Dr2* (**f→g**), a water layer formation *A-Dr2* (**g→p**) and a water layer collapse *C-Dr2* (**p→d**). The MS-P based entry radius solutions for secondary drainage displacements in equilateral triangles have been presented by Helland and Skjaeveland (2004, 2006a) and can be generalized to n-cornered star shapes. However, we do not describe them in detail here, since they can be derived from the previously described drainage and water

invasion displacement criteria (see **Table 4.2**). All possible displacement scenarios, which may happen during the secondary drainage, are shown in the flowcharts in **Figure 4.6** (part 1, $\theta_{pd} \geq \pi/2 - \gamma$) and **Figure 4.7** (part 2, $\theta_{pd} < \pi/2 - \gamma$).

4.5 Summary and Conclusions

In this chapter we have considered all possible fluid configurations and displacements that can occur during primary drainage, water invasion (after ageing) and secondary drainage. We presented corresponding entry pressure solutions for *Star* and *CTS* shapes. In particular, the existing solutions for the regular n-sided polygons and three-cornered stars have been generalized to n-cornered star shapes.

The main focus of this chapter was stability of oil layers that can exist in the corners of pores with non-uniform wettability caused by ageing. Recently, van Dijke and Sorbie (2006) derived a thermodynamically based criterion (*Therm*) for the existence of oil layers. This *Therm* criterion is consistent with the MS-P capillary entry pressures for water invasion displacements and it is more restrictive than the previously used geometrically based formation and collapse criterion (*Geom*). The *Geom* criterion was later adjusted as *Geom2* to make it more consistent with other water invasion entry pressures. *Geom2* is less restrictive than *Therm* but more restrictive than *Geom*.

In Chapters 6 and 7 all oil layers existence criteria (*Them, Geom, Geom2*) will be implemented in a two-phase network model. In Chapter 6 we will analyse the effect of the oil layers existence criterion on residual or remaining oil saturation and relative permeabilities for various wettability conditions (from water-wet to oil-wet). In Chapter 7 we will show the importance of the physically correct *Therm* criterion for prediction of oil-wet and mixed-wet experiments.

Table 4.2 Displacements which may occur during secondary oil drainage. See Sections 4.4 for details.

Displacement	Configuration before	Configuration after	Description	θ_{pd}			θ_a			θ_r			θ_h		L		Entry curvature iterative/ explicit
				$\theta_{pd} < \pi/2-\gamma$	$\pi/2-\gamma \le \theta_{pd} \le \pi/2+\gamma$	$\theta_{pd} > \pi/2+\gamma$	$\theta_a < \pi/2-\gamma$	$\pi/2-\gamma \le \theta_a \le \pi/2+\gamma$	$\theta_a > \pi/2+\gamma$	$\theta_r < \pi/2-\gamma$	$\pi/2-\gamma \le \theta_r \le \pi/2+\gamma$	$\theta_r > \pi/2+\gamma$	$\theta_h \le \theta_r$	$\theta_h > \theta_r$	$L = L^{dr} / L = L^{imb}$	$L > L^{dr} / L > L^{imb}$	
A-Dr2	**g**	**p**	piston-like with water sandwiched layers formation	✓					✓	✓							$F_{entry}^{A-Dr}\left(\theta_r,\gamma,n\right)$, explicit
A1-Dr2	**f**	**e**	piston-like with pinned water corner films formation	✓			✓	✓	✓	✓	✓	✓	✓		✓		$F_{entry}^{B-\mathrm{Imb}}\left(L^{dr},\theta_r,\gamma,n\right)$, iterative
A2-Dr2	**f**	**h**	piston-like with water corner films formation (AM3 moving with θ_r)	✓			✓	✓	✓	✓				✓		✓	$F_{entry}^{A-Dr}\left(\theta_r,\gamma,n\right)$, explicit
A3-Dr2	**a**	**c**	piston-like with water corner films formation	✓													$F_{entry}^{A-Dr}\left(\theta_{pd},\gamma,n\right)$, explicit
B-Dr2	**g**	**e**	piston-like with sandwiched oil layers before (AM2 pinned)	✓					✓	✓	✓	✓		✓	✓		$-F_{entry}^{B-\mathrm{Imb}}\left(L^{\mathrm{Im}b},\pi-\theta_r,\gamma,n\right)$, iterative
B1-Dr2	**q**	**e**	piston-like with oil sandwiched layers before (AM2 moving with θ_r)	✓					✓			✓	✓			✓	$-F_{entry}^{A-Dr}\left(\pi-\theta_r,\gamma,n\right)$, explicit
B2-Dr2	**k**	**j**	piston-like with oil pinned corner films before (AM2 pinned)		✓	✓			✓		✓	✓		✓	✓		$-F_{entry}^{B-\mathrm{Imb}}\left(L^{\mathrm{Im}b},\pi-\theta_r,\gamma,n\right)$, iterative
B3-Dr2	**n**	**j**	piston-like with oil corner films before, moving with θ_r (AM2 moving with θ_r)		✓	✓			✓			✓	✓			✓	$-F_{entry}^{A-Dr}\left(\pi-\theta_r,\gamma,n\right)$, explicit
B4-Dr2	**l**	**j**	piston-like without oil corner films		✓			✓			✓						$F_{entry}^{B-Dr}\left(\theta_r,\gamma,n\right)$, explicit
B5-Dr2	**a**	**b**	piston-like without water corner films formation		✓	✓											$F_{entry}^{B-Dr}\left(\theta_{pd},\gamma,n\right)$, explicit

Table 4.2 Displacements which may occur during secondary oil drainage. See Sections 4.4 for details.

Displacement	Configuration before	Configuration after	Description	θ_{pd}			θ_a			θ_r			θ_h		L		Entry curvature iterative/ explicit
				$\theta_{pd} < \pi/2-\gamma$	$\pi/2-\gamma \le \theta_{pd} \le \pi/2+\gamma$	$\theta_{pd} > \pi/2+\gamma$	$\theta_a < \pi/2-\gamma$	$\pi/2-\gamma \le \theta_a \le \pi/2+\gamma$	$\theta_a > \pi/2+\gamma$	$\theta_r < \pi/2-\gamma$	$\pi/2-\gamma \le \theta_r \le \pi/2+\gamma$	$\theta_r > \pi/2+\gamma$	$\theta_h \le \theta_r$	$\theta_h > \theta_r$	$L = L^{dr} / L = L^{imb}$	$L > L^{dr} / L > L^{imb}$	
C-T/G-Dr2	**p**	**d**	sandwiched water layers collapse (thermodynamical/ geometrical criteria)	✓					✓	✓							$-F_{entry}^{C-\text{Imb-T/G}}\left(L^{\text{Im}b}, \pi-\theta_r, \gamma, n\right)$, iterative
C1-T/G-Dr2	**f**	**g**	oil layers reformation (AM1 pinned, AM2 moving with θ_r)	✓					✓			✓					$F_{entry}^{C-\text{Imb-T/G}}\left(L^{dr}, \theta_r, \gamma, n\right)$, iterative
D-Dr2	**s**	**d**	snap-off (forced) with oil sandwiched layers before (AM2 hinging until θ_r)	✓					✓	✓	✓	✓					$-F_{entry}^{D-\text{Im}b}\left(L^{imb}, \pi-\theta_r, \gamma, n\right)$, explicit
D1-Dr2	**r**	**l**	snap-off (spontaneous) with oil sandwiched layers before (AM1 pinned, AM2 moving with θ_r)	✓					✓			✓					$-F_{entry}^{D1-\text{Im}b}\left(\pi-\theta_r, \gamma, n\right)$, explicit
D2-Dr2	**m**	**d**	snap-off (forced) with oil corner films before (AM2 hinging until θ_r)		✓				✓		✓						$-F_{entry}^{D-\text{Im}b}\left(L^{imb}, \pi-\theta_r, \gamma, n\right)$, explicit
D3-Dr2	**o**	**l**	snap-off (spontaneous) with oil corner films before (AM2 moving with θ_r)		✓	✓			✓			✓					$-F_{entry}^{D1-\text{Im}b}\left(\pi-\theta_r, \gamma, n\right)$, explicit

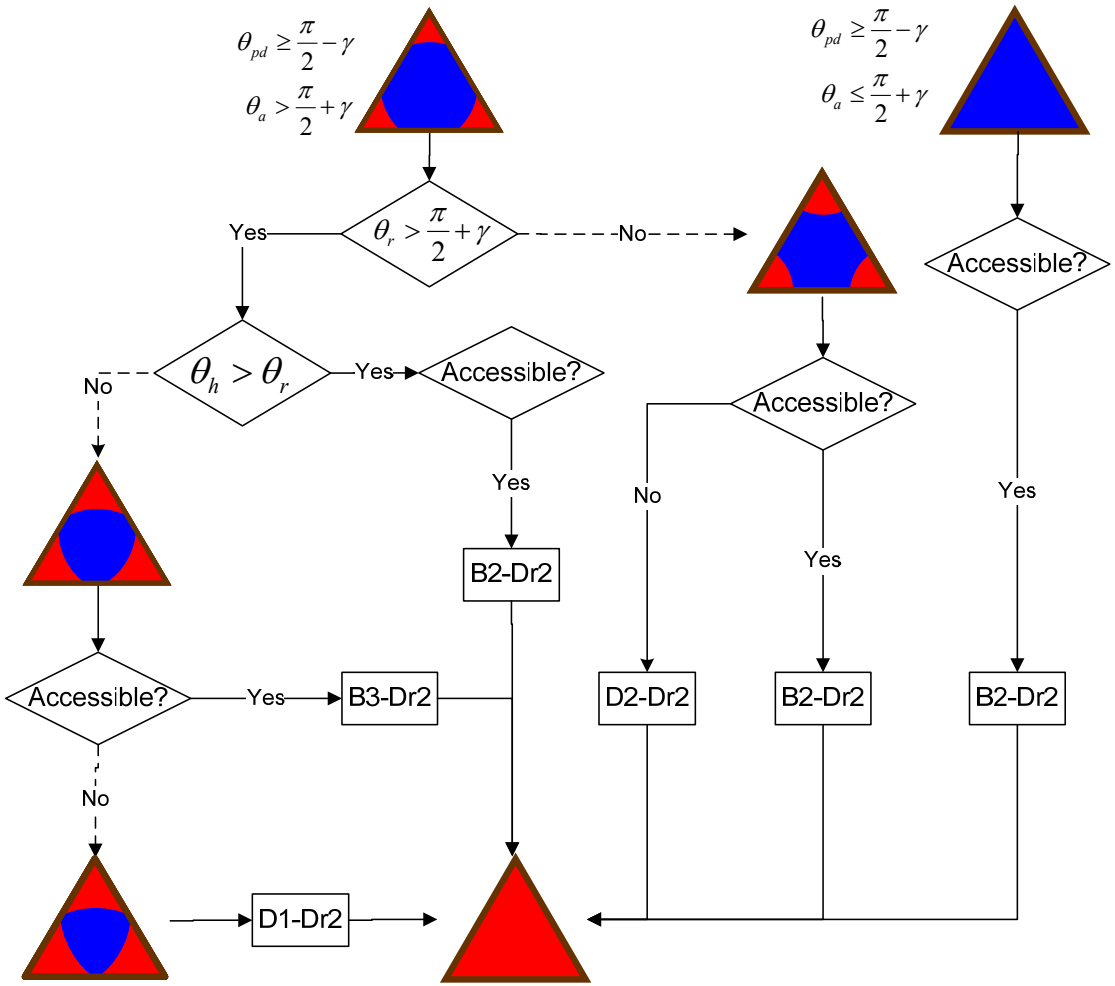

Figure 4.6 Flowchart of possible displacement scenarios during secondary drainage (part 1) for the *n*-cornered star. Note, that for each displacement the defending phase should be connected to the outlet by means of continuous defending cluster.

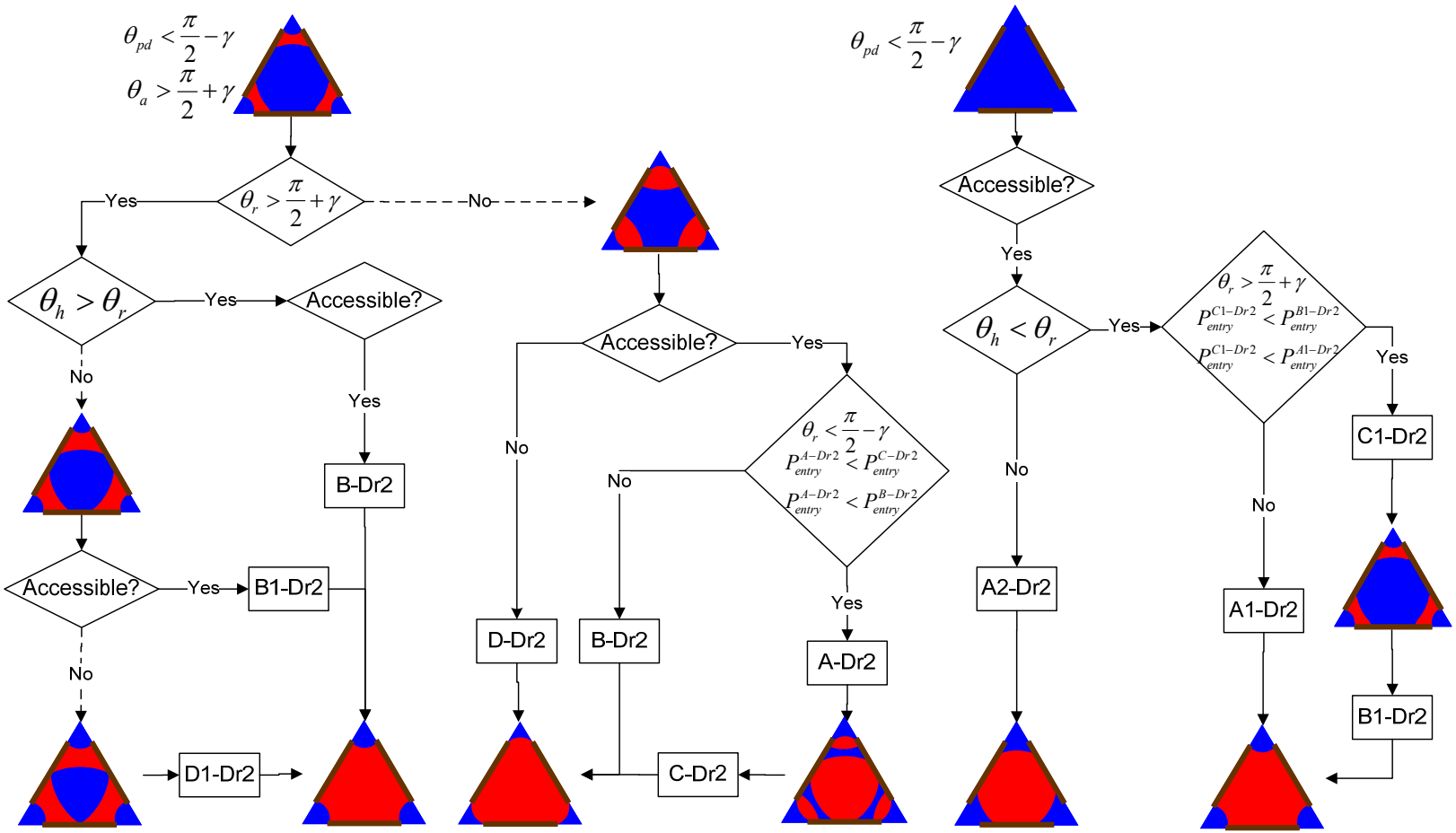

Figure 4.7 Flowchart of possible displacement scenarios during secondary drainage (part 2) for the *n*-cornered star. Note, that for each displacement the defending phase should be connected to the outlet by means of continuous defending cluster

CHAPTER 5 - ACCURACY OF PORE SHAPES CHARACTERIZATION

5.1 Introduction

Previously, we have considered two pore shape approximations: the most commonly used Circle, Triangle, Square (CTS; Section 3.4.1) and the newly introduced Star (Section 3.4.2). To test the accuracy of the pore shape characterizations (Star and CTS), we will consider 70 real pore cross-sections extracted from high-resolution 2D images of a Bentheimer rock sample and for each real pore derive shape representations using both approximations. Then, the approximation error of various resulting pore flow parameters (as described in Chapters 3 and 4) will be calculated for each pore. Finally, a capillary bundle model will be constructed from the 70 pores and the predictive capabilities of the characterizations will be investigated in terms of its relative permeabilities and capillary pressure.

5.2 Single Phase Conductance

The expressions (correlations) for single phase conductance have been presented for the CTS approximation in Section 3.4.1 and for the Star approximation in Section 3.4.2.

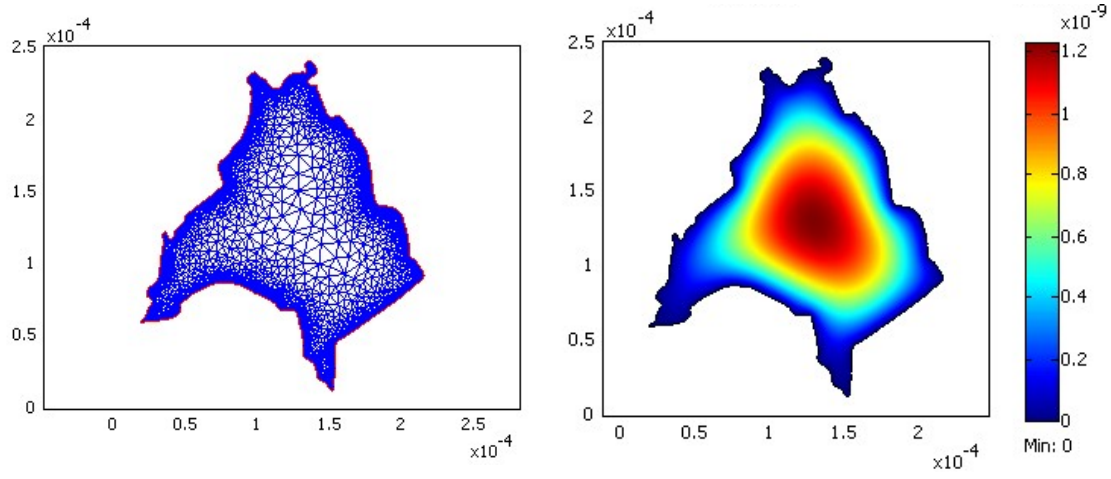

(a) **(b)**

Figure 5.1 Mesh (a) and corresponding "reduced" velocity field (b) calculated by FEM (MATLAB PDE toolbox) for one of the real shapes

Similar to numerical calculations for the Star conductance (Section 3.4.2), we solve the elliptic Poisson equation for the "reduced" velocity for single-phase flow in a given arbitrary cross-section Eq. (3.11). Again, we apply no-slip boundary conditions and use

FEM (MATLAB PDE toolbox) (**Figure 5.1**). Then, the real pore conductane is calculated by averaging the "reduced" velocity over the pore cross-section and multiplying by the cross-sectional area (Eq. (3.12)).

5.3 Capillary Entry Pressure

The most important parameter in multi-phase flow network simulation is the capillary entry pressure. Here, we focus on the two-phase capillary entry pressure in straight uniformly wetted tubes, such as the oil-water entry pressure during primary oil drainage.

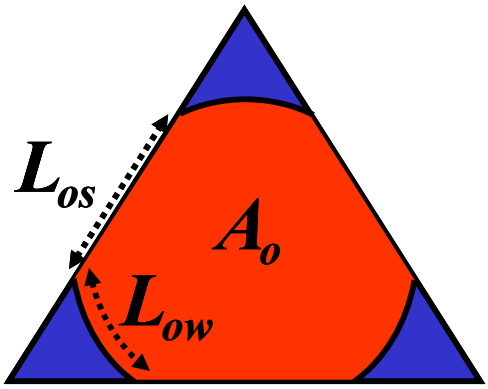

Figure 5.2 Fluid configuration with oil in the centre and water in the corners after piston-like displacement of water by oil. A_o is the cross-sectional area invaded by oil, L_{os} and L_{ow} are the cross-sectional lengths of the oil-solid boundary and the oil-water arc menisci respectively

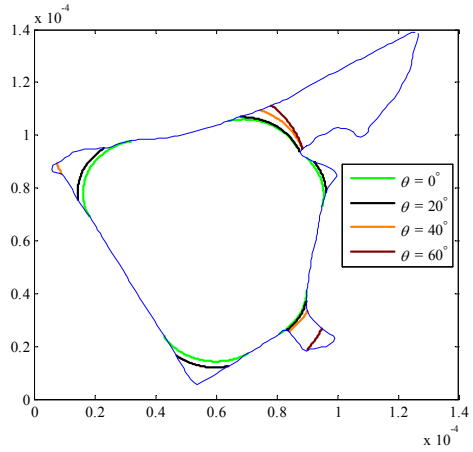

Figure 5.3 Entry pressure configurations in a Bentheimer sandstone pore plotted for different contact angles (Helland et al. 2008)

5.3.1 Capillary Entry Pressure for Arbitrary Shapes

To calculate the capillary entry pressure for piston-like displacement in arbitrary pore shapes, a new semi-analytical approach has been applied (Helland et al. 2008, Frette and Helland 2010, Helland and Frette 2010). This approach is based on the MS-P energy balance equation (Mayer and Stowe 1965, Princen 1969a, b, 1970) written as

$$R \equiv F(R) = \frac{A_o(R)}{L_{os}(R)\cos\theta + L_{ow}(R)}, \tag{5.1}$$

which is valid for oil invasion into a completely water filled capillary. In Eq.(5.1), A_o denotes the cross-sectional area invaded by oil, while L_{os} and L_{ow} denote the cross-sectional lengths of the oil-solid boundary and the oil-water arc menisci (AMs), respectively (shown for a triangular pore in **Figure 5.2**). The relevant solution for R of

equation (5.1) is indeed the entry radius R_{entry}. The entry radius R_{entry} is related to the capillary entry pressure through Eq. (4.1).

The novel algorithm (Helland et al. 2008, Frette and Helland 2010, Helland and Frette 2010) requires a two-dimensional binary image representation of the pore cross-section as input. The individual pores used in this work have been extracted by Helland et al. (2008) from high-resolution images of Bentheimer rock samples taken by SEM (scanning electron microscopy) (Hildebrand-Habel et al. 2007). According to this algorithm, the pore boundary is identified and smoothed by the least-squares method. It allows calculating the entry pressure for arbitrary non-zero contact angles. A similar algorithm was previously developed by Lindquist (2006), but this required a polygonized boundary, and only results for zero contact angle were presented.

The algorithm (Helland et al. 2008, Helland and Frette 2010) is an iterative scheme to estimate R_{entry}. The first guess for R_{entry} may be the inscribed radius R_{ins}. During each iteration, with number *iter*, a circles with radius R_{iter} are moved along the pore boundary in both counter-clockwise and clockwise directions, such that their circular arcs intersect with the pore wall under the given contact angle θ at every boundary point. The trajectories of the circle centres define two "drainage curves" (Lindquist 2006). The set of points where the two "drainage curves" intersect, are identified as the locations of the centres of the AMs in the pore corners (see **Figure 3.8**) with radii R_{iter}. Using R_{iter} the lengths L_{ow}, L_{os} and area A_o are determined, similar to those for an angular pore, shown in **Figure 5.2**. Then the MS-P function Eq.(5.1) is used to estimate the radius for the next iteration R_{iter+1}:

$$R_{iter+1} = F(R_{iter}) \tag{5.2}$$

The iterative scheme continues until convergence, which is usually obtained in less than 10 iterations. **Figure 5.3** shows an example of entry configurations (cross-sections of fluid configurations with AM radii that satisfy the capillary entry pressure) obtained by our algorithm for different contact angles in one of the Bentheimer pore cross-sections (Helland et al. 2008). A more detailed algorithm description can be found in (Helland et al. 2008, Frette and Helland 2010, Helland and Frette 2010).

5.3.2 Capillary Entry Pressures for CTS Shapes

For the circular cross-section the entry pressure is given by the Young-Laplace equation as shown in Section 4.1 (Eq. (4.3)).

The entry pressure for the arbitrary triangle is given by (Øren et al. 1998, Patzek 2001, Valvatne and Blunt 2004)

$$R_{entry} = \frac{R_{ins}}{2\cos\theta_{pd}\left(1+2\sqrt{\pi G}\right)}\frac{1}{F_d\left(\theta_{pd},G\right)} \tag{5.3}$$

where F_d denotes the dimensionless correction factor for wetting fluid that might be retained in the corners as wetting films. For the strongly water-wet case ($\theta_{pd}=0^o$) F_d is equal to 1. In the absence of corner wetting films (for sufficiently large contact angles) Eq.(5.3) will simplify to Eq. (4.3).

The square is the limiting case of the 4-cornered star when $\gamma = \pi/4$, hence its entry pressure follows from the generalized MS-P entry pressure formula for the regular *n*-cornered star in the next section.

5.3.3 Capillary Entry Pressure for n-cornered Star Shapes

For the regular *n*-cornered stars the entry pressure can be derived from MS-P theory in terms of the entry radius of curvature R_{entry}, as a function of (n, γ), as shown in Section

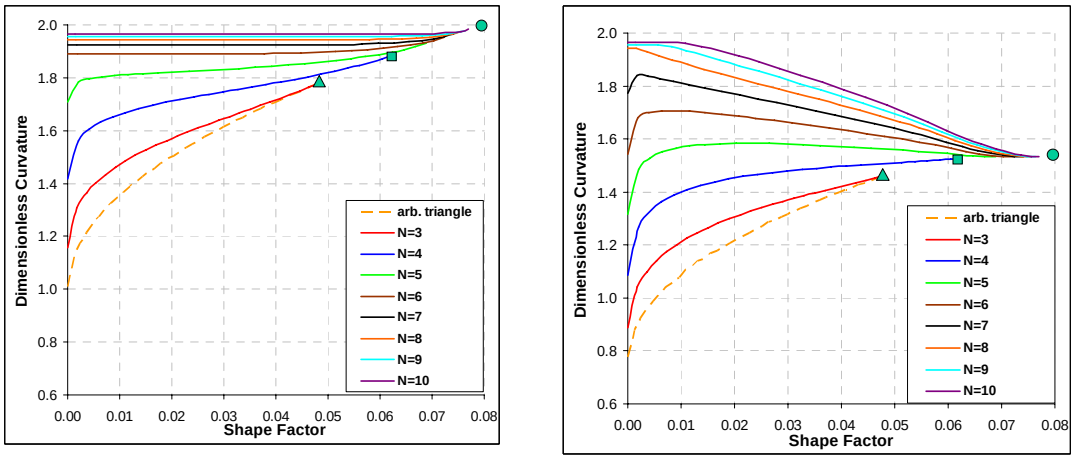

Figure 5.4 Dimensionless entry curvature versus shape factor for n-cornered stars and arbitrary triangles with (a) 0° and (b) 40° contact angle

4.2.2 (Eq. (4.7)).

Figure 5.4 shows the dimensionless entry curvature (R_{ins}/R_{entry}) as a function of the shape factor for n-cornered stars and arbitrary triangles with 0^o (**Figure 5.4a**) and 40^o (**Figure 5.4b**) contact angles. For the same shape factor, the difference between the n-cornered star and arbitrary triangle increases with the number of corners n. Moreover, for the same number of corners, this difference increases as the shape factor decreases.

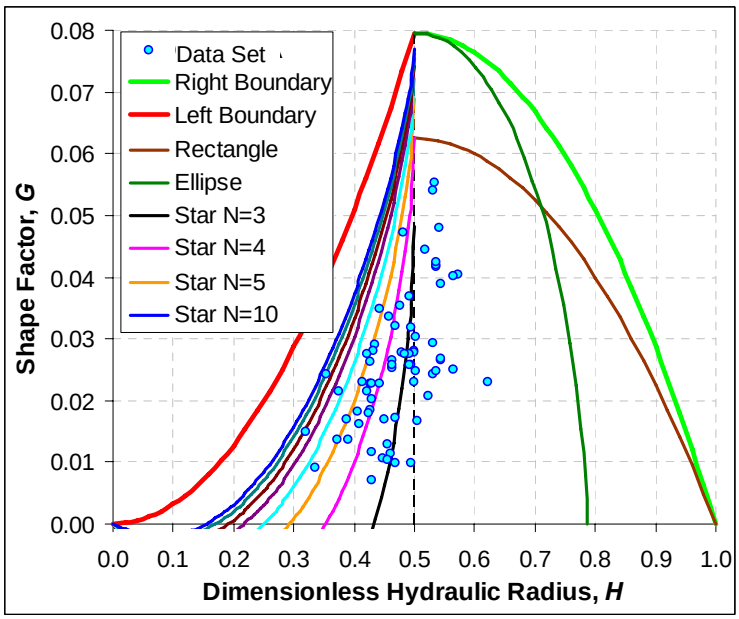

Figure 5.5 Shape factor G against dimensionless hydraulic radius H for 70 real shapes extracted from a 2D Bentheimer SEM image. At least the 70% of shapes that have $H<0.5$ are non-convex.

5.4 Results and Discussion

A set of 70 pore cross-sections was extracted from the 2D SEM image of Bentheimer sandstone. From **Figure 5.5** it can be clearly seen that 70% of real pores have dimensionless hydraulic radii H less than 0.5 and at least these pores are non-convex. For these real shapes the entry radii R_{entry} (for 0^o and 40^o contact angles) were calculated using the newly developed numerical method described above (Helland et al. 2008, Helland and Frette 2010). Single-phase hydraulic conductances g were calculated using the FEM method in the MATLAB PDE toolbox. The real shapes were approximated using both the CTS and the Star approaches, based on the shape factor $G=A/P^2$ and dimensionless hydraulic radius $H=(A/P)/R_{ins}$, as explained in Section 3.4. Entry pressures (for both 0^o and 40^o contact angles) and conductances for these approximations were calculated as described above.

5.4.1 Single Pore Approximations

Figure 5.6 and **Figure 5.7** show two real shapes and the corresponding shape approximations by both CTS and Star, as well as the relative errors that the respective approximations introduce for the parameters area, perimeter, hydraulic radius R_h, conductance, entry radius R_{entry} (for 0^o and 40^o contact angles). For these examples, the predictions made by the *n*-cornered star are much more accurate than those by CTS (arbitrary triangle), especially for area and conductance. Note that these 2D cross-sectional shapes (**Figure 5.6** and **Figure 5.7**) could be the cross-sections of multiple pores since they may not have been taken perpendicular to medial axis.

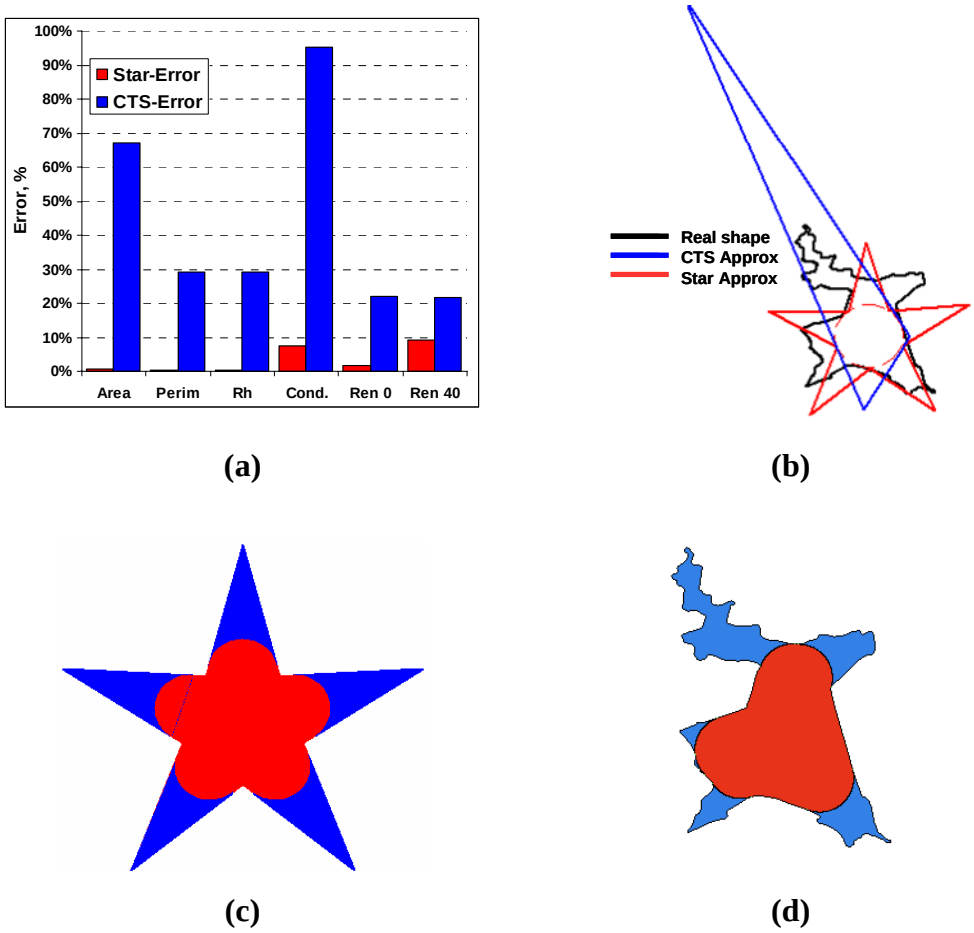

Figure 5.6 (a) Errors of real pore shape parameter prediction by CTS and Star approximations; (b) real shape with CTS and Star shape boundaries; (c) phase occupancy after drainage for the Star shape approximation (0^o contact angle); (d) phase occupancy for real shape (0^o contact angle)

5.4.2 Set of Pores Approximations

The comparison between predicted and real shape parameters for the entire set of pores (entry radii for 0^o and 40^o degrees, hydraulic radius, conductance) is shown in **Figure 5.8**. From **Figure 5.8(a,b)** it can clearly be seen that the accuracy of the entry radius

prediction for both approaches is approximately the same and reasonably good. However, CTS tends to overestimate, while Star tends to underestimate the radii. Since Star approximates the area and perimeter with much more accuracy than CTS, the n-cornered star hydraulic radius shows better agreement with real shape data (**Figure 5.8c**). In addition, because the *n*-cornered star has a much more accurate shape boundary representation, the single phase conductance estimation is also much better (**Figure 5.8d**).

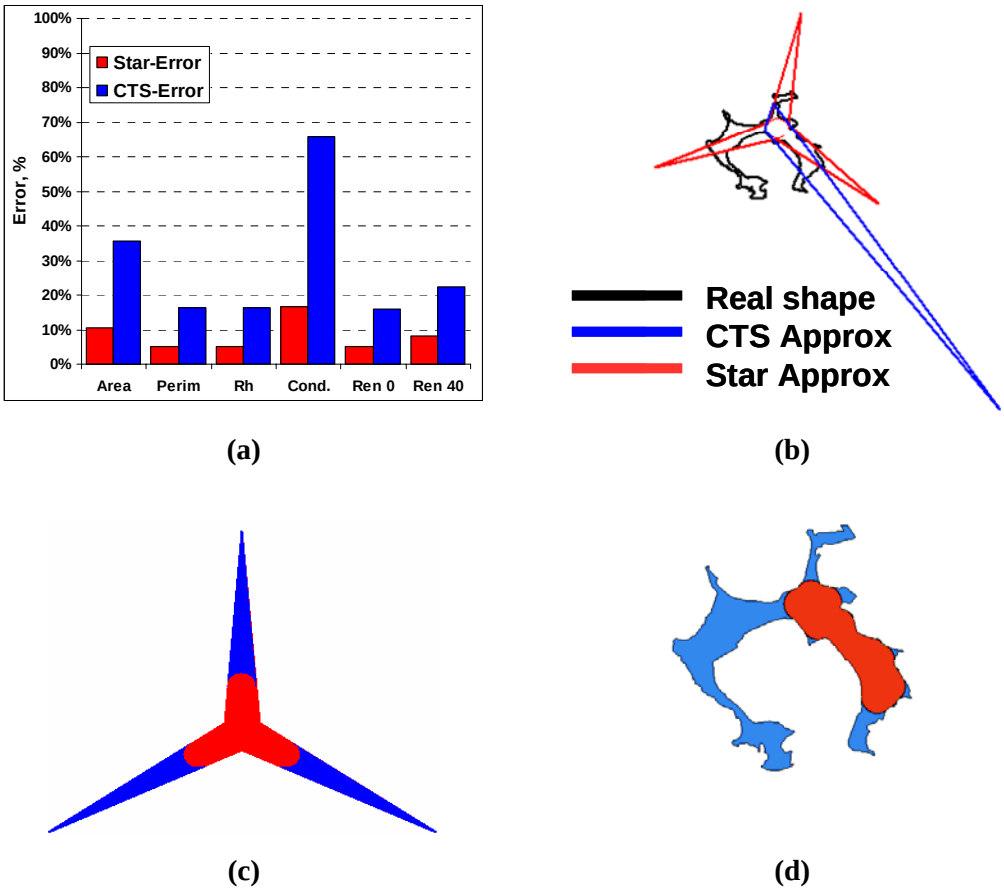

Figure 5.7 (a) Errors of real pore shape parameters prediction by CTS and Star approximations; (b) real shape, CTS and Star shape boundaries; (c) phase occupancy for Star shape approx.(0^o cont. angle); (d) phase occupancy for real shape (0^o cont. angle)

Observe that the larger errors in all approximations occur for the larger pores. The reason is that the shapes of larger pores are much more irregular, and often more non-convex, than those of the smaller pores. This, in turn, stems from the poorer X-Ray CT resolution of the smaller pores, which could not resolve all irregular features. In the latter case, the estimated dimensionless hydraulic radius *H* could be greater than 0.5 and hence the pore shape would be approximated by a convex arbitrary triangle or *n*-cornered regular polygon rather than by a non-convex *n*-cornered star.

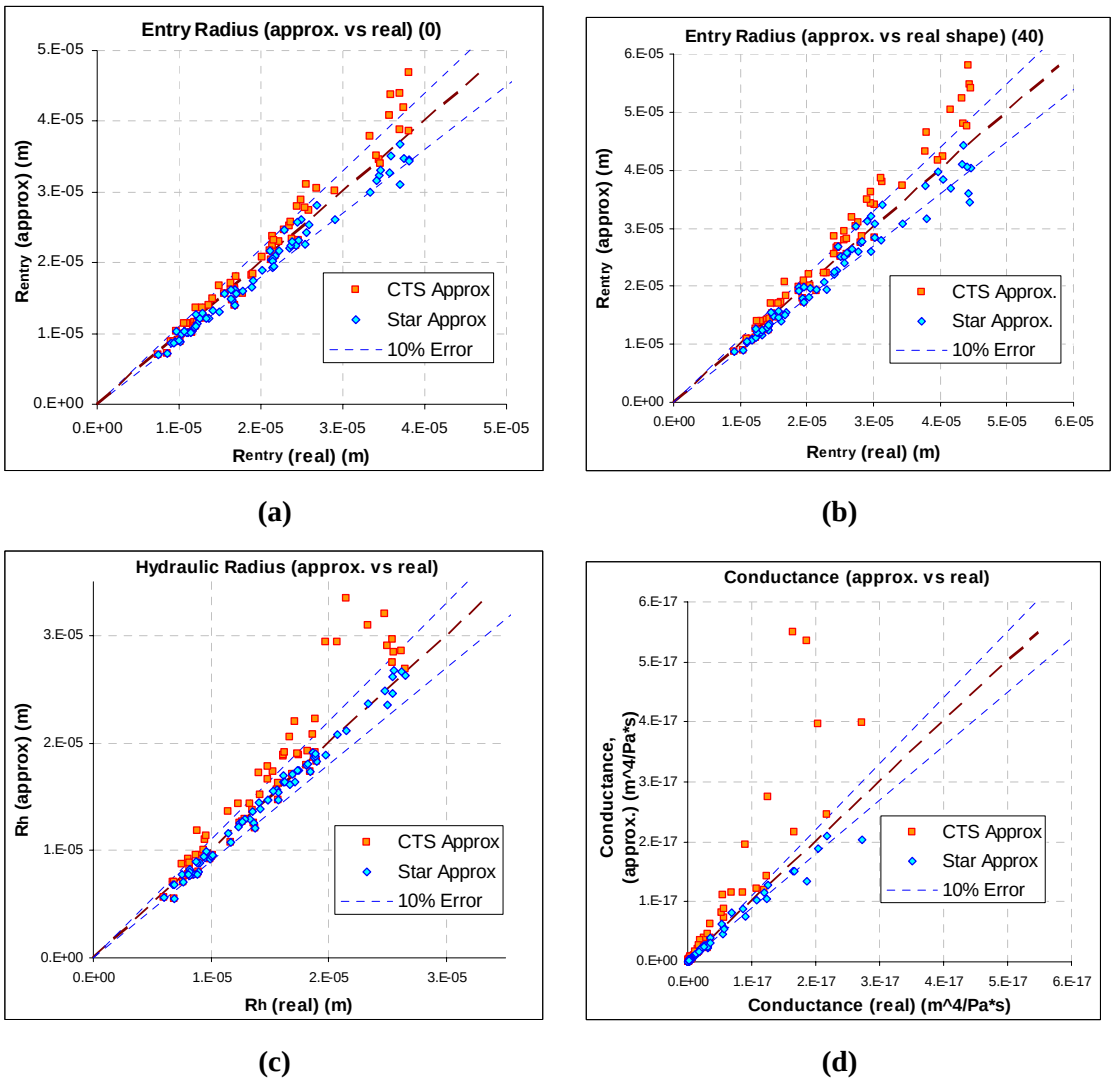

Figure 5.8 (a), (b) Cross plots for approximated and real shape entry radii for 0^o and 40^o contact angles respectively; (c) Cross plot for hydraulic radius between approximated and real shapes; (d) Cross plot for single-phase conductance between approximated and real shapes.

In the following, we investigate the relationship between the entry radius R_{entry} and the hydraulic radius R_h or the dimensionless hydraulic radius $H = R_h/R_{ins}$. Lindquist (2006) showed that for regular n-sided polygons R_h is a good predictor of R_{entry} for contact angles less than 10^o and the ratio R_h/R_{entry} lies between 0.88 and 1.0. Lindquist also showed results of entry radius calculations for 21,500 polygonal real pore shapes deducted from CT images and he demonstrated that R_h is also a good approximation of the entry radii of real shapes for 0^o contact angle (average value for ratio R_h/R_{entry} was 0.96±0.03). He also commented on the fact that his shapes were not very non-convex, in other words, the corresponding H values were generally not much smaller than 0.5.

Obviously, for non-zero contact angles the R_h should be compared against the entry radius corrected for the contact angle θ, i.e. $R_{entry}cos\theta$.

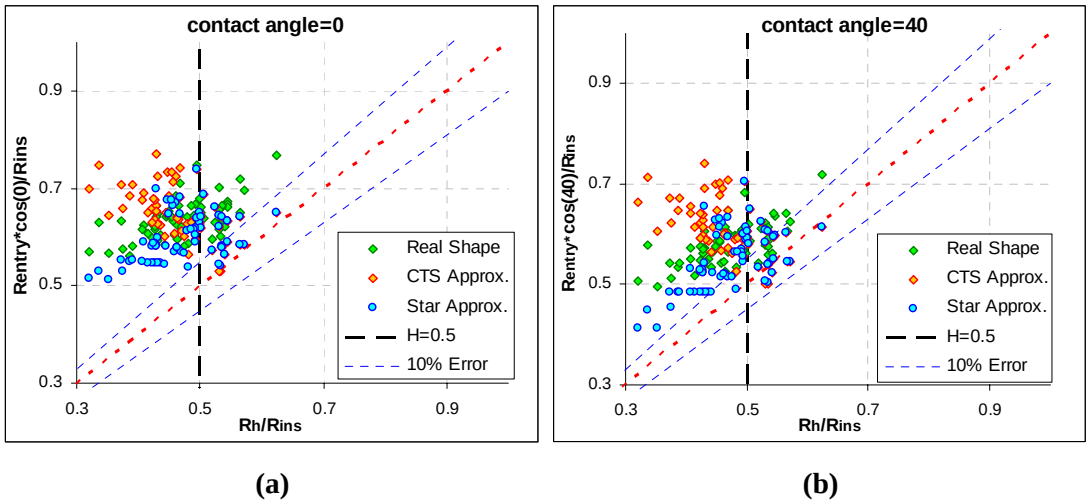

(a) **(b)**

Figure 5.9 (a),(b)– Dimensionless entry radius $R_{entry}\cos(\theta)/R_{ins}$ versus dimensionless real shape hydraulic radius $H=R_h/R_{ins}$ correspondingly for 0^o and 40^o contact angles.

Figure 5.9 shows a comparison of the dimensionless (contact angle corrected) entry radii $R_{entry}\cos(\theta)/R_{ins}$ versus dimensionless hydraulic radii $H=R_h/R_{ins}$ of the real shapes. The real shape entry radii deviate significantly from the hydraulic radii, in particular for small values of H, i.e. for very non-convex shapes. We have H <0.5 in 70 % of our 70 pore shapes. For the 40^o degree contact angle (**Figure 5.9b**) the deviations tend to be slightly smaller than for the 0^o degree angle (**Figure 5.9a**). Observe also that the n-cornered star entry radii quite closely follow the real shape entry radii, but that the CTS approximation is poor for the very non-convex shapes with H<0.5, which indeed arise for the larger pores, as observed above.

5.4.3 Capillary Bundle Simulations

To test the predictive capabilities of the approximated shapes by CTS and Star we have constructed a capillary bundle model from the 70 Bentheimer pores assuming each individual pore has a constant and uniform cross-section along its axis. However, it is quite clear, that the true 3D shape of the single pore is much more complex than just a cylinder and could have a varying cross-section along its axis. We simulated primary drainage capillary pressure and relative permeabilities for the two contact angle values 0^o and 40^o. Two types of calculation have been done, i.e. with and without taking into

account corner wetting films for both volume and conductance calculations. The latter had to be assumed because for the real shapes accurate film areas were not available.

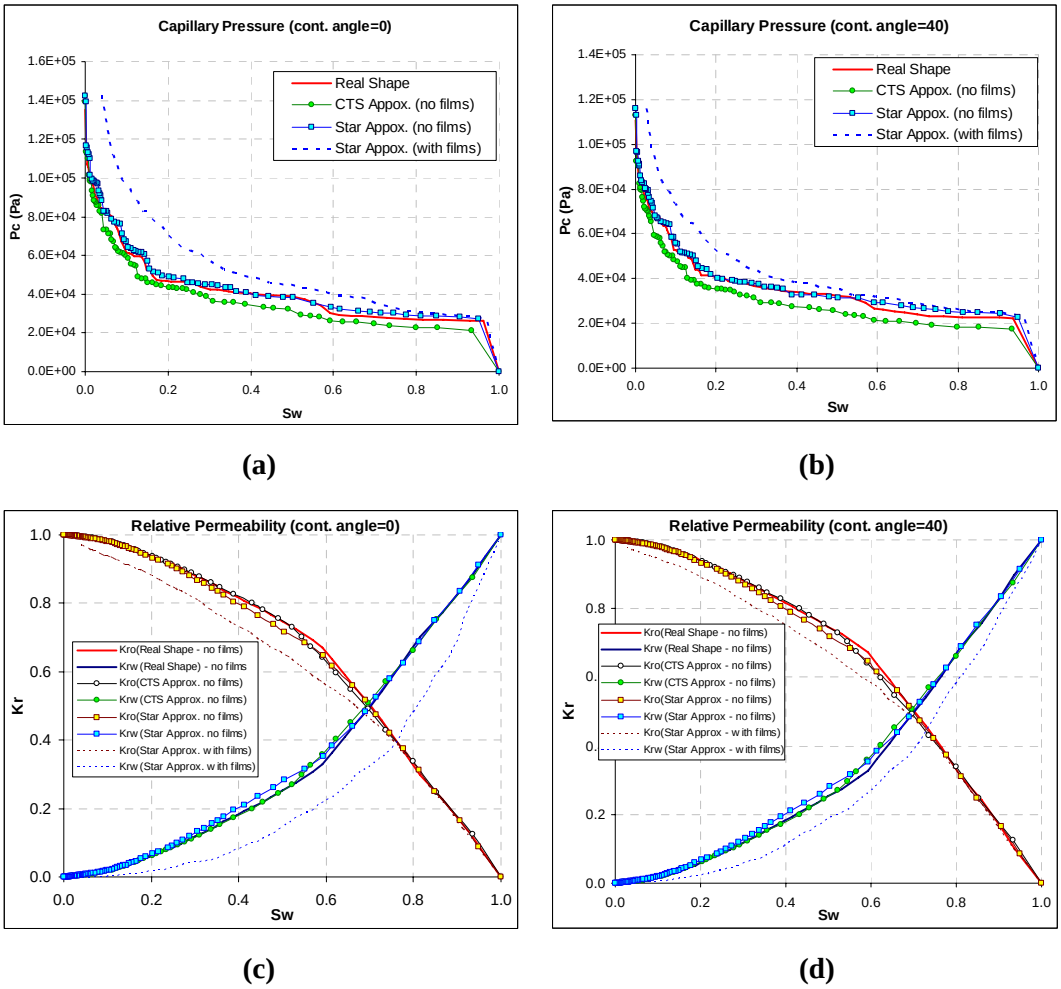

Figure 5.10 Capillary pressure and relative permeabilities curves from the capillary bundle model for real shape parameters, as well as for CTS and Star approximations for (a), (c) 0^o contact angle and (b), (d) 40^o contact angle.

Figure 5.10a,b show that Star provides a very good approximation of the real shape capillary pressure curve, while CTS gives a significant underprediction. Given that both entry radii approximations were reasonable good (**Figure 5.8a,b**), the underprediction probably follows from poor prediction of the areas, hence the saturations, for the CTS approach. On the other hand, **Figure 5.10c,d** show very good approximations of the relative permeability curves using both shape representations, despite the poor conductance approximation using CTS (**Figure 5.8d**). Note, that the corner wetting films have a significant effect on both capillary pressure and relative permeability curves and cannot be ignored, especially for small contact angles.

5.5 Summary and Conclusions

Comparison between predicted and real shape parameters has shown that:

- In general, the predictions made by the Star pore model are more accurate than those by CTS, especially for pore area and conductance
- Larger errors occurred in all approximations for the larger pores, as these had more irregular and non-convex shapes.

Comparison of the dimensionless (contact angle corrected) entry radii versus dimensionless hydraulic radii of the real shapes has shown that:

- The real shape entry radii deviate significantly from the hydraulic radii for very non-convex shapes
- The Star entry radii follow the real shape entry radii quite closely, but the CTS approximation is poor for the very non-convex shapes.

Using the real shapes as well as their approximations in a capillary bundle model has shown that:

- The n-cornered star provides a very good approximation of the real shape capillary pressure curve, while CTS gives a significant underprediction, which follows from poor prediction of the areas.
- Very good approximations of the relative permeability curves were obtained using both approximations despite the poor conductance approximation by CTS.
- Corner wetting films have a significant effect on both capillary pressure and relative permeability curves, especially for small contact angles.

In the following chapters we will show results using our two-phase pore network model with the two shape characterizations: CTS and Star. In Chapter 6 the effect of pore shape characterization on residual oil saturation and water invasion relative permeabilities will be investigated. In Chapter 7, to compare the predictive capabilities of CTS and Star in a pore-scale network model, we will predict experimental relative permeabilities for a water-wet Berea sandstone using both approximations.

CHAPTER 6 - SENSITIVITY STUDIES

6.1 Introduction

In this chapter we perform a wide range of network model sensitivity calculations of water invasion residual oil saturation S_{or} to various fractionally-wet wettability conditions and we also analyze the effect of pore shape characterization on S_{or}. For simulations on two Berea networks with different wettability conditions we compare S_{or} following the *Therm* oil layer existence scenario with those following the two other scenarios. Sensitivity results of remaining oil saturation and statistics of pore-scale displacements are analysed with respect to varying end-point capillary pressure. Additionally, we examine the sensitivity of relative permeability to average advancing contact angle and to fraction of oil-wet pores. We also investigate the effect of oil layer existence scenarios and pore shape characterization on the relative permeability curves.

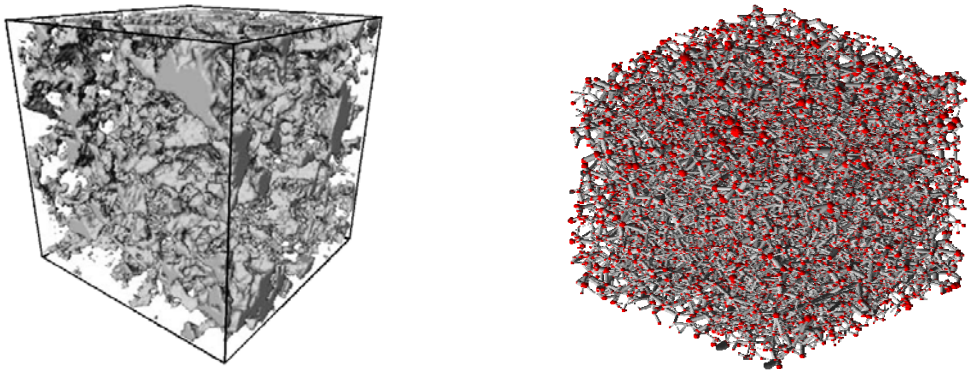

(a) **(b)**

Figure 6.1 (a) Pore space reconstructed by process-based approach for a Berea sandstone sample; (b) network extracted from the process-based reconstructed Berea sandstone sample (BereaPB) (Øren and Bakke 2003).

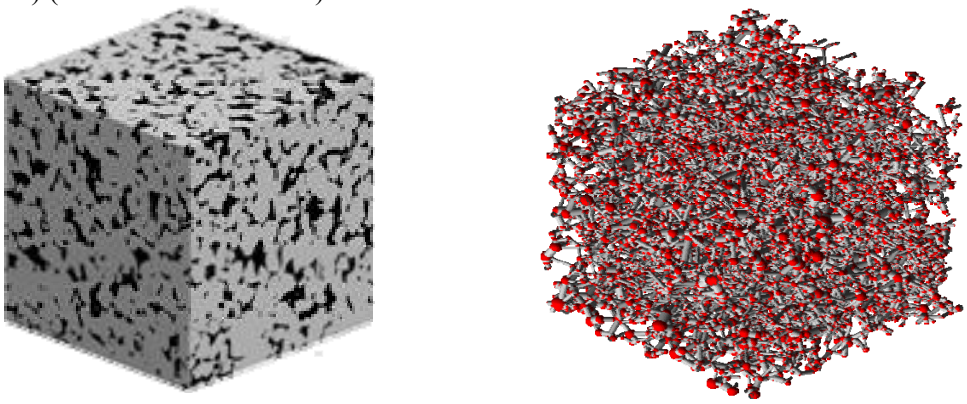

(a) **(b)**

Figure 6.2 (a) 3D CT image of a Berea sandstone sample (Dong and Blunt 2009b); (b) network extracted from the 3D CT image of the Berea sandstone sample (BereaCT) (Jiang et al. 2007).

6.2 Berea Networks

Two networks have been used for the network modeling sensitivity calculations and for predicting experimental data (Chapter 7): Model *BereaPB*, was extracted from a process based reconstruction of Berea sandstone (Øren and Bakke 2003), and Model *BereaCT*, was extracted, using the enhanced extraction technique of Jiang et al. (2007), from a Berea sandstone CT-image, which was imaged at Imperial College by a phoenix v|tome|x micro-CT system (Dong and Blunt 2009b). The pore space images and the corresponding extracted networks are shown in **Figure 6.1** and **Figure 6.2**. The main parameters of the networks are given in **Table 6.1**. Notice that the two networks have quite different coordination numbers, which may be due to different methods of obtaining the digital pore space and different extraction techniques. Porosity and absolute permeability have been calculated based on the procedures described in Section 3.7.

Table 6.1 Network parameters - Models *BereaPB* and *BereaCT*

	BereaPB	*BereaCT*	
Shape characterization	*CTS*	*STAR*	*CTS*
Circle (%)	1.2	0.4	1.1
Arb. Triangle (%)	92.3	22.8	71.8
Square (%)	6.5	0.5	27.1
n-Star (%)	0.0	76.3	0.0
Number of Voxels	300^3	400^3	
Resolution, μm	10	5.345	
Number of nodes	12349	7776	
Number of bonds	26146	14475	
Coordination number	4.195	3.69	
Permeability, mD	2668.33	1595.18	1699.26
Net Porosity, %	18.30	18.98	
Clay Porosity, %	5.7	0.0	
Size, x/y/z (mm)	3.00	2.14	
Volume (mm^3)	27.00	9.77	

The total porosity φ_{tot} is the sum of net porosity φ_{net} and clay porosity $\varphi_{cl,}$, which is effectively pore volume occupied by water that cannot be displaced. Note that unlike *BereaCT*, *BereaPB* has a clay bound porosity of φ_{cl}=5.7%. The clay volume for *BereaPB* has been distributed during the process-based reconstruction approach, whereas *BereaCT* was extracted from a micro CT-image which did not have any clay

amount information. However, to get a realistic connate water saturation S_{wc}^{targ} we can introduce the clay bound porosity φ_{cl} for *BereaCT* by adding extra pore volume (as a fraction α_{cl} of its original pore volume) to the network and distribute it among the pore elements:

$$\alpha_{cl} = \frac{\varphi_{cl}}{\varphi_{net}},\ \varphi_{cl} = \frac{S_{wc}^{\text{targ}} - S_{wc}^{\text{int}}}{1 - S_{wc}^{\text{targ}}} \varphi_{net} \tag{6.1}$$

where φ_{net} is the net porosity, S_{wc}^{int} is the intrinsic connate water saturation in a network with zero clay porosity, which consists of trapped bulk water and water films.

For *BereaPB* pore shapes are represented by circles, (arbitrary) triangles and squares (*CTS*), while for *BereaCT* both the *CTS* and the *Star* approaches (Chapter 4) have been used. For *Star*, shapes are additionally represented by *n*-cornered regular stars, as explained in Section 3.4.2. As indicated by Piri and Blunt (2005a), for *CTS* most shapes are arbitrary triangles for both networks. For *Star* (only *BereaCT*) most shapes are *n*-cornered stars (76.3%), which are all non-convex, although a significant fraction of pores (22.8%) are still represented by arbitrary triangles.

6.3 Without Pore Bodies

For simplicity, in this section we first apply network modelling using only the *without PB* (without pore bodies) option (see definition in Section 3.1). The other option, with pore bodies (*with PB*), will be used in Section 6.4. Here *CTS* is applied for *BereaPB* and *Star* for *BereaCT*. For both networks zero clay porosity is specified and only intrinsic connate water S_{wc}^{int} is achieved during primary drainage, which is 0.0056 for *BereaCT* and 0.0025 for *BereaPB*.

To analyze the effect of layer displacements (*A*-formation and *C*-collapse) and the difference between the corresponding scenarios (*Therm*, *Geom* and *Geom2*) on residual oil saturation, we consider a series of different wettability distributions after ageing. During drainage the network is assumed to be water-wet with drainage contact angle θ_{pd} uniformly distributed between 0^{o} and 60^{o}. The contact angles of the oil-contacted parts of the oil-filled bonds are taken according to a uniform oil-wet distribution (UOW) with nine ranges of advancing contact angles

$$\theta_a \in \left[\theta_a^i - 5^o, \theta_a^i + 5^o\right],\ \theta_a^i = 95^o + 10^o\left(i-1\right),\ i = 1..9. \tag{6.2}$$

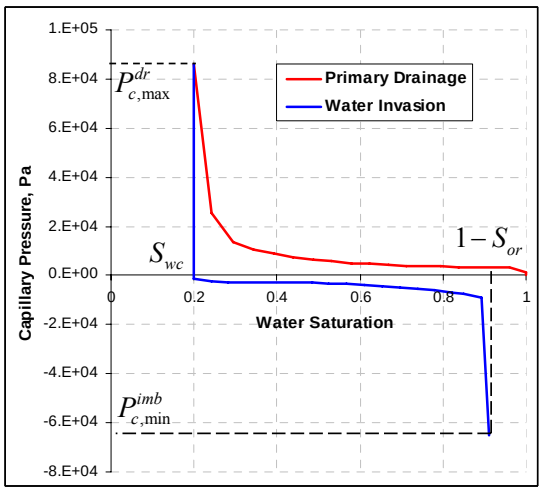

Figure 6.3 Capillary pressure curves for primary drainage and water invasion (after ageing) in *BereaPB without PB* for wettability case with average contact angle θ_a^i=125^o and layers existence scenario *Therm*. S_{wc} is the connate water saturation, $P_{c,\max}^{dr}$ the maximum P_c value achieved at the end of primary drainage, $P_{c,\min}^{imb}$ the minimum P_c value achieved at the end of water invasion (water imbibition).

We characterize each case by the average contact angle θ_a^i. The first case corresponds to UOW with $\theta_a \in \left[90^o, 100^o\right]$ and $\theta_a^i = 95^o$, and so on.

6.3.1 Residual Oil Saturation

The residual oil saturation S_{or} is the minimum achievable oil saturation (or true residual oil saturation) during the network water flood (water invasion) and corresponds to the lowest achievable capillary pressure $P_{c,\min}^{imb}$ (**Figure 6.3**). At that capillary pressure all oil clusters are trapped, i.e. no further oil displacement is possible under capillary dominated flow conditions. Consequently, at that capillary pressure (or at S_{or}) the total oil flow through the network will be zero. The corresponding water relative permeability value is known as end-point relative permeability.

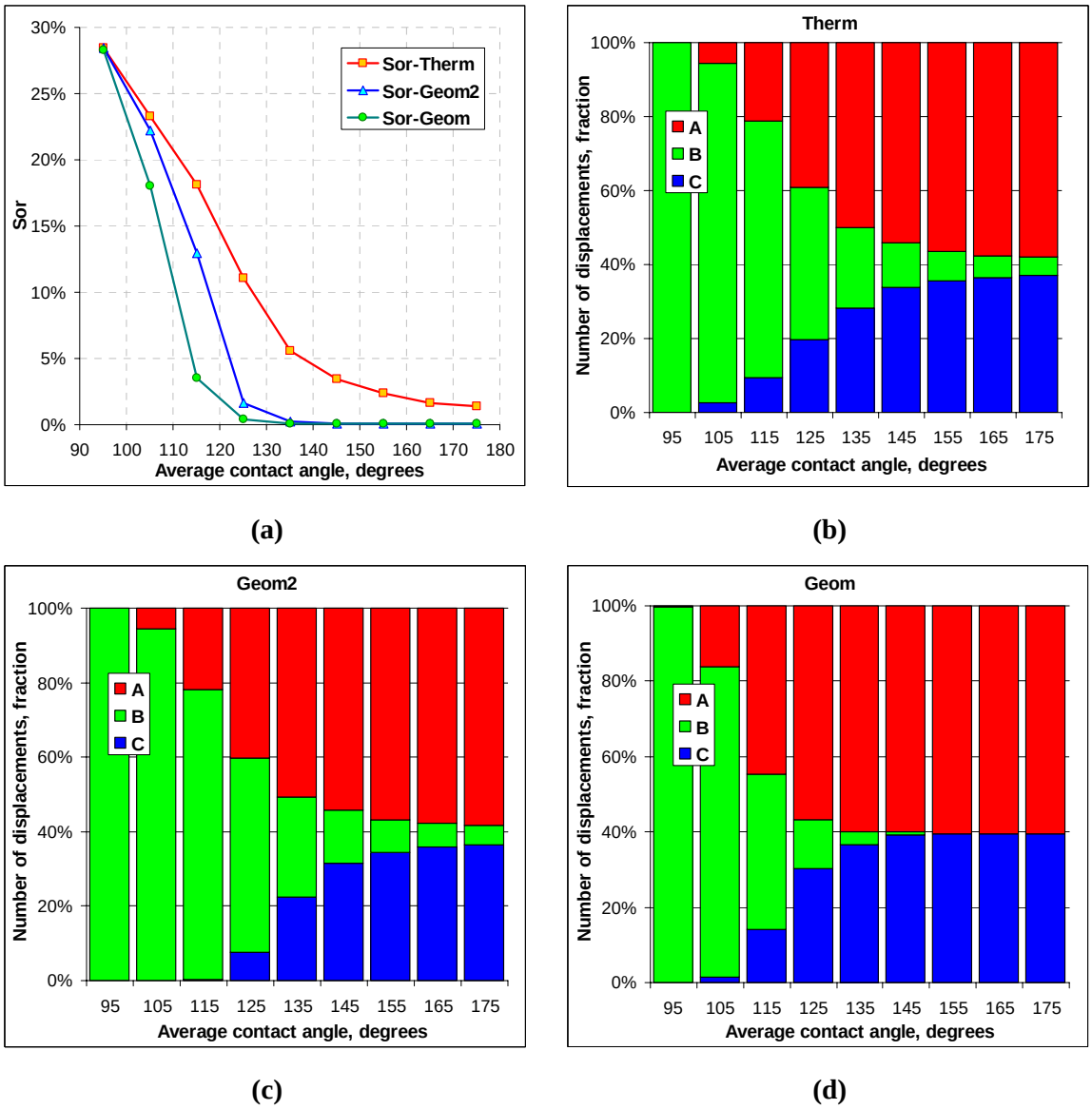

Figure 6.4 (a) S_{or} versus average contact angle θ_a^i for the three oil layer existence scenarios (*Therm*, *Geom2*, *Geom*) for *BereaPB without PB*; fraction of the number of layer formation (*A*), piston-like (*B*) and layer collapse (*C*) events according to (b) *Therm*, (c) *Geom2* and (d) *Geom* scenarios for *BereaPB*

For the nine wettability cases (see Eq.(6.2)), we have simulated primary drainage, ageing and water invasion (see example in **Figure 6.3** for the case with θ_a^i=125°). For each case we calculated the residual oil saturation S_{or} after water invasion for the three different oil layers existence scenarios. For *BereaPB* (**Figure 6.1b**), the residuals have been plotted as a function of increasing average contact angle θ_a^i in **Figure 6.4a**. In the next subsection we consider residuals at prescribed end-point capillary pressures, which we define as remaining oil saturations.

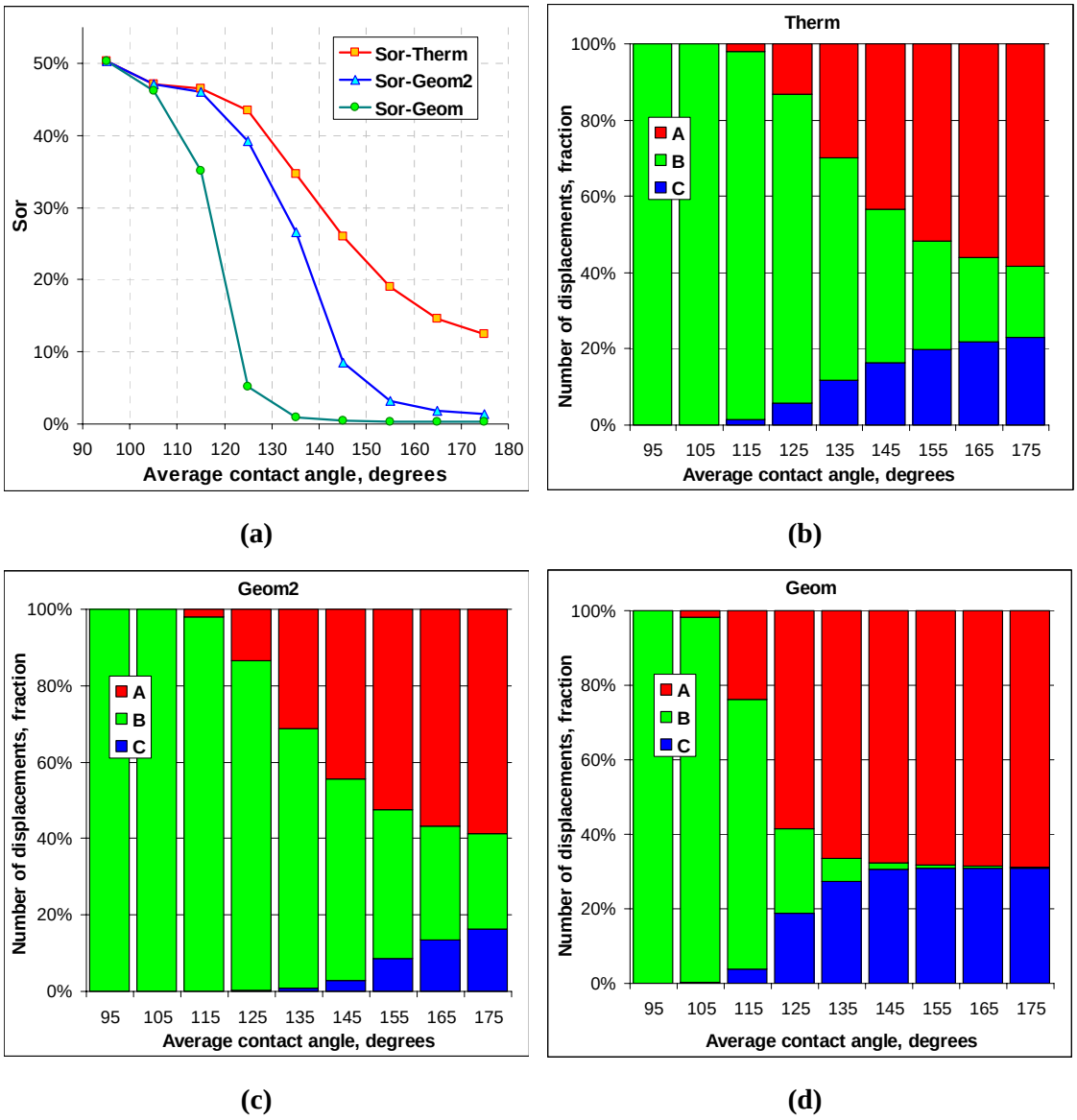

Figure 6.5 (a) S_{or} versus average contact angle θ_a^i for the three oil layer existence scenarios (*Therm*, *Geom2*, *Geom*) for *BereaCT without PB* and *Star*; fraction of the number of layer formation (*A*), piston-like (*B*) and layer collapse (*C*) events according to (b) *Therm*, (c) *Geom2* and (d) *Geom* scenarios for *BereaCT*

We find that S_{or} strongly decreases with increasing θ_a^i (increasing degree of oil wettability) for all scenarios (*Therm*, *Geom2*, *Geom*). Although the respective curves are quite different, they start with the same S_{or} value at $\theta_a^i = 105^o$ due to absence of any oil layers for all scenarios. The decrease in S_{or} can be explained from the fraction of the various displacements during water invasion, as presented in **Figure 6.4b**, **c** and **d** for the three scenarios. For example, for the thermodynamic scenario *Therm* (**Figure 6.4b**) more bulk water displacements with layer formations (*A*) occur for the more strongly oil-wet cases (large θ_a^i), fewer bulk displacements without layer formations (*B*) and more layer collapse displacements (*C*), in agreement with the oil layer existence

scenario presented in **Figure 4.5a**. The layer formation events (*A*) maintain oil phase continuity, while events *B* and *C* reduce continuity and hence oil production. For more strongly oil-wet cases, the range of capillary pressures between layer formation and layer collapse is larger than for more weakly oil-wet cases, which allows better oil displacement through these thick layers.

According to **Figure 4.5c** the *Geom* scenario is least restrictive in terms of layer formations compared to the other scenarios (**Figure 6.4b,c,d**). On the other hand, the *Therm* and *Geom2* scenarios have approximately the same fraction of layer formation occurrence. The *Geom* and *Geom2* scenarios have the same layer collapse entry pressures, which are less restrictive than the thermodynamical scenario, *Therm*. As a result, the *Geom* scenario allows a larger range of layer existence, yielding the lowest oil residuals. The *Therm* residuals are higher than those of *Geom2* due to a more restrictive collapse criterion. For the more strongly oil-wet cases, the residuals for the *Geom* and *Geom2,* are almost the same, i.e. zero, despite differences in the fractions of the different displacements.

For the second network *BereaCT* (**Figure 6.2b**), residuals are generally higher, as shown in **Figure 6.5a**, due to the lower coordination number. For more strongly oil-wet pores (large θ_a^i), the *Geom* and *Geom2* scenarios still produce very small (near zero) residuals, unlike the *Therm* scenario. For *Therm*, significantly fewer layer formation events occur (**Figure 6.5b**), compared to *Geom* (**Figure 6.5d**), and significantly more layer collapses takes place compared to *Geom2* (**Figure 6.5c**).

Based on the experimental S_{or} data presented in Chapter 2, we find that the *Geom* scenario shows unrealistically low residuals for both networks, even for intermediate oil-wet cases. Similarly, the corrected *Geom2* scenario shows very low residuals for the more strongly oil-wet cases. Only the *Therm* scenario produces reasonable residuals, as it incorporates the correct thermodynamic layers collapse criterion. Note, that for a lower maximum P_c value at the end of primary drainage $P_{c,\max}^{dr}$ (see **Figure 6.3**) the altered wettability pore surfaces after ageing are smaller (van Dijke and Sorbie 2006), which leads to a narrower range of water invasion capillary pressures for which oil

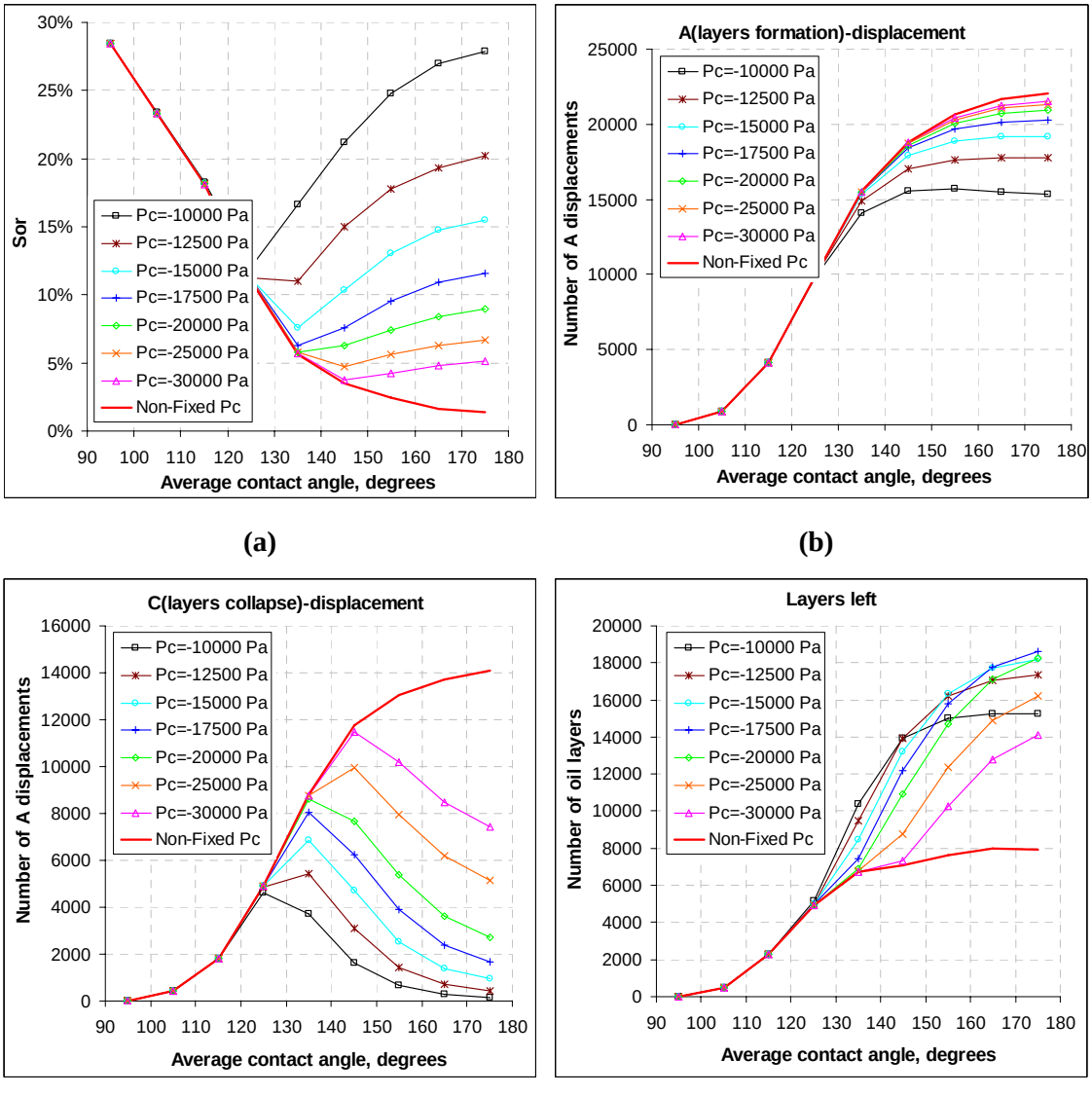

Figure 6.6 Sensitivity to end-point P_c for *BereaPB without PB* and *Therm* scenario: (a) S_{or} versus θ_a^i; the number of layers formations (b) and collapses (c) versus θ_a^i and (d) number of layers left versus θ_a^i. Non-fixed P_c case corresponds to lowest achievable $P_{c,\min}^{imb}$.

layers exist and as a consequence to a higher S_{or}, in particular for the *Geom* scenario. The latter behaviour is valid only for relatively high endpoint $P_{c,\max}^{dr}$ values or corresponding small initial water saturations after drainage $S_{wi.}$ In general, this behaviour is non-monotonic and after some critical $P_{c,\max}^{dr}$ value (S_{wi} value) the S_{or} starts decreasing as $P_{c,\max}^{dr}$ decreases (S_{wi} increases) (Blunt 1998, Jackson et al. 2005, Spiteri et al. 2008).

6.3.2 Remaining Oil Saturation

In most experiments the very low capillary pressure to trap (or displace) all oil, yielding the minimum (true) residual oil saturations of **Figure 6.4a** and **Figure 6.5a**, is not reached. Therefore, we have carried out a sensitivity analysis of remaining oil saturation (Skauge and Ottesen 2002, Høiland et al. 2007) with respect to different end-point capillary pressures for the *Therm* scenario. For *BereaPB* the end-point P_c varied from -10000 Pa to -30000 Pa (**Figure 6.6a**) and for *BereaCT* from -5500 Pa to -8500 Pa (**Figure 6.7a**). The lower capillary pressure values for *BereaPB* are due to the presence of pores of smaller radii. For intermediate oil-wet cases ($\theta_a^i = 125^o$ for *BereaPB* and $\theta_a^i = 145^o$ for *BereaCT*), the minimum residual is already obtained.

For strongly oil-wet cases, S_{or} increases strongly with increasing end-point capillary pressure. At the lower end-point capillary pressures (up to -17500 Pa) fewer layers collapse than are formed (**Figure 6.6b, c**), hence more layers remain in the system, (**Figure 6.6d**). Additionally, oil layers are thicker when capillary pressures are higher. Consequently, the oil volume contained in layers accounts for the increased S_{or}. However, for higher capillary pressures (above -17500 Pa), the number of remaining layers decreases, since significantly fewer layers have formed (*A* events). In this situation more bulk oil-filled pores remain and these make a large contribution to S_{or}.

There is a trade-off between the number of layers remaining (which affects oil cluster continuity) and end-point capillary pressure (which affects the volumes of the remaining oil layers and the volume of the bulk oil-filled pores). The strongly oil-wet cases result in lower remaining oil saturation for low end-point capillary pressures, which can be explained from the improved oil phase continuity and the small oil layer volumes.

However, for the higher end-point capillary pressures, oil layer volumes and eventually the bulk volume of oil-filled pores become more important than phase continuity. This balance is quite different for the intermediate oil-wet cases, where fewer layers form (and remain or collapse). Hence, the remaining oil is not very sensitive to the end-point capillary pressures, to such an extent that S_{or} is lower for intermediate oil-wet, compared to strongly oil-wet, at higher end-point capillary pressures.

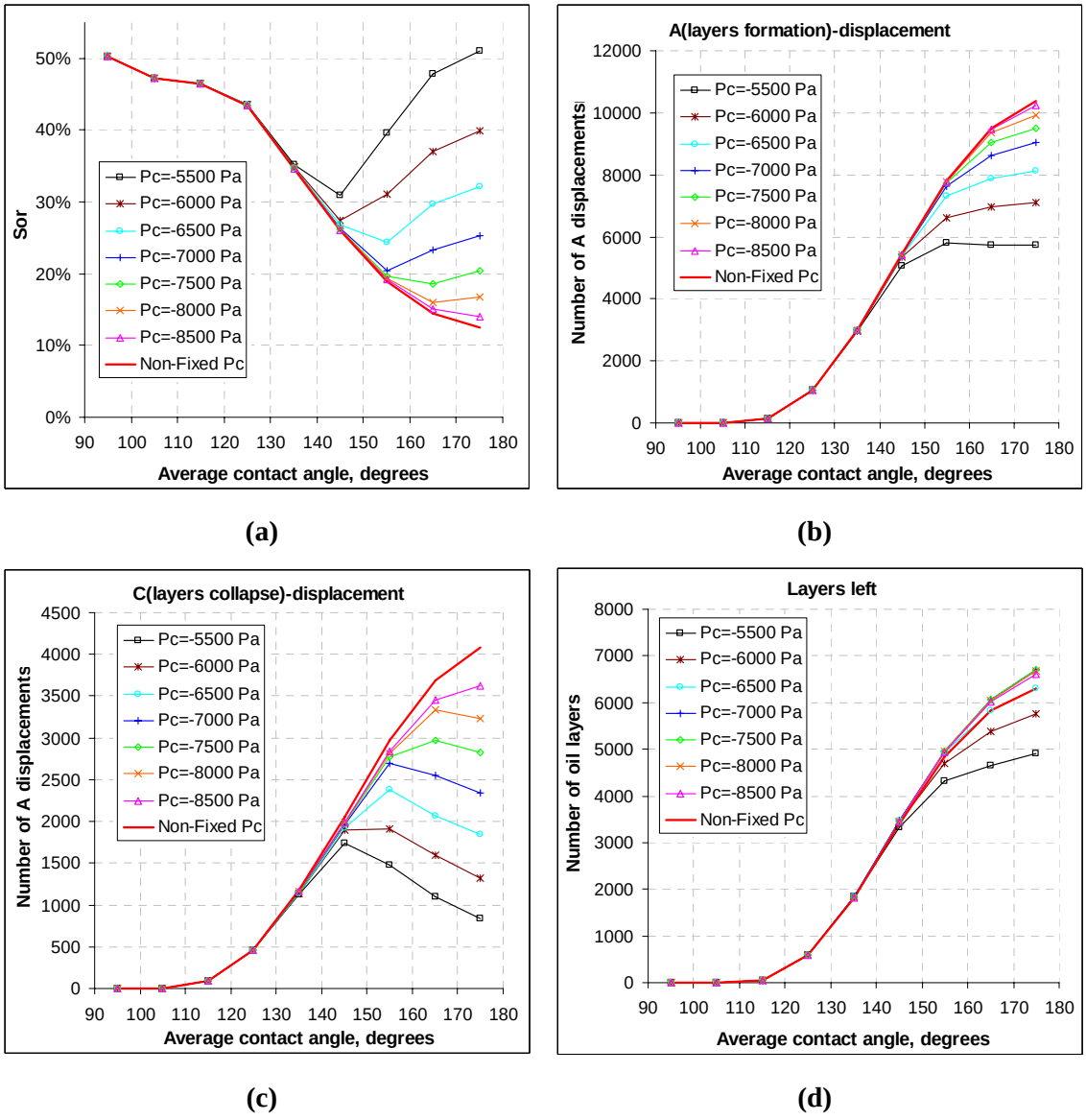

Figure 6.7 Sensitivity due to various end-point P_c for *BereaCT without PB* and *Therm* scenario: (a) S_{or} versus θ_a^i; (b,c) the number of layers formations/collapses occurred versus θ_a^i and (d) number of layers left versus θ_a^i. Non-fixed P_c case corresponds to lowest achievable $P_{c,\min}^{imb}$.

For the second network (*BereaCT*) which has a lower coordination number, the sensitivities with respect to the end-point capillary pressures are shown in **Figure 6.7a,b,c,d**. The trends are similar to those for *BereaPB*, although for the strongly oil-wet cases the numbers of layers left in the system (**Figure 6.7d**) become significantly

lower for the higher endpoint capillary pressures, compared to the numbers for the true residual oil saturation.

6.4 With Pore Bodies

Here, we consider only the *BereaCT* network (*CTS* and *Star* characterization) and apply network modelling using the *with PB* option (see Section 3.1). Thus, the pore bodies are included explicitly in the flooding process and they are allowed to experience the same type of displacements as the pore throats, as well as pore-body filling (PBF) events in the case of spontaneous displacement (see Section 4.3.3). To obtain a realistic (target) connate water saturation S_{wc}=0.23 a clay porosity φ_{cl}=5.5% has been introduced for the *BereaCT* network by adding a pore volume fraction α_{cl} =0.291 for each pore element (see Eq.(6.1)).

To analyze the effect of wettability on residual oil saturation and relative permeabilities, we consider a series of different wettability distributions for *BereaCT* network. During drainage the network is assumed to be water-wet with drainage contact angle θ_{pd} uniformly distributed between 0° and 60°. After ageing the advancing contact angles θ_a of the oil-contacted parts of the oil-filled pores are taken according to a fractionally wet distribution (FW) with six values of oil-wet fractions

$$\alpha_j = 0.5 + 0.1(j-1),\ j = 1..6 \tag{6.3}$$

and for each of those α_j values we define nine ranges of advancing oil-wet contact angles similar to Eq. (6.2). Whereas, the advancing water –wet contact angles $\theta_{a,ww}$ are uniformly distributed between 60° and 90°.

We characterize each case by the pair of values $\left(\alpha_j, \theta_a^i\right)$. For all sensitivity cases we have simulated primary drainage and water invasion with ageing included after drainage.

6.4.1 Residual Oil Saturation

The (true) residual oil saturations are plotted against the average advancing contact angle θ_a^i for the different oil-wet fractions α (**Figure 6.8**). The residual oil behaviour for the uniformly oil-wet case (α=1) with *Therm* and *Geom* layers existence scenarios (**Figure 6.9**) is in agreement with previous findings, where pore bodies were excluded from the displacement process. Similar to the previous case *without PB* (**Figure 6.5a**),

the least restrictive scenario *Geom* gives S_{or} values lower than for the most restrictive scenario *Therm* and produces near zero oil residuals for the more strongly oil-wet cases (**Figure 6.9**). However, there are significant differences in S_{or} behaviour between the *with PB* and *without PB* cases for the same layers existence scenario as explained below.

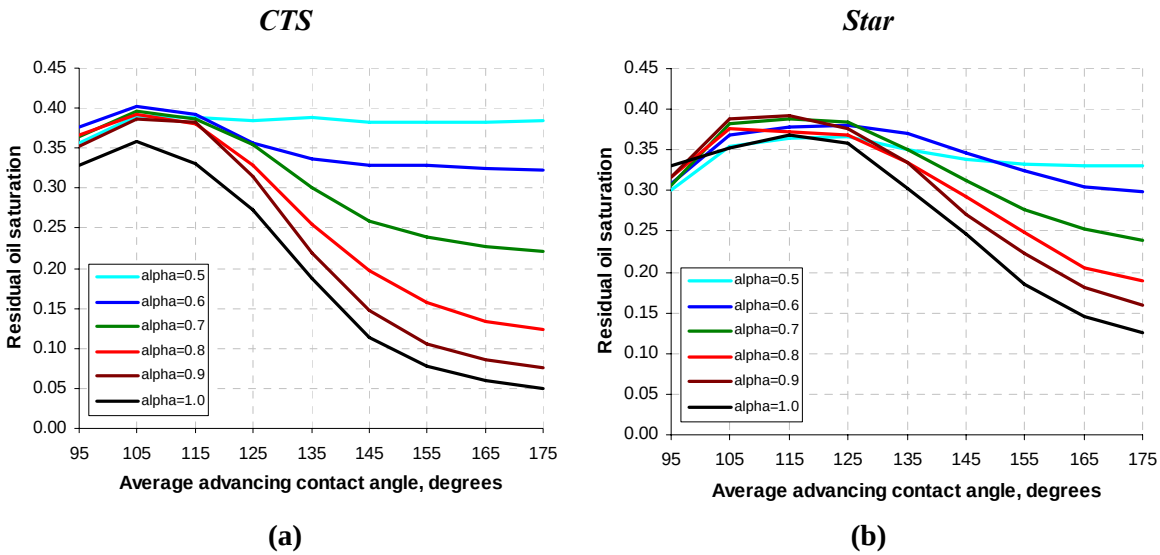

Figure 6.8 Residual oil saturation sensitivity (BereaCT network *with PB* and Therm scenario) to oil-wet fraction α and average advancing contact angle θ_a^i; (a) CTS approach, (b) Star approach.

The residual oil saturation decreases with increasing average contact angle (beyond θ_a^i of around 115 degrees) with a more rapid decline for the higher oil-wet fraction values (**Figure 6.8a,b**). On the other hand, residual oil decreases with increasing oil-wet fraction for the same average advancing contact angle and the larger the contact angle the more rapid the decline of the oil residual. This can be explained by the increasing presence of oil layers during waterflooding, which improves oil phase continuity and results in increased oil recovery (see Section 6.3). These sensitivity results are also consistent with previously published studies for the case *with PB* and *Geom* scenario (Blunt 1998, Øren et al. 1998, Al-Futaisi and Patzek 2003b, 2004).

Modelling pore shapes by *Star* (**Figure 6.8b**), rather than by *CTS* (**Figure 6.8a**), has a significant effect on the residual oil saturations for the larger contact angles. The residual oil variation range for *Star* is narrower than that for *CTS*. This can be explained from the presence of more arbitrary triangular shapes for *CTS* than for *Star*. Since the drainage contact angle values are distributed according to $\theta_{pd} \in \left[0^o, 60^o\right]$, a

significant number of arbitrary triangles will not have corner water films after drainage (at least in the largest corner) contrary to the regular stars. The corners without water films may become oil-wet during ageing and have stable oil wetting films, instead of conditionally stable oil layers, during waterflooding, which better maintains oil continuity.

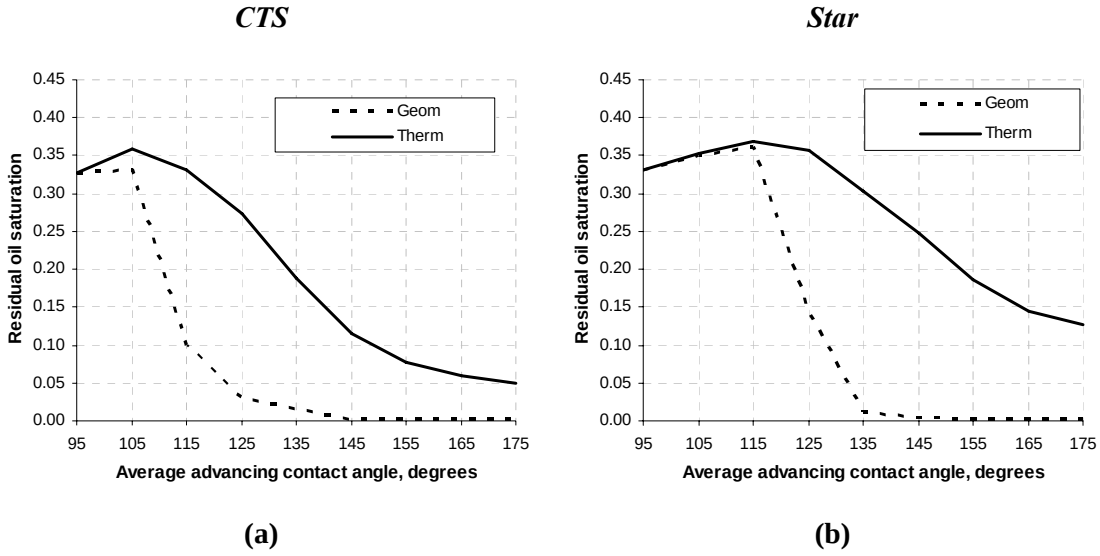

Figure 6.9 Effect of layers existence scenario (Therm, Geom) on residual oil saturation sensitivity (*BereaCT* network *with PB*) to average advancing contact angle θ_a^i for UOW case (α=*1*); (a) *CTS* approach, (b) *Star* approach.

The effect of including pore bodies in the model can be investigated by comparing the S_{or} sensitivities to θ_a^i for UOW *with PB* and *without PB* (**Figure 6.10**). Generally, the qualitative behaviour for both cases is similar, S_{or} decreases with θ_a^i, although the S_{or} curve *with PB* shows some non-monotonic behavior for weakly oil-wet conditions as discussed above. However, if we extend the sensitivity to average contact angle below 95 degrees then the S_{or} behaviour (*without PB*) will also be non-monotonic with the maximum at 85 degrees. Quantitatively, there is a significant difference, as S_{or} for the case *with PB* is higher than for the case *without PB*. This can be explained from a topological point of view. In the case *with PB* we have additional displacements which happen in PB piston-like (PL), layers formation and collapse etc. (see Chapter 4). When the defending phase is displaced from the PB either PL or by layers collapse displacement, the defending cluster, to which the occupied PB belonged, may be divided into several separate clusters. Some of those clusters can become trapped, which increases the S_{or}.

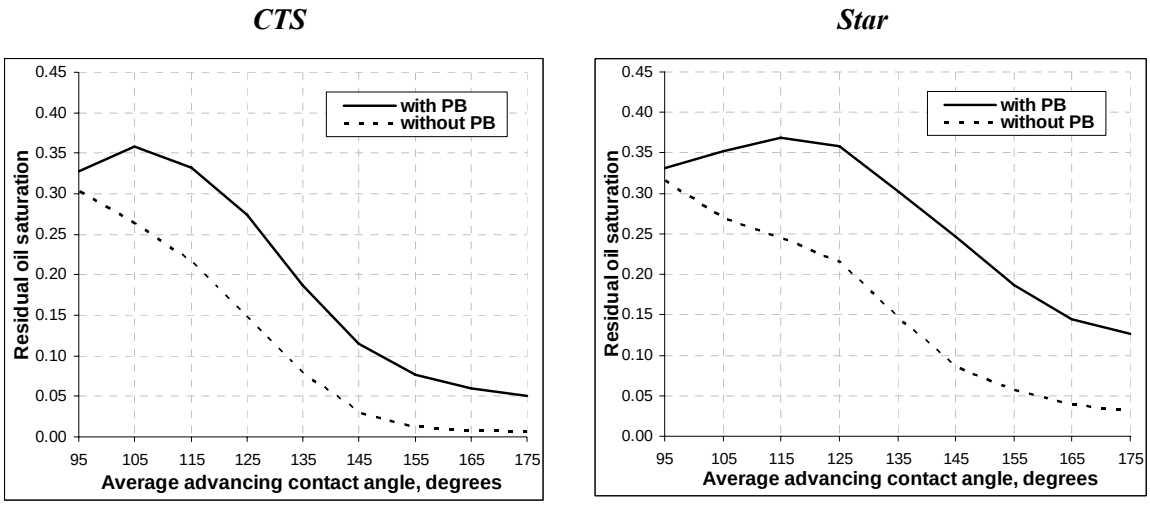

(a) **(b)**

Figure 6.10 Effect of PB on residual oil saturation sensitivity (*BereaCT* network) to average advancing contact angle θ_a^i for UOW case (α=*1*) with *Therm* scenario; (a) *CTS* approach, (b) *Star* approach.

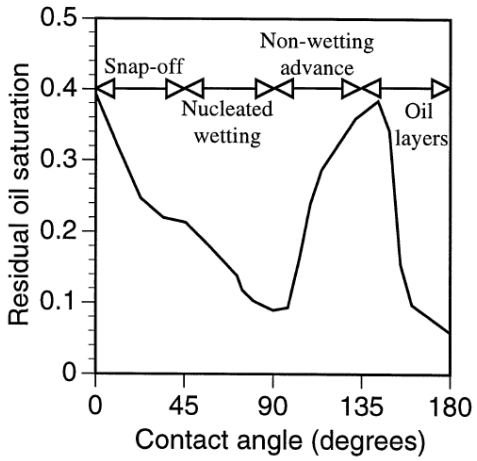

Figure 6.11 Residual oil saturation S_{or} as a function of advancing contact angle θ_a^i. (cubic lattice with pore bodies and throats with square cross-section, $\theta_{dr} = 22.5^o$) (Blunt 1998)

Similar non-monotonic S_{or} behaviour against the advancing contact angle on **Figure 6.10** (*with PB*) was shown before by Blunt (1997b, 1998) (**Figure 6.11**). He calculated S_{or} using a cubic lattice (*with PB*) with square pore cross-sections and identified 4 flow regimes depending on advancing contact angle, in particular, *non-wetting advance* and *oil layers*.

The *non-wetting advance* regime corresponds to the weakly oil-wet system (θ_a >90^o). In this case water invasion is impeded by the pore throats and pore bodies can only be filled by piston-like displacement since the PBF I_n events are suppressed completely due to forced water invasion. The water displaces oil from the largest pore throats and pore bodies which results in a *dendritic advance* and bypassing of significant amounts of oil. Only a few oil layers can be formed which is not enough to maintain the oil phase continuity and leads to significant trapped oil. The *oil layers* regime corresponds to the more strongly oil-wet system where the oil layers are more stable. This case has been already discussed in this chapter, the oil layers formation

improves the oil phase continuity and results in the lower oil residual S_{or} for larger advancing contact angles θ_a .

These two regimes (*non-wetting advance* and *oil layers*) can be easily seen on **Figure 6.10(***with PB***)** and **Figure 6.12**. The *non-wetting advance* regime corresponds to $\theta_a \in \left[90^o, 110^o\right]$ and $\theta_a \in \left[90^o, 120^o\right]$ for the *CTS* and *Star* shape characterizations, respectively, and the *oil layers* regime occurs for the rest of the oil-wet contact angles.

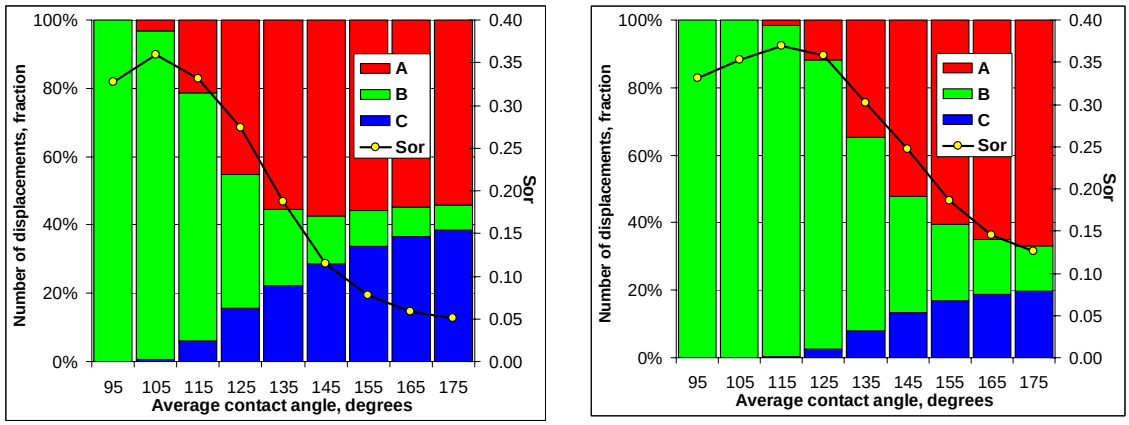

Figure 6.12 S_{or} and fraction of the number of displacements versus average contact angle θ_a^i for the *BereaCT with PB* case, *Therm* layers existence criterion, pore shape characterization (a) *CTS* and (b) *Star*. (notation of displacements A, B, C as in **Figure 6.4** and **Figure 6.5**)

The way the pore bodies are represented in the model and the corresponding PBF I_n events are formulated parametrically is still an unresolved problem. Therefore, the true S_{or} is situated between 2 limiting cases: *with PB* and *without PB*. It will be shown in Chapter 7 that fairly good agreement with experimental data can be obtained for both cases.

6.4.2 Relative Permeabilities

To show the effect of wettability on the water flood relative permeability curves, we have considered two sensitivities for the *BereaCT* network with *CTS* and *Star* pore shape approximations: 1) sensitivity to average advancing contact angle θ_a^i for a uniformly oil-wet system (α=1.0) (**Figure 6.13**); 2) sensitivity to oil-wet fraction α with the strongly oil-wet advancing contact angle distribution $\theta_a \in [170^o, 180^o]$ (**Figure 6.14**). In addition, for the *CTS* approximation in sensitivity 1 we show the impact of using the new thermodynamic criterion for the existence of oil layers (*Therm* scenario),

as compared to the conventional geometrical criterion (*Geom* scenario). This complements earlier results for the effects of these scenarios on residual oil saturations (see Section 6.3), which are very significant.

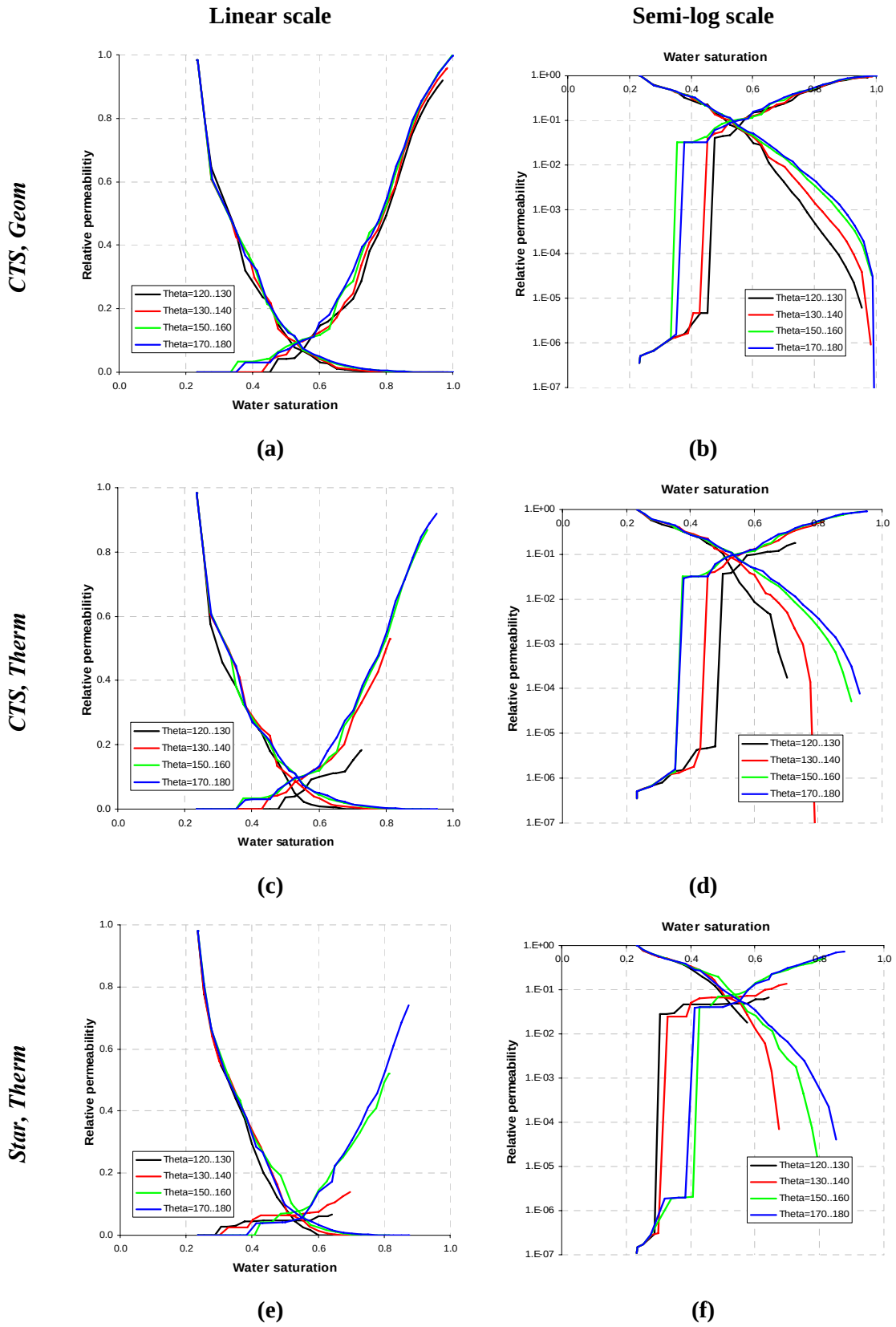

Figure 6.13 Sensitivity of relative permeabilities to average advancing contact angle with oil-wet fraction α=1.0 (BereaCT network with PB). (a,b) CTS approach with Geom criterion; (c,d) CTS approach with Therm criterion; (e,f) Star approach with Therm criterion

For sensitivity 1 we have calculated relative permeabilities for the *CTS* approach with the *Geom* (**Figure 6.13a,b**) and *Therm* (**Figure 6.13c,d**) oil layers existence scenarios and for the *Star* approach with the *Therm* scenario (**Figure 6.13e,f**). First, the less restrictive oil layer existence scenario *Geom* produces lower S_{or} and higher K_{rw} end-points (**Figure 6.13a,b**) compared to the more restrictive *Therm* scenario (**Figure 6.13c,d**). The K_{rw} curves for *Geom* are very similar for all values of θ_a^i, at the higher S_w, while for *Therm* the K_{rw} curves increase gradually with θ_a^i. Similarly, for *Star* (**Figure 6.13e,f**) the K_{rw} curves are lower, the K_{rw} end-point is lower and S_{or} is higher compared to the corresponding *CTS* curves. This is a consequence of the larger number of arbitrary triangular shapes in *CTS* than in *Star*, leading to more stable corner films instead of oil layers, as explained above.

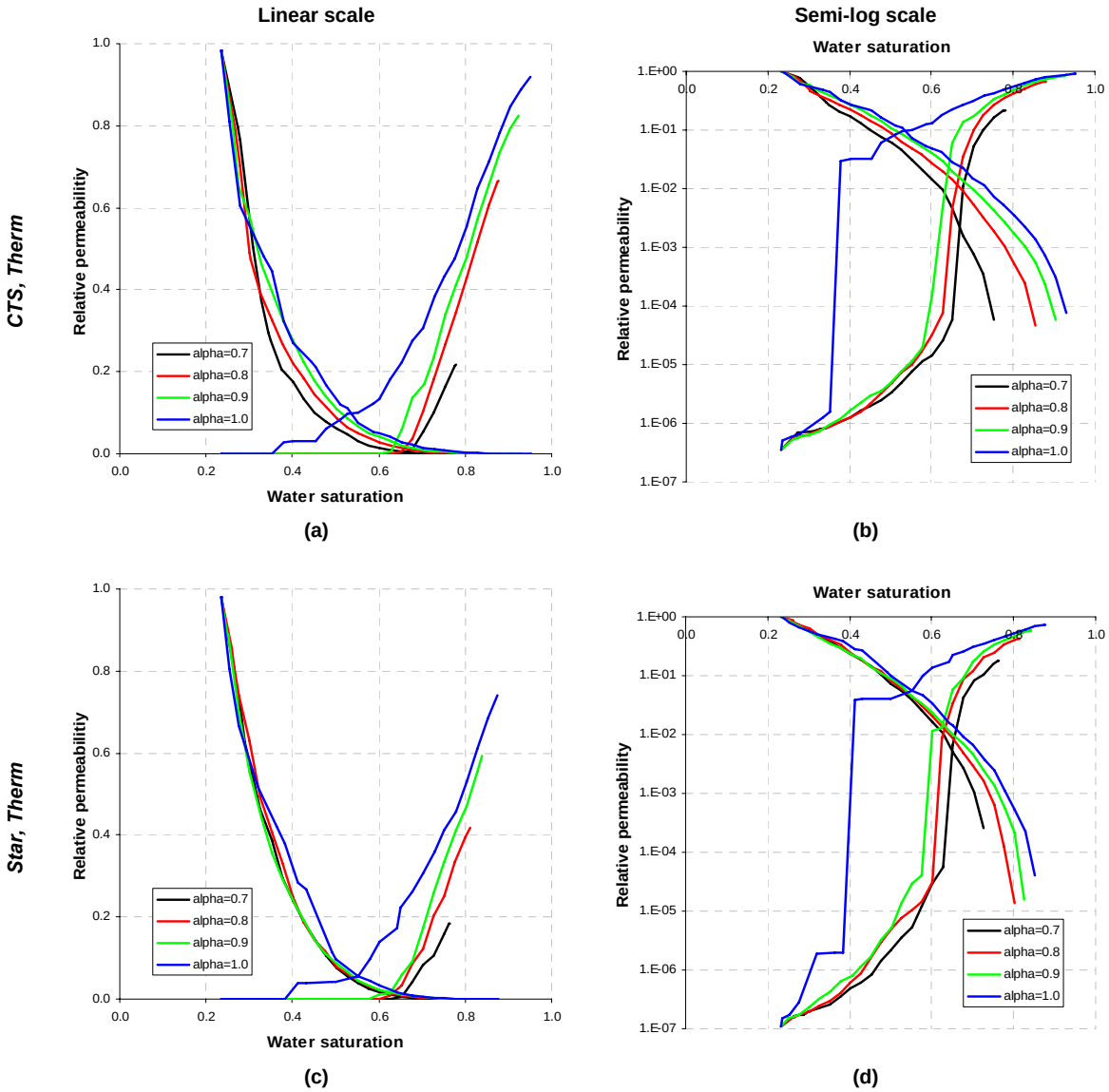

Figure 6.14 Sensitivity of relative permeabilities to fraction of (strongly) oil-wet pores (BereaCT network with PB, layers existence scenario Therm). (a,b) CTS approach, (c,d,) Star approach.

For all cases K_{ro} increases with θ_a^i (**Figure 6.13b,d,f**) at high S_w. This is the result of increased oil phase conductivity due to the existence of many oil layers. Similarly, K_{rw} increases with θ_a^i at low S_w. The latter is the result of a different fluid redistribution at the same S_w: for higher θ_a^i more oil layers are formed in the model, which results in more bulk water filled pores with less water in each. Consequently, the crossover of the K_{rw} and K_{ro} curves hardly shifts to lower S_w with increasing oil-wetness.

For sensitivity 2, **Figure 6.14** shows the relative permeability behavior for varying oil-wet fractions of strongly oil-wet pores ($\theta_a^i = 175^o$). Contrary to sensitivity 1 (**Figure 6.13**), the relative permeability crossover shows a significant shift towards lower S_w, as the oil-wet fraction α increases. The K_{ro} curves show two opposing trends as α increases: a decrease at low S_w values and an increase at high S_w values. At the start of the water flood, displacements occur in the small water-wet pores, followed by displacements in the large oil-wet pores. For increasing fractions of oil-wet pores, α, the latter displacements start earlier during the flood, which explains the decrease of K_{ro} at low S_w. On the other hand, for decreasing α (more water wet pores) more pore body filling events occur at higher water saturations, resulting in more trapped oil clusters which do not contribute to K_{ro}. Thus, for higher S_w the trend changes and K_{ro} increases with α. In a previous sensitivity study by McDougall and Sorbie (1995) for the fraction of oil-wet pores in FW systems K_{ro} also showed 2 opposite trends, but the change of trends happened for much higher water saturations and lower K_{ro} values. One possible reason for this earlier result is that the pore bodies and the corresponding PBF events were not included.

6.5 Summary and Conclusions

In this chapter we have included the full thermodynamically based oil layer formation and collapse model (*Therm* scenario) in our two-phase pore network simulator. The *Therm* layer criterion is more restrictive than the previously used geometrical criterion (*Geom*). In the network model, the new *n*-cornered star (*Star*) shape characterization technique has been also implemented, in addition to the commonly used Circle-arbitrary Triangle-Square (*CTS*) shape representation. Two networks have been used for a number of sensitivities of the water invasion residual oil saturation and relative

permeabilities: *BereaPB*, extracted from a process based reconstruction of a Berea sandstone, and *BereaCT*, extracted from a 3D CT image of a different Berea sample. For *BereaPB* pore shapes are represented by *CTS*, while for *BereaCT* both the *CTS* and the *Star* approaches have been used. We have considered two variants of the model: *without pore bodies* (*PB*) and *with pore bodies.*

For the first case *without PB,* we used both networks (*BereaPB* with *CTS*, *BereaCT* with *Star*). The oil residuals S_{or} have been estimated for different oil layers existence scenarios (*Therm, Geom, Geom2*) and various wettability scenarios, by varying the contact angles in oil-filled pores after ageing from weakly to strongly oil-wet. Moreover, a sensitivity analysis has been carried out of remaining oil saturation with respect to water flood end-point capillary pressures.

The following conclusions have been made:

(i) The thermodynamically based oil layers existence scenario *Therm* gives realistic non-zero residual oil saturations compared with the other scenarios, consistent with findings for the single pore throat (van Dijke and Sorbie 2006).

(ii) The geometrically based inconsistent layer existence scenario *Geom* is least restrictive and produces near-zero oil residuals, even for intermediate oil-wet cases.

(iii) The corrected geometrically based formation and collapse scenario *Geom2* produces higher residuals than *Geom*, but for the higher coordination number network the oil residuals are still close to the unrealistically low values obtained using *Geom*.

(iv) The more strongly oil-wet cases lead to lower oil residuals, which can be explained from improved oil phase continuity resulting from the abundant presence of oil layers.

(v) However, for prescribed end-point capillary pressures, higher than that corresponding to the residual oil saturation, remaining oil saturations are lower for intermediate oil-wet cases.

For the case *with PB* again two networks (*BereaPB, BereaCT*) have been used for various sensitivity calculations.

The sensitivity of residual oil saturation S_{or} to the average advancing contact angle θ_a^i for different oil-wet fractions α has been investigated. S_{or} decreases with increasing average contact angle (beyond θ_a^i of around 115 degrees) with a more rapid decline for the higher oil-wet fractions and S_{or} decreases with increasing oil-wet fraction. Modelling pore shapes by *Star*, rather than by *CTS*, has a significant effect on S_{or} for the larger contact angles, as the S_{or} range for *Star* is narrower compared to that for *CTS*. Similar to the *with PB* case, the S_{or} for the *without PB* case decreases with θ_a^i with non-monotonic behaviour for the water-wet cases with θ_a^i below 95°. Quantitatively, the S_{or} for *without PB* are generally lower than the corresponding residuals for the *with PB* case.

Two sensitivities of relative permeability have been performed: 1) sensitivity to average advancing contact angle θ_a^i for a uniformly oil-wet system (α=1.0), for *CTS* with *Geom* and *Therm* scenario, as well as for *Star* with *Therm* scenario; 2) sensitivity to the fraction of oil-wet pores α with strongly oil-wet advancing contact angle, for *CTS* and *Star* with *Therm* scenario. For sensitivity 1, the less restrictive oil layers existence scenario *Geom* produces lower S_{or} and higher K_{rw} end-points compared to the more restrictive *Therm* scenario. The K_{rw} curves for *Geom* are very similar for all values of θ_a^i, at the higher S_w, while for *Therm* the K_{rw} curves increase gradually with θ_a^i. Similarly, the *Star* curves show lower K_{rw} values, lower K_{rw} end-points and higher S_{or} compared to the corresponding *CTS* curves. For sensitivity 2, contrary to sensitivity 1, the relative permeability crossover shows a significant shift towards low S_w, as the oil-wet fraction α increases. The K_{ro} curves have two opposite trends as α increases: a decrease at low S_w values and an increase at high S_w values. For *Star* the entire K_{rw} curves are lower, K_{rw} end-points are lower and S_{or} is higher compared to the corresponding *CTS* curves.

CHAPTER 7 - COMPARISON OF NETWORK SIMULATIONS WITH EXPERIMENTAL DATA

7.1 Introduction

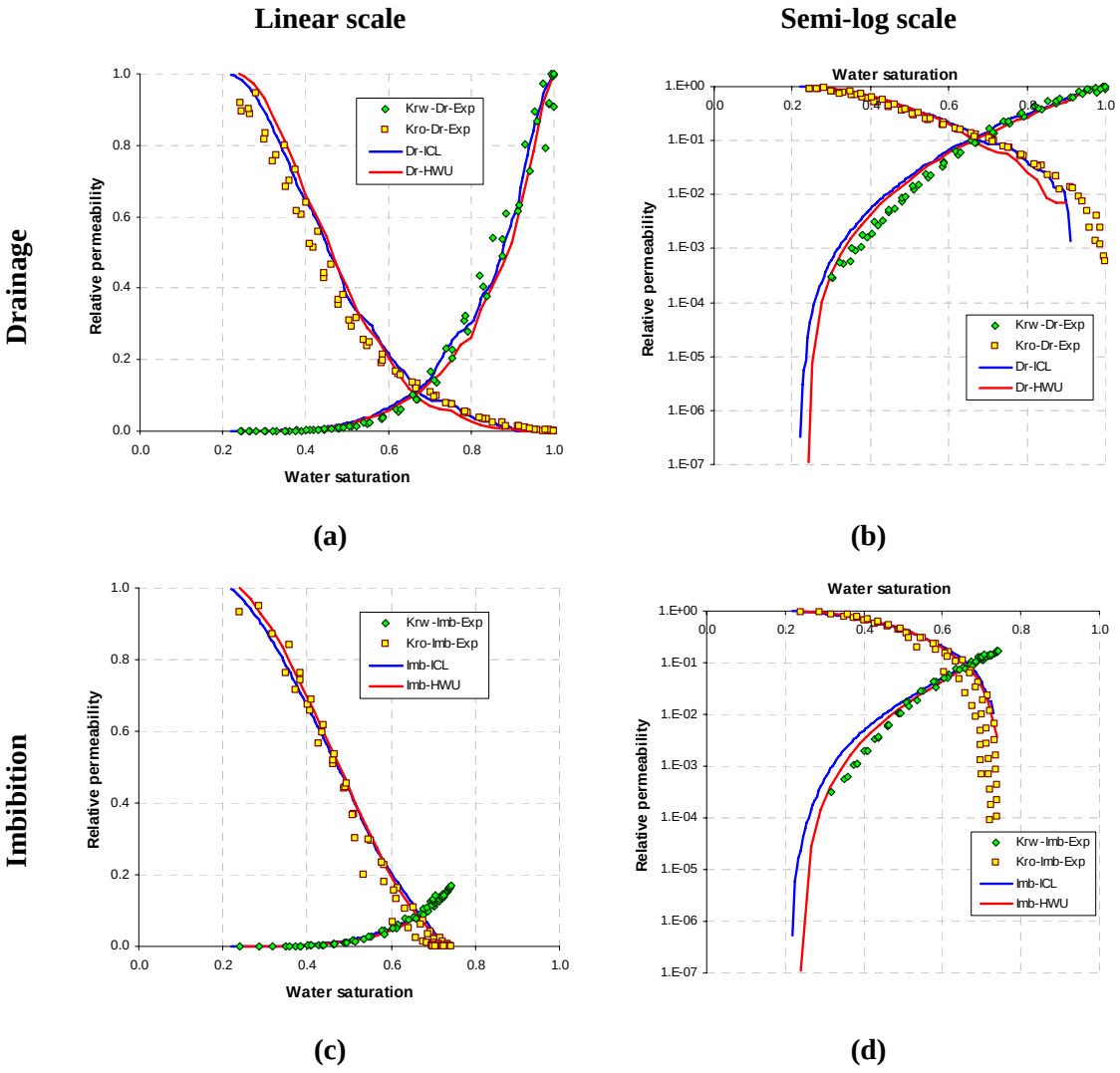

Figure 7.1 Comparison of calculated relative permeabilities (*BereaPB* network) with experimental data for a water-wet Berea sandstone (Oak 1990) for Drainage (**a,b**) and Imbibition (Water Invasion) (**c,d**)

In this chapter we validate the pore-scale network model through comparisons with relative permeability data for a water-wet Berea sandstone (Oak 1990) and with experimental data for an oil-wet sandstone (Valvatne and Blunt 2004). Additionally, waterflood recovery experiments in cores with a range of wettability conditions by Jadhunandan and Morrow (1995) are modelled using the pore-scale simulated relative permeabilities in 1D continuum scale Buckley-Leverett (BL) model.

7.2 Matching relative permeability data for a water-wet Berea sandstone

In this section network simulations have been compared with two-phase oil-water experiments conducted by Oak (1990), including primary drainage and water invasion (water imbibition). Oak performed a number of steady-state measurements of relative permeabilities on three core samples of water-wet Berea sandstone. These core samples 6, 13 and 14 have absolute permeabilities 200 mD, 1000 mD and 800 mD, respectively. High permeable samples 13 and 14 have similar relative permeability curves which are different from low permeable sample 6. For the network simulations, the two Berea networks (*BereaPB* and *BereaCT*, with *Star* or *CTS*, in Section 6.2) have been considered, which have the relatively high absolute permeabilities of 2668 mD and 1595 mD (*Star*) 1699 mD (*CTS*) (**Table 6.1**), respectively. Therefore, we have only used experimental relative permeabilities for the high permeable samples 13 and 14. A match with experiments has been obtained using both networks, but with slightly different wettability scenarios, for which the input parameters are shown in **Table 7.1.**

Table 7.1 Input parameters used for comparison with Oak's water-wet experiments

Network		*BereaPB*	*BereaCT*
Pore Shape Representation		*CTS*	*CTS or Star*
Pore Bodies		*with PB*	*with PB*
Contact angle, degrees	Drainage	θ_{dr}=0	θ_{dr} =0
	Imbibition (Water Invasion)	θ_a =56..76	θ_a =36..56
Water viscosity (10^{-3} Pa/s)		1	1
Oil viscosity (cP)		0.29	0.29
Interfacial tension (10^{-3} N/m)		30	30

For the *BereaPB* network (only *CTS* shape characterization) we used the same input parameters as in previous predictions of this data by the Imperial College London group (*ICL*) (Valvatne and Blunt 2004). The *ICL* model is very similar to our network modelling tool (*HWU*) for water-wet conditions. During drainage, the network is assumed to be strongly water-wet with 0^o contact angle θ_{dr}. No further adjustment is required since the network *BereaPB* captured all the topological and geometrical information during extraction from the process based reconstructed 3D digital rock (Bakke and Øren 1997, Øren and Bakke 2003). During imbibition the distribution of advancing contact angles θ_a is UWW between 56 and 76 degrees, which is consistent

with the typical range of water-wet advancing contact angles due to pore surface roughness (Morrow 1975, Dullien 1992). The relative permeabilities calculated by the *ICL* and *HWU* groups are compared to steady-state experimental data by Oak (**Figure 7.1**). Very good matches can be achieved with both models for these water-wet data, in particular the S_{or} of 25% has been matched quite closely and the endpoint K_{rw} at S_{or} is also in a good agreement with the data. Note, that there are only small differences between the two matches which are caused by slightly different treatment of boundary conditions, random distribution of advancing contact angles and random selection of the intermediate corner half angles for arbitrary triangles (Øren et al. 1998, Patzek 2001).

For the *BereaCT* network we have considered the two pore shape approximations *CTS* and *Star*. The wettability scenario is almost the same as for *BereaPB*, but the advancing contact angle distribution is slightly shifted towards strongly water-wet conditions (see **Table 7.1** and **Figure 7.2**). Relative permeability predictions for both pore shape approximations show very good agreement with the experimental drainage curves, but the *Star* approach gives a better match with the imbibition curves compared to *CTS*, as the latter overestimates the K_{rw} (**Figure 7.2**). This illustrates the general improvement of the *Star* over the *CTS* approach and it is consistent with the findings for capillary bundle models in Chapter 4 (Helland et al. 2008). Interestingly, the experiments could have been better matched by *CTS* than by *Star*, if we had selected a different set of advancing contact angles. However, because the *Star* shape characterization represents the pore cross-sections more accurately than *CTS* (see Chapter 4) we believe that *Star* should be used for matching the experimental data, as this leads to a better estimation of the wettability conditions..

We have matched the same water-wet Berea experimental data set (including S_{or}) using two different networks, *BereaPB* and *BereaCT*, by only adjusting the advancing contact angle distribution. Thus, the water-wet experiments can be matched straightforwardly if the geometrically and topologically equivalent network is extracted from the pore space reconstruction of the same rock. In particular, the more accurate pore shape characterization *Star* should be used when possible to identify the wettability distribution more accurately.

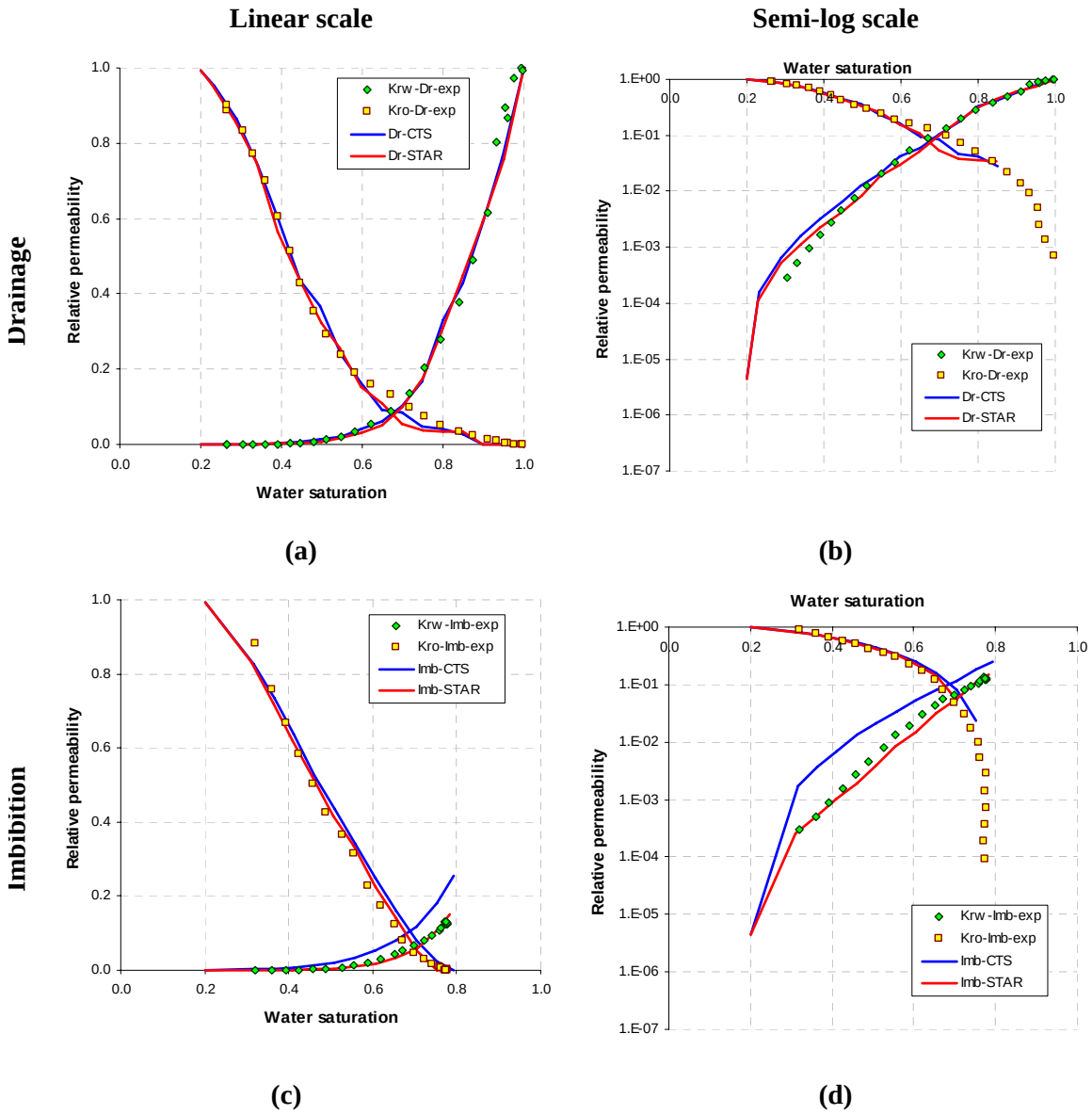

Figure 7.2 Comparison of calculated relative permeabilities (*BereaCT* network, *Star* and *CTS*) with experimental data for a water-wet Berea sandstone (Oak 1990) for Drainage (**a,b**) and Imbibition (Water Invasion) (**c,d**)

7.3 Matching relative permeability data for an oil-wet sandstone

In this section, network simulations are compared with a set of steady state measurements of relative permeabilities on two oil-wet sandstone core samples with absolute permeabilities 248 mD and 328 mD (Valvatne and Blunt 2004). Using the *BereaPB* network, these data were previously modelled by the *ICL* group (Valvatne and Blunt 2004). We modified the *BereaPB* network in the same way as Valvatne and Blunt (2004) by changing the pore body and pore throat size distribution to match the centrifuge drainage capillary pressure curve. The drainage contact angles were specified according to a UWW distribution with contact angles between 20 and 60 degrees, which was identified during matching of the drainage capillary pressure curve (Valvatne and Blunt 2004).

To match the water flooding curves, we specified the advancing contact angles, after wettability alteration, according to a UOW distribution between 90 and 173 degrees, which was supported by the Amott indices I_w=0.0, I_o=0.14, I_{wo}=-0.14, indicating oil-wetness (Valvatne and Blunt 2004). In our calculations we additionally used the more accurate layers existence scenario *Therm* instead of *Geom* used by Valvatne and Blunt (2004). All other input parameters are presented in **Table 7.2** (*ICL model*).

Table 7.2 Input parameters used for prediction of oil- wet experiments

		ICL model	*HWU model*
Contact angle, degrees	Drainage	θ_{dr} =20..60	θ_{dr} =0
	Imbibition	θ_a =90..173	θ_a =96..158
Oil layers existence scenario		*Geom*	*Therm*
Initial water saturation		0.03	0.02
Water viscosity (10^{-3} Pa/s)		1	1
Oil viscosity (cP)		0.29	0.29
Interfacial tension (10^{-3} N/m)		51.8	51.8

The comparisons between predicted and experimental data for *ICL* and *HWU* with the same wettability scenario but different layers existence criteria are generally very good (**Figure 7.3** (a,b)). However, the *ICL* model slightly overpredicts the oil relative permeability at high water saturations and significantly underpredicts the S_{or}. The latter is due to the less restrictive layers existence scenario *Geom*, which allows the oil to drain through layers to near zero saturations. On the other hand, the *HWU* model with the *Therm* criteria predicts the S_{or} value very well, but it underpredicts the water relative permeability at low water saturations.

To improve the matches, we made the network less oil-wet (see *HWU model* in **Table 7.2**). The results for the new set of parameters (**Figure 7.3** (c,d)) show much better agreement with experiments.

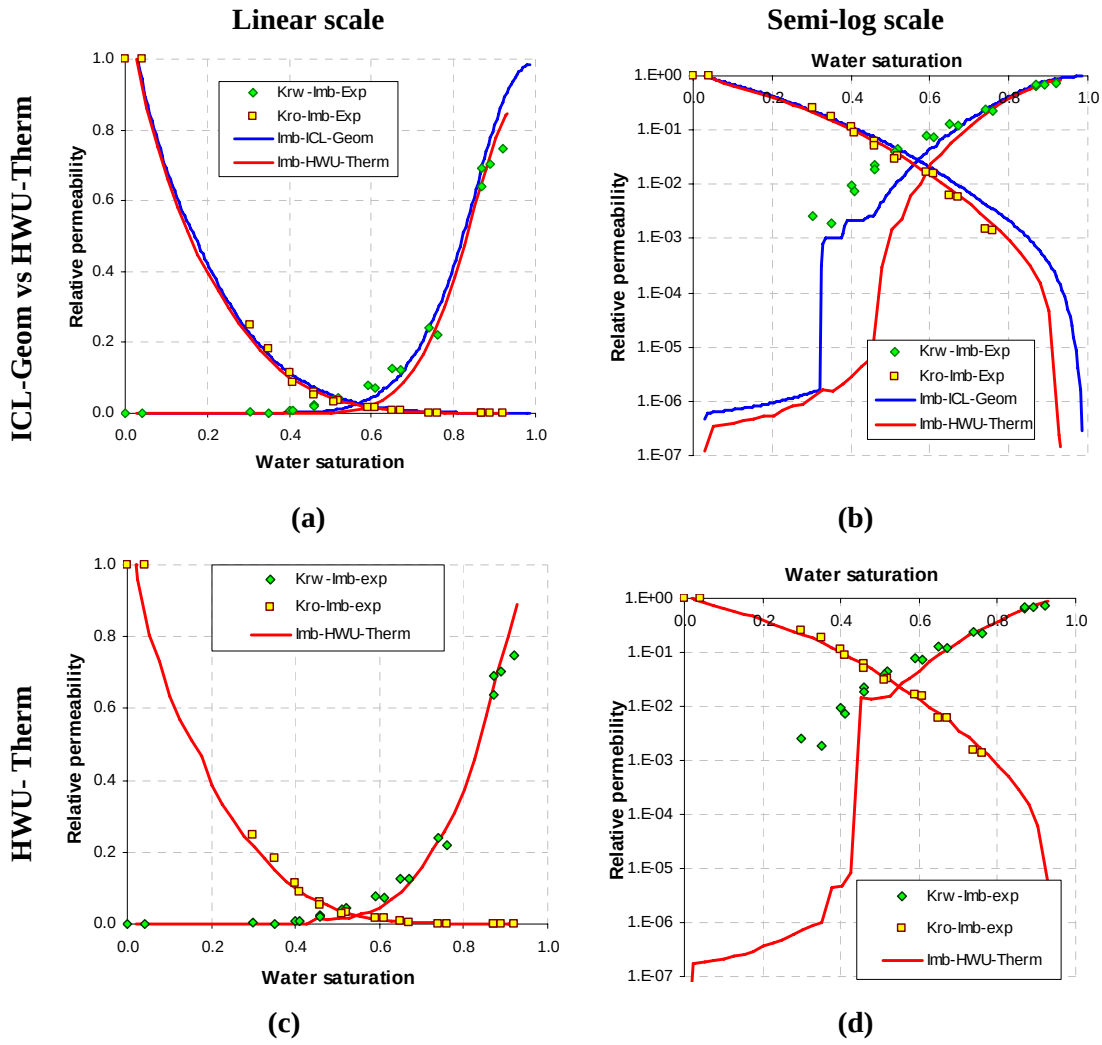

Figure 7.3 Comparison of simulated Imbibition relative permeabilities with oil-wet experimental data (BereaPB network) (a,b) - HWU model with Therm vs ICL model with Geom; (c,d) HWU model with Therm and with modified wettability distribution (see HWU model in **Table 7.2**)

This exercise shows that using the correct layers existence criteria is a significant step towards the improved prediction of waterflood residual oil saturations. Additionally, relative permeabilities can be predicted in principle, but this critically depends on accurate estimation of the wettability distribution. This distribution must be obtained from other data, for example waterflood capillary pressures or the composition of the porous medium.

7.4 Modelling Waterflood Recovery data for Mixed-wet Berea Sandstone cores

The effect of wettability on oil recovery efficiency has been reported experimentally by Jadhunandan and Morrow (1995) and has also been numerically studied by a number of researchers (McDougall and Sorbie 1995, Øren and Bakke 2003, Valvatne and Blunt

2004) (for details see review in Section 2.9.3). They used a number of Berea sandstone core samples to perform slow-rate waterfloods. Initially, oil primary drainage was performed to some initial water saturation S_{wi}. Then, after ageing, up to 20 pore volumes of water were injected. During the waterflood the remaining oil saturations and the corresponding oil recoveries were measured. Note that the remaining oil saturation is not the true residual S_{or}, but it is the oil saturation at some fixed condition, such as a predetermined end point capillary pressure, pressure gradient or indeed number of pore volumes injected (Skauge and Ottesen 2002, Høiland et al. 2007), and as discussed in Section 2.9. Jadhunandan and Morrow determined the Amott-Harvey wettability index I_{wo} by the modified Amott approach (Boneau and Clampitt 1977) and presented the remaining oil saturations as functions of I_{wo}.

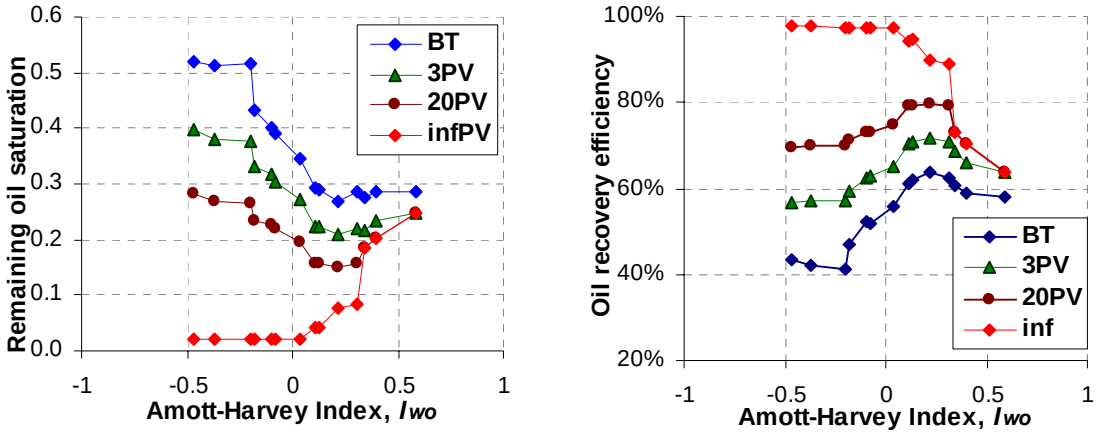

Figure 7.4 Calculated remaining oil saturations (a) and oil recovery efficiencies (b) vs Amott-Harvey wettability index I_{wo}, after different numbers of pore volumes (PV) injected (BT is breakthrough and infPV is infinite pore volumes) from a Buckley-Leverett analysis based on network simulations using the parameters in **Table 7.3**.

Using network simulated waterflooding relative permeabilities in the Buckley-Leverett analysis (Dullien 1992) the remaining oil saturation and oil recovery were estimated after breakthrough, after 3 and after 20 pore volumes (PV) of water injection. This analysis was first presented by Welge (1952), who used the advancing water front solution (Leverett 1941, Buckley and Leverett 1942) to derive an equation relating the average water saturation behind the water front and hence the oil recovery and remaining oil saturation, the cumulative water injected (in pore volumes) to the water fractional flow.

To match the Jadhunandan and Morrow (1995) data we used the *BereaPB* network and the same input data set as in the *ICL* study (Valvatne and Blunt 2004). Apart from the *with PB* model as it was used by Valvatne and Blunt (2004), we also considered the *without PB* model, since we noticed that for water-wet data points the S_{or} was overpredicted for the *with PB* model, which was probably caused by PBF I_n events. We also applied the *Therm* oil layers existence criteria instead of *Geom*. Each case (data point) corresponds to one of the waterflooding experiments on individual core samples. To match the (experimental) target connate water saturation S_{wc}^{targ}, a fraction of the pore space was assumed to consist of clay bound porosity, similar to the *ICL* study. To achieve this, a constant fraction α_{cl}^{*} of each pore element was assumed to be occupied by clay bound water, satisfying

$$\alpha_{cl}^{*} = \frac{S_{wc}^{targ} - S_{wc}^{\text{int}}}{1 - S_{wc}^{\text{int}}}, \tag{7.1}$$

This formula is different from Eq. (6.1)**,** since here we keep the total porosity constant, whereas in Section 6.2 the porosity is increased by φ_{cl}.

The network is assumed to be strongly water-wet during primary drainage with θ_{dr} =0. Drainage is terminated at the initial water saturation S_{wi} which is taken from the laboratory experiments. The target S_{wc}^{targ} is identified as S_{wi} for S_{wi}<0.22, otherwise S_{wc}^{targ} is assumed to be 0.22, since the experiment description indicates that it cannot be more than 22% (Jadhunandan and Morrow 1995).

After ageing the advancing contact angles are assigned according to a mixed-wet large (MWL) distribution with oil-wet fraction α chosen from the largest pores. Valvatne and Blunt (2004) proposed an iterative method for pore-to-pore scale wettability characterization based on matching the measured Amott indices I_w and I_o (see Section 2.6.2). For each wettability case the oil-wet fraction α is adjusted by matching the Amott water index I_w, whereas the contact angle distribution in the oil-wet pores is specified by matching the Amott oil index I_o. More specifically, the advancing contact angle for the water-wet oil-filled pores is uniformly distributed as UWW with $\theta_a^{ww} \in \left[56^{\circ}, 76^{\circ}\right]$, while the contact angle distribution for the oil-wet oil-filled pores is taken as UOW with $\theta_a^{ow} \in \left[117^{\circ}, \theta_a^{ow,\max}\right]$, where $\theta_a^{ow,\max}$ is adjusted to match I_o. All parameters $I_{wo}, I_w, I_o, S_{wc}^{targ}, S_{wi}, \alpha, \theta_a^{ow,\max}$ for the 14 cases are presented in **Table 7.3**.

The remaining oil saturations and corresponding oil recoveries (fraction of initial oil volume that has been displaced) derived from the Buckley-Leverett analysis using network waterflooding relative permeabilities are plotted against the measured Amott-Harvey wettability index I_{wo} after different pore volumes injected in **Figure 7.4**. The infinite pore volumes case (non-fixed P_c case in Section 6.3.2) corresponds to the true residual oil and ultimate oil recovery. Similar to sensitivities to the endpoint P_c values higher than the non-fixed $P_{c,\min}^{imb}$ (Section 6.3.2**, Figure 6.7**), the trend of remaining oil versus (finite) number of pore volumes injected is non-monotonic (**Figure 7.4a**). Although there is no direct relation between the number of PV injected and the network modelling endpoint P_c (Section 6.3.2), the remaining S_o for given PV (**Figure 7.4a**) can be matched to the network modelling remaining oil (Section 6.3.2**, Figure 6.7**) by adjusting the endpoint P_c. As indicated in **Figure 7.4a** the minimum remaining oil saturation and hence the maximum oil recovery occur at weakly water-wet conditions for all finite PVs, as defined by the small positive Amott-Harvey index I_{wo}. The true residual oil saturation reaches its minimum at strongly oil-wet conditions and thus is significantly lower than the remaining oil saturation after injection of as many as 20 pore volumes, especially for the oil-wet cases.

The calculated results based on our *without PB* model (**Figure 7.4**) and experimental data (Jadhunandan and Morrow 1995), show very good quantitative agreement (**Figure 7.5**). Remaining S_o versus wettability (oil-wet fraction) for the Jadhunandan and Morrow data (1995) was previously modelled (see Section 2.9.3). McDougall and Sorbie (1995) obtained only qualitative agreement. In the study by Valvatne and Blunt (2004), reasonable quantitative agreement with the experiments was obtained only for 3PV, but otherwise, especially at BT, agreement was poor. Similar lack of agreement was found in the study by Øren and Bakke (2003). Although there is a slight underprediction for the 3PV case in our results (see **Figure 7.5**), overall they represent a significant improvement on the earlier simulations of the same experiments by Valvatne and Blunt (2004).

Moreover, although the wettability distributions have to be matched using the Amott indices, the agreement between simulation and experiment at BT extends to 3 and 20 PV injected, without further adjustment of the parameters. This is an indication of true predictive capability of our model.

Comparison between experimental S_{or} (RF) and corresponding calculated values for the *with PB* case (with *Therm* oil layers existence criterion) shows a relatively poor agreement (see **Figure 7.6**) similar to the comparison by Valvatne (2004) (*Geom* oil layers existence criterion). Observe that the deviation between experimental and calculated values is bigger for the more water wet cases (I_{wo}>0.3). As mentioned above, this might be the consequence of the non-rigorous parametric formulation for PBF I_n events in fractionally–wet systems. Notice that the presented contact angles data set is not optimal and our *with PB* model results can be improved by identifying contact angles while matching the experiments separately.

Table 7.3 Input parameters for matching mixed-wet waterflooding experiments, including $I_{wo,}$ $I_{w,}$ I_o and S_{wi} taken from the experiments by Jadhunandan and Morrow (1995)

N	I_w	I_o	I_{wo}	Connate water saturation S_{wc}^{targ},%	Initial water saturation S_{wi},%	Oil-wet fraction, α	Oil-wet advancing contact angle, upper bound $\theta_a^{ow,\max}$, degrees
1	0.00	0.47	-0.47	7.90	7.90	1.00	178
2	0.00	0.37	-0.37	11.29	11.29	1.00	177
3	0.00	0.20	-0.20	12.09	12.09	1.00	173
4	0.02	0.20	-0.18	18.07	18.07	0.99	173
5	0.05	0.15	-0.10	15.87	15.87	0.97	172
6	0.05	0.13	-0.08	18.77	18.77	0.97	172
7	0.08	0.04	0.04	22.75	22.75	0.95	170
8	0.13	0.02	0.11	22.75	24.95	0.90	170
9	0.20	0.07	0.13	22.75	24.25	0.84	171
10	0.26	0.04	0.22	22.75	26.64	0.79	170
11	0.34	0.03	0.31	22.75	24.95	0.73	170
12	0.34	0.00	0.34	22.75	31.12	0.73	169
13	0.40	0.00	0.40	22.75	31.62	0.68	167
14	0.59	0.00	0.59	22.75	32.02	0.60	167

7.5 Summary and Conclusions

To validate the pore-scale network model, comparisons with relative permeability data for both a water-wet and an oil-wet Berea sandstone have been made. For the *BereaPB* network a very good match has been achieved with the water-wet Berea sandstone

experimental data by Oak (1990). For the *BereaCT* network we have considered the two pore shape approximations *CTS* and *Star* to match Oak's data. Both pore shape approximations gave very good agreement with the drainage curves, but the *Star* approach gave a better match of the imbibition curves. Thus, the water-wet experiments can be matched straightforwardly if the geometrically and topologically equivalent network is extracted from the pore space reconstruction of the same rock. In particular, the more accurate pore shape characterization *Star* should be used when possible to identify the wettability distribution more accurately.

The modified *BereaPB* network has been used to improve the match of oil-wet sandstone water flooding relative permeabilities (Valvatne and Blunt 2004). Using the oil layers existence scenario *Therm* instead of *Geom* and a less oil-wet network, our calculations showed a much improved agreement with experiments than obtained by Valvatne and Blunt (2004). This exercise has shown that using the correct layers existence criteria is a significant step towards prediction of waterflood residual oil saturation. Additionally, relative permeabilities can be predicted in principle, but this critically depends on accurate estimation of the wettability distribution. This distribution must be obtained from other data, for example waterflood capillary pressures or the composition of the porous medium.

The *BereaPB* network has also been used to match mixed-wet waterflooding recovery experimental data by Jadhunandan and Morrow (1995). Using the network simulated waterflooding relative permeabilities in the Buckley-Leverett analysis (Welge approach (1952)) the remaining oil saturation and oil recovery have been estimated after breakthrough, 3 and 20 pore volumes injected and these showed very good quantitative agreement with experiments. Contrary to previous attempts to match this data set (Valvatne and Blunt 2004), the good agreement with the remaining oil saturations (or oil recovery) at breakthrough, as well as for 3 and 20 PV injected without further adjustment of the parameters is an indication of true predictive capability of our model.

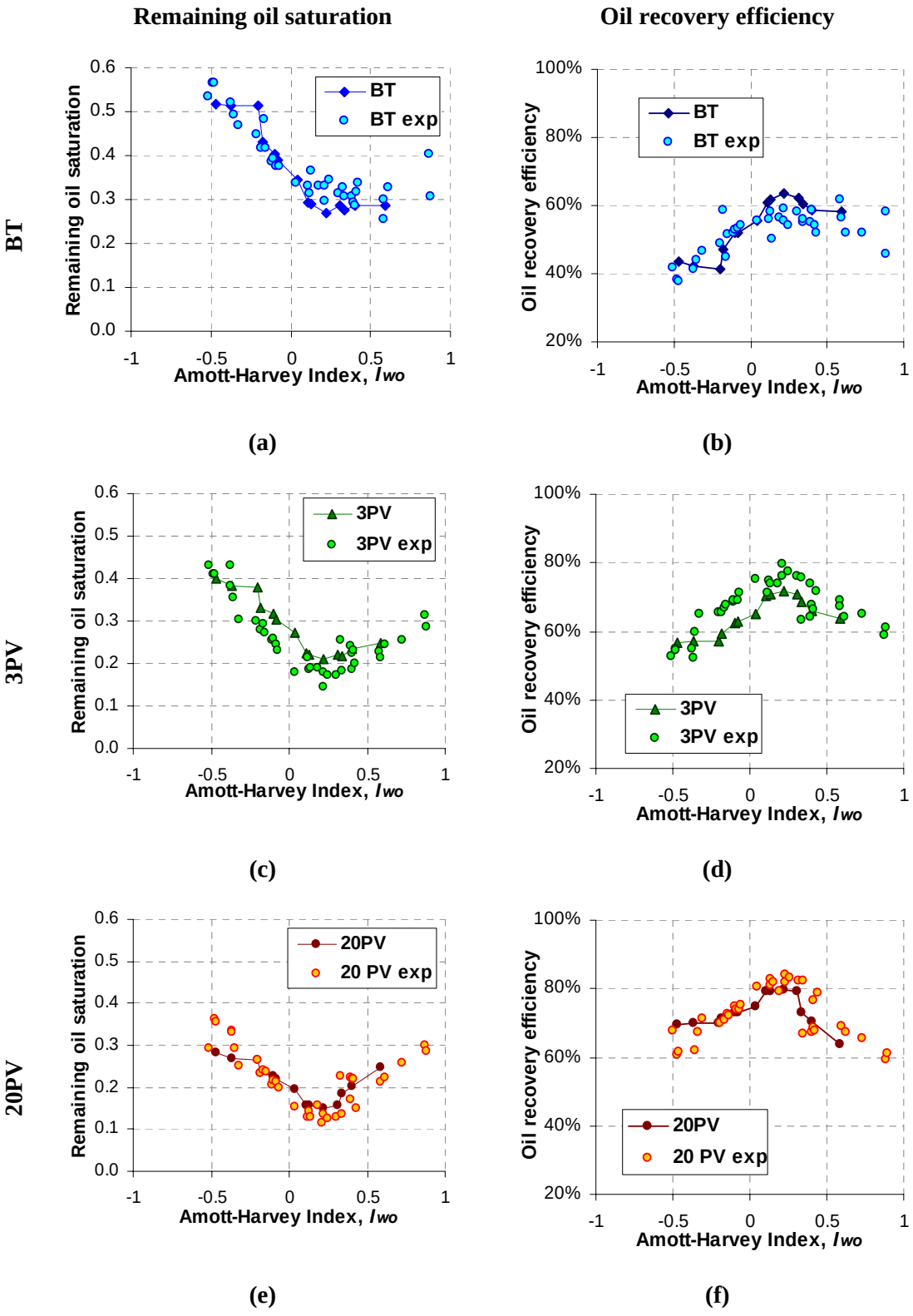

Figure 7.5 Calculated and experimental remaining oil saturations (a,c,e) and oil recovery efficiencies (b,d,f) vs Amott-Harvey wettability index I_{wo} (experimental data by Jadhunandan and Morrow (1995). *Without PB* case.

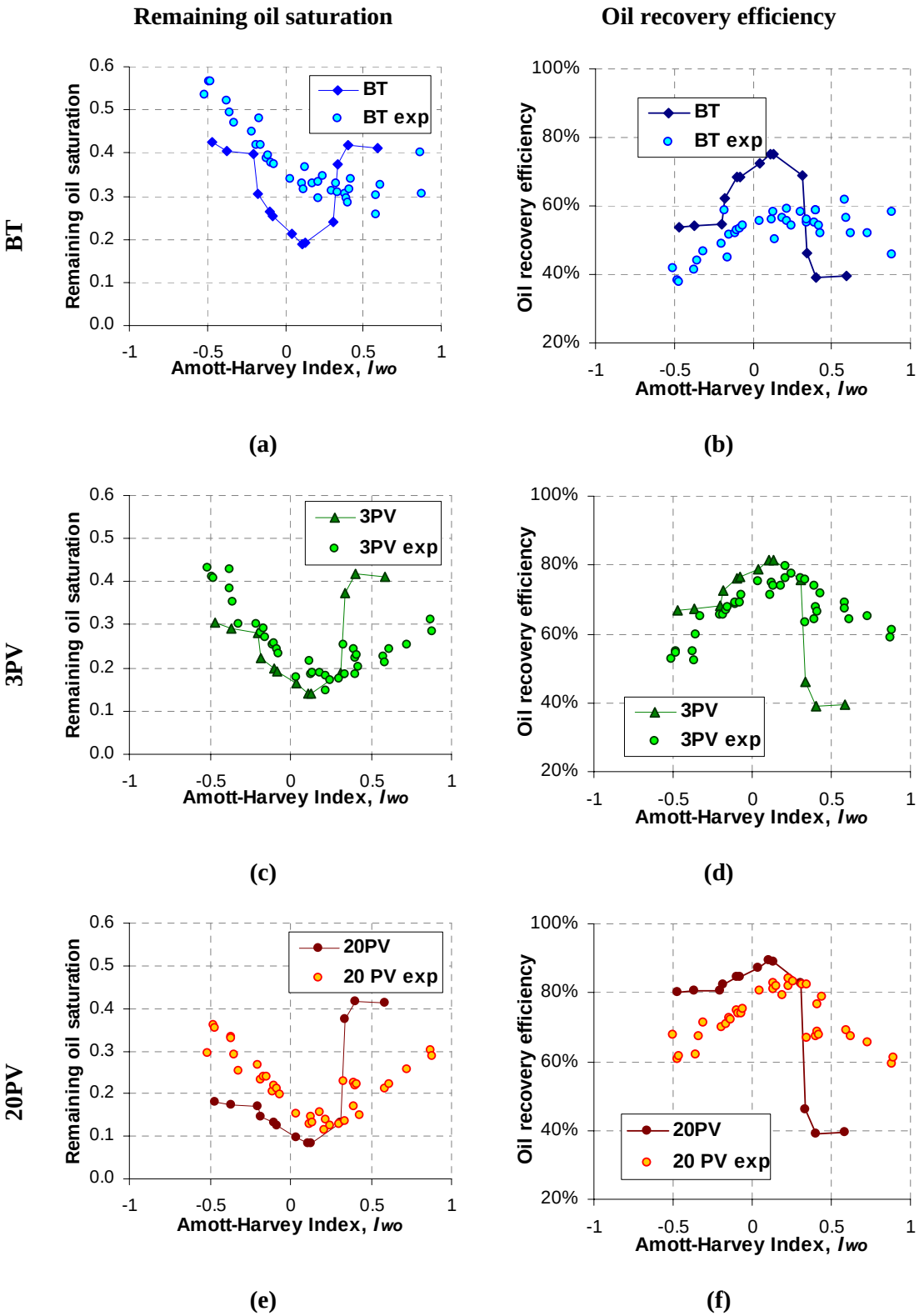

Figure 7.6 Calculated and experimental remaining oil saturations (a,c,e) and oil recovery efficiencies (b,d,f) vs Amott-Harvey wettability index I_{wo} (experimental data by Jadhunandan and Morrow (1995)). *With PB* case.

CHAPTER 8 - CONCLUSIONS

Since EOR methods mobilize oil trapped by capillary and viscosity forces during waterflooding, the prediction of residual oil saturation (S_{or}) after waterflooding is very important before carrying out improved oil recovery process. The mechanism through which a particular EOR method, such as gas displacement, actually works to reduce residual oil depends in turn on how that oil is trapped at the pore scale. In this respect, pore-scale network modelling can be used to estimate both the *nature* of the trapped residual oil and the relevant flow parameters in its subsequent mobilization, if the correct physics of oil drainage are properly included.

8.1 Network model description

In this thesis, we presented a newly developed state-of-the-art pore-scale network modelling tool which takes as input the geometrically and topologically equivalent network (extracted) from a real pore space. This model is used to simulate the 3 consecutive floods: primary drainage followed by an "ageing" step in which wettability is reassigned, water invasion (imbibition) and secondary drainage.

Based on the ageing process and contact angle hysteresis a wettability classification is used to implement various wettability scenarios for the 3 consecutive floods.

Besides the commonly used *CTS* (circle, triangle, square) characterization of the shape of pore cross-sections, which is based on the shape factor, we also introduced a new *n*-cornered star shape characterization technique (*Star*), which takes one extra input parameter, the dimensionless hydraulic radius. In addition, we derived the new relation between *n*-cornered star single-phase conductances and shape factor.

All possible fluid configurations and displacements that can occur during primary drainage, water invasion (after ageing) and secondary drainage have been implemented. All corresponding entry pressure solutions for both the *Star* and *CTS* shapes have been derived and presented. In particular, the existing solutions for the regular n-sided polygons and three-cornered stars have been generalized to n-cornered star shapes. We also focused on stability of oil layers that can exist in the corners of pores with non-uniform wettability caused by ageing. Recently, van Dijke and Sorbie (2006) derived a

thermodynamically based criterion (*Therm*) for the existence of these oil layers. This criterion is consistent with the MS-P derived entry pressures for water invasion displacements and it is more restrictive than the previously used geometrically based criterion (*Geom*). The *Geom* criterion was later adjusted as *Geom2* to make it more consistent with other water invasion entry pressures. *Geom2* is less restrictive than *Therm* but more restrictive than *Geom*.

8.2 Simulation studies

The accuracy of real pore shape approximation by *CTS* and *Star* approaches has been investigated based on a set of 70 real pore shapes with the shape factor and dimensionless hydraulic radius as input parameters. Initially, the approximation error of various resulting pore flow parameters was estimated for each real pore shape. Finally, predictive capabilities of the characterizations were tested based on a capillary bundle model constructed from these 70 pores.

Two networks have been used for a number of sensitivities of the water invasion residual oil saturation and relative permeabilities: *BereaPB*, extracted from a process based reconstruction of a Berea sandstone, and *BereaCT*, extracted from a 3D CT image of a different Berea sample. For *BereaPB* pore shapes are represented by *CTS*, while for *BereaCT* both the *CTS* and the *Star* approaches have been used. We have considered two variants of the model: *without pore bodies* (*PB*) and *with pore bodies.*

For the first case *without PB,* we used both networks (*BereaPB* with *CTS*, *BereaCT* with *Star*). The oil residuals S_{or} have been estimated for different oil layers existence scenarios (*Therm, Geom, Geom2*) and various wettability scenarios, by varying the contact angles in oil-filled pores after ageing from weakly to strongly oil-wet. Moreover, a sensitivity analysis has been carried out of remaining oil saturation with respect to water flood end-point capillary pressures.

For the case *with PB* the *BereaCT* network has been used for various sensitivity calculations. Firstly, we implemented sensitivity of residual oil saturation S_{or} with respect to average advancing contact angle and oil-wet fractions. Then, two further sensitivities studies on relative permeability were carried out as follows: 1) sensitivity to average advancing contact angle θ_a for a uniformly oil-wet system (fraction of oil-wet

pores α=1.0), for *CTS* with *Geom* and *Therm* scenario, as well as for *Star* with *Therm* scenario; and 2) sensitivity to α with θ_a =175 degrees, for *CTS* and *Star* with *Therm* scenario.

Both networks *BereaPB* and *BereaCT* have been used to compare simulated relative permeabilities with the water-wet experiments of Oak (1990). The modified *BereaPB* network has been used to improve the match of oil-wet sandstone water flooding relative permeabilities (Valvatne and Blunt 2004). The *BereaPB* network has also been used to match mixed-wet waterflooding recovery experimental data by Jadhunandan and Morrow (1995).

8.3 Results and Conclusions

The accuracy of real pore shape approximation by *CTS* and *Star* approaches has been estimated from a comparison of the corresponding calculated pore and flow parameters. The comparison has shown that:

- In general, the predictions made by the *Star* pore model are more accurate than those by *CTS*, especially for pore area and conductance
- Larger errors occurred in all approximations for the larger pores, as these had more irregular and non-convex shapes.
- The Star entry radii follow the real shape entry radii quite closely, but the *CTS* approximation is poor for the very non-convex shapes.

Using the real shapes as well as their approximations (*CTS* and *Star*) in a capillary bundle model has shown that:

- The *n*-cornered star provides a very good approximation of the real shape capillary pressure curve, while *CTS* gives a significant underprediction, which follows from poor prediction of the areas.
- Very good approximations of the relative permeability curves were obtained using both approximations despite the poor conductance approximation by *CTS*.

From the sensitivities for both *Berea* networks *without PB* the following conclusions have been made:

- The thermodynamically based oil layers existence scenario *Therm* gives realistic non-zero residual oil saturations compared with the other scenarios. The geometrically based inconsistent layer existence scenario *Geom* is least

restrictive and produces near-zero oil residuals, even for intermediate oil-wet cases.

- The more strongly oil-wet cases lead to lower oil residuals, which can be explained from improved oil phase continuity resulting from the abundant presence of oil layers.
- However, for prescribed end-point capillary pressures, higher than that corresponding to the residual oil saturation, remaining oil saturations are lower for intermediate oil-wet cases.

For the *BereaCT* network *with PB*, sensitivity of residual oil saturation S_{or} has shown that S_{or} decreases with increasing average contact angle (beyond θ_a of around 115 degrees) with a more rapid decline for the higher oil-wet fractions and S_{or} decreases with increasing oil-wet fraction. Modelling pore shapes by *Star*, rather than by *CTS*, has a significant effect on S_{or} for the larger contact angles, as the S_{or} range for *Star* is narrower compared to that for *CTS*.

For relative permeabilities sensitivity 1 (varying advancing contact angle), the less restrictive oil layers existence scenario *Geom* produces lower S_{or} and higher K_{rw} end-points compared to the more restrictive *Therm* scenario. The K_{rw} curves for *Geom* are very similar for all values of θ_a, at the higher S_w, while for *Therm* the K_{rw} curves increase gradually with θ_a. For sensitivity 2 (varying fractions of oil-wet pores), contrary to sensitivity 1, the relative permeability crossovers show a significant shift towards low S_w, as the oil-wet fraction α increases. The K_{ro} curves have two opposite trends as α increases: a decrease at low S_w values and an increase at high S_w values. For both sensitivities, the *Star* curves show lower K_{rw} values, lower K_{rw} end-points and significantly higher S_{or} compared to the corresponding *CTS* curves.

For the *BereaPB* (*CTS*) network, a very good match has been achieved with the water-wet Berea sandstone experimental data by Oak (1990). For the *BereaCT* network both pore shape approximations gave very good agreement with the drainage curves, but the *Star* approach gave a better match of the imbibition curves. Thus, the water-wet experiments can be matched straightforwardly if the GT network is extracted from the pore space reconstruction of the same rock. In particular, the more accurate pore shape

characterization *Star* should be used when possible to identify the wettability distribution more accurately.

Using the oil layers existence scenario *Therm* instead of *Geom* and a less oil-wet network, our calculations showed an improved agreement with experiments than obtained by Valvatne and Blunt (2004). This exercise has shown that using the correct layers existence criteria is a significant step towards the accurate calculation of waterflood residual oil saturation. Additionally, relative permeabilities can be predicted in principle, but this critically depends on accurate estimation of the wettability distribution.

Using the network simulated waterflooding relative permeabilities in the Buckley-Leverett analysis (Welge approach (1952)) the remaining oil saturation and oil recovery have been estimated after breakthrough, 3 and 20 pore volumes injected and these showed very good quantitative agreement with experiments. The good agreement with the remaining oil saturations (or oil recovery) at breakthrough, as well as for 3 and 20 PV injected without further adjustment of the parameters is an indication of improved predictive capability of the pore-scale network model.

8.4 Final conclusions

The most important contribution of this work is the introduction of a new model of oil trapping in systems of arbitrary wettability by incorporating the correct physics of oil layer existence and collapse. This improves our understanding of the distribution of the residual oil and it provides a tool for more accurate estimation of S_{or} and relative permeabilities. In addition, this improved description of the nature of the trapped oil will greatly assist in assessing the mechanics of subsequent tertiary displacement of this residual oil by gas injection for example.

Pore shape has been shown to be a very important network parameter, especially in situations where oil layers exist. For example, we may try to match S_{or} through variation of the contact angles and then predict the relative permeabilities. However, the comparison of calculated results with lab data will probably be poor even if we try different wettability scenarios. In this case, the pore shape must be adjusted as well as the other geometrical network parameters.

Network modelling is a central component of numerical (digital) petrophysics, which includes pore space reconstruction, network extraction and finally the direct pore-scale simulation of fluid displacements. With our new modelling tool, we expect that the digital petrophysics approach will become more attractive, more reliable and better founded on the underlying physics of multiphase flow in mixed and fractionally wet rocks.

8.5 Suggestions for further work

The model developed in this thesis has been shown to be a useful modelling tool for two-phase flow in non-uniformly wetted porous media.. However, we believe that much future work remains in the area of pore scale modelling, as follows

- Our model can be extended to simulate ***three phase*** flow, including more complex cross-sectional fluid configurations and multiple displacements, for example: gas- displacing oil displacing water and so on, which require much additional computational power to model.
- The computational efficiency of our pore scale model needs to be improved using faster pressure solvers (Algebraic MultiGrid solver) and more efficient search algorithms for trapped cluster identification.
- Structure and spatial distribution of S_{or} can be visualized and analyzed for different wettability scenarios, based on the different cross-sectional pore occupancies of bulk phase, films and layers, to guide the choice of EOR techniques.
- Wettability alterations due to salinity effects can be simulated by including the effect of transported ions in the aqueous phase using the outline physics of our existing model.
- Dynamic effects can be incorporated into our pore scale model to simulate processes where, in addition to capillary forces viscous effects become important, for example under high injection rates and during near-miscible gas injection.
- Much work remains to be done on the representation of **wettability** in pore scale network models. The Kovscek type model is universally used in current network simulators but it has not been proved rigorously that this model is valid and this requires further study.

- The issue of pore shape characterisation has been shown to be important in our work. However, it is still not certain if what is done at present is *sufficient* to model all types of rock system. For example, should multiple shapes be used (rather like the CTS system) for different micro- and macro-pore systems in carbonates?
- We have applied pore scale modelling only to homogeneous sandstone examples in this work. Such calculations can also be performed for systems of pore networks for the other rock types e.g. siltstones, carbonates, shales etc., although in these rocks larger variations of pore sizes are expected.

LIST OF REFERENCES

Al-Futaisi A. and T.W. Patzek, 2003a, *Extension of Hoshen-Kopelman algorithm to non-lattice environments*, Physica a-Statistical Mechanics and Its Applications, **321**(3-4), 665-678.

Al-Futaisi A. and T.W. Patzek, 2003b, *Impact of wettability alteration on two-phase flow characteristics of sandstones: A quasi-static description*, Water Resources Research, **39**(2).

Al-Futaisi A. and T.W. Patzek, 2003c, *Three-phase hydraulic conductances in angular capillaries*, SPE Journal, **8**(3), 252-261.

Al-Futaisi A. and T.W. Patzek, 2004, *Secondary imbibition in NAPL-invaded mixed-wet sediments*, Journal of Contaminant Hydrology, **74**(1-4), 61-81.

Al-Gharbi M.S. and M.J. Blunt, 2004, *2D dynamic pore-scale network model of imbibition*, Computational Methods in Water Resources, Vols 1 and 2, **55**, 71-82.

Al-Gharbi M.S. and M.J. Blunt, 2005, *Dynamic network modeling of two-phase drainage in porous media*, Physical Review E, **71**(1).

Al-Kharusi A.S. and M.J. Blunt, 2007, *Network extraction from sandstone and carbonate pore space images*, Journal of Petroleum Science and Engineering, **56**(4), 219-231.

Amott E., 1959, *Observations Relating to the Wettability of Porous Rock*, Trans AIME, **216**, 156-162.

Anderson W.G., 1986, *Wettability literature survey .2. wettability measurement*, Journal of Petroleum Technology, **38**(12), 1246-1262.

Anderson W.G., 1987a, *Wettability literature survey .5. the effects of wettability on relative permeability*, Journal of Petroleum Technology, **39**(11), 1453-1468.

Anderson W.G., 1987b, *Wettability literature survey .6. the effects of wettability on waterflooding*, Journal of Petroleum Technology, **39**(12), 1605-1622.

Bakke S. and P.E. Øren, 1997, *3-D pore-scale modeling of sandstone and flow simulations in pore networks*, SPE J, **2**(2), 136-149.

Blunt M.J., 1997a, *Effects of heterogeneity and wetting on relative permeability using pore level modeling*, SPE Journal, **2**(1), 70-87.

Blunt M.J., 1997b, *Pore level modeling of the effects of wettability*, SPE J, **2**(4), 494-510.

Blunt M.J., 1998, *Physically-based network modeling of multiphase flow in intermediate-wet porous media*, Journal of Petroleum Science and Engineering, **20**(3-4), 117-125.

Blunt M.J. and H. Scher, 1995, *Pore-level modeling of wetting*, Physical Review E, **52**(6), 6387.

Boneau D.F. and R.L. Clampitt, 1977, *Surfactant system for oil-wet sandstone of north burbank unit*, Journal of Petroleum Technology, **29**(MAY), 501-506.

Brown R.J.S. and I. Fatt, 1956, *Measurements Of Fractional Wettability Of Oil Fields' Rocks By The Nuclear Magnetic Relaxation Method*, In Fall Meeting of the Petroleum Branch of AIME, Los Angeles, California: American Institute of Mining, Metallurgical, and Petroleum Engineers.

Bryant S. and M. Blunt, 1992, *Prediction of relative permeability in simple porous-media*, Physical Review A, **46**(4), 2004-2011.

Bryant S. and S. Raikes, 1995, *Prediction of elastic-wave velocities in sandstones using structural models*, Geophysics, **60**(2), 437-446.

Bryant S.L., P.R. King and D.W. Mellor, 1993a, *Network model evaluation of permeability and spatial correlation in a real random sphere packing*, Transport in Porous Media, **11**(1), 53-70.

Bryant S.L., D.W. Mellor and C.A. Cade, 1993b, *Physically representative network models of transport in porous media*, Aiche Journal, **39**(3), 387-396.

Buckley J.S., 1995, *Asphaltene Precipitation and Crude Oil Wetting*, SPE Advanced Technology Series, **3**(1), 53-59.

Buckley J.S., 1996, *Mechanisms and Consequences of Wettability Alteration by Crude Oils*, In Department of Petroleum Engineering, PhD Thesis, Edinburgh: Heriot-Watt University.

Buckley J.S., C. Bousseau and Y. Liu, 1996, *Wetting alteration by brine and crude oil: from contact angles to cores*, SPE Journal, **1**(3), 341-350.

Buckley J.S., K. Takamura and N.R. Morrow, 1989, *Influence of Electrical Surface Charges on the Wetting Properties of Crude Oils*, SPE Reservoir Engineering, **4**(3), 332-340.

Buckley S.E. and M.C. Leverett, 1942, *Mechanism of Fluid Displacement in Sands*, Trans AIME, **146**, 107-116.

Coenen J., E. Tchouparova and X. Jing, 2004, *Measurement parameters and resolution aspects of micro X-ray tomography for advanced core analysis*, In Proceedings of International Symposium of the SCA, October (2004), Abu Dhabi, UAE.

Coles M.E., R.D. Hazlett, E.L. Muegge, K.W. Jones, B. Andrews, B. Dowd, P. Siddons, A. Peskin, P. Spanne and W.E. Soll, 1996, *Developments in Synchrotron X-Ray Microtomography with Applications to Flow in Porous Media*, In SPE Annual Technical Conference and Exhibition, Denver, Colorado: 1996 Copyright 1996, Society of Petroleum Engineers, Inc.

Constantinides G.N. and A.C. Payatakes, 2000, *Effects of Precursor Wetting Films in Immiscible Displacement Through Porous Media*, Transport in Porous Media, **38**(3), 291-317.

Craig F.F.J., 1971, *The Reservoir Engineering Aspects of Waterflooding*, SPE Monograph Series, **3**, New York: H. L. Doherty Memorial Fund of AIME.

Cuiec L.E., 1991, *Evaluation of Reservoir Wettability and Its Effect on Oil Recovery*. In Interfacial Phenomena in Petroleum Recovery, ed. N.R. Morrow, New York: Marcel Dekker Inc.

Devereux O.F., 1967, *Effect of Crude Oil on the Nuclear Magnetic Relaxation of Water Protons in Sandstone*, Nature, **215**(5101), 614-615.

Dias M.M. and D. Wilkinson, 1986, *Percolation with trapping*, Journal of Physics A: Mathematical and General, **19**(15), 3131.

Dixit A.B., J.S. Buckley, S.R. Mcdougall and K.S. Sorbie, 2000, *Empirical measures of wettability in porous media and the relationship between them derived from pore-scale modelling*, Transport in Porous Media, **40**(1), 27-54.

Dixit A.B., S.R. Mcdougall, K.S. Sorbie and J.S. Buckley, 1999, *Pore-scale modeling of wettability effects and their influence on oil recovery*, SPE Reservoir Evaluation & Engineering, **2**(1), 25-36.

Donaldson E.C. and R.D. Thomas, 1971, *Microscopic Observations of Oil Displacement in Water-Wet and Oil-Wet Systems*, In Fall Meeting of the Society of Petroleum Engineers of AIME, New Orleans, Louisiana: 1971.

Donaldson E.C., R.D. Thomas and P.B. Lorenz, 1969, *Wettability Determination and Its Effect on Recovery Efficiency*, SPE Journal, **9**(1), 13 - 20.

Dong H. and M.J. Blunt, 2009a, *Pore-network extraction from micro-computerized-tomography images*, Physical Review E - Statistical, Nonlinear, and Soft Matter Physics, **80**(3).

Dong H. and M.J. Blunt, 2009b, *Pore-network extraction from micro-computerized-tomography images*, Physical Review E, **80**(3), 036307.

Dong H., M. Touati and M.J. Blunt, 2007, *Pore network modeling: Analysis of pore size distribution of arabian core samples*, In SPE Middle East Oil and Gas Show and Conference, MEOS, Proceedings, Bahrain, Bahrain: Society of Petroleum Engineers (SPE).

Dullien F.A.L., 1992, *Porous media: fluid transport and pore structure*, 2nd Edition, San Diego, Calif.: Academic Press.

Dunsmuir J.H., S.R. Ferguson, K.L. D'amico and J.P. Stokes, 1991, *X-Ray Microtomography: A New Tool for the Characterization of Porous Media*, In SPE Annual Technical Conference and Exhibition, Dallas, Texas: 1991 Copyright 1991, Society of Petroleum Engineers, Inc.

Fassi-Fihri O., M. Robin and E. Rosenberg, 1995, *Wettability Studies at the Pore Level: A New Approach by the Use of Cryo-Scanning Electron Microscopy*, SPE Formation Evaluation, **10**(1), 11-19.

Fenwick D.H. and M.J. Blunt, 1998a, *Network Modeling of Three-Phase Flow in Porous Media*, SPE Journal, **3**(1), 86-97.

Fenwick D.H. and M.J. Blunt, 1998b, *Three-dimensional modeling of three phase imbibition and drainage*, Advances in Water Resources, **21**(2), 121-143.

Frette O.I. and J.O. Helland, 2010, *A semi-analytical model for computation of capillary entry pressures and fluid configurations in uniformly-wet pore spaces from 2D rock images*, Advances in Water Resources, **33**(8), 846-866.

Helland J.O. and O.I. Frette, 2010, *Computation of fluid configurations and capillary pressures in mixed-wet 2D pore spaces from rock images*, In Proceedings - Computational Methods in Water Resources XVI International Conference (CMWR XVIII), Barcelona, Spain.

Helland J.O., A.V. Ryazanov and M.I.J. Van Dijke, 2008, *Characterization of pore shapes for pore network models*, In Proceedings of the 11th European Conference on the Mathematics of Oil Recovery (ECMOR XI), September (2008), Bergen, Norway.

Helland J.O. and S.M. Skjaeveland, 2004, *Physically-based capillary pressure correlation for mixed-wet reservoirs from a bundle-of-tubes model*, In Proceedings of the SPE/DOE Improved Oil Recovery Symposium, Tulsa, OK, April (2004)

Helland J.O. and S.M. Skjaeveland, 2006a, *Physically based capillary pressure correlation for mixed-wet reservoirs from a bundle-of-tubes model*, SPE J, **11**(2), 171-180.

Helland J.O. and S.M. Skjaeveland, 2006b, *Three-phase mixed-wet capillary pressure curves from a bundle of triangular tubes model*, Journal of Petroleum Science and Engineering, **52**(1-4), 100-130.

Helland J.O., M.I.J. Van Dijke, K.S. Sorbie and S.M. Skjaeveland, 2006, *Three-phase relative permeability from mixed- wet triangular and star-shaped pores*, In Proceedings of the Symposium on Reservoir Wettability, September (2006), Bergen, Norway.

Hildebrand-Habel T., G. Virnovsky, O.I. Frette and I. And Fjelde., 2007, *SEM imaging of dry and saturated porous rocks for modeling fluid distribution on pore scale*, In Proceedings of International Symposium of the SCA, September (2007), Calgary, Canada.

Høiland L.K., K. Spildo and A. Skauge, 2007, *Fluid flow properties for different classes of intermediate wettability as studied by network modelling*, Transport in Porous Media, **70**(1), 127-146.

Holbrook O.C. and G.G. Bernard, 1958, *Determination of Wettability by Dye Adsorption*, Trans AIME, **213**, 261-264.

Hughes R.G. and M.J. Blunt, 2000, *Pore Scale Modeling of Rate Effects in Imbibition*, Transport in Porous Media, **40**(3), 295-322.

Hui M.H. and M.J. Blunt, 2000a, *Effects of wettability on three-phase flow in porous media*, Journal of Physical Chemistry B, **104**(16), 3833-3845.

Hui M.H. and M.J. Blunt, 2000b, *Pore-Scale Modeling of Three-Phase Flow and the Effects of Wettability*, In SPE/DOE Improved Oil Recovery Symposium, Tulsa, Oklahoma: Copyright 2000, Society of Petroleum Engineers Inc.

Hwang S.-T., 1977, *The Gauss Equation in Capillarity*, Z. Physik. Chemie Neue Folge., **105**(5-6), 225-235.

Jadhunandan P.P. and N.R. Morrow, 1991, *Spontaneous imbibition of water by crude-oil brine rock systems*, In Situ, **15**(4), 319-345.

Jadhunandan P.P. and N.R. Morrow, 1995, *Effect of wettability on waterflood recovery for crude-oil/brine/rock systems*, SPE Reservoir Engineering, **10**(1), 40-46.

Jiang Z., K. Wu, G. Couples, M.I.J. Van Dijke, K.S. Sorbie and J. Ma, 2007, *Efficient extraction of networks from three-dimensional porous media*, Water Resources Research, **43**(12).

Joekar-Niasar V.J., S.M. Hassanizadeh and H.K. Dahle, 2010a, *Non-equilibrium effects in capillarity and interfacial area in two-phase flow: dynamic pore-network modelling*, Journal of Fluid Mechanics, **655**, 38-71.

Joekar-Niasar V.J., M. Prodanovic, D. Wildenschild and S.M. Hassanizadeh, 2010b, *Network model investigation of interfacial area, capillary pressure and saturation relationships in granular porous media*, Water Resources Research, **46**(6), W06526.

Johnson E.F., D.P. Bossler and V.O. Naumann, 1959, *Calculation of Relative Permeability from Displacement Experiments*, Trans AIME, **216**, 370-372.

Kennedy H.T., E.O. Burja and R.S. Boykin, 1955, *An Investigation of the Effects of Wettability on Oil Recovery by Water flooding*, The Journal of Physical Chemistry, **59**(9), 867-869.

Knackstedt M.A., M. Sahimi and A.P. Sheppard, 2000, *Invasion percolation with long-range correlations: First-order phase transition and nonuniversal scaling properties*, Physical Review E, **61**(5), 4920-4934.

Kovscek A.R., H. Wong and C.J. Radke, 1993, *A pore-level scenario for the development of mixed-wettability in oil reservoirs*, Aiche Journal, **39**(6), 1072-1085.

Kumar J., I. Fatt and D.N. Saraf, 1969, *Nuclear magnetic relaxation time of water in a porous medium with heterogeneous surface wettability*, Journal of Applied Physics, **40**(10), 4165-4171.

Lago M. and M. Araujo, 2001, *Threshold pressure in capillaries with polygonal cross section*, Journal of Colloid and Interface Science, **243**(1), 219-226.

Lago M. and M. Araujo, 2003, *Threshold capillary pressure in capillaries with curved sides*, Physica A: Statistical Mechanics and its Applications, **319**, 175-187.

Larsen J.K., N. Bech and A. Winter, 2000, *Three-Phase Immiscible WAG Injection: Micromodel Experiments and Network Models*, In Proceedings of SPE/DOE Improved Oil Recovery Symposium, Tulsa, Oklahoma: 2000,. Society of Petroleum Engineers Inc.

Leach R.O., O.R. Wagner, H.W. Wood and C.F. Harpke, 1962, *A Laboratory and Field Study of Wettability Adjustment in Water Flooding*, SPE Journal of Petroleum Technology, **14**(2), 206-212.

Legait B., 1983, *Laminar flow of two phases through a capillary tube with variable square cross-section*, Journal of Colloid and Interface Science, **96**(1), 28-38.

Lenormand R. and C. Zarcone, 1984, *Role of roughness and edges during imbibition in square capillaries*, In Proceedings - SPE Annual Technical Conference and Exhibition, Houston, TX, USA: Soc of Petroleum Engineers of AIME, USA SPE 13264.

Lenormand R., C. Zarcone and A. Sarr, 1983, *Mechanisms of the displacement of one fluid by another in a network of capillary ducts*, Journal of Fluid Mechanics, **135**(OCT), 337-353.

Lerdahl T.R., P.-E. Øren and S. Bakke, 2000, *A Predictive Network Model for Three-Phase Flow in Porous Media*, In SPE/DOE Improved Oil Recovery Symposium, Tulsa, Oklahoma: Society of Petroleum Engineers.

Leverett M.C., 1941, *Capillary Behavior in Porous Solids*, Trans AIME, **142**, 142-169.

Lindquist W.B., 2006, *The geometry of primary drainage*, Journal of Colloid and Interface Science, **296**(2), 655-668.

Lindquist W.B., S.-M. Lee, D.A. Coker, K.W. Jones and P. Spanne, 1996, *Medial axis analysis of void structure in three-dimensional tomographic images of porous media*, J. Geophys. Res., **101**(B4), 8297-8310.

Lindquist W.B. and A. Venkatarangan, 1999, *Investigating 3D geometry of porous media from high resolution images*, Physics and Chemistry of the Earth Part a-Solid Earth and Geodesy, **24**(7), 593-599.

Lorenz P.B., E.C. Donaldson and R.D. Thomas, 1974, *Use of centrifugal measurements of wettability to predict oil recovery*, Report of Investigations - United States, Bureau of Mines, (7873).

Lucia F.J., 2007, *Carbonate Reservoir Characterization*, Second Edition, Berlin: Springer.

Ma S.X., G. Mason and N.R. Morrow, 1996, *Effect of contact angle on drainage and imbibition in regular polygonal tubes*, Colloids and Surfaces a-Physicochemical and Engineering Aspects, **117**(3), 273-291.

Man H.N. and X.D. Jing, 2000, *Pore network modelling of electrical resistivity and capillary pressure characteristics*, Transport in Porous Media, **41**(3), 263-286.

Man H.N. and X.D. Jing, 2001, *Network modelling of strong and intermediate wettability on electrical resistivity and capillary pressure*, Advances in Water Resources, **24**(3-4), 345-363.

Mason G. and N.R. Morrow, 1984, *Meniscus curvatures in capillaries of uniform cross-section*, Journal of the Chemical Society-Faraday Transactions I, **80**, 2375-2393.

Mason G. and N.R. Morrow, 1991, *Capillary behavior of a perfectly wetting liquid in irregular triangular tubes*, Journal of Colloid and Interface Science, **141**(1), 262-274.

Mathworks, 1998, *MATLAB-The Language of Technical Computing*, Natick, Massachusetts: Math-Works, Inc.

Mayer R.P. and R.A. Stowe, 1965, *Mercury porosimetry--breakthrough pressure for penetration between packed spheres*, Journal of Colloid Science, **20**(8), 893.

Mcdougall S.R., A.B. Dixit and K.S. Sorbie, 1996, *The development of a regime-based framework for the analysis of wettability experiments*, Chemical Engineering Research & Design, **74**(A2), 206-219.

Mcdougall S.R. and K.S. Sorbie, 1995, *The impact of wettability on waterflooding - pore-scale simulation*, SPE Reservoir Engineering, **10**(3), 208-213.

Mogensen K. and E.H. Stenby, 1998, *A Dynamic Two-Phase Pore-Scale Model of Imbibition*, Transport in Porous Media, **32**(3), 299-327.

Mohanty K.K., H.T. Davis and L.E. Scriven, 1980, *Physics of Oil Entrapment in Water-Wet Rock*, In Proceedings of 55th Annual Technical Conference of the SPE, Dallas, USA.

Morrow N.R., 1975, *The effects of surface roughness on contact angle with special reference to petroleum recovery*, Journal of Canadian Petroleum Technology, **14**(4), 42-53.

Morrow N.R., P.J. Cram and F.G. Mccaffery, 1973, *Displacement Studies in Dolomite With Wettability Control by Octanoic Acid*, Society of Petroleum Engineers of AIME Journal, **13**(4), 221-232.

Morrow N.R., H.T. Lim and J.S. Ward, 1986, *Effect of Crude-Oil-Induced Wettability Changes on Oil Recovery*, SPE Formation Evaluation, **1**(1), 89-103.

Morse R.A., P.L. Terwillinger and S.T. Yuster, 1947, *Relative Permeability Measurements on Small Core Samples*, Oil and Gas J., 109.

Oak M.J., 1990, *Three-phase relative permeability of water-wet Berea*, In Proceedings of the SPE/DOE Enhanced Oil Recovery Symposium, Tulsa, Oklahoma, USA: Soc of Petroleum Engineers of AIME.

Okabe H. and M.J. Blunt, 2007, *Pore space reconstruction of vuggy carbonates using microtomography and multiple-point statistics*, Water Resour. Res., **43**(12), W12S02.

Or D. and M. Tuller, 1999, *Liquid Retention and Interfacial Area in Variably Saturated Porous Media: Upscaling from Single-Pore to Sample-Scale Model*, Water Resour. Res., **35**(12), 3591-3605.

Øren P.E. and S. Bakke, 2002, *Process based reconstruction of sandstones and prediction of transport properties*, Transport in Porous Media, **46**(2-3), 311-343.

Øren P.E. and S. Bakke, 2003, *Reconstruction of Berea sandstone and pore-scale modelling of wettability effects*, Journal of Petroleum Science and Engineering, **39**(3-4), 177-199.

Øren P.E., S. Bakke and O.J. Arntzen, 1998, *Extending predictive capabilities to network models*, SPE J, **3**(4), 324-336.

Øren P.E. and W.V. Pinczewski, 1995, *Fluid distribution and pore-scale displacement mechanisms in drainage dominated three-phase flow*, Transport in Porous Media, **20**(1), 105-133.

Owens W.W. and D.L. Archer, 1971, *The Effect of Rock Wettability on Oil-Water Relative Permeability Relationships*, SPE Journal of Petroleum Technology, **23**(7), 873-878.

Patzek T.W., 2001, *Verification a complete pore network simulator of drainage and imbibition*, SPE Journal, **6**(2), 144-156.

Patzek T.W. and J.G. Kristensen, 2001, *Shape factor correlations of hydraulic conductance in noncircular capillaries II. Two-phase creeping flow*, Journal of Colloid and Interface Science, **236**(2), 305-317.

Patzek T.W. and D.B. Silin, 2001, *Shape factor and hydraulic conductance in noncircular capillaries I. One-phase creeping flow*, Journal of Colloid and Interface Science, **236**(2), 295-304.

Piri M. and M.J. Blunt, 2002, *Pore-scale modeling of three-phase flow in mixed-wet systems*, In Procedings of SPE Annual Technical Conference and Exhibition, San Antonio, Texas: Copyright 2002, Society of Petroleum Engineers Inc.

Piri M. and M.J. Blunt, 2004, *Three-phase threshold capillary pressures in noncircular capillary tubes with different wettabilities including contact angle hysteresis.*, Physical Review E, **70**(6 Pt 1), 061603.

Piri M. and M.J. Blunt, 2005a, *Three-dimensional mixed-wet random pore-scale network modeling of two- and three-phase flow in porous media. I. Model description*, Physical Review E, **71**.

Piri M. and M.J. Blunt, 2005b, *Three-dimensional mixed-wet random pore-scale network modeling of two- and three-phase flow in porous media. II. Results*, Physical Review E, **71**.

Princen H.M., 1969a, *Capillary phenomena in assemblies of parallel cylinders : I. Capillary rise between two cylinders*, Journal of Colloid and Interface Science, **30**(1), 69.

Princen H.M., 1969b, *Capillary phenomena in assemblies of parallel cylinders : II. Capillary rise in systems with more than two cylinders*, Journal of Colloid and Interface Science, **30**(3), 359.

Princen H.M., 1970, *Capillary phenomena in assemblies of parallel cylinders : III. Liquid Columns between Horizontal Parallel Cylinders*, Journal of Colloid and Interface Science, **34**(2), 171.

Radke C.J., A.R. Kovscek and H. Wong, 1992, *Pore-level scenario for the development of mixed wettability in oil reservoirs*, In Proceedings - SPE Annual Technical Conference and Exhibition, Washington, DC, USA: Publ by Soc of Petroleum Engineers of AIME.

Raza S.H., L.E. Treiber and D.L. Archer, 1968, *Wettability of reservoir rocks and its evaluation*, Prod. Mon., **32**(4), 2-7.

Ryazanov A.V., M.I.J. Van Dijke and K.S. Sorbie, 2008, *Two-phase pore-network modelling with non-uniform wettability: existence of oil layers*, In Proceedings of 10th International Symposium on Evaluation of Reservoir Wettability and Its Effect on Oil Recovery, Abu Dhabi, United Arab Emirates.

Ryazanov A.V., M.I.J. Van Dijke and K.S. Sorbie, 2009, *Two-phase pore-network modelling: existence of oil layers during water invasion*, Transport in Porous Media, **80**(1), 79-99.

Ryazanov A.V., M.I.J. Van Dijke and K.S. Sorbie, 2010a, *Pore-network Prediction of Residual Oil Saturation Based on Oil Layer Drainage in Mixed-wet Systems*, In Proceedings of SPE Improved Oil Recovery Symposium, Tulsa, Oklahoma, USA: Society of Petroleum Engineers.

Ryazanov A.V., M.I.J. Van Dijke and K.S. Sorbie, 2010b, *Prediction of residual oil saturation in mixed-wet networks using accurate pore shape descriptors*, In Proceedings - Computational Methods in Water Resources XVIII International Conference (CMWR XVIII), Barcelona, Spain.

Salathiel R.A., 1973, *Oil recovery by surface film drainage in mixed-wettability rocks*, JPT, Journal of Petroleum Technology, **25**, 1216-1224.

Scott P.R. and P.W. Awyong, 2000, *Inequalities for convex sets*, J. Inequal. Pure Appl. Math., **1**(1).

Sharma M.M. and R.W. Wunderlich, 1985, *The Alteration of Rock Properties Due to Interactions With Drilling Fluid Components*, In Proceeding of SPE Annual Technical Conference and Exhibition, Las Vegas, Nevada.

Sharma M.M. and R.W. Wunderlich, 1987, *The alteration of rock properties due to interactions with drilling-fluid components*, Journal of Petroleum Science and Engineering, **1**(2), 127-143.

Sheppard A.P., M. Sok, H. Averdunk, V. Robins and M. Saadatfar, 2006, *Analysis of Rock microstructure using high-resolution x-ray tomography*, In Proceedings of International Symposium of the Society of Core Analysts, Trondheim, Norway.

Sheppard A.P., R.M. Sok and H. Averdunk, 2005, *Improved pore network extraction methods*, In Proceedings of International Symposium of the Society of Core Analysts, Toronto, Canada.

Silin D. and T. Patzek, 2006, *Pore space morphology analysis using maximal inscribed spheres*, Physica A: Statistical and Theoretical Physics, **371**(2), 336-360.

Silin D.B., G. Jin and T.W. Patzek, 2003, *Robust Determination of the Pore Space Morphology in Sedimentary Rocks*, In SPE Annual Technical Conference and Exhibition, Denver, Colorado: Society of Petroleum Engineers.

Singh M. and K.K. Mohanty, 2003, *Dynamic modeling of drainage through three-dimensional porous materials*, Chemical Engineering Science, **58**(1), 1-18.

Skauge A. and B. Ottesen, 2002, *A Summary of Experimentally derived Relative Permeability and Residual Saturation on North Sea Reservoir Cores*, In Proceedings of International Symposium of the SCA, September (2002), Monterey, CA.

Spanne P., J.F. Thovert, C.J. Jacquin, W.B. Lindquist, K.W. Jones and P.M. Adler, 1994, *Synchrotron Computed Microtomography of Porous Media: Topology and Transports*, Physical Review Letters, **73**(14), 2001.

Stauffer D. and A. Aharony, 1992, *Introduction to percolation theory*, London: Taylor & Francis.

Treiber L.E., D.L. Archer and W.W. Owens, 1972, *A Laboratory Evaluation of the Wettability of Fifty Oil-Producing Reservoirs*, SPE Journal, **12**(6), 531-540.

Tuller M., D. Or and L.M. Dudley, 1999, *Adsorption and Capillary Condensation in Porous Media: Liquid Retention and Interfacial Configurations in Angular Pores*, Water Resour. Res., **35**(7), 1949-1964.

Valvatne P.H., 2004, *Predictive pore-scale modelling of multiphase flow*, In Department of Earth Science and Engineering, PhD Thesis, London: Imperial College London.

Valvatne P.H. and M.J. Blunt, 2004, *Predictive pore-scale modeling of two-phase flow in mixed wet media*, Water Resour. Res., **40**(7).

Valvatne P.H., M. Piri, X. Lopez and M.J. Blunt, 2005, *Predictive pore-scale modeling of single and multiphase flow*, Transport in Porous Media, **58**(1-2), 23-41.

Van Dijke M.I.J., A. Lago, K.S. Sorbie and M. Araujo, 2004, *Free energy balance for three fluid phases in a capillary of arbitrarily shaped cross-section: capillary entry pressures and layers of the intermediate-wetting phase*, Journal of Colloid and Interface Science, **277**(1), 184-201.

Van Dijke M.I.J., M. Piri, J.O. Helland, K.S. Sorbie, M.J. Blunt and S.M. Skjaeveland, 2007, *Criteria for three-fluid configurations including layers in a pore with nonuniform wettability*, Water Resources Research, **43**(12).

Van Dijke M.I.J. and K.S. Sorbie, 2003, *Three-phase capillary entry conditions in pores of noncircular cross-section*, Journal of Colloid and Interface Science, **260**(2), 385-397.

Van Dijke M.I.J. and K.S. Sorbie, 2006, *Existence of fluid layers in the corners of a capillary with non-uniform wettability*, J. Coll. Int. Sci., **293**(2), 455-463.

Welge H.J., 1952, *A Simplified Method for Computing Oil Recovery by Gas or Water Drive*, Trans AIME, **195**, 91-98.

Wilkinson D. and J.F. Willemsen, 1983, *Invasion percolation: a new form of percolation theory*, Journal of Physics A-Mathematical and General, **16**(14), 3365-3376.

Wu K.J., M.I.J. Van Dijke, G.D. Couples, Z.Y. Jiang, J.S. Ma, K.S. Sorbie, J. Crawford, I. Young and X.X. Zhang, 2006, *3D stochastic modelling of heterogeneous porous media - Applications to reservoir rocks*, Transport in Porous Media, **65**(3), 443-467.

Zhao X., M.J. Blunt and J. Yao, 2010, *Pore-scale modeling: Effects of wettability on waterflood oil recovery*, Journal of Petroleum Science and Engineering, **71**(3-4), 169-178.

Zhou D., M. Blunt and F.M. Orr, 1997, *Hydrocarbon Drainage along Corners of Noncircular Capillaries*, Journal of Colloid and Interface Science, **187**(1), 11-21.

Zisman W.A., 1964, *Relation of the Equilibrium Contact Angle to Liquid and Solid Constitution*. In Contact Angle, Wettability, and Adhesion, Washington, D.C.: American Chemical Society

APPENDIX A -NETWORK MODELLING TOOL WITH GUI

A.1 Introduction

The two-phase pore-scale network modeling tool (2Phase-NWM-HWU) has been written in C++ from scratch and has a graphical user interface (GUI - see main dialogue window in **Figure A.1**).

There are several input data types needs to be supplied before running this tool:

- Pore network data (See **Section A.2** for details)
- Wettability distribution (See **Section A.3** for details)
- Linear system solver parameters
- Two- phase floods parameters
- Shape characterization
- Oil layers existence criteria
- Wettability sensitivity parameters (See **Section A.4** for details)

List of output data:

- *.csv files:
    - Flood data: S_w, k_{rw}, k_{ro}, P_c
    - Displacement statistics
    - Pore occupancy statistics
    - Cluster statistics
- real-time plotting of $k_{ro,w}$ and P_c (main dialogue window)
- real-time 3D visualization of network two-phase occupancy (main dialogue window)

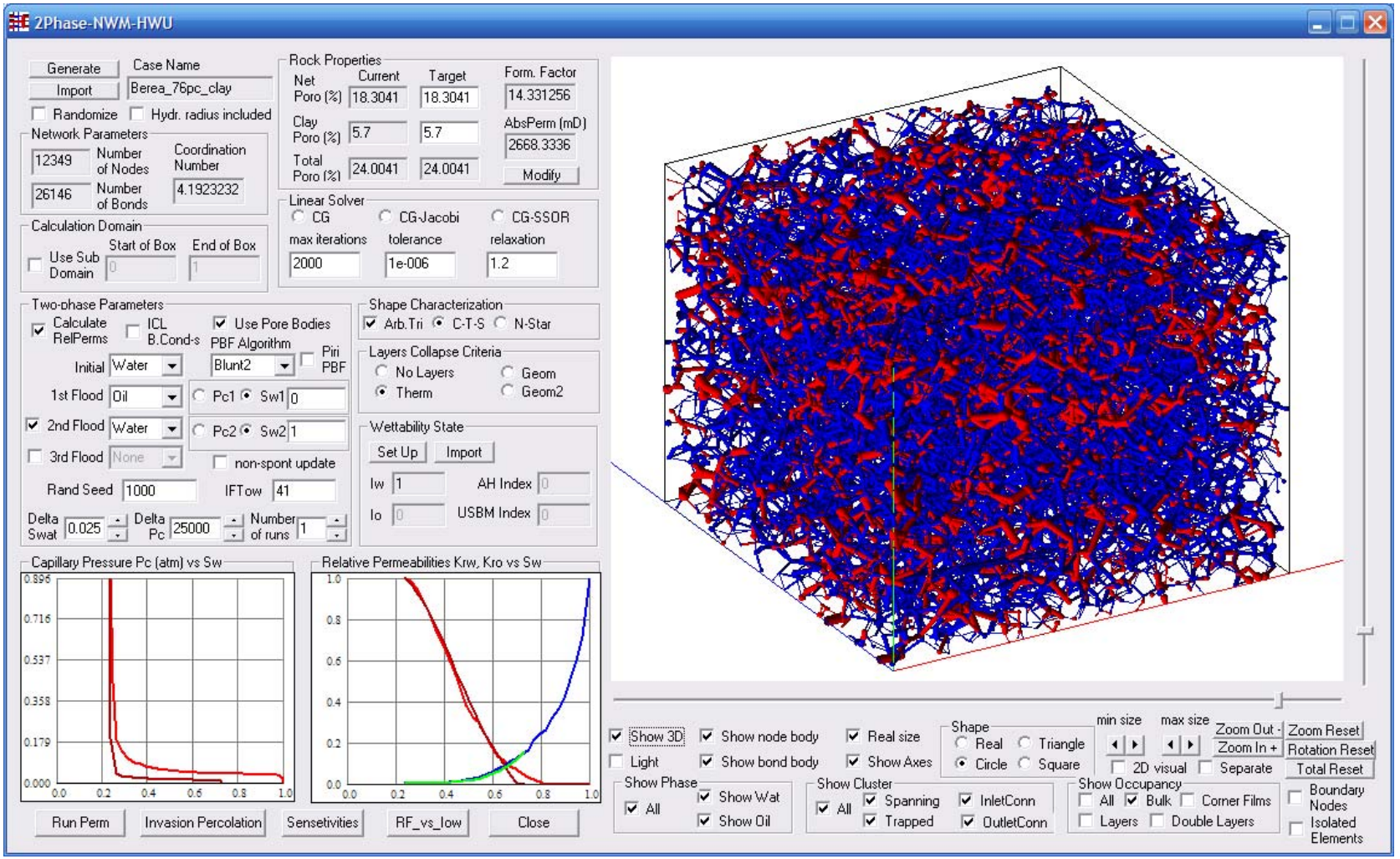

Figure A.1 2Phase-NWM-HWU - Main dialogue window: input and output.

A.2 Network Data

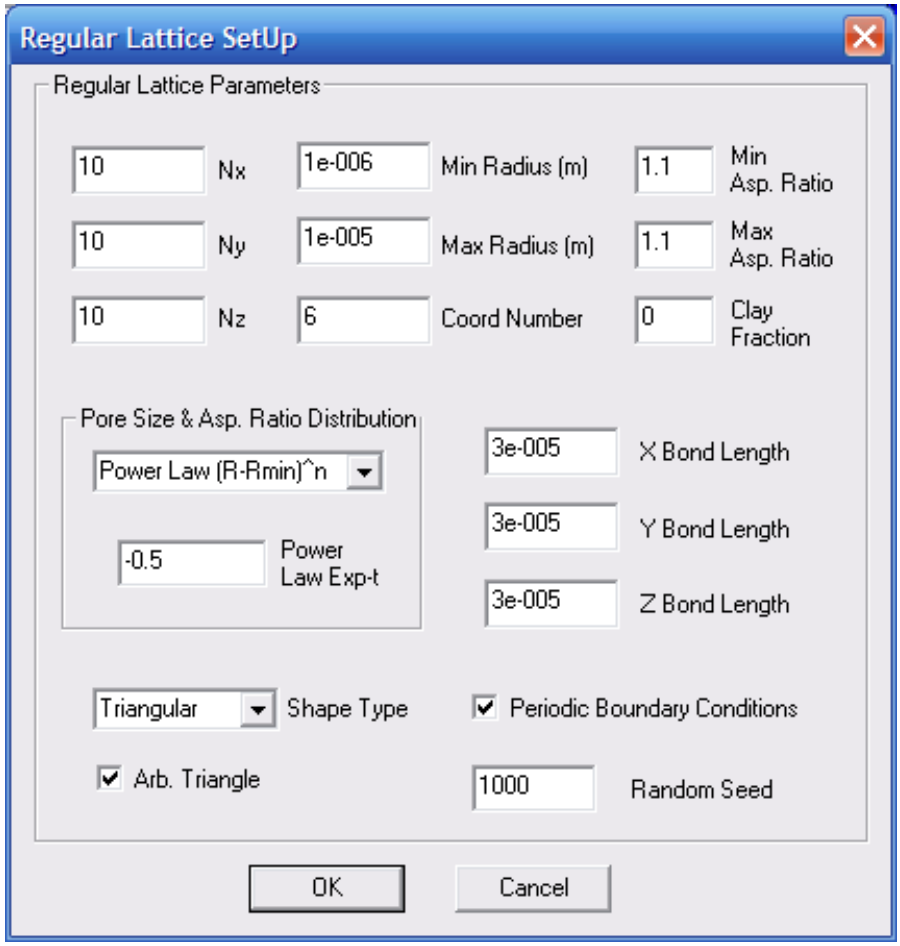

Figure A.2 Regular lattice set up - input dialog window.

Network data can be imported (button "Import" **Figure A.1**) from four files: netname_link1.dat, netname_link2.dat, netname_node1.dat, netname_node2.dat with predefined format (Piri and Blunt 2005a). In addition, the optional input parameter hydraulic radius R_h can be imported as well, which is required for the n-cornered star shape approximation.

The network can also be generated by using *Regular Lattice Setup* dialogue window (**Figure A.2)** which is opened from the main window by pressing the button "*Generate*". This requires specification of lattice size (number of nodes in each direction), PSD, bond lengths, coordination number and type of cross-sectional shapes.

A.3 Wettability Distribution

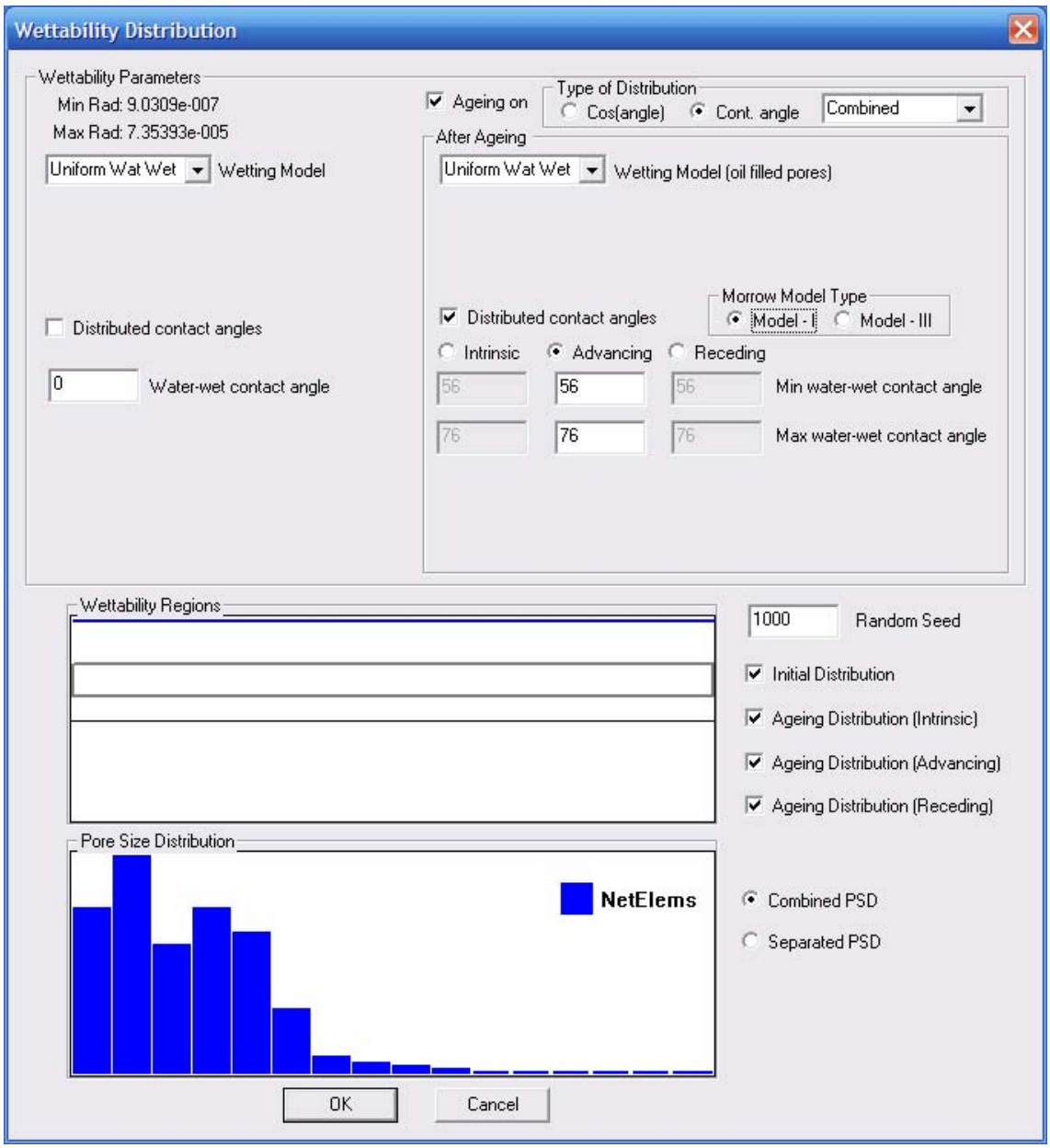

Figure A.3 Wettability distribution - input dialog window.

Wettability distribution can be specified in *Wettability Distribution* dialogue window (**Figure A.3**) which is opened from the main window by pressing the button "*SetUp*" in the *Wettability State* box. Initially, the distribution of primary drainage contact angle is specified. If the ageing option is selected, then advancing and receding contact angles after the ageing have to be defined as well.

Alternatively, the wettability for each pore element can be specified by importing two files of specific format (one for pore bodies and one for pore throats) by pressing the button "*Import*" in *Wettability State* box in the main dialogue window (**Figure A.1)**.

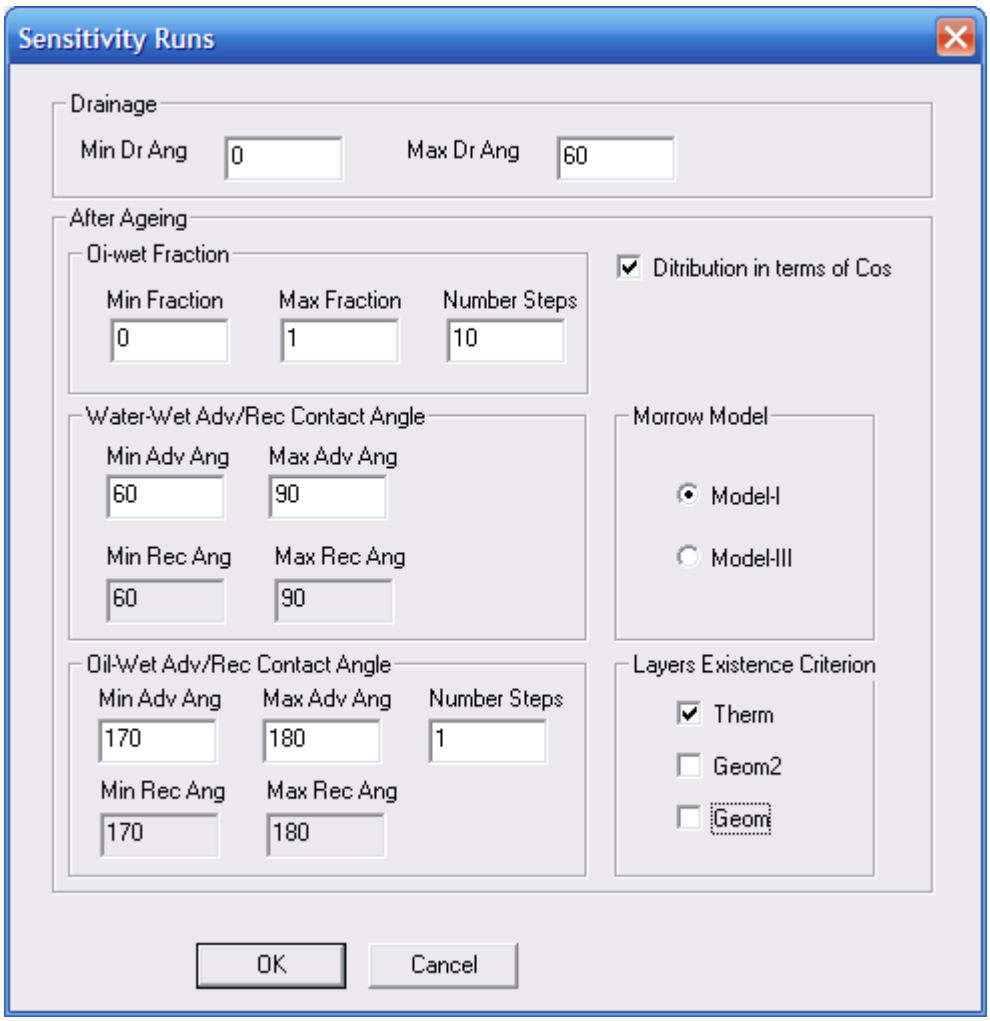

Figure A.4 Sensitivity runs - input dialogue window: settings for sensitivity to oil-wet fraction α=0..1 with advancing contact angle $\theta_a \in \left[170^o, 180^o\right]$ and *Therm* oil layers existence criterion.

A.4 Sensitivity Runs

Parameters for sensitivity runs can be specified in the *Sensitivity Runs* dialogue window (**Figure A.4, Figure A.5**) which is opened from the main window by pressing the button "*Sensitivities*". Parameters for all sensitivities considered in this thesis can be defined in this window, e.g.:

1) Sensitivity to oil-wet fraction α=0..1 with the strongly oil-wet advancing contact angle distribution $\theta_a \in [170^o, 180^o]$ (**Figure A.4**)

2) Sensitivity to average advancing contact angle θ_a^i for a uniformly oil-wet system (α=1.0) (**Figure A.5**)

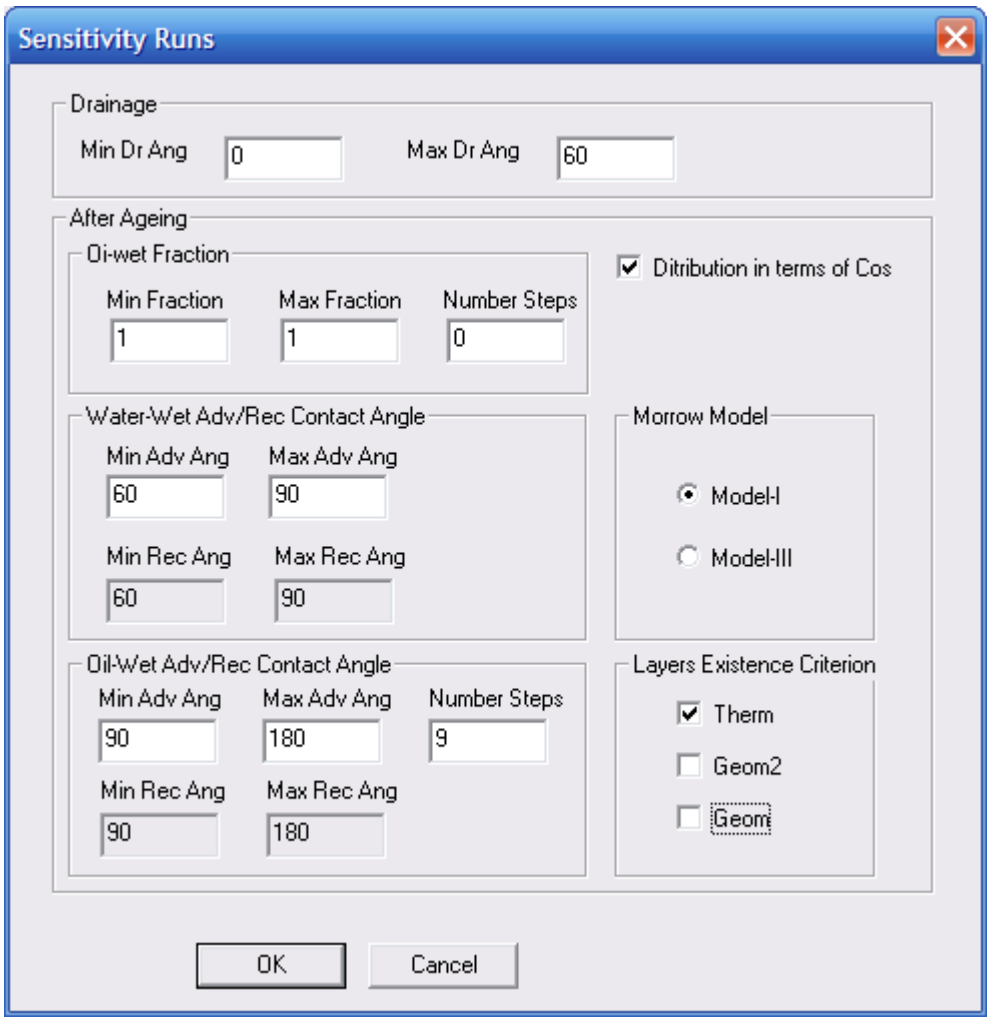

Figure A.5 Sensitivity runs - input dialogue window: settings for sensitivity to average advancing contact angle θ_a^i=95°,..,175° with oil-wet fraction α=1 and *Therm* oil layers existence criterion.

APPENDIX B -EQUATIONS

B.1 Right boundary of the shapes envelope

Here, we derive the inequality for the right boundary of the shapes envelope on (*G,H*) plot (**Figure 3.4**):

$$G \le \frac{H - H^2}{\pi}. \tag{B.1}$$

This can be obtained from one of the inequalities collected by Scott and Awyong (2000):

$$A \le R_{ins}\left(L - \pi R_{ins}\right). \tag{B.2}$$

Firstly, multiply both sides of Eq.(B.2) by $A/(L^2R^2_{ins})$ and replace $A/(R_{ins}L)$ with dimensionless hydraulic radius H and A/L^2 with shape factor G:

$$H^2 \le H - \pi G. \tag{B.3}$$

Then Eq. (B.1) can be derived from Eq. (B.3) very easily.

B.2 Half Angle Expression for n-Star

Here, we derive expression for *n*-cornered star half-angle γ:

$$\gamma = f(n,G) = -\frac{\pi}{2n} + \frac{1}{2}\cos^{-1}\left(\cos\left(\frac{\pi}{n}\right) - 8nG\cdot\sin\left(\frac{\pi}{n}\right)\right). \tag{B.4}$$

Eq. (B.4) can be obtained from the second Eq (3.2) for the n-cornered star shape factor. Applying the following trigonometry rule:

$$\sin\alpha\cdot\sin\beta = \frac{1}{2}\left(\cos\left(\alpha-\beta\right) - \cos\left(\alpha+\beta\right)\right). \tag{B.5}$$

the second Eq (3.2) can be rearranged as follows

$$4n\sin\left(\frac{\pi}{n}\right)G = \frac{1}{2}\left(\cos\left(\frac{\pi}{n}\right) - \cos\left(2\left(\gamma + \frac{\pi}{2n}\right)\right)\right). \tag{B.6}$$

Then it can be rearranged as

$$\cos\left(2\left(\gamma + \frac{\pi}{2n}\right)\right) = -8Gn\sin\left(\frac{\pi}{n}\right) + \cos\left(\frac{\pi}{n}\right). \tag{B.7}$$

Eventually, Eq. (B.4) can be derived straightforward from Eq. (B.7).

B.3 Poisson's equation for single phase conductance calculation

To derive the Poisson equation for single phase conductance calculations, we have made the following assumptions

- steady-state laminar flow of incompressible fluid
- constant viscosity
- gravity forces are neglected
- fluid flow is parallel to capillary tube medial axis (Z axis)

- no-slip boundary conditions at the pore wall.
- constant pressure gradient along the pore

For laminar flow of a Newtonian fluid the continuity and the Navier-Stokes equations are given as following:

$$\begin{aligned} &\frac{\partial \rho}{\partial t} + \nabla \cdot \left(\rho \overline{v} \right) = 0, \\ &\rho \left(\frac{\partial \overline{v}}{\partial t} + \overline{v} \cdot \nabla \left(\overline{v} \right) \right) = -\nabla p - \mu \Delta \overline{v} + \left(\frac{1}{3} \mu + \mu^{v} \right) \nabla \left(\nabla \cdot \overline{v} \right) + \rho \overline{g}, \end{aligned} \tag{B.8}$$

where ρ – fluid density, μ – dynamic viscosity, μ^{v}- volume viscosity, g – gravity constant, $v = (v_x, v_y, v_z)$– fluid velocity vector.

Assuming steady-state flow ($\partial \overline{v} / \partial t = 0,\ \partial \rho / \partial t = 0$) of an incompressible fluid (ρ=const) and that gravity forces are negligible (g=0) Eq.(B.8) can be reduced to:

$$\begin{aligned} &\nabla \cdot \overline{v} = 0, \\ &\rho \overline{v} \cdot \nabla \overline{v} = -\nabla p - \mu \Delta \overline{v}, \end{aligned} \tag{B.9}$$

Since flow is parallel to Z axis, the fluid velocity vector becomes $\overline{v} = (0, 0, v_z)$ and Eq. (B.9) is simplified further:

$$\begin{aligned} &\frac{\partial v_z}{\partial z} = 0, \\ &\mu \left(\frac{\partial^2 v_z}{\partial x^2} + \frac{\partial^2 v_z}{\partial y^2} \right) = -\frac{\partial p}{\partial z}, \end{aligned} \tag{B.10}$$

Therefore $v_z = f(x,y)$. We also assume constant viscosity μ and the constant pressure gradient $dp/dz = \Delta P/l$ (ΔP pressure drop alone the tube and l is the tube length). Thus, Eq. (B.10) can be rewritten in terms of a "reduced" velocity u (dimension – length^2):

$$\begin{aligned} &u = v_z \frac{\mu l}{\Delta P}, \\ &\left(\frac{\partial^2 u}{\partial x^2} + \frac{\partial^2 u}{\partial y^2} \right) = -1, \end{aligned} \tag{B.11}$$

Finally, we assume no-slip boundary conditions at the pore walls, which means that u=0 at the boundary.

$$\begin{aligned} &u\big|_{\Gamma = \partial\Omega} = 0, \\ &\Delta u = -1,\ (x, y) \in \Omega \end{aligned} \tag{B.12}$$

B.4 Shape Factor for Elementary Triangle in n-Star

Here we derive the expression for the shape factor $G^t_{n,\gamma}$ (Eq. (3.14)) of an elementary triangle COD (**Figure 3.3**):

$$G^t_{n,\gamma} = \frac{1}{2}\frac{\sin(\gamma)\sin\left(\frac{\pi}{n}\right)\sin\left(\gamma+\frac{\pi}{n}\right)}{\left(\sin(\gamma)+\sin\left(\frac{\pi}{n}\right)+\sin\left(\gamma+\frac{\pi}{n}\right)\right)^2},\ 0<\gamma\le\frac{\pi}{2}-\frac{\pi}{n}. \tag{B.13}$$

Based on the shape factor definition and **Figure 3.3** we can obtain:

$$G^t_{n,\gamma} = \frac{A^t_{n,\gamma}}{\left(L^t_{n,\gamma}\right)^2},\ A^t_{n,\gamma}\ A^t_{n,\gamma} = \frac{1}{2}DC\cdot DO\cdot\sin\left(\gamma+\frac{\pi}{n}\right),\ L^t_{n,\gamma} = DC+DO+OC, \tag{B.14}$$

where $A^t_{n,\gamma}$ and $L^t_{n,\gamma}$ - area and perimeter of triangle COD respectively, $DO=R_{ins}$, while DC and OC can be derived from trigonometry (**Figure 3.3**):

$$DC = \frac{R_{ins}\sin\left(\frac{\pi}{n}\right)}{\sin(\gamma)},\ OC = \frac{R_{ins}\sin\left(\gamma+\frac{\pi}{n}\right)}{\sin(\gamma)}. \tag{B.15}$$

Expressions for $A^t_{n,\gamma}$ and $L^t_{n,\gamma}$ can be obtained now by substituting Eq.(B.15) into Eq.(B.14):

$$A^t_{n,\gamma} = \frac{1}{2}\left(R_{ins}\right)^2\frac{\sin\left(\frac{\pi}{n}\right)\sin\left(\gamma+\frac{\pi}{n}\right)}{\sin(\gamma)},\ L^t_{n,\gamma} = R_{ins}\frac{\sin(\gamma)+\sin\left(\frac{\pi}{n}\right)+\sin\left(\gamma+\frac{\pi}{n}\right)}{\sin(\gamma)}. \tag{B.16}$$

Finally, Eq.(B.13) (or Eq.(3.14)) can be derived now by substituting Eq.(B.16) into Eq.(B.14).